Electrochemical and Spectroscopic Studies of Copper Oxide Modified Electrodes for CO_2 Reduction

Liying Wang

A thesis submitted in partial fulfilment of the requirement for the degree of Doctor of Philosophy

University College London

August 2016

I, Liying Wang, confirm that the work presented in this thesis is my own. Where information has been derived from other sources, I confirm that this has been indicated in the thesis.

Signed _____

Date _____

Abstract

The global carbon balance has changed substantially with major increases in atmospheric CO_2 levels by anthropogenic emission, causing growing concerns about global warming and extreme climate issues. This is one of the crucial global challenges in the 21st century. Electrochemical reduction of CO_2 is a promising technology to convert CO_2 to chemicals and fuels. There are various candidate materials for CO_2 reduction, but only copper and copper oxide catalysts are effective for the reduction of CO_2 to hydrocarbons and organic substances. This research aims to explore CuO nanoparticle materials for CO_2 reduction by electrochemical and spectroscopic studies.

Different techniques are used in this research. The electrochemical behaviour of CuO was monitored by cyclic voltammetry. The oxidation states and proportion of different components of copper were investigated by ex situ XPS and Raman spectroscopy. A novel in situ spectroelectrochemical experiment was designed using electrocatalysis and FTIR technique to study adsorption of solution species onto the CuO surface. Two types of buffer solutions with five pH values, from pH 4 to pH 11, were introduced to investigate the appropriate pH conditions for the CO_2 reduction processes.

Based on the present experimental data and further analysis, it reveals the electrochemical behaviour of CuO catalyst, including the reduction reaction equations, proportion of different oxidation states and adsorption species at different applied potentials. The pH 4 solutions shows the most suppression of current magnitude in cyclic voltammograms in CO_2 saturated conditions. CuO was reduced to Cu_2O and Cu at cathodic potential, then oxidised to CuO in pH 4 and 7 solutions, while oxidised to $Cu(OH)_2$ in higher pH solutions after application of one cyclic potential. The lower pH conditions show better stability of CuO catalyst after multi-cyclic sweeps. Therefore, the pH 7, 8 and 9 solutions are shown to be suitable pH conditions for CO_2 reduction on CuO catalyst. The major liquid phase product of CO_2 electrochemical reduction obtained in our study was formic acid. Combining our research results, a reaction pathway is proposed. Adsorbed CO_2^- is the first reduction step and carboxyl is an important intermediate to form formic acid.

Finally, several future areas of research are proposed to improve the understanding of the CO_2 reduction processes on CuO catalyst. Copper oxide materials of different oxidation states and mixed phases can be used to clarify the active sites. Gas phase products and quantitative liquid phase products can be measured to study the reduction rate and efficiency.

Acknowledgements

I would like to express my sincere gratitude to all the people who help and support me for this thesis.

Firstly, I want to thank my primary supervisor Dr. Katherine Holt for her guidance, support and encouragement. I appreciate her background knowledge and suggestions on the experimental work. She has been very patient and helpful in our discussions. I have learned a lot from the last four years study.

I also wish to thank Dr. Josie Goodall, Dr. Nathan Hollingsworth and Dr. Thomas Varley for their expertise and advice. I am thankful to my colleagues in Katherine's group for their help from all aspects. I will keep all the cheerful time in heart that we spend on attending conferences and group activities. I would like to express my thanks to Dr. Zhimei Du for encouragement and advice. I would like to thank all the technical and supporting staff in UCL Chemistry for their instructions and trainings on operating departmental facilities.

I would like to thank my friends for their moral support and practical help. A special thanks to my landlady and landlord for providing me a warm, comfortable and friendly place to stay, and my roommates for their company and pressure sharing.

This work is supported under M3S Industrial Doctorate Centre at UCL and China Scholarship Council. I express my gratitude to my financial sponsors.

Last but not least I would like to thank my parents for their love, support and encouragement whenever needed. Without them it would not be possible for me to complete this work.

Table of Contents

List of Figures

List of Tables

Chapter 1

Introduction

1.1 Aims and objectives

Electrochemical reduction of carbon dioxide (CO_2) is an attractive method to remove and convert CO_2 under mild conditions. Many catalyst materials have been investigated for CO_2 reduction. This Ph.D. project focuses on electrochemical and spectroscopic studies of CuO nanoparticle (NP) materials for CO_2 reduction. Different measurements on electrochemical and spectroscopic methods are presented in the following chapters of this thesis.

The objectives of this Ph.D. project are as follows:

1. To design proper experimental setup for CO_2 reduction on CuO catalysts by modifying electrodes with the catalyst and exploring the potential dependence of the redox response.

2. To explore the CuO catalyst performance for CO_2 reduction in different electrolytes with various measurements, including cyclic voltammetry, X-ray photoelectron spectroscopy, Raman spectroscopy and infrared spectroscopy.

3. To clarify the surface bonded species and the influence on CO_2 reduction.

4. To gain fundamental understanding of the mechanism of CO_2 reduction on the CuO catalyst surface and the relationship of catalyst oxidation states and composition.

1.2 Carbon and carbon dioxide in nature

Carbon dioxide occurs in nature as part of the carbon cycle in the Earth's system [1] and serves as source of carbon for photosynthesis of plants and crops [2]. Most of the Earth's carbon is stored in carbonate rocks (65,000,000 gigatons (Gt)), shales (8,000,000 Gt), and dissolved CO_2 in the oceans (38,000 Gt) [1]. The amount of gaseous carbon dioxide stores 750 Gt of Earth's carbon in the atmosphere [1], which is the $\sim 10^{-5}$ of the total carbon.

The residence times of carbon in its different forms are compared. Most of the carbon cycle takes place between the atmosphere and the biosphere on a time scale of under

100 years [1]. The residence time for carbon in the solid Earth is approximately 10^8 years [1]. The atmospheric residence time of CO_2 through photosynthesis and dissolution into the oceans is about 4 years [1]. The main sinks for atmospheric carbon dioxide are uptake by plants through photosynthesis and dissolution into the oceans, in which the annual fluxes are estimated to be 110,000 Gt and 90,000 Gt, respectively [1]. The main sources are plant respiration and release of dissolved CO_2 back into the atmosphere from oceans [1].

The concentration of carbon dioxide in the atmosphere has risen from around 277 parts per million (ppm) in 1750 — the beginning of the Industrial Era [3] to 385 ppm in 2008 [4, 5], 395 ppm in 2013 [4], and 406 ppm in 2016 [4]. Daily averages went above 400 ppm for the first time in May 2013 from Mauna Loa station [6]. The concentration of CO_2 is projected to be around 530 ppm in 2050 and 780 ppm in 2100 [7]. The surface average atmospheric CO_2 concentration grows substantially since the 18th century, which is shown in Figure 1-1.

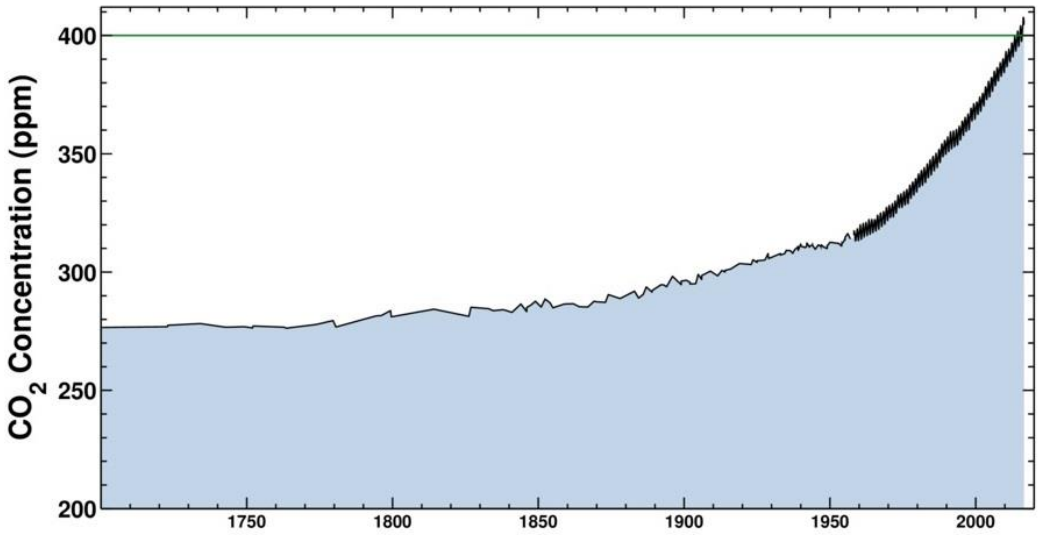

Figure 1-1. Surface average atmospheric CO_2 concentration. Ice-core data before 1958, Mauna Loa data after 1958, measured as a dry mole fraction defined as the number of molecules of carbon dioxide divided by the number of molecules of dry air multiplied by one million (ppm) [6].

The atmospheric CO_2 increase before the Industrial Era was initially caused by the release of carbon to the atmosphere from deforestation and some land-use-change

activities [8]. Human activity has introduced new sources of carbon dioxide into the carbon cycle, most importantly the combustion of fossil fuels. The emissions from fossil fuel combustion became dominant source of anthropogenic emissions to the atmosphere from 1920s and continued to increase till present [9, 10]. The International Energy Agency (IEA) reported 43% of the CO_2 was generated from the burning of coal fuels, 36 % was from oil and 20% from gas [11]. The IEA also reported that within the total CO_2 emission, 41% of the CO_2 generated from electricity generation and heat, 20% from industry, 22% from transport, 6% from residential, and 10% from other sources including commercial/public services, agriculture, etc. [11]. At the same time, deforestation both releases CO_2 and reduces the capacity of the greatest sink for CO_2 removal, photosynthesis [12]. This suggests that the sinks for the removal of carbon dioxide from the Earth's atmosphere, though able to adapt by increasing the removal rate, cannot accommodate the increased rate of emissions [1]. The highest growth rate was recorded in the decade from 2006 to 2015, the average of the growth rate is as high as 2.20 ppm·yr^{-1} [4].

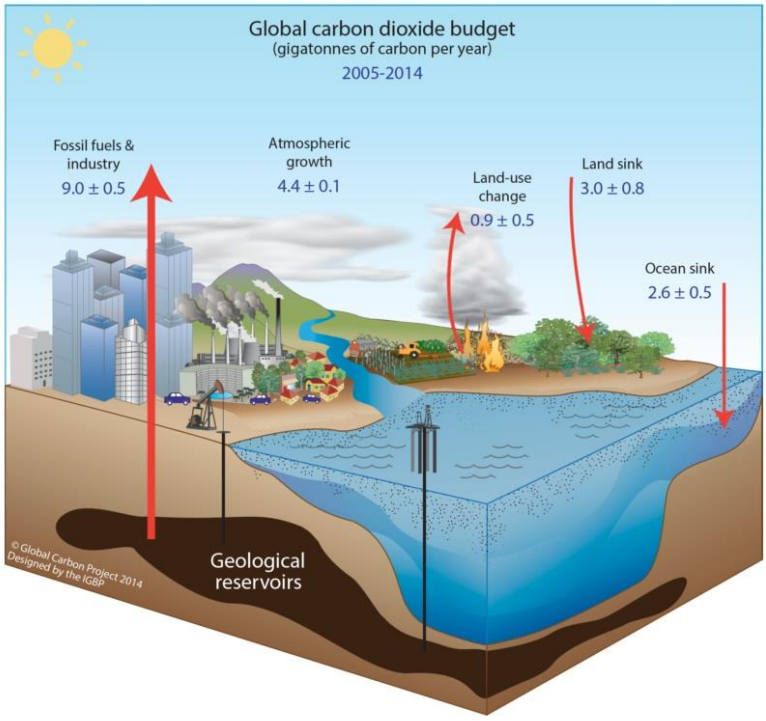

Figure 1-2. Schematic representation of the overall perturbation of the global carbon cycle caused by anthropogenic activities, averaged globally for the decade 2005-2014. All fluxes are in units of Gt·yr^{-1} [13].

The global carbon budget presented in Figure 1-2 refers to the variations and trends in the perturbation of CO_2 in the atmosphere. This would quantify the input of CO_2 to the atmosphere by emissions from human activities, the growth of CO_2 in the atmosphere, and the resulting changes in the storage of carbon in the land and ocean reservoirs in response to increasing atmospheric CO_2 levels, climate and variability and other anthropogenic and natural changes [13]. The arrows in Figure 1-2 represent (1) emissions from fossil fuels combustion and oxidation and cement production (E_{FF}); (2) emissions from deforestation and other land-used change (E_{LUC}); (3) the growth of carbon in the atmosphere (G_{ATM}); (4) the uptake of carbon by the "sinks" in the ocean (S_{OCEAN}) and land (S_{LAND}). The global emissions and their partitioning among the atmosphere, ocean and land are in balance [13]. It is a straight forward way to calculate the growth amount of carbon in the atmosphere by the equation given below.

$$E_{FF} + E_{LUC} = G_{ATM} + S_{OCEAN} + S_{LAND} \quad (1\text{-}1)$$

Burning 1 ton of carbon in fossil fuels releases more than 3.67 tons of carbon dioxide [14]. Compared with the amount of CO_2 emission from fossil fuels in 1900, the value tripled by 1950 and increased 12 times by 2000 [15]. The IEA reported the total CO_2 emission had reached 30.3 Gt in 2010 [11], 31.6 Gt in 2012 [16]. The emissions are predicted to rise to over 50 Gt by 2050 by the Organisation for Economic Co-operation and Development (OECD) [7]. Since the amount of CO_2 emissions from anthropogenic sources is increasing, the CO_2 concentration in atmosphere is rising fast. One of the major concerns caused by the increasing CO_2 concentration is the impact on global climate. Although there are debates on this topic, many studies have demonstrated the links between CO_2 emission and global climate change [17].

1.3 Carbon dioxide and climate change

Sunlight passes through the Earth's atmosphere and transmits solar energy to Earth in form of solar radiation. Solar radiation is the most important source of thermal energy for the living-beings on earth. The Earth's surface re-emits radiation into the Earth's atmosphere to balance the thermal energy which is accumulated on the Earth's surface. Most of this radiation escapes to outer space, allowing the Earth to cool. But some part of energy is trapped by gases in the air to keep the Earth's surface warm. This series

of energy transfer processes and the warming effect caused by the greenhouse gas is known as the greenhouse effect, which is shown in Figure 1-3 [18].

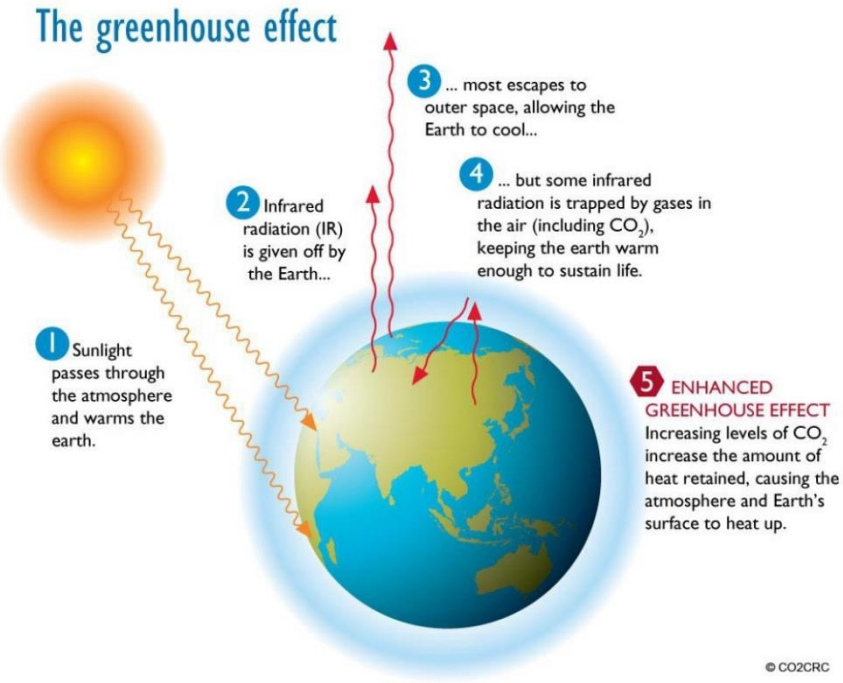

Figure 1-3. An illustration of greenhouse effect and CO_2 emissions are enhancing the greenhouse effect of the atmosphere [18].

The greenhouse gas molecules absorb radiation of wavelengths from 5 to 50 μm, which covers most of the terrestrial radiation (5-20 μm). The gas molecule absorbs radiation and excites to a higher energy level. The excited molecule tends to return to the stable state and emits radiation back to the Earth's surface simultaneously and spontaneously [19]. This leads to the warming effect on the Earth's surface. The greenhouse effect is an important mechanism to keep the Earth's surface warm. However, increasing atmospheric greenhouse gases levels cause increasing amount of heat retained, which further raises the temperature on the Earth's surface, changes the climate, causing unaccommodated consequences for living-beings on Earth.

Several gases contribute to climate change, the three most potent are carbon dioxide (CO_2), methane (CH_4), and nitrous oxide (N_2O), accounting for 98% of the global greenhouse gas emissions covered by Kyoto Protocol (Figure 1-4) [7]. The other three gases, hydrofluorocarbons (HFCs), perfluorocarbons (PFCs), and sulphur hexafluoride (SF_6) account for less than 2%. These gases differ in terms of their

warming effect and their longevity in the atmosphere. As mentioned previously, the lifespan of atmospheric CO_2 is about 100 years, which can impact on the Earth's climate system in long scale. Besides, a larger amount of CO_2 emissions to the atmosphere are produced by anthropogenic activities. Hence CO_2 emissions account for around 75% of global greenhouse gas emissions, shown in Figure 1-3. The Intergovernmental Panel on Climate Change (IPCC) claims that "scientists are 95% certain that humans are the dominant cause of global warming since the 1950s" [8].

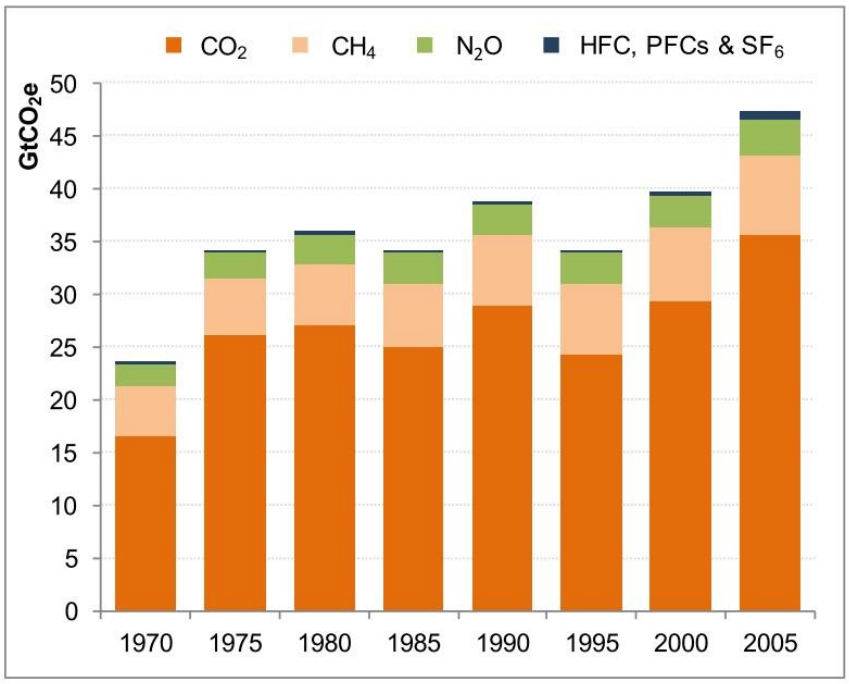

Figure 1-4. Greenhouse gases emissions from 1970 to 2005 [7].

The global mean temperature has risen about 0.7 ℃ to 0.8 ℃ on average above pre-industrial levels [7]. The global mean temperature is expected to increase 2.0 ℃ to 2.8 ℃ at the middle of the century, and 3.7 ℃ to 5.6 ℃ at 2100, compared to the pre-industrial times [7]. The rise of the Earth's surface temperature may lead to a lot negative effects. (1) Water: the increased temperature can encourage the evaporation and precipitation of water, which will lead to decrease water availability and increase drought in mid-latitudes and semi-arid low latitudes. Hundreds of millions of people will be exposed to increased water stress [20]. (2) Ecosystems: up to 30% of species at increasing risk of extinction, and cause significant extinctions around the globe eventually. Increased wildfire risk leads to weakening of the overturning circulation

[20]. (3) Food: complex, localised negative impacts on small holders, subsistence farmers and fishers. Tendencies for cereal productivity decrease in low latitudes [20]. (4) Coasts: millions of people could experience increased damage from floods and storms. About 30% of global coastal wetlands will disappear, based on average rate of sea level rise of 4.2 $mm \cdot yr^{-1}$ [20]. (5) Health: There will be increased burden from malnutrition, diarrhoeal, and infectious diseases. Heat waves, floods, and droughts will cause increased morbidity and mortality of diseases [20].

All regions are predicted to suffer significant net damage from unabated climate change according to most estimates [7]. To minimise the impact of global climate change, a long-term target was adopted in 1996 and confirmed by the European Council (EU) in 2005 [21]. The aim of the target is to limit global mean temperature rise to 2 ℃ above pre-industrial levels (EU 2 ℃ target). In order to achieve the EU 2 ℃ target, greenhouse gas concentrations need to be stabilized below 450 ppm or lower of CO_2 equivalent.

1.4 Reduction of carbon dioxide emissions

To achieve the EU 2 ℃ target and minimise the impact of global climate change caused by greenhouse gases, the reduction of anthropogenic CO_2 emissions is an urgent issue faced by scientific researchers. The IPCC suggests a goal of reducing global CO_2 emissions by 50%-85% of the CO_2 level in 2000 to limit the temperature rise about 2 ℃ to 2.4 ℃ by 2050 [22].

Several different approaches have been attempted to reduce CO_2 emissions, such as efficient use of carbon-based energy sources and replace fossil fuels by clean and/or renewable carbon-free energy sources (solar, hydro, biomass and nuclear power). However, all of these approaches face their own challenges from research to practical applications and commercialisation [17]. The development of solar power is limited by inefficiencies of light utilisation and electricity conversion [23]. Hydropower is confined by limited installation locations and would impact on local ecosystems and public community [17]. The conversion of biomass materials to biofuels conflicts with global food shortage [24]. The utilisation of nuclear power suffers a lot of issues from

public acceptance to the disposal of nuclear waste. The Fukushima Daiichi nuclear disaster on 11 March 2011 has aroused great controversy for nuclear safety and nuclear power development around the world. Several countries announced to pause or phase out their nuclear power plants in construction or operation [17]. In this case, either technical or societal issues of these clean and/or renewable energy technologies slow their application on modern industries and replacement of traditional fossil fuel energy sources. Although some of these issues may be overcome in the future, we still need to face the reality that the replacement of fossil fuels is not a mature scheme at present.

CO_2 post treatment technology has been gaining attention around the world. One approach is called CO_2 capture and storage (CCS). CCS is a carbon negative technology to capture CO_2 from anthropogenic emission sources by a gas separation process prior to release to the atmosphere and transport to a storage location and long-term isolation from the atmosphere [25]. Figure 1-5 illustrates a CCS pilot project launched in Lacq basin in France [17, 26].

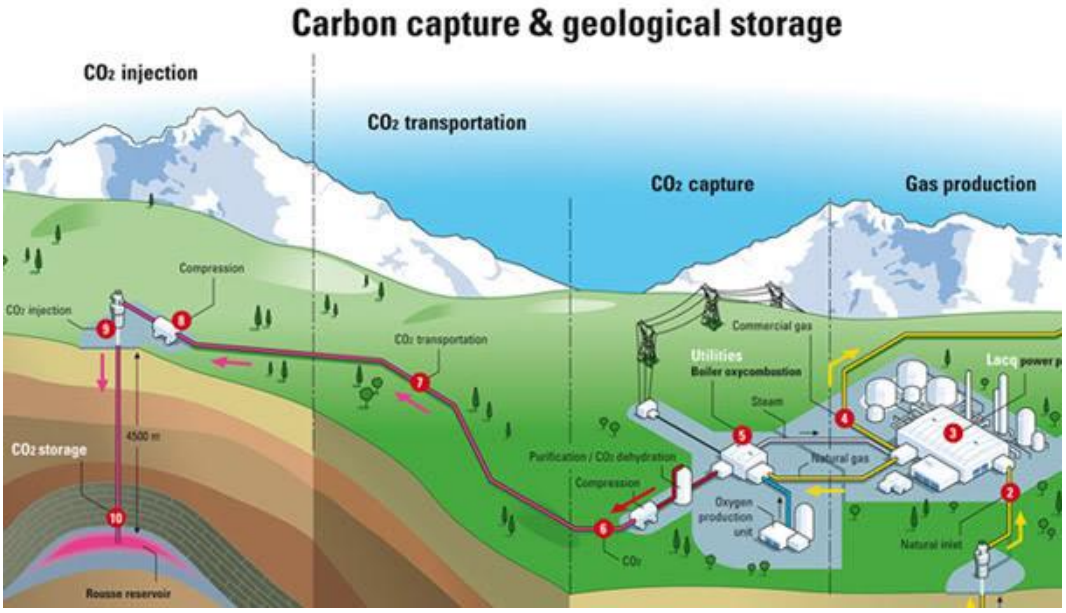

Figure 1-5. An illustration of Lacq CCS pilot project, showing CO_2 capture from a power station, transportation, and injection to storage in an underground reservoir [17].

The complete CCS path includes gas production, CO_2 capture, CO_2 transportation, and CO_2 injection for storage [26]. However the development of CO_2 capture is still in its early stage. The low capacity and efficiency of CO_2 capture materials are the main challenge in research. The CO_2 capture capabilities of various materials have been

investigated, including monoethanolamine and calcium oxide as representative chemical sorbents, zeolites, activated carbon and metal-organic frameworks as representative physical sorbents [17]. However, some of these CO_2 capture materials require high energy consumption and/or produce corrosive, toxic products. A compromise is needed between material performance and costs, energy consumption and environmental impact [17]. Despite recent advances in CCS, it still faces many problems and is not ready to be launched in practice.

CCS provides a solution to the current problem of CO_2 emissions and allows whole human society to enjoy the benefits from burning fossil fuels from daily life to industrial utilisation. Actually, the process reduces the atmospheric CO_2 concentration but the net amount of CO_2 emissions is not changed by the physical storage. Another prospective approach to reduce net CO_2 amount is chemical conversion of CO_2 to chemical feedstocks. CO_2 is the most oxidised form of carbon, and therefore the only chemical transformation at normal energy is chemical reduction. A wide range of CO_2 conversion techniques have been attempted as listed below [27].

(1) Chemical reduction by metals which occurs at relatively high temperatures, e.g. [28]

$$2Mg + CO_2 \rightarrow 2MgO + C \quad (1\text{-}2)$$

$$Sn + 2CO_2 \rightarrow SnO_2 + 2CO \quad (1\text{-}3)$$

$$2Na + 2CO_2 \rightarrow Na_2C_2O_4 \quad (1\text{-}4)$$

(2) Thermochemical chemical conversion, e.g. [29]

$$CO_2 \xrightarrow{Ce^{4+},\ T>900^oC} CO + \frac{1}{2}O_2 \quad (1\text{-}5)$$

(3) Radiochemical method, e.g. [30, 31]

$$CO_2 \xrightarrow{\gamma\text{-Radiation}} HCOOH，\ HCHO \quad (1\text{-}6)$$

(4) Photochemical conversion, e.g. [32]

$$CO_2 \xrightarrow{h\upsilon} CO，\ HCHO，\ HCOOH \quad (1\text{-}7)$$

(5) Biochemical conversion, e.g. [33]

$$CO_2 + 4H_2 \xrightarrow{Bacteria} CH_4 + 2H_2O \quad (1\text{-}8)$$

The bacteria Methanobacterium thermoautotrophicum can be immobilized in a fixed bed or on hollow fibres, and fed stoichiometric ratios for the reaction attaining 80% of the theoretical yield [27].

(6) Electrochemical conversion, e.g. [34]

$$CO_2 + xe^- + yH^+ \xrightarrow{eV} CO,\ HCOOH,\ (COOH)_2 \quad (1\text{-}9)$$

(7) Bio-photochemical conversion, e.g. [35]

The "bio-" part of the energy relies on catalysis and enzyme.

$$CO_2 + \text{oxoglutaric acid} \xrightarrow{h\upsilon} \text{isocitric acid} \quad (1\text{-}10)$$

(8) Photo-electrochemical conversion, e.g. [36]

$$CO_2 + 2e^- + 2H^+ \xrightarrow{eV,\ h\upsilon} CO + H_2O \quad (1\text{-}11)$$

Other products are possible in photo-electrochemical conversion, the products distribution and yields depend on many factors, such as catalyst materials, morphology of catalyst surface [37].

(9) Bio-electrochemical conversion, e.g. [38]

$$CO_2 + \text{oxoglutaric acid} \xrightarrow{\text{enzyme, eV}} \text{isocitric acid} \quad (1\text{-}12)$$

(10) Bio-photoelectrochemical conversion, e.g. [39]

$$CO_2 \xrightarrow{\text{enzyme, eV, } h\upsilon} HCOOH \quad (1\text{-}13)$$

Among various possible approaches, the electrochemical reduction of CO_2 seems to be an attractive method for the removal and conversion of CO_2 under mild conditions [27, 40]. Developed catalysts for electrochemical reduction of CO_2 can produce carbon-based sources for industrial chemical feedstocks and energy sources (fuels). In such carbon-based energy cycles (Figure 1-6), energy from renewable power can be used to reduce CO_2 from captured and produce external hydrogen to render its viable and sustainable [41].

Figure 1-6. Clean carbon-based energy cycle showing CO_2 capture, electrochemical reduction using clean energy sources to chemicals, fuels and combustion in human society.

The whole process would not release additional CO_2 to the atmosphere. The clean energy sources are stored as chemical energy, which means they can be more widely used. The main advantages of such carbon based fuels compared to storing electricity in batteries or as hydrogen, are the ease of use within existing infrastructures and the higher energy density. Because this involves converting electrical energy to chemical energy, electrochemistry is an important enabling technology. One example of a carbon-based energy cycle is the reduction of carbon dioxide to yield methanol in aqueous solution at room temperature (Equation 1-14), then produce liquid methanol after distillation [42]. The methanol is an important chemical feedstock for several organic compounds and also can be further yielded to fuels, such as dimethyl ether, synthetic gasoline [43].

$$CO_2 + 2H_2O \rightarrow CH_3OH + 1.5O_2 \quad (1\text{-}14)$$

It is clear that CO_2 conversion to liquid fuels is thus an attractive field of research. Hori and coworkers found the direct reduction of CO_2 to hydrocarbons (methane and ethylene) at copper electrode, with the current density of 5-10 $mA \cdot cm^{-2}$ and current efficiency of up to 69% at 0 ℃ [44]. This approach may suggest possible ways to decrease atmospheric CO_2 level to chemical fuels and combat global warming.

1.5 Electrochemical reduction of carbon dioxide

1.5.1 Structure of carbon dioxide and behaviours in aqueous solution

Carbon dioxide is a stable compound with a linear structure, two oxygen atoms covalently bond to the central carbon atom, with the C-O distance of 1.16 Å [45]. According to Freund and Messmer's research, both oxygen atoms are 8.33 e^- and carbon atom is 5.35 e^-, based on Mulliken population analysis [46]. Therefore, the electrons in the C-O bonds are polarized towards the oxygen atoms, which results in low electron density at the carbon atom. The different electronegativities of carbon

and oxygen lead to a partial positive charge on the central carbon atom and a partial negative charge on the oxygen atom [45]. When one electron is added to CO_2 molecule, it forms the CO_2^- anion, both C-O bonds elongating by 0.06 Å, and the bond angle decreasing to 133º [46]. This is due to the extra electron being accommodated on the carbon atom by breaking one double bond, resulting in a new lone pair on oxygen and a single C-O bond. The electron distribution of the CO_2^- anion is 8.62 e^- on the oxygen atoms, and 5.83 e^- on the carbon atom, calculated by Mulliken population analysis [46].

CO_2 is a very weak Lewis acid [47], which is demonstrated by the small formation constant $K_f = 1.7x10^{-3}$ of H_2CO_3 [48], from CO_2 complexation with a water molecule in acidic solution. In neutral solution, OH^- attacks the electrophilic carbon atom to form HCO_3^- [47]. CO_2 is the anhydride of carbonic acid and reacts in aqueous solution with the following reactions [47],

$$CO_2 + H_2O \rightarrow H_2CO_3 \qquad K_f = 1.7x10^{-3} \qquad (1\text{-}15)$$

$$H_2CO_3 \rightarrow HCO_3^- + H^+ \qquad K_{a1} = 4.5x10^{-7} \qquad (1\text{-}16)$$

$$HCO_3^- \rightarrow CO_3^{2-} + H^+ \qquad K_{a2} = 4.8x10^{-11} \qquad (1\text{-}17)$$

Hence, CO_2 saturated solution is acidic, and carbonic acid may lose protons to form bicarbonate and carbonate. In this case, the proton is liberated to the water then decreasing the solution pH. The dissolved species of CO_2 in aqueous solution depends on pH value. The fraction of the dissolved CO_2 related species is plotted as a function of pH value in Figure 1-7 [49].

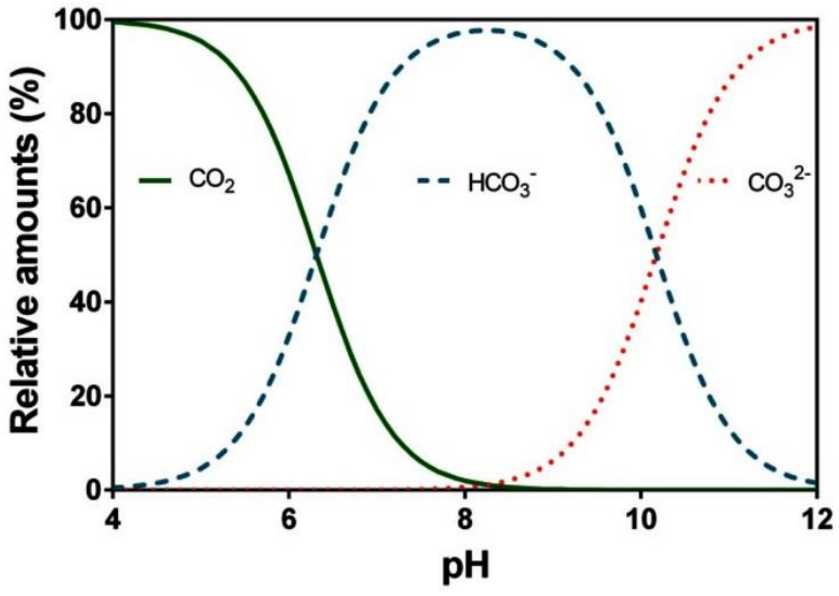

Figure 1-7. Equilibrium distribution of carbon dioxide, bicarbonate and carbonate as a function of pH at room temperature [49].

Two cross points shown in Figure 1-7 are positioned at 6.4 and 10.3 from left to right. For pH<6.4, molecular CO_2 is the predominant species; for pH between 6.4 and 10.3, HCO_3^- is the predominant species; for pH>10.3, CO_3^{2-} is the predominant species in the solution. Since CO_2 dissolves to give different related species in different pH solutions, buffer solution is introduced to CO_2 reduction experiments to balance the formation of H^+ ions and maintaining the pH of solution during the experiments. Bicarbonate solution and phosphate buffer solution (PBS) are normally used in CO_2 reduction experiments.

1.5.2 Carbon dioxide reduction reactions

The nature of reduction product has a strong influence on the thermodynamic accessibility from CO_2. Therefore, the number of electrons involved in the reduction processes is particularly important. The CO_2 reduction potentials (vs. Ag/AgCl) of various reactions in pH 7 aqueous solutions at 25 ℃ are given below [27, 50].

$$CO_2 + e^- \rightarrow CO_2^- \qquad E^0 = -2.17\ V \qquad (1\text{-}18)$$

$$CO_2 + 2H^+ + 2e^- \rightarrow CO + H_2O \qquad E^0 = -0.49\ V \qquad (1\text{-}19)$$

$$CO_2 + 2H^+ + 2e^- \rightarrow HCOOH \qquad E^0 = -0.57\ V \qquad (1\text{-}20)$$

$$CO_2 + 4H^+ + 4e^- \rightarrow HCHO + H_2O \qquad E^0 = -0.44\ V \qquad (1\text{-}21)$$

$$CO_2 + 6H^+ + 6e^- \rightarrow CH_3OH + H_2O \qquad E^0 = -0.34\ V \qquad (1\text{-}22)$$

$$CO_2 + 8H^+ + 8e^- \rightarrow CH_4 + 2H_2O \qquad E^0 = -0.20\ V \qquad (1\text{-}23)$$

The value of the CO_2/CO_2^- redox potential is -2.17 V vs. Ag/AgCl, hence the monoelectron reduction mechanism is highly unfavourable [50]. The transfer of one electron (equation 1-18) is highly endergonic, due to the large reorganisational energy required in the irreversible reduction from the linear molecule to the bent radical anion [51]. Pacansky and co-workers calculated that the bond angle of CO_2^- vibrates between 121º and 149º, and the equilibrium bond angle is 135.3º [52]. This geometry difference between linear CO_2 molecule and the radical CO_2^- anion is the reason for the large activation barrier, which should be overcome for the first reduction step to take place [53]. The redox potentials become less negative as the number of electrons involved

in the multielectrons reduction process increases, because the products are thermodynamically stable molecules [27].

The radical anion is a key intermediate in all of the above processes, which is the reason for the high overpotentials required in CO_2 reduction [54]. Hence, as the reaction proceeds via the radical anion intermediate, they are observed at more negative potentials than predicted thermodynamically [50]. The radical anion may be disproportioned to carbon monoxide and carbonate; be protonated leading to formate; or be dimerized to give oxalate, showing in Figure 1-8 [55].

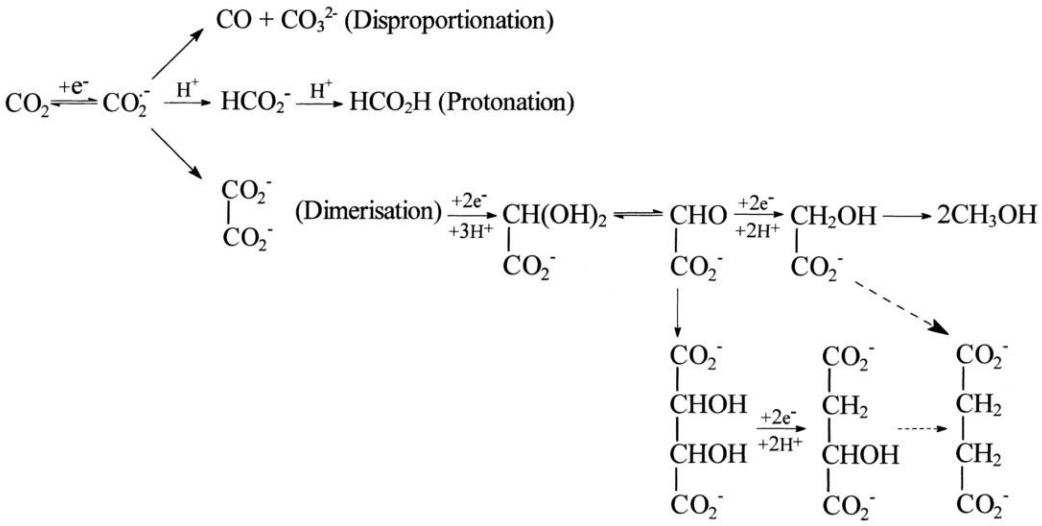

Figure 1-8. Overall electrochemical reduction of carbon dioxide [55].

CO_2 chemical reduction is not a single step reaction. With further reduction of oxalate, possible reduction products are glyoxylate [56], glycolate [57], tartrate [58], malate [59] and methanol [55].

1.6 Reduction of carbon dioxide on metal electrodes

One of the most practical proposed electrocatalytic applications is the electrochemical reduction of carbon dioxide to hydrocarbons and organic substances. Unfortunately, the reduction potential of carbon dioxide is very close to water reduction and so is a competitive process. As mentioned in section 1.5.2, the CO_2 reduction potentials with multielectrons transfer pathways range from -0.49 V to -0.20 V vs. Ag/AgCl. The

hydrogen evolution reaction (HER) is demonstrated in 3 steps in pH 7 solution at 25 ℃ [60, 61].

Volmer electrochemical discharge step: $H_2O + e^- + Me \rightarrow MeH^* + OH^-$ (1-24)

Heyrovsky electrochemical desorption step: $MeH^* + H_2O + e^- \rightarrow H_2 + OH^- + Me$ (1-25)

Tafel catalytic recombination step: $2MeH^* \rightarrow H_2 + 2Me$ (1-26)

where Me means metal, an asterisk (*) indicates that the species is adsorbed on the electrode surface. The potential for the HER is -0.61 V vs. Ag/AgCl. We would like to utilize all the potential to achieve the highest yield. However, increasing the reduction rate of carbon dioxide may also lead to increased reduction of water, which will result in hydrogen formation. The key to this process is to find a stable catalyst with a low overpotential for CO_2 reduction, but with a high overpotential for the HER, allowing further H^+ transfer steps selectively towards forming hydrocarbons and organic substances.

Several studies about CO_2 reduction on metal electrodes have been conducted to find the optimal catalysts for the process. The products of CO_2 reduction vary with the electrode materials and the electrolyte solution used in the reactions [62]. Some other factors, such as electrode surface, the concentration and the stability of the reactants may all influence the reduction reactions [63]. The product selectivity in CO_2 reduction is also influenced by whether reactants are adsorbed and the strength of the adsorption.

Hori, Kikuchi and Suzuki studied CO_2 reduction at a number of metal electrodes and carried out a total analysis of gaseous and soluble products. The electrolyte was aqueous $KHCO_3$ solution, the concentration of which varied from 1.0 M for Cu electrode to 0.5 M for all other electrodes [64]. The galvanostatic electrolyses were carried out using constant current density of 5.0 or 5.5 $mA \cdot cm^{-2}$ [64]. Cd, In, Sn and Pb were found to predominantly produce $HCOO^-$, whereas the major product when using Ag and Au electrodes was CO [64]. At Ni and Fe, hydrogen gas was overwhelmingly produced, with only minor amounts of CO and CH_4 as CO_2 reduction products [64]. Results at Zn were not reproducible and varied over a wide range. The major product of CO_2 production at Cu was CH_4 [64].

Hori continued studies on extensive electrode materials and grouped the metal electrodes by major reaction products [62]. Electrolysis was carried out in 0.1 M $KHCO_3$ aqueous electrolyte, at current density of 0.5 $mA \cdot cm^{-2}$ for Pb and 5.0 $mA \cdot cm^{-2}$ for all other electrodes. Pb, Hg, In, Sn, Cd and Tl gave predominantly formate as the reduction product. Au, Ag, Zn, and Pd reduced CO_2 to CO. At Ga electrode, the only CO_2 reduction product was CO, but hydrogen evolution dominated. Fe, Pt and Ti were all found to negligibly reduce CO_2. At Ni electrode, slight quantities of $HCOO^-$ and CH_4 were formed, but, like Fe, Pt and Ti, the principal reaction was HER. Cu was found to reduce CO_2 to CH_4, which is similar to Hori's previous reports [64], but it was also found to form appreciable amounts of ethylene, some alcohols and formate, and slight amounts of CO. The choice of metal electrode determines the product selectivity, which is summarized in Table 1-1 [62].

Table 1-1. Faradaic Efficiencies (FE) for major CO_2 reduction products at various metal electrodes in CO_2 saturated 0.1 M aqueous $KHCO_3$ solution [62], potential vs. Ag/AgCl.

Electrode	E/V	CH_4 FE/ %	C_2H_4 FE/ %	CO FE/ %	$HCOO^-$ FE/ %	H_2 FE/ %
Cu	-1.64	33.3	25.5	1.3	9.4	20.5
Au	-1.34	0.0	0.0	87.1	0.7	10.2
Ag	-1.57	0.0	0.0	81.5	0.8	12.4
Zn	-1.74	0.0	0.0	79.4	6.1	9.9
Pd	-1.40	2.9	0.0	28.3	2.8	26.2
Ga	-1.44	0.0	0.0	23.2	0.0	79.0
Pb	-1.83	0.0	0.0	0.0	97.4	5.0
Hg	-1.71	0.0	0.0	0.0	99.5	0.0
In	-1.75	0.0	0.0	2.1	94.9	3.3
Sn	-1.68	0.0	0.0	7.1	88.4	4.6
Cd	-1.83	1.3	0.0	13.9	78.4	9.4
Tl	-1.80	0.0	0.0	0.0	95.1	6.2

Ni	-1.68	1.8	0.1	0.0	1.4	88.9
Fe	-1.11	0.0	0.0	0.0	0.0	94.8
Pt	-1.27	0.0	0.0	0.0	0.1	95.7
Ti	-1.80	0.0	0.0	tr.	0.0	99.7

The total current efficiency below 100% is observed, this has been attributed to hydrogen dissolution into the electrode. When CO was the major reduction product, the potentials needed to drive the reaction were generally less negative than those required to produce $HCOO^-$ [62]. The higher potentials required by metals producing mainly formate were balanced by better product selectivity. Cu was the only metal capable of reducing CO_2 to hydrocarbons in significant amounts, but the reduction required a high overpotential and the product distribution was very wide. H_2 was a major side product in the reaction at nearly all metal electrodes, but Hg was the only exception. Hori suggested the electrochemical product selectivity and efficiency of CO_2 reduction reactions are highly dependent on the electrocatalysts and operating conditions [62].

A systematic rule for the electrocatalytic reduction of CO_2 on metal surfaces was suggested by Azuma and colleagues. They measured the reduction products for 32 type of metals in $KHCO_3$ solution at low temperature (0 ℃) [65]. The current efficiency of CO_2 reduction on Ni, Pd, Ag, Pb increased significantly with decreasing temperature. The temperature also affects the distribution of reduction products. The formation of methane and ethylene is observed on almost all metal electrodes measured in their study, but only Cu is able to produce these in relatively high efficiency, while other metals yield primarily formic acid [65]. Based on the dependence of reduction products on various metals, a periodic table for CO_2 reduction was drawn (Figure 1-9) [65].

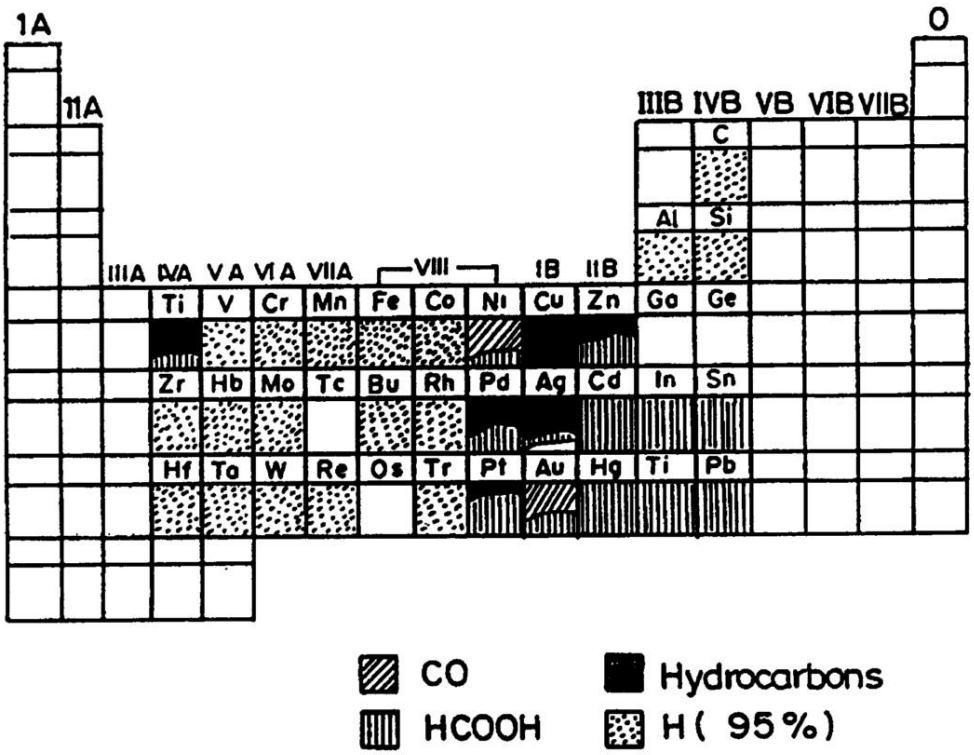

Figure 1-9. Periodic table for CO_2 reduction products at -2.2V vs. saturated calomel electrode (SCE) in low temperature 0.05 M $KHCO_3$ solution [65].

Heavy transition metals in the IIB, IIIB, and IVB groups reduced carbon dioxide to formate [65]. Some of VIII and IB metals are effective for carbon monoxide production [65]. Copper is located between these two groups and acts selectively to reduce CO_2 to hydrocarbons [65]. Similarly, Broden had found a relationship between metals' position in the periodic table and their CO adsorption ability [66]. However, there is no consensus on the molecular mechanism of the metal electrodes and their properties toward electrocatalytic activities and selectivities for CO_2 reduction.

1.7 Carbon dioxide reduction on copper and copper oxide electrode

With the discovery of copper as an active catalyst for CO_2 reduction to hydrocarbons and other organic compounds, electrocatalytic research has focused on this metal, its alloys and oxides.

1.7.1 Carbon dioxide reduction on copper electrode

Copper plays a significant role among other metallic electrode materials in CO_2 reduction. Kaneco and colleagues designed a series of experiments in different solvents using copper as catalyst to produce formic acid, methane, ethylene and carbon monoxide [67-70]. Apart from low hydrocarbons, alcohols and esters, some relatively high hydrocarbons, such as paraffins and olefins containing up to 6 carbon atoms can be formed using Cu electrodes [17, 44, 71, 72, 73].

The FE of products were highly dependent on temperature, type and concentration of electrolyte, electrode potential, and pH value. For example, Hori's group found that increasing temperature from 0 to 40 ℃ caused the FE of CH_4 to decrease from 65% to almost 0, and that of C_2H_4 increased to 20% using copper sheet cathode in 0.5 M $KHCO_3$ CO_2 saturated solutions [71]. In KCl, K_2SO_4, $KClO_4$ and dilute HCO_3^- solutions, C_2H_4 and alcohols are the main products, while in concentrated HCO_3^- and K_2HPO_4 solutions, CH_4 was the predominant product [74]. Using electrochemical measurement, Hori observed that CO was predominantly produced at -1.2 V vs. normal hydrogen electrode (NHE) (-1.4 V vs. Ag/AgCl), while hydrocarbons (CH_4, C_2H_4) and alcohols (CH_3CH_2OH, $CH_3CH_2CH_2OH$) were formed at lower potential below -1.3 V (-1.5 V vs. Ag/AgCl), and the FE of CO decreased [75].

The electrode surface conditions and purity of the catalyst material also have a major effect on catalytic activity in CO_2 reduction. For example, some significant performance differences were found between rough and smooth electrodes and between thermally and non-thermally treated electrodes [78]. Kim found that the formation rate of CH_4 was even influenced by electrode surface cleaning procedures [77]. The electrode that was prepared and cleaned by HCl has higher CH_4 production than HNO_3 treated [77].

It has been reported that modifying the surface of electrodes is an efficient method to promote the activity toward CO_2 reduction [78]. A Cu NP covered electrode was reported to give better selectivity towards hydrocarbons than the copper electrode which surface was electropolished and argon (Ar) sputtered [79]. The electrode was covered with Cu NPs with size of 50-100 nm, creating a surface area 2-3 times greater

than the geometric surface area of the Cu electrode. The cyclic voltammetry measurements in CO_2 showed that the current density of the NP covered electrode at -0.75 V vs. reversible hydrogen electrode (RHE) (-1.36 V vs. Ag/AgCl) was 10 times higher than electropolished electrode. This implied that current density was influenced by surface morphology. The author explained this effect that the roughened surface has greater abundance of undercoordinated sites by density functional theory (DFT) calculations [79].

Regarding the catalytic stability of Cu electrodes for CO_2 reduction, several factors have been identified, such as CO adsorption, electrode purity, the formation of carbon deposits, and the presence of other surface poisoning species [74]. For example, a black film was formed on the surface of the Cu cathode when reduction of CO_2 to CH_4 and C_2H_4 was carried on in 0.5 M $KHCO_3$ solution at a constant potential of -2.0 V vs. SCE (-1.96 V vs. Ag/AgCl) [80]. X-ray photoelectron and Auger electron spectroscopic studies indicated that the film was graphitic carbon, formed by CO_2 reduction through $HCOO^-$. The graphitic carbon deposit would cause decline of Cu electrode's catalytic activity [81].

1.7.2 Carbon dioxide reduction mechanism and reaction intermediates on copper catalysts

Finding out the reduction pathways would promote the understanding of CO_2 reduction mechanism. It is generally agreed that in the electrochemical reduction of CO_2 at solid electrodes, the first electron transfer forms CO_2^- anion radical [70] and is the rate determining step (r.d.s.) [82]. (Asterisk (*) indicates that the species is adsorbed on the electrode surface.)

$$CO_2* + e^- \rightarrow CO_2^-* \quad (1\text{-}27)$$

Several pathways have been proposed for the possible intermediates to form formate or CO for the further reactions. The reaction to form formate (OCHO) could occur by protonation then reduction [83].

$$COO^-* + H^+ \rightarrow OCHO* \quad (1\text{-}28)$$

$$OCHO* + e^- \rightarrow OCHO^- \quad (1\text{-}29)$$

This reaction mechanism would appear on high hydrogen overpotential electrodes (e.g. Hg, Cd, Pb, Tl, In and Sn) [83]. Formate could also be formed by reaction with adsorbed hydrogen, which is an intermediate in the HER [83].

$$COO^{-}* + H* \rightarrow OCHO^{-} \quad (1\text{-}30)$$

Another possible pathway forms CO through carboxyl (COOH). Similarly, this pathway might also be protonation then reduction. But the proton adds to the oxygen atom [84].

$$COO^{-}* + H^{+} \rightarrow COOH* \quad (1\text{-}31)$$

$$COOH* + e^{-} \rightarrow CO* + OH^{-} \quad (1\text{-}32)$$

Also CO could be formed with adsorbed hydrogen [84].

$$COO^{-}* + H* \rightarrow CO* + OH^{-} \quad (1\text{-}33)$$

Hydrocarbons are formed by the interaction between adsorbed CO and atomic hydrogen at the reaction site [70]. An overview of the reaction taking place on the electrode surface can be summarized in Figure 1-10, which shows CO_2 reduction and hydrogen evolution. Two proposed pathways for CO_2 reduction are illustrated in Figure 1-10. One pathway leads to formate and the other leads to adsorbed CO and hydrocarbon products. Figure 1-10 also indicates the adsorbed hydrogen might be involved in the reaction.

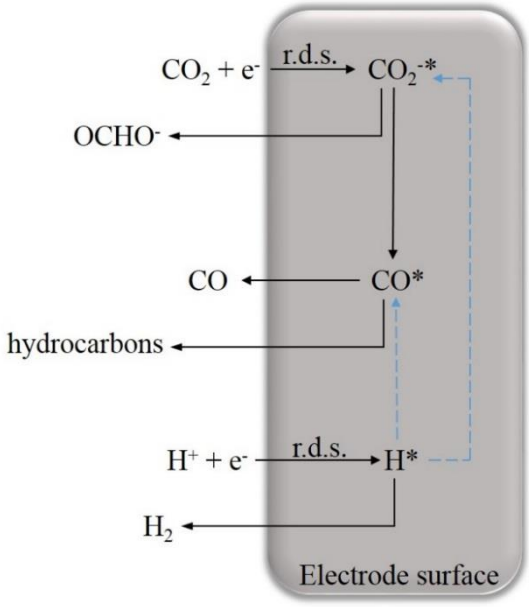

Figure 1-10. Schematic reaction pathways on electrode surface.

Nørksov also suggested two pathways for the mechanism of formic acid production on copper surfaces by theoretical calculations [85, 86]. The DFT calculations predict the intermediate reaction to be key in the pathway [85]. In the carboxyl pathway (C-intermediated pathway), CO_2 and a proton-electron pair react to form adsorbed carboxyl species [85, 86]. This pathway is predicted to require low potential to convert CO_2 on electrode surface at -0.41 V vs. RHE (-1.02 V vs. Ag/AgCl) by computational hydrogen electrode model. The addition of a second proton-electron pair to this adsorbate results in the production of HCOOH. The C-intermediated pathway leads to formation of formic acid and other higher order hydrocarbons. This pathway is illustrated in the following equations [85].

$$CO_2 + H^+ + e^- \rightarrow COOH^* \quad (1\text{-}34)$$

$$COOH^* + H^+ + e^- \rightarrow HCOOH^* \quad (1\text{-}35)$$

The second pathway is explained as an F-intermediated pathway. CO_2 adsorbs as formate. The formic acid will be generated at more negative potential, calculated at -0.61 V vs. RHE (-1.22 V vs. Ag/AgCl). The F-intermediated pathway leads to exclusive formation of formic acid [86].

$$CO_2 + H^+ + e^- \rightarrow OCHO^* \quad (1\text{-}36)$$

From above discussion, CO and formate are formed before further reaction to hydrocarbons at more negative potentials in CO_2 reduction. Researchers carried out some testing experiments to clarify the reaction intermediates to recognize the pathways defined above. Experiments using formate rather than CO_2 as reactant do not show measurable products [75, 87]. Additionally, the experiments starting with CO lead to similar product distribution as reduction of CO_2 [75, 88, 89] but at less negative potential [77]. This is consistent with the calculation model that a barrier for the conversion of CO_2 to CO is predicted, resulting from the adsorption of the COOH species [86]. Hence the C-intermediated pathway would be the proper pathway. It is reported that the potential and pH dependencies of the CO reduction could be determined [84].

Paik reported that H^+ ions was thought to participate in the reduction mechanism of carbon dioxide to formic acid at a mercury electrode [53]. Formic acid was the only reduction product. In neutral solution, all the current was consumed by HCOOH

production. At weakly acidic solutions (pH 4.7), the FE for CO_2 reduction was about 60%. In acidic solutions (pH 1.4), the reaction was dominated by HER, the FE for CO_2 reduction was dropped to around 10%. This implies that protons were involved in the reduction process through being reduced to hydrogen atoms and adsorbed onto the electrode surface. The protons would react with another hydrogen atom to produce H_2 gas, or with CO_2 to produce an intermediate to HCOOH [53].

Jaramillo's group reported the formation of 16 products of CO_2 reduction on copper electrode at neutral solution [90]. Several products have been observed in other studies, such as carbon monoxide, formate, methanol, methane, acetate, acetaldehyde, ethylene, ethanol, allyl alcohol, propionaldehyde, and 1-propanol [90, 91, 92]. The other 5 products, ethylene glycol, glycolaldehyde, hydroxyacetone, acetone, and glyoxal, have never been reported before. In particular, 2 products, glycol and hydroxyacetone are C_2 and C_3 products which require the fewest number of electrons and protons transfer. This indicates that some C-C coupling occurs at early stage of reduction [90]. It requires two electrons to form formate and carbon monoxide, so these two products can be observed at the lowest overpotential. At higher overpotential, more reduction products can be formed, since there are larger kinetic barriers. Hence, C-C coupling rate increased with increasing overpotential initially [90]. Figure 1-11 shows proposed reaction pathway for the reduction of C_2 and C_3 species observed in their study. All possible C_1 species are listed in Figure 1-11. In this proposed pathway, enol-like compounds are major intermediates to produce C_2 and C_3 products. Each electrochemical step contains $2H^+$ and $2e^-$ transfer, to form more reduced products by replacing hydroxyl group to a hydrogen atom [90].

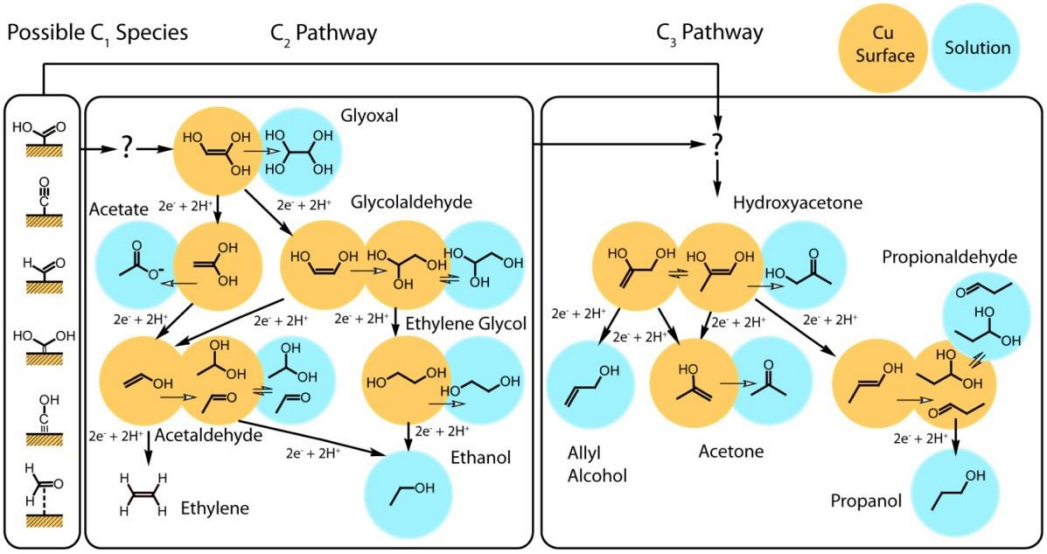

Figure 1-11. Proposed reaction pathway for C_2 and C_3 products with enol-like surface intermediates [90].

1.7.3 Carbon dioxide reduction on copper oxide electrode

It is known that Cu is the only metal catalyst which could efficiently reduce CO_2 to hydrocarbons at moderate experimental conditions. However, polycrystalline Cu has demonstrated poor product selectivity, stability and low efficiency [93]. Hence, a lot of efforts have been made to improve the electrochemical performance of Cu catalysts, and several reports suggested to use copper oxide catalyst.

Frese studied the CO_2 reduction on different copper oxide electrodes. They found that copper oxides show high yield and efficiency for CO_2 reduction to methanol, and the reduction reaction takes place at less negative potential compared with Cu electrode [94]. Terunuma and colleagues found that surfaces containing copper oxide demonstrated higher activity for hydrocarbon production than metallic Cu [95]. This may be caused by Cu metal having high affinity for adsorbed oxygen, so is easily contaminated with organic compounds [95]. However, the Cu_2O surface has a stronger ability to adsorb CO than the Cu surface, and as stated above CO is an important intermediate to yield selected hydrocarbons. Hence, controlling electrode surface with Cu_2O is important in reduction product selectivity. Chang also investigated Cu_2O in electrochemical reduction of carbon dioxide and found that methanol was the only

product [96]. This indicated that Cu(I) is directly involved in the catalytic actions to promote carbon dioxide reduction [96].

Recently, it was indicated from the Lee research group that electrodeposited Cu_2O catalyst could enhance the yield of C_2H_4, and further conversion CO_2 to C_2-C_4 species with FE over 10% [97]. They pointed out that Cu(I) can bond and preserve the reaction intermediates on the electrode surface, which is the key factor for the forming of carbon chains during the reduction [97]. The distribution of products is plotted with respect to the potential from -0.6 V to -1.8 V vs. RHE (-1.2 V to -2.4 V vs. Ag/AgCl) in Figure 1-12 (a) [97]. It can be observed that multi-carbon products are formed at more negative potentials. Based on the results observed from Figure 1-12 (a), a long-term electrocatalytic measurement with selected potential at -1.6 V (-2.2 V vs. Ag/AgCl) was carried out (Figure 1-12 (b)). The yields of C_3 and C_4 species decreased with decreased relative ratio of Cu(I) to Cu(0) with respect to time. This means the selectivity of CO_2 reduction products can be affected by oxidised phase concentration on the electrode surface [97, 98]. Hence, Cu(I) is important to form carbon chains.

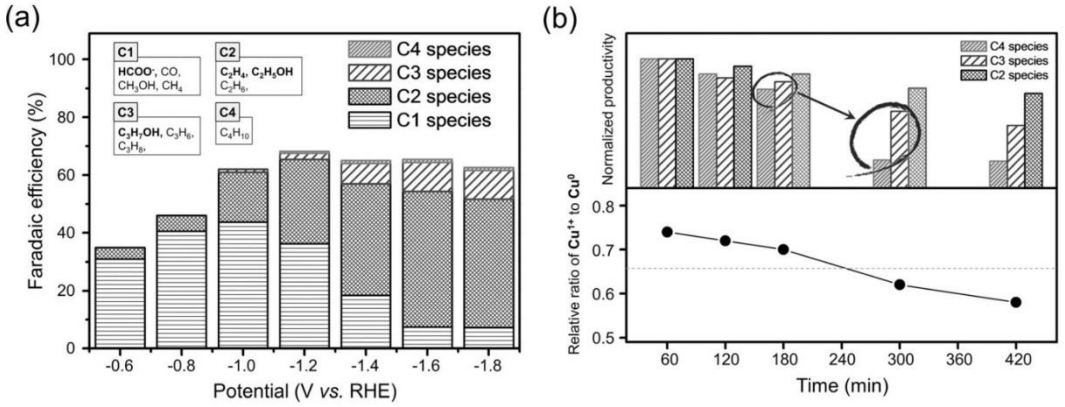

Figure 1-12. (a) FE for carbon fuels generated from electrocatalytic conversion of CO_2 on Cu_2O at each cathodic potential; (b) Long-term electrocatalytic measurement over 7 hours at -1.6 V vs. RHE [97].

Yeo's group investigated an electrodeposited Cu_2O film in the CO_2 reduction to produce C_1 and C_2 species. The larger roughness Cu_2O electrodes show higher current densities, since they have larger electrochemical active surface areas [98], which is similar to previous Cu electrode discussion. A proposed mechanism for the CO_2 reduction is shown in Figure 1-13. Similar to the CO_2 reduction on Cu electrode, the

first step involves proton and electron transfer to form adsorbed COOH on surface. The COOH* then hydrogenates to adsorbed CO and H_2O. The intermediate CO* can then hydrogenate to CH_4, or dimerize/hydrogenate to $C_2H_xO_2$. The intermediate $C_2H_xO_2$ can be reduced to C_2H_4 or C_2H_5OH. The thickness of Cu_2O film can influence the C_2 products selectivity. The optimum thickness for C_2 products is 1.7-3.6 μm. When the thickness of the Cu_2O film increases to 6.4-8.8 μm, the yields of all products decreases while HER increases, since mass transport is limited for CO_2 to electrode.

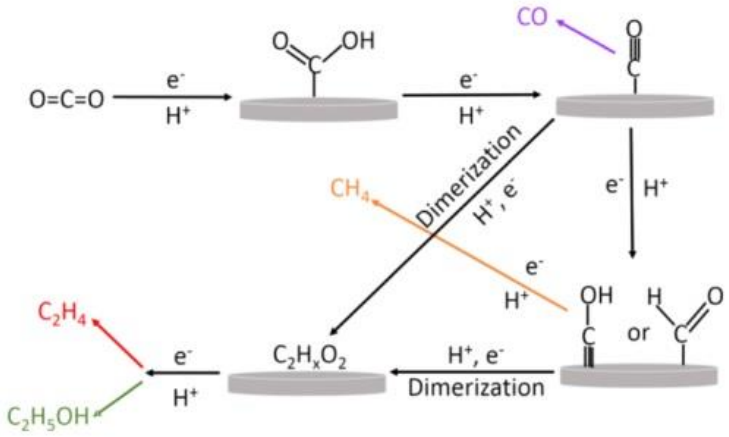

Figure 1-13. Proposed mechanism for the electroreduction of CO_2 to CH_4, C_2H_4, and C_2H_5OH on copper oxide surfaces [98].

Mikosch group investigated the CO_2 reduction mechanism in both experimental and DFT computational methods. They used Cu_2O NPs to reduce CO_2 to methanol. From the results of calculation, the CO_2 molecule can be adsorbed on Cu_2O surface either retaining linear form at copper sites, or forming a surface carbonate at coordinative unsaturated oxygen centres [99]. The surface carbonate bonds on neighbouring oxygen and copper with one oxygen and one carbon atom (Figure 1-14a). In the presence of adsorbed CO_2^-, the low adsorption energy can be calculated for a bridging position between two copper cations, to form Cu-O and Cu-C bonds, resulting in strongly bent CO_2^-* (Figure 1-14b). In the hydrogenation step, the non-bonded oxygen atom accepts hydrogen to form carboxyl intermediate (Figure 1-14c). The second hydrogenation step occurs at the carbon site and produce HCOOH (Figure 1-14d). The strongly adsorbed formic acid molecules on Cu_2O would further participate in the next hydrogenation step to form dihydroxymethylene ($H_2C(OH)_2^-$*) intermediate (Figure 1-14e). Then dihydroxymethylene intermediate would yield methanol (Figure 1-14f).

The author indicated that different reaction intermediates suggested for metallic Cu and Cu_2O is due to the stronger adsorption ability for Cu_2O [99].

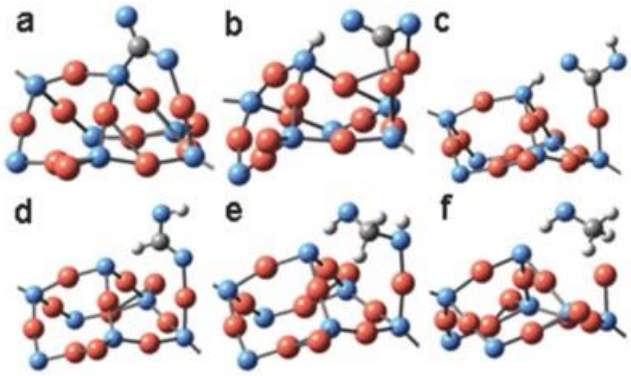

Figure 1-14. The bonding position of (a) surface carbonate species, (b) adsorbed CO_2^- *, (c) carboxyl intermediate, (d) formic acid, (e) dihydroxymethylene intermediate, (f) methanol on Cu_2O electrode surface [99].

The stability of catalyst is critical for the industrial application in the CO_2 reduction. Generally, there are two ways to maintain the catalyst stability, (a) prevent the electrode degradation by keeping homogeneity of the metal particle dispersion with time; (b) avoid the poisoning or blocking of the Cu_2O surfaces [100]. Irabien and colleagues found that Cu_2O electrode lost its activity due to the above two ways. They also found Cu_2O/ZnO mixture electrode shows longer stability period than Cu_2O electrode. The results demonstrated ZnO could stabilize Cu atoms and remove impurities [100]. Other researchers hypothesized that ZnO could strengthen the Cu-CO link, stabilize Cu in the HER, and increase the products selectivity [101]. A Cu_2O nanowire decorated with tin catalysts were developed by Wallace group. The Cu_2O-Sn electrode shows good selectivity, activity and durability to reduce CO_2 to CO at moderate overpotentials [102]. They suggested the activity for CO_2 conversion is attributed by the synergistic interaction between Sn NPs and Cu_2O nanowires [102]. The Sn atom could disrupt the multifold sites on the Cu_2O surface [103]. This would perturb the adsorption of H, and adsorb relatively more CO on electrode surface. Hence the hydrogenation process is influenced, the product selectivity strongly trend to CO with over 90% of FE. They added Au to Cu_2O-Sn electrode, which increase the electrode activity by decreasing the reduction overpotential and further enhance the product selectivity for CO [102].

Except metal and metal oxides, adding some conductive organic polymers to the electrodes could be beneficial in CO_2 reduction. For example, polyaniline matrix decorated with Cu_2O NPs electrode was designed by Grace and colleagues [104]. The products are formic and acetic acids in 0.1 M tetrabutylammonium perchlorate and methanol electrolyte [104]. They suggested the Cu_2O could adsorb more CO_2 molecules, and polyaniline matrix assist to protonate and reduce to formic acid [104]. Since the reduction starts at -0.3 V vs. SCE (-0.26 V vs. Ag/AgCl), it is not possible to generate CO_2^{-}*, which is the general first step in CO_2 reduction. The author found one feasible mechanism, described with Equation 1-37 to 1-39. The adsorbed CO_2 molecule bonds on polyaniline via hydrogen bonding [105]. At negative potential, the H* atoms transfer to the CO_2 molecules through hydrogen bonding and form HCOO*, then further react with H* to produce formic acid. The HCOOH reacts with methanol from electrolyte to produce acetic acid.

$$CO_2 + H^* \rightarrow HCOO^* \quad (1\text{-}37)$$

$$HCOO^* + H^* \rightarrow HCOOH \quad (1\text{-}38)$$

$$HCOO^* + CH_3OH \rightarrow CH_3COOH + OH^* \quad (1\text{-}39)$$

Cu_2O and the Cu(I) species has been widely studied, the interaction between CO_2 and Cu(II) species from CuO could enhance the electrochemical and photochemical CO_2 reduction [106]. Copper oxides should be reduced before CO_2 reduction taking place theoretically, since the potential required for Cu(II) and Cu(I) reduction is less negative than CO_2 reduction [107]. From the Equation 1-40 to 1-42 (potential vs. Ag/AgCl) [107], Cu(II) is more difficult to be reduced to Cu(0) than Cu(I) at same conditions, which might be the vital point to maintain the activity of the catalyst.

$$Cu_2O + 2H^+ + 2e^- \rightarrow 2Cu + H_2O \qquad E^0 = -0.249\ V \quad (1\text{-}40)$$

$$CuO + 2H^+ + 2e^- \rightarrow Cu + H_2O \qquad E^0 = -0.324\ V \quad (1\text{-}41)$$

$$2CuO + 2H^+ + 2e^- \rightarrow Cu_2O + H_2O \qquad E^0 = -0.394\ V \quad (1\text{-}42)$$

It is not yet fully understood how the metal oxides contribute to the reduction, several studies about CuO based electrode for CO_2 reduction will be summarized below.

A novel structure with Cu core/CuO shell has been firstly reported for the CO_2 electrochemical reduction by Lan and Kenis [108]. Except CO and H_2, the main products are HCOOH and CH_3OH, with the highest FE of 20.2% at -1.73 V and 2.5% at -1.35 V for two products in 1.0 M $KHCO_3$ electrolyte. They suggested the

interaction between Cu core and CuO shell would be beneficial for the organic compounds production [108].

Experimental and theoretical studies have revealed that nanostructures would enlarge surface area and enhance the adsorption ability to promote the CO_2 reduction activity. CuO nanomaterials with different surface morphology, such as nanowires (NW), nanoneedles (NN) were synthesized on Cu foils by Xie [93]. The results measured in 0.1 M $KHCO_3$ solution show high CO_2 reduction activity of the nanomaterials, and the NN structure has better performance in high overpotential regions compared with the NW structure. The product selectivity is also influenced by the surface structure [79], where NW produced more C_2H_4 than CH_4, and NN show opposite behaviour. Another novel nanostructure is 3-dimension hierarchical Cu_xO (mixture of CuO and Cu_2O) nanosphere particles synthesized by Qiao and colleagues [109]. The FE of formate and current density increased with potential between -0.5 V and -0.7 V. The results show that the morphology of the catalyst is important in controlling the activity and selectivity for CO_2 reduction [109]. Some treatments on CuO NPs for ligand stabilization can influence electrochemical reduction of CO_2. For example, Kauffman used oleic acid to ligand stabilize CuO NPs [110]. The results show increased CO/H_2 production ratios from stabilized CuO NPs, compared to weakly stabilized and nonstabilized CuO NPs, which can promote the production of methanol and reduction products selectivity [110].

The adsorption of CO_2 on CuO was investigated using DFT calculations in Kasai group and de Leeuw group. The study on CuO(110) surface shows CO_2 adsorbs preferably on top of surface Cu atom in CuO(110) surface, and the increased catalyst reactivity can be attributed by electron charge transfer from surface Cu atom to CO_2 molecule [111]. They also suggested copper oxides are potentially useful for electrochemical and photoelectrochemical catalytic reduction of CO_2, since the copper oxides surface are more reactive to CO_2 compared with pure Cu surface [111]. de Leeuw group found that the configuration of CO_2 molecule bonding on CuO surface depends on different surface structure. For example, on CuO(111) surface, CO_2 loses linearity and one O atom bonds to surface Cu atom (Cu-O), C carbon bonds to surface O atom (C-O) [112]. A significant structural change can be observed in the CO_2 molecule as a result of activation, the neutral linear molecule changed to negatively

charged bents species CO_2^-, and C-O bond distances elongated compared to gas phase molecule [112]. Although these surface studies can provide very useful information about adsorption, the catalyst conditions, such as oxidation methods, structure and morphology of the copper oxides and electrode interfaces, are different from each electrochemical experiments are conducted. It is therefore difficult to use the results of surface study to draw conclusions directly, but can help to describe and interpret electrochemical results.

Many researchers have pointed out that morphology, nanostructure and surface oxidation states of catalyst material on electrode surface play important role in determining catalyst activity, product distribution and reduction efficiency [113]. The copper oxides and their reduction products in CO_2 reduction has been studied using a wide range of techniques: DFT to predict intermediates and adsorbed species; on-line mass spectrometry to identify products formed from electroreduction of various compounds which would be intermediates on the products pathways; gas phase/liquid phase chromatography to measure gas/liquid phase reduction products over a range of potentials on electrode; SEM to study the characterisation and morphology of the catalyst surface; X-ray diffraction, Auger X-ray photoelectron spectroscopy and near edge X-ray absorption fine structure spectroscopy to monitor oxidation state changes and determine activity sites [113].

1.8 Challenges in the carbon dioxide reduction research

The development of electrochemical CO_2 reduction is still at an experimental stage. In order to overcome the barrier for practical application to produce usable low-carbon organic compounds and fuels, the material is the core issue of CO_2 reduction. Researchers are pursuing catalyst materials, from transition metals and related complexes (Ti, Cr, Fe, Co, Ni, Pt, Cu, Ag, Au, Zn, Cd, Hg, etc.), Sn and Pb, alkaline metals and alkaline earth metals, to conductive polymer, radical anion, ionic liquid, enzyme catalysts [74]. The catalytic activity (the onset potential of reduction and the FE) and stability (variations in catalyst behaviour with electrolysis time) need to be assessed for the catalyst materials. Product selectivity in the CO_2 reduction is also important for practical applications. The product distribution generally depends on

reduction mechanism, with different reaction pathways leading to different products. The pathways for the reduction process are affected by experimental conditions, such as catalyst material, electrode potential, electrolyte, pH value, CO_2 concentration, pressure, and temperature.

Regarding CO_2 electrochemical reduction process, several challenges remain. (1) Low catalyst activity. The overpotential for CO_2 electroreduction is too high as discussed above. This indicates the catalyst activity is not good enough in terms of energy efficiency [74]. (2) Low product selectivity. As discussed above, certain structure and treatment of catalyst give better product selectivity and stable yields. But it is not possible to select reduction products so far [74]. For some major catalysts explored, although they show high activity, some undesired by-products still yield. (3) Insufficient stability. In literature, catalyst materials show low stability during the catalysis processes. The decreased performance could be caused by deposition of non-catalytic species from reaction intermediates in the reduction or from contaminants in the electrolyte [114]. The reaction intermediates and contaminants could block and poison the catalyst active sites and lead to cathodic degradation of catalyst surfaces. (4) Insufficient fundamental understanding. Although the literature contains fundamental understanding in experimental and theoretical approaches of CO_2 reduction process, the work, such as surface adsorption, activation sites and catalyst oxidation states studies seems to be insufficient [74].

Therefore, the general objective of this project is to design proper experimental conditions, explore the CuO catalyst performance for CO_2 reduction with various measurements, and gain better fundamental understanding of the mechanisms of CO_2 reduction on catalyst surface and the relationship of catalyst oxidation states and composition. The corresponding experimental details, results and discussions are presented in the following chapters.

References

[1] Hobbs PV. Introduction to atmospheric chemistry. Cambridge University Press; 2000 Sep 25.

[2] Boutton TW. Stable carbon isotope ratios of natural materials: II. Atmospheric, terrestrial, marine, and freshwater environments. Carbon Isotope Techniques. 1991;1:173.

[3] Joos F, Spahni R. Rates of change in natural and anthropogenic radiative forcing over the past 20,000 years. Proceedings of the National Academy of Sciences. 2008 Feb 5;105(5):1425-30.

[4] Trends in Atmospheric Carbon Dioxide, National Oceanic & Atmospheric Administration, Earth System Research Laboratory, 5 July 2016. [Accessed 4 August 2016]; Available from: http://www.esrl.noaa.gov/gmd/ccgg/trends/.

[5] Earth's CO_2, 5 July 2016. [Accessed 4 August 2016]; Available from: https://www.co2.earth/.

[6] The Keeling curve, Scripps institution of oceanography, 2 August 2016. [Accessed 4 August 2016]; Available from: https://scripps.ucsd.edu/programs/keelingcurve/.

[7] Marchal V, Dellink R, van Vuuren D, Clapp C, Château J, Lanzi E, Magné B, van Vliet J. OECD environmental outlook to 2050: climate change chapter. Pre-release Version. 2011.

[8] Ciais P, Sabine C, Bala G, Bopp L, Brovkin V, Canadell J, Chhabra A, DeFries R, Galloway J, Heimann M, Jones C. Carbon and other biogeochemical cycles. In: Climate Change 2013: The Physical Science Basis. Contribution of Working Group I to the Fifth Assessment Report of the IPCC. 2014 Apr (pp. 465-570). Cambridge University Press.

[9] Archer D, Eby M, Brovkin V, Ridgwell A, Cao L, Mikolajewicz U, Caldeira K, Matsumoto K, Munhoven G, Montenegro A, Tokos K. Atmospheric lifetime of fossil fuel carbon dioxide. Annual Review of Earth and Planetary Sciences. 2009 Apr 27;37(1):117.

[10] Le Quéré C, Moriarty R, Andrew RM, Peters GP, Ciais P, Friedlingstein P, Jones SD, Sitch S, Tans P, Arneth A, Boden TA. Global carbon budget 2014. Earth System Science Data. 2015;7:47-85.

[11] International energy agency, CO_2 emission from fuel combustion 2012. OECD Publishing, Pairs. 2012.

[12] Forster P, Ramaswamy V, Artaxo P, Berntsen T, Betts R, Fahey DW, Haywood J, Lean J, Lowe DC, Myhre G, Nganga J. Changes in atmospheric constituents and in radiative forcing. In: Climate Change 2007: the physical science basis.

Contribution of Working Group I to the Forth Assessment Report of the Intergovernmental Panel on Climate Change 2007. Cambridge University Press. 2007.

[13] Le Quéré C, Moriarty R, Andrew RM, Canadell JG, Sitch S, Korsbakken JI, Friedlingstein P, Peters GP, Andres RJ, Boden TA, Houghton RA. Global carbon budget 2015. Earth System Science Data. 2015;7(2):349-96.

[14] Maginn EJ. What to Do with CO_2. The Journal of Physical Chemistry Letters. 2010 Dec 16;1(24):3478-9.

[15] Marland G, Boden TA, Andres RJ, Brenkert AL, Johnston CA. Trends: a compendium of data on global change. Carbon dioxide Information Analysis Center, Oak Ridge National Lab, US Department of Energy, Oak Ridge, Tennessee. 2007.

[16] Birol F. World Energy Outlook Special Report 2013: Redrawing the Energy-Climate Map. IEA, Paris. 2013

[17] Zhu BJ. Engineering carbon-based porous materials from selected precursors for high-capacity CO_2 capture. Thesis (Ph.D.), University College London, 2015.

[18] Gunter W, CO_2 capture and storage overview. APEC Capacity Building in the APEC Region, Phase II Revised and updated by CO2CRC and ICF International.

[19] Jacob D. Introduction to atmospheric chemistry. Princeton University Press; 1999 Dec 21. p. 126.

[20] Parry ML, Canziani OF, Palutikof JP, Van der Linden PJ, Hanson CE. Impacts, adaptation and vulnerability. In: Climate Change 2007: the physical science basis. Contribution of Working group II to the fourth assessment report of the IPCC 2007. Cambridge University Press; 2007.

[21] den Elzen M, Meinshausen M. Meeting the EU 2 ℃ climate target: global and regional emission implications. Climate Policy. 2006 Jan 1;6(5):545-64.

[22] Pachauri RK, Reisinger A. IPCC fourth assessment report. IPCC, Geneva. 2007:2007.

[23] Wolf M. Limitations and possibilities for improvement of photovoltaic solar energy converters: part I: considerations for earth's surface operation. Proceedings of the IRE. 1960 Jul;48(7):1246-63.

[24] Pimentel D, Marklein A, Toth MA, Karpoff MN, Paul GS, McCormack R, Kyriazis J, Krueger T. Food versus biofuels: environmental and economic costs. Human Ecology. 2009 Feb 1;37(1):1-2.

[25] Metz B, editor. Carbon dioxide capture and storage: special report of the

intergovernmental panel on climate change. Cambridge University Press; 2005 Dec 19. p. 3.

[26] Ha-Duong M, Gaultier M. Social aspects of total's Lacq CO_2 capture, transport and storage pilot project. Energy Procedia. 2011 Dec 31;4:6263-72.

[27] Scibioh MA, Viswanathan B. Electrochemical reduction of carbon dioxide: a status report. In: Proceedings of Indian National Science Academy. 2004 (Vol. 70, pp. 1-56).

[28] Quinn EL, Jones CL. Carbon dioxide. Reinhold Publishing Corporation. New York. 1936.

[29] Bamberger CE, Robinson PR. Thermochemical splitting of water and carbon dioxide with cerium compounds. Inorganica Chimica Acta. 1980 Jan 1;42:133-7.

[30] Willis C, Boyd AW. Excitation in the radiation chemistry of inorganic gases. International Journal for Radiation Physics and Chemistry. 1976 Dec 31;8(1):71-111.

[31] Getoff N, Scholes G, Weiss J. Reduction of carbon dioxide in aqueous solutions under the influence of radiation. Tetrahedron Letters. 1960 Jan 1;1(39):17-23.

[32] Lehn JM, Ziessel R. Photochemical generation of carbon monoxide and hydrogen by reduction of carbon dioxide and water under visible light irradiation. Proceedings of the National Academy of Sciences. 1982 Jan 1;79(2):701-4.

[33] Jee HS, Nishio N, Nagai S. CH_4 production from H_2 and CO_2 by Methanobacterium thermoautotrophicum cells fixed on hollow fibers. Biotechnology Letters. 1988 Apr 1;10(4):243-8.

[34] Amatore C, Saveant JM. Mechanism and kinetic characteristics of the electrochemical reduction of carbon dioxide in media of low proton availability. Journal of the American Chemical Society. 1981 Aug;103(17):5021-3.

[35] Mandler D, Willner I. Photochemical fixation of carbon dioxide: enzymic photosynthesis of malic, aspartic, isocitric, and formic acids in artificial media. Journal of the Chemical Society, Perkin Transactions 2. 1988(6):997-1003.

[36] Taniguchi I, Aurian-Blajeni B, Bockris JM. The reduction of carbon dioxide at illuminated p-type semiconductor electrodes in nonaqueous media. Electrochimica Acta. 1984 Jul 31;29(7):923-32.

[37] Ulman M, Aurian-Blajeni B, Halmann M. Fuel from CO_2: an electrochemical study. Chemtech. 1984;14(4):235-9.

[38] Sugimura K, Kuwabata S, Yoneyama H. Electrochemical fixation of carbon dioxide in oxoglutaric acid using an enzyme as an electrocatalyst. Journal of the

American Chemical Society. 1989 Mar;111(6):2361-2.

[39] Parkinson BA, Weaver PF. Photoelectrochemical pumping of enzymatic CO_2 reduction. Nature.1984:148-149.

[40] Olah GA, Goeppert A, Prakash GS. Chemical recycling of carbon dioxide to methanol and dimethyl ether: from greenhouse gas to renewable, environmentally carbon neutral fuels and synthetic hydrocarbons. The Journal of Organic Chemistry. 2008 Dec 8;74(2):487-98.

[41] Nam SS, Kshan G, Choi MJ, Lee KW. Catalytic conversion of CO_2 to hydrocarbons over rare earth promoted iron catalysts supported on KY Zeolite. Preprints-American Chemical Society. Division of Petroleum Chemistry. 2000;45 (1):77-8.

[42] Noda H, Ikeda S, Oda Y, Ito K. Potential dependencies of the products on electrochemical reduction of carbon dioxide at a copper electrode. Chemistry Letters. 1989(2):289-92.

[43] Lee S, Gogate M, Kulik CJ. Methanol-to-gasoline vs. DME-to-gasoline II. Process comparison and analysis. Fuel Science & Technology International. 1995 Aug 1;13(8):1039-57.

[44] Hori Y, Murata A, Takahashi R, Suzuki S. Enhanced formation of ethylene and alcohols at ambient temperature and pressure in electrochemical reduction of carbon dioxide at a copper electrode. Journal of the Chemical Society, Chemical Communications. 1988(1):17-9.

[45] Viswanathan B, Scibioh M. Proceedings of the Indian National Science Academy - Part A. Indian National Science Academy. 2004, 70, 407-462.

[46] Freund HJ, Messmer RP. On the bonding and reactivity of CO_2 on metal surfaces. Surface Science. 1986 Jun 2;172(1):1-30.

[47] Atkins P, Overton T, Rourke J, Weller M. F. Armstrong in Shriver & Atkins Inorganic Chemistry. Oxford University Press. Oxford. 2006.

[48] Housecroft CE, Constable EC. Chemistry: An introduction to organic, inorganic and physical chemistry. Pearson Education Limited. 2010.

[49] Pedersen O, Colmer TD, Sand-Jensen K. Underwater photosynthesis of submerged plants–recent advances and methods. Plant Responses to Flooding. 2015 Jan 5;4(140):18.

[50] Hori Y. Electrochemical CO_2 reduction on metal electrodes. In: Modern Aspects of Electrochemistry. Springer New York. 2008, 42:89-189.

[51] Benson EE, Kubiak CP, Sathrum AJ, Smieja JM. Electrocatalytic and homogeneous approaches to conversion of CO_2 to liquid fuels. Chemical Society Reviews. 2009;38(1):89-99.

[52] Pacansky J, Wahlgren U, Bagus PS. SCF ab-initio ground state energy surfaces for CO_2 and CO_2^-. The Journal of Chemical Physics. 1975 Apr 1;62(7):2740-4.

[53] Paik W, Andersen TN, Eyring H. Kinetic studies of the electrolytic reduction of carbon dioxide on the mercury electrode. Electrochimica Acta. 1969 Dec 1;14(12):1217-32.

[54] Jordan J, Smith PT. Free-radical intermediate in the electroreduction of carbon dioxide. Proceedings of the Chemical Society of London. 1960 Jan 1(7):246-7.

[55] Eggins BR, Robertson PK, Murphy EP, Woods E, Irvine JT. Factors affecting the photoelectrochemical fixation of carbon dioxide with semiconductor colloids. Journal of Photochemistry and Photobiology A: Chemistry. 1998 Oct 15;118(1):31-40.

[56] Bennett EM, Eggins BR, McNeill J, McMullan EA. Recycling carbon dioxide from fossil fuel combustion. Analytical Proceedings. 1980, 17:356-9.

[57] Eggins BR, Ennis C, McConnell R, Spence M. Improved yields of oxalate, glyoxylate and glycolate from the electrochemical reduction of carbon dioxide in methanol. Journal of Applied Electrochemistry. 1997 Jun 1;27(6):706-12.

[58] Eggins BR, Robertson PK, Murphy EP, Woods E, Irvine JT. Factors affecting the photoelectrochemical fixation of carbon dioxide with semiconductor colloids. Journal of Photochemistry and Photobiology A: Chemistry. 1998 Oct 15;118(1):31-40.

[59] Eggins BR, Bennett EM, McMullan EA. Voltammetry of carbon dioxide. Part 2. Voltammetry in aqueous solutions on glassy carbon. Journal of Electroanalytical Chemistry. 1996 May 30;408(1):165-71.

[60] Hori Y. Modern aspects of electrochemistry. Vayenas, C. 2008:89-189.

[61] Pierozynski B. On the hydrogen evolution reaction at nickel-coated carbon fibre in 30 wt.% KOH solution. International Journal of Electrochemical Science. 2011 Jan 1;6:63-77.

[62] Hori Y, Wakebe H, Tsukamoto T, Koga O. Electrocatalytic process of CO selectivity in electrochemical reduction of CO_2 at metal electrodes in aqueous media. Electrochimica Acta. 1994 Aug 1;39(11-12):1833-9.

[63] Summers DP, Leach S, Frese KW. The electrochemical reduction of aqueous

carbon dioxide to methanol at molybdenum electrodes with low overpotentials. Journal of Electroanalytical Chemistry and Interfacial Electrochemistry. 1986 Jun 25;205(1-2):219-32.

[64] Hori Y, Kikuchi K, Suzuki S. Production of CO and CH_4 in electrochemical reduction of CO_2 at metal electrodes in aqueous hydrogencarbonate solution. Chemistry Letters. 1985(11):1695-8.

[65] Azuma M, Hashimoto K, Hiramoto M, Watanabe M, Sakata T. Electrochemical Reduction of Carbon Dioxide on Various Metal Electrodes in Low-Temperature Aqueous $KHCO_3$ Media. Journal of the Electrochemical Society. 1990 Jun 1;137(6):1772-8.

[66] Broden G, Rhodin TN, Brucker C, Benbow R, Hurych Z. Synchrotron radiation study of chemisorptive bonding of CO on transition metals — Polarization effect on Ir (100). Surface Science. 1976 Oct 31;59(2):593-611.

[67] Kaneco S, Iiba K, Hiei NH, Ohta K, Mizuno T, Suzuki T. Electrochemical reduction of carbon dioxide to ethylene with high Faradaic efficiency at a Cu electrode in CsOH/methanol. Electrochimica Acta. 1999 Sep 15;44(26):4701-6.

[68] Kaneco S, Hiei NH, Xing Y, Katsumata H, Ohnishi H, Suzuki T, Ohta K. High-efficiency electrochemical CO_2-to-methane reduction method using aqueous $KHCO_3$ media at less than 273 K. Journal of Solid State Electrochemistry. 2003 Mar 1;7(3):152-6.

[69] Kaneco S, Katsumata H, Suzuki T, Ohta K. Electrochemical reduction of carbon dioxide to ethylene at a copper electrode in methanol using potassium hydroxide and rubidium hydroxide supporting electrolytes. Electrochimica Acta. 2006 Apr 10;51(16):3316-21.

[70] Ohya S, Kaneco S, Katsumata H, Suzuki T, Ohta K. Electrochemical reduction of CO 2 in methanol with aid of CuO and Cu_2O. Catalysis Today. 2009 Nov 30;148(3):329-34.

[71] Hori Y, Kikuchi K, Murata A, Suzuki S. Production of methane and ethylene in electrochemical reduction of carbon dioxide at copper electrode in aqueous hydrogencarbonate solution. Chemistry Letters. 1986;15(6):897-8.

[72] Shibata H, Moulijn JA, Mul G. Enabling electrocatalytic Fischer — Tropsch synthesis from carbon dioxide over copper-based electrodes. Catalysis Letters. 2008 Jul 1;123(3-4):186-92.

[73] Wang XY, Liu SQ, Huang KL, Feng QJ, Liu B, Liu JL, Jin GH. Fixation of CO_2 by electrocatalytic reduction to synthesis of dimethyl carbonate in ionic liquid using effective silver-coated nanoporous copper composites. Chinese Chemical Letters. 2010 Aug 31;21(8):987-90.

[74] Qiao J, Liu Y, Hong F, Zhang J. A review of catalysts for the electroreduction of carbon dioxide to produce low-carbon fuels. Chemical Society Reviews. 2014;43(2):631-75.

[75] Hori Y, Murata A, Takahashi R. Formation of hydrocarbons in the electrochemical reduction of carbon dioxide at a copper electrode in aqueous solution. Journal of the Chemical Society, Faraday Transactions 1: Physical Chemistry in Condensed Phases. 1989;85(8):2309-26.

[76] Kyriacou G, Anagnostopoulos A. Electroreduction of CO_2 on differently prepared copper electrodes: The influence of electrode treatment on the current efficiences. Journal of Electroanalytical Chemistry. 1992 Jan 10;322(1):233-46.

[77] Kim JJ, Summers DP, Frese KW. Reduction of CO_2 and CO to methane on Cu foil electrodes. Journal of Electroanalytical Chemistry and Interfacial Electrochemistry. 1988 Apr 25;245(1):223-44.

[78] Liu L, Tian N, Huang L, Hong YH, Xie AY, Zhang FY, Xiao C, Zhou ZY, Sun SG. Influence of transition metal modification of oxide-derived Cu electrodes in electroreduction of CO_2. Chinese Journal of Catalysis. 2016 Jul 31;37(7):1070-5.

[79] Tang W, Peterson AA, Varela AS, Jovanov ZP, Bech L, Durand WJ, Dahl S, Nørskov JK, Chorkendorff I. The importance of surface morphology in controlling the selectivity of polycrystalline copper for CO_2 electroreduction. Physical Chemistry Chemical Physics. 2012;14(1):76-81.

[80] DeWulf DW, Jin T, Bard AJ. Electrochemical and surface studies of carbon dioxide reduction to methane and ethylene at copper electrodes in aqueous solutions. Journal of the Electrochemical Society. 1989 Jun 1;136(6):1686-91.

[81] Yano H, Tanaka T, Nakayama M, Ogura K. Selective electrochemical reduction of CO_2 to ethylene at a three-phase interface on copper (I) halide-confined Cu-mesh electrodes in acidic solutions of potassium halides. Journal of Electroanalytical Chemistry. 2004 Apr 15;565(2):287-93.

[82] Frese Jr KW. Sullivan, BP; Krist, K.; Guard, HE, editors. Electrochemical and electrocatalytic reactions of carbon dioxide. Amsterdam; Elsevier; 1993. p. 145.

[83] Taniguchi I, Bockris JO, White RE, Conway BE, editors. Electrochemical and

photoelectrochemical reduction of carbon dioxide. Modern Aspects of Electrochemistry. New York Springer; 1989.

[84] Gattrell M, Gupta N, Co A. A review of the aqueous electrochemical reduction of CO_2 to hydrocarbons at copper. Journal of Electroanalytical Chemistry. 2006 Aug 15;594(1):1-9.

[85] Durand WJ, Peterson AA, Studt F, Abild-Pedersen F, Nørskov JK. Structure effects on the energetics of the electrochemical reduction of CO_2 by copper surfaces. Surface Science. 2011 Aug 31;605(15):1354-9.

[86] Peterson AA, Abild-Pedersen F, Studt F, Rossmeisl J, Nørskov JK. How copper catalyzes the electroreduction of carbon dioxide into hydrocarbon fuels. Energy & Environmental Science. 2010;3(9):1311-5.

[87] Cook RL, MacDuff RC, Sammells AF. Evidence for formaldehyde, formic acid, and acetaldehyde as possible intermediates during electrochemical carbon dioxide reduction at copper. Journal of the Electrochemical Society. 1989;136(7):1982-4.

[88] Hori Y, Murata A, Takahashi R, Suzuki S. Electroreduction of carbon monoxide to methane and ethylene at a copper electrode in aqueous solutions at ambient temperature and pressure. Journal of the American Chemical Society. 1987 Aug;109(16):5022-3.

[89] Bertheussen E, Verdaguer-Casadevall A, Ravasio D, Montoya JH, Trimarco DB, Roy C, Meier S, Wendland J, Nørskov JK, Stephens IE, Chorkendorff I. Acetaldehyde as an Intermediate in the Electroreduction of Carbon Monoxide to Ethanol on Oxide-Derived Copper. Angewandte Chemie. 2016 Jan 1;128(4):1472-6.

[90] Kuhl KP, Cave ER, Abram DN, Jaramillo TF. New insights into the electrochemical reduction of carbon dioxide on metallic copper surfaces. Energy & Environmental Science. 2012;5(5):7050-9.

[91] Le M, Ren M, Zhang Z, Sprunger PT, Kurtz RL, Flake JC. Electrochemical reduction of CO_2 to CH_3OH at copper oxide surfaces. Journal of the Electrochemical Society. 2011 May 1;158(5):E45-9.

[92] Eilert A, Roberts FS, Friebel D, Nilsson A. Formation of Copper Catalysts for CO_2 Reduction with High Ethylene/Methane Product Ratio Investigated with In Situ X-ray Absorption Spectroscopy. The Journal of Physical Chemistry Letters. 2016 Apr 6;7(8):1466-70.

[93] Xie J, Huang Y, Yu H. Tuning the catalytic selectivity in electrochemical CO_2 reduction on copper oxide-derived nanomaterials. Frontiers of Environmental

Science & Engineering. 2015 Oct 1;9(5):861-6.

[94] Frese KW. Electrochemical reduction of CO_2 at intentionally oxidized copper electrodes. Journal of the Electrochemical Society. 1991 Nov 1;138(11):3338-44.

[95] Terunuma Y, Saitoh A, Momose Y. Relationship between hydrocarbon production in the electrochemical reduction of CO_2 and the characteristics of the Cu electrode. Journal of Electroanalytical Chemistry. 1997 Aug 15;434(1):69-75.

[96] Lee S, Kim D, Lee J. Electrocatalytic Production of C_3-C_4 Compounds by Conversion of CO_2 on a Chloride-Induced Bi-Phasic Cu_2O-Cu Catalyst. Angewandte Chemie. 2015 Dec 1;127(49):14914-8.

[97] Kim D, Lee S, Ocon JD, Jeong B, Lee JK, Lee J. Insights into an autonomously formed oxygen-evacuated Cu_2O electrode for the selective production of C_2H_4 from CO_2. Physical Chemistry Chemical Physics. 2015;17(2):824-30.

[98] Ren D, Deng Y, Handoko AD, Chen CS, Malkhandi S, Yeo BS. Selective electrochemical reduction of carbon dioxide to ethylene and ethanol on copper (I) oxide catalysts. ACS Catalysis. 2015 Mar 31;5(5):2814-21.

[99] Uzunova EL, Seriani N, Mikosch H. CO_2 conversion to methanol on Cu(I) oxide nanolayers and clusters: an electronic structure insight into the reaction mechanism. Physical Chemistry Chemical Physics. 2015;17(16):11088-94.

[100] Albo J, Sáez A, Solla-Gullón J, Montiel V, Irabien A. Production of methanol from CO_2 electroreduction at Cu_2O and Cu_2O/ZnO-based electrodes in aqueous solution. Applied Catalysis B: Environmental. 2015 Oct 31;176:709-17.

[101] Andrews E, Ren M, Wang F, Zhang Z, Sprunger P, Kurtz R, Flake J. Electrochemical reduction of CO_2 at Cu nanocluster/(1010) ZnO electrodes. Journal of the Electrochemical Society. 2013 Jan 1;160(11):H841-6.

[102] Zhao Y, Wang C, Wallace GG. Tin Nanoparticles Decorated Copper Oxide Nanowires for Selective Electrochemical Reduction of Aqueous CO_2 to CO. Journal of Materials Chemistry A. 2016.

[103] Sarfraz S, Garcia-Esparza AT, Jedidi A, Cavallo L, Takanabe K. Cu–Sn Bimetallic Catalyst for Selective Aqueous Electroreduction of CO_2 to CO. ACS Catalysis. 2016 Apr 5;6(5):2842-51.

[104] Grace AN, Choi SY, Vinoba M, Bhagiyalakshmi M, Chu DH, Yoon Y, Nam SC, Jeong SK. Electrochemical reduction of carbon dioxide at low overpotential on a polyaniline/Cu_2O nanocomposite based electrode. Applied Energy. 2014 May 1;120:85-94.

[105] Köleli F, Röpke T, Hamann CH. The reduction of CO_2 on polyaniline electrode in a membrane cell. Synthetic Metals. 2004 Jan 6;140(1):65-8.

[106] Ghadimkhani G, de Tacconi NR, Chanmanee W, Janaky C, Rajeshwar K. Efficient solar photoelectrosynthesis of methanol from carbon dioxide using hybrid CuO–Cu_2O semiconductor nanorod arrays. Chemical Communications. 2013;49(13):1297-9.

[107] Wang X, Hanson JC, Frenkel AI, Kim JY, Rodriguez JA. Time-resolved studies for the mechanism of reduction of copper oxides with carbon monoxide: complex behavior of lattice oxygen and the formation of suboxides. The Journal of Physical Chemistry B. 2004 Sep 9;108(36):13667-73.

[108] Lan Y, Ma S, Lu J, Kenis PJ. Investigation of a Cu (core)/CuO (shell) Catalyst for Electrochemical Reduction of CO_2 in Aqueous Soultion. International Journal of Electrochemical Science. 2014 Dec 1;9:7300-8.

[109] Qiao J, Fan M, Fu Y, Bai Z, Ma C, Liu Y, Zhou XD. Highly-active copper oxide/copper electrocatalysts induced from hierarchical copper oxide nanospheres for carbon dioxide reduction reaction. Electrochimica Acta. 2015 Jan 20;153:559-65.

[110] Kauffman DR, Ohodnicki PR, Kail BW, Matranga C. Selective electrocatalytic activity of ligand stabilized copper oxide nanoparticles. The Journal of Physical Chemistry Letters. 2011 Jul 28;2(16):2038-43.

[111] Moreno JL, Arevalo RL, Escaño MC, Padama AA, Kasai H. A Theoretical Study on the Adsorption of CO_2 on CuO (110) Surface. Journal of the Physical Society of Japan. 2014 Dec 16;84(1):015003.

[112] Mishra AK, Roldan A, de Leeuw NH. CuO surfaces and CO_2 activation: a dispersion-corrected DFT+U study. The Journal of Physical Chemistry C. 2016 Jan 22;120(4):2198-214.

[113] Wang L, Gupta K, Goodall J, Darr JA, Holt KB. In situ spectroelectrochemical monitoring of CO_2 reduction at copper oxide electrodes. Faraday Discussions. 2016.

[114] Kaneco S, Iwao R, Iiba K, Ohta K, Mizuno T. Electrochemical conversion of carbon dioxide to formic acid on Pb in KOH/methanol electrolyte at ambient temperature and pressure. Energy. 1998 Dec 31;23(12):1107-12.

Chapter 2

Experimental Theory and Techniques

2.1 Cyclic voltammetry

Cyclic voltammetry (CV) is a widely used technique for its effective and versatile ability to study mechanism in electrochemical reactions. It enables the electrode potential to be rapidly scanned in search of redox processes. Once located, a redox process can be characterized from the potentials of peaks in the cyclic voltammogram and from changes caused by variation of the scan rate. CV also can be used to gain information on reversibility of redox reactions and reaction kinetics [1]. The applications of CV range from the study of simple redox processes in organic and inorganic chemistry to the characterisation of multielectron-transfer processes in biochemistry and macro-molecular chemistry [2].

The repetitive triangular potential excitation signal for CV (Figure 2-1) causes the potential of the working electrode to sweep back and forth between two designated values. In the forward scan, the potential first scans positively, starting from a lower potential (a) and ending at a greater potential (b). The potential extreme (b) is called the switching potential. From (a) to (b), the voltage is sufficient enough to have caused an oxidation of an analyte. The reverse scan occurs from (b) to (c). Figure 2-1 shows typical oxidation from (a) to (b) and reduction from (b) to (c). It is important to note that some analytes undergo reduction first, in which case the potential would first scan negatively. This cycle can be repeated, and the scan rate can be varied. The slope of the excitation signal gives the scan rate.

$$\nu = \frac{\mathrm{dE}}{\mathrm{dt}} \tag{2-1}$$

The scan rate can range from ~$mV \cdot s^{-1}$ to ~$V \cdot s^{-1}$ [3].

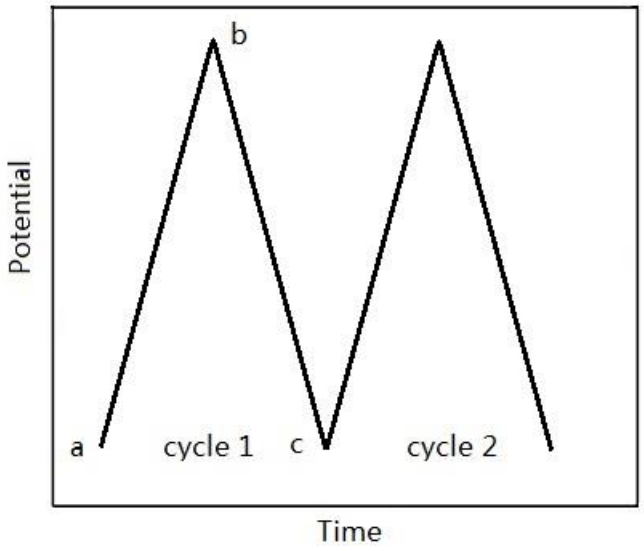

Figure 2-1. Excitation signal for cyclic voltammetry.

To explain the CV process, Figure 2-2 shows a typical voltammogram resulting from a single electron redox event.

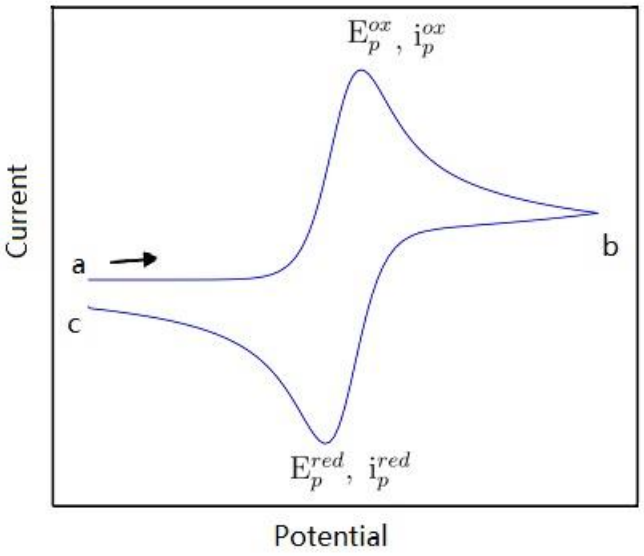

Figure 2-2. Voltammogram of a single electron oxidation-reduction.

Considering the following simple reversible reaction:

$Cu^{+} \leftrightarrow Cu^{2+} + e^{-}$ (2-2)

at starting potential (a), only Cu^{+} is assumed to be present in the solution. When the applied potential become more positive from (a) to (b), Cu^{+} is oxidised to Cu^{2+} at the working electrode. The oxidation reaction increases until reaching a maximum, i_p^{ox} at

E_p^{ox}. After this potential, Cu^+ is slowly depleted and an increasing amount of Cu^{2+} is present at the electrode surface. The applied potential is reversed at (b), then similar to the anodic scan when the applied potential becomes sufficiently negative, Cu^{2+} is reduced to Cu^+, yielding a negative reductive current. After the reduction reaction reaches its maximum i_p^{red} at E_p^{red}, Cu^{2+} at the electrode surface is depleted. When the applied potential is scanned to (c), the first cycle is completed.

The voltammogram obtained by anodic scan from (a) to (b) can be divided into two regions: the region before and the region after reaching the peak current i_p^{ox} at E_p^{ox}. The current at potentials less than E_p is dependent on electrode kinetics (increased driving force for electron transfer), and the current at potentials after the peak is controlled by the rate of mass transport of reactant to the electrode surface (assuming the electron transfer is fast enough) [3].

The shape of the cyclic voltammogram reveals the reversibility of the redox couple by peak potential, E_p, peak current, i_p, and scan rate, ν. Due to different characteristic features, three classes of electron transfer kinetics will be described below. For a reversible couple, there is a significant current flow starting at small overpotential, the height of the oxidised and reduced current peaks are same in magnitude. The peak separation, ΔE_p, is a constant of 59 mV for one electron transfer at all rates at 298 K. The magnitude of the oxidised and reduced current peak should have a ratio of unity. An irreversible couple has larger peak separation, which indicates a bigger overpotential is required to excite the electron transfer. The height of the reversed peak is smaller than the forward peak. The potential of the peak E_p depends on the scan rate. A quasi-reversible reaction is an intermediate between reversible and irreversible reaction. Like a reversible reaction, the quasi-reversible couple has an oxidation forward and reduction backward peak current ratio of close to unity. But the peak separation of quasi-reversible reaction is dependent on scan rate. The characteristic features of different electron transfer kinetics are listed in Table 2-1.

Table 2-1. Characteristic CV features of reversible, irreversible and quasi-reversible electron transfer kinetics [3].

	Reversible	Irreversible	Quasi-reversible
ΔE_p	59 mV	>59 mV	>59 mV
$\left\lvert \frac{i_p^{red}}{i_p^{ox}} \right\rvert$	1	$\neq 1$	1
i_p	$\propto \nu^{1/2}$	$\propto \nu^{1/2}$	increase with $\nu^{1/2}$
E_p	independent of ν	dependent of ν	dependent of ν

A CV experiment consists of an electrochemical cell and a potentiostat, illustrated in Figure 2-3. The electrolysis cell consists of a working electrode (WE), counter electrode (CE), reference electrode (RE), and electrolytic solution. The WE is where the electrochemical reaction takes place, the potential is varied by the potentiostat with respect to the RE. The RE maintains a constant potential. The CE conducts electricity to complete the circuit from the signal source to the WE [5]. The purpose of the electrolytic solution is to provide conductivity during oxidation and reduction. A potentiostat is an electronic device which uses a direct current power source to produce a potential which can be maintained and accurately determined, while allowing small currents to be drawn into the system without changing the voltage [6].

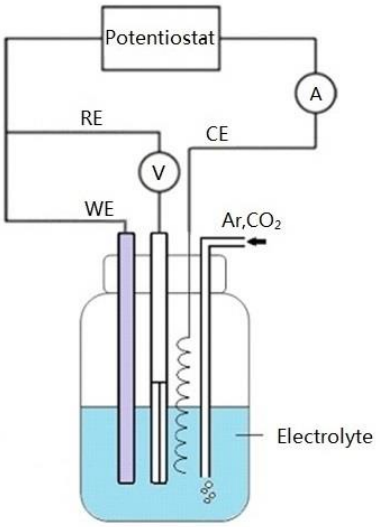

Figure 2-3. A typical three-electrode cyclic voltammetry setup.

2.2 X-ray photoelectron spectroscopy

X-ray photoelectron spectroscopy (XPS) is a surface sensitive ionisation technique that can be used for qualitative and quantitative identifying of elements (with the exception of single electron shell elements H and He), chemical state, and relative composition of surface structure. X-rays with energies in the range of 1-5 keV are used to ionise samples. Photons irradiate the sample and eject core electrons. Since each core orbital is associated with a characteristic binding energy in a specific set of peaks in spectrum, XPS is a chemically specific technique [7, 8].

The surface-sensitivity of XPS arises from the emission and detection of the ejected electrons. Even though the penetration depth of the X-rays employed in XPS is measured in micrometres, the overwhelming majority of electrons ejected from the sample at those depths collide with other atoms in the sample before reaching the surface. These collision lead to loss of energy and prevent the electron from contributing to XPS peaks. Only electrons from the top 4-5 monolayers are likely to be ejected and reach the detector without any energy loss [7, 8].

The exact binding energy of an electron depends on the chemical environment and the formal oxidation state of the atom, hence a shift in the peak position caused by changes is observable in XPS. Therefore XPS will also give information on the oxidation state of the atom and the surface structure.

The binding energy, E_B, can be determined according to the pre-known value of the incident photon energy, $h\upsilon$, and kinetic energy of ejected electron, E_K, which can be measured by Equation 2-3 [7].

$$E_B = h\nu - (E_K + \Delta\Phi) \tag{2-3}$$

where $\Delta\Phi$ is the work function of spectrometer.

The XPS signal is proportional to the amount of species on the surface, hence the technique can be used for quantitative analysis. The composition of the surface can be determined by peak intensity in spectrum and atomic sensitivity factor [7].

2.3 Raman spectroscopy

The Raman effect, named after Nobel prize winner Chandrasekhara Venkata Raman, can be described as an inelastic light scattering process. This inelastically scattered light provides vibrational transition information on chemical structures and identifies substances by fingerprint spectral patterns. When a strong light source incidents on a substance, photons may be absorbed, scattered, or not interact with the material and pass straight through it. If incident energy equals to the energy difference between the ground state and excited state of a molecule, the molecule may absorb the photon and be promoted to an excited state. The photon then scatters from the molecule after the interaction, but the scattered photon may or may not have same energy as the incident photon. The inelastic scattering is Raman scattering. When interacting with incident light, the electron cloud around nuclei are polarised to form a short lived 'virtual' state. The de-excitation from the virtual state to first excited vibrational state or the ground state happens in $<10^{-14}$ seconds [9]. Raman spectroscopy uses single frequency radiation as incident light, so the radiation scattered from the molecule can be detected.

The transitions for one vibration are shown in Figure 2-4. If the photon energy of this scattered light is equal to that of the incoming light, this process is elastic scattering, called Rayleigh scattering. The majority of all scattered photons are Rayleigh scattering, only about 1 in 10^6-10^8 photons are scattered as inelastic scattering (Raman scattering) [9]. There are two types of photon transitions in Raman scattering. If the molecule starts at ground vibrational state, after absorption of energy from incident light, it can fall back to a higher vibrational state, which is Stokes scattering. In other cases, molecules maybe present in a higher vibrational state at beginning due to thermal energy. The molecule scattered from higher energy state to the ground state is anti-Stokes scattering. The relative intensities of Stokes and anti-Stokes scattering depend on the population of energy levels. When incident light has energy of $h\upsilon_0$, the scattered photon gain energy of $h\upsilon_1$. Then Stokes scattering has energy transfer of $h\upsilon_0 > h\upsilon_1$, and anti-Stokes scattering has energy transfer of $h\upsilon_0 < h\upsilon_1$. Since anti-Stokes scattering has energy transfer to the scattered photon, at room temperature, it would be weaker than Stokes scattering. The difference in intensities of Raman scattering in Stokes and anti-Stokes can be used to measure temperature [9].

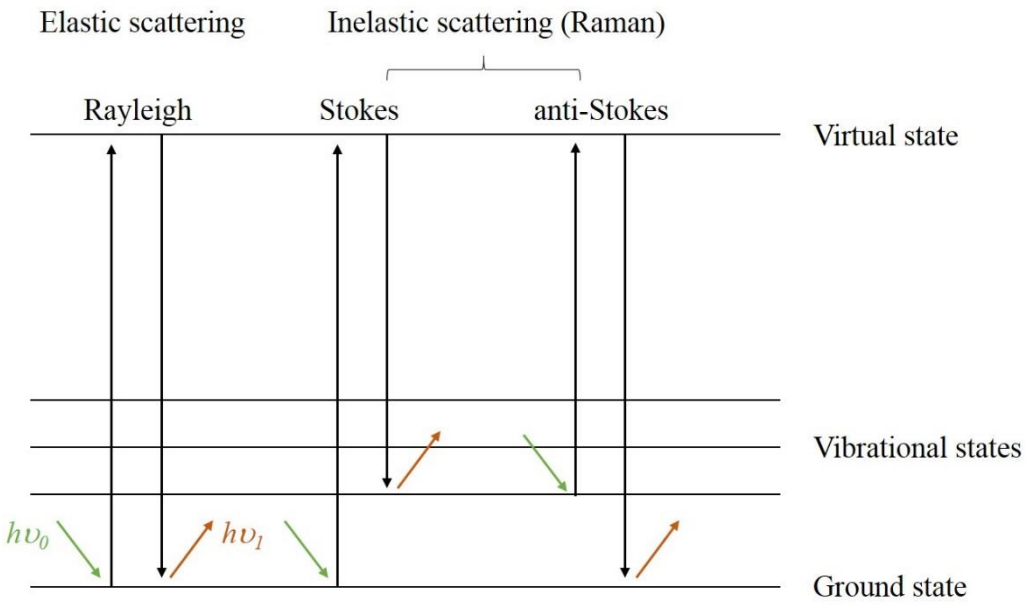

Figure 2-4. Energy level diagram showing the states involved Rayleigh and Raman scattering.

The difference in energy between the incoming and scattered photon (Raman shift) corresponds to the energy difference between vibrational energy levels of the molecule. The different vibrational modes of a molecule can therefore be identified by recognizing Raman shifts in the inelastically scattered light spectrum [10].

The oscillating electric field of incident light induces polarization in the molecule. The strength of polarization, P, is directly proportional to the polarizability, α, and the incident electric field, E, of electron cloud round the nuclei.

$$P = \alpha E \tag{2-4}$$

The polarizability of the molecule is altered by the molecular vibrations

$$\alpha = \alpha_0 + \left(\frac{\partial \alpha}{\partial Q_j}\right) Q_j + \cdots \tag{2-5}$$

Q_j is the j-th normal mode of a molecular vibration. The magnitude of the elastic Rayleigh scattering is proportional to α_0, the inherent polarizability of the molecule. While $\frac{\partial \alpha}{\partial Q_j}$ is generally smaller than α_0, the intensity of Raman scattering is weaker than Rayleigh scattering. The intensity of Raman scattering depends on the change of polarizability, α, during vibration, which can be described by the polarizability derivative,

$$\frac{\partial \alpha}{\partial Q_j} \neq 0 \qquad (2\text{-}6)$$

Raman peaks occur for molecules that contain vibrational symmetric π systems, symmetric conjugated π systems and large or electron-rich atoms. In contrast, many asymmetric vibrations are weak in Raman [11].

A Raman system typically consists of four major components: excitation source (Laser), sample illumination system and light collection optics, wavelength selector (Filter or Spectrophotometer), and detector. A sample is normally illuminated with a laser beam in the ultraviolet, visible or near infrared range. Scattered light is collected with a lens and is sent through interference filter or spectrophotometer to obtain Raman spectrum of a sample [12].

2.4 Attenuated total reflectance - Fourier transform infrared spectroscopy

In infrared spectroscopy (IR spectroscopy), infrared radiation is irradiated to a sample. Some of the infrared radiation is absorbed by the sample and some is passed through — that is transmitted. The resulting spectrum represents the molecular absorption and transmission, creating a molecular fingerprint of the sample. Any unique molecular structure would produce the specific infrared spectrum. This makes IR spectroscopy useful for several types of analysis, such as identification of unknown materials, determination of the quality or consistency of a sample and determination of the amount of components in a mixture [13].

When exposed to infrared radiation, sample molecules selectively absorb radiation of specific wavelengths which causes the change of dipole moment of molecules. Consequently, the vibrational energy levels of molecule transfer from ground state to excited state. The frequency of the absorption peak is determined by the vibrational energy gap. The number of absorption peak is related to the number of vibrational modes of the molecule. The intensity of absorption peak is related to the change of dipole moment and the probability of the transition between energy levels. Therefore, by analyzing the infrared spectrum, abundant structure information of a molecule

would be obtained readily [14].

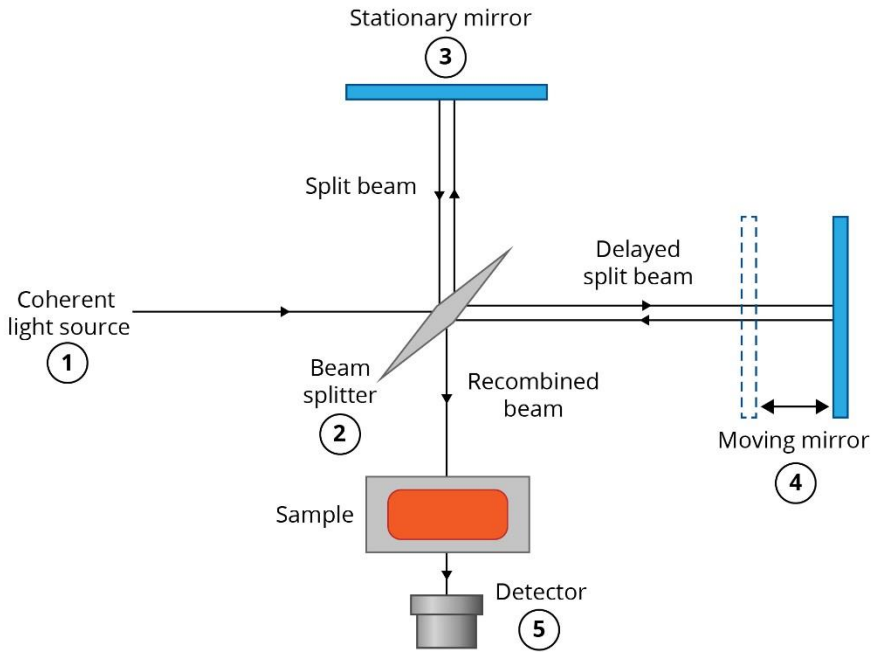

Figure 2-5. Schematic diagram of Michelson interferometer [15].

IR spectroscopy is typically based on the Michelson interferometer, an example is shown in Figure 2-5 [15]. The interferometer consists a beam splitter, a stationary mirror, and a moving mirror. The moving mirror can translate back and forth precisely. Radiation from the source strikes the beam splitter and is separated into two beams. The beam splitter is made of a special material that transmits half of the radiation and reflects the other half. One beam is transmitted through the beam splitter to the stationary mirror and the other is reflected off the beam splitter to the moving mirror. The stationary and moving mirror reflect the radiation back to the beam splitter. Again, half of this reflected radiation is transmitted and half is reflected at the beam splitter, resulting in one beam passing to the detector and the second back to the source. The signal acquired by an IR spectrometer is an interferogram. The interferogram needs to be translated into a spectrum (emission, absorption, transmission, etc.). The process of conversion is through the fast Fourier transform (FT) algorithm. A number of steps are involved in calculating the spectrum. Instrumental electronic and optical imperfections and basic scan limitations need to be accommodated by performing phase correction and apodization steps.

FTIR spectroscopy in the attenuated total reflectance (ATR) mode allows the quantitative and qualitative evaluation of samples in ~10^{-9} g. The sample is placed on an optically dense crystal directly. The IR beam is totally internally reflected within the crystal in a high refractive index at a specific angle. An evanescent wave is produced by the internal reflectance, which extends ~1 μm beyond the crystal surface to the sample. The depth of IR beam penetration into the sample, d_p, is defined as the distance required for the electric field amplitude to fall to the e^{-1} of its value at the surface [16, 17].

$$d_p = \frac{\lambda_1}{2\pi n_1 \sqrt{\sin^2\theta - (n_2 / n_1)^2}} \tag{2-7}$$

In the equation, λ_1 is the wavelength of the IR light in crystal material, θ is the angle of incidence of the IR beam, n_1 and n_2 are the refractive index of the crystal and sample. The evanescent wave would be attenuated or altered in the regions of the IR spectrum, where the sample absorbs energy. The attenuated or altered energy from the evanescent wave is reflected back to the IR beam and passed to the detector in the IR spectrometer, as shown in figure 2-6.

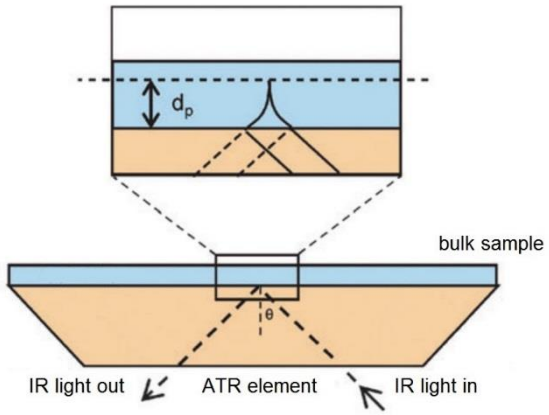

Figure 2-6. Schematic representation of a reflection ATR system.

In this study we use CV, ex situ XPS and Raman spectroscopy and in situ IR spectroscopy to gain insight into the interaction of CO_2 with CuO electrodes during electrochemical reduction. Extensive catalytic studies have been carried out at Cu, Cu_2O and CuO electrodes, but most of the studies have focussed on product distribution analysis. There is relatively few reported study about in situ measurements of the catalyst material. Hence we study the initial interaction of the CO_2 with the catalyst surface at low overpotentials during the first potential cycle to understand how

CO_2 binds to the CuO surface. Besides, we determine how the presence of CO_2 in solution influences the reactivity of the CuO material and how the oxidation state of the copper centres changes during potential cycling, and study the stability of catalyst materials with multi potential cycles.

References

[1] Heinze J. Cyclic voltammetry—electrochemical spectroscopy. Angewandte Chemie International Edition in English. 1984 Nov 1; 23(11): 831-47.

[2] Hirani M. Electrochemical reactions catalyzed by insulators. Thesis (Ph.D.), University College London, 2015.

[3] Pletcher D, Greff R, Peat R, Peter LM, Robinson J. Instrumental methods in electrochemistry. Elservier, 2001 Apr 1.

[4] Hamann CH, Hamnett A, Vielstich W. Electrochemistry. Weinheim: Wiley-VCH; 1998.

[5] Dickinson EJF, Limon-Petersen JG, Rees NV, Compton RG. How much supporting electrolyte is required to make a cyclic voltammetry experiment quantitatively diffusional—A theoretical and experimental investigation. Journal of Physical Chemistry C. 2009; 11(1): 157-171.

[6] Atkins P, de Paula J. Atkins' Physical Chemistry. 8th ed. Oxford: Oxford University Press. 2006.

[7] Brown WA. Techniques in Surface Science. Frontiers in experimental physical chemistry. London: University College London; 2009.

[8] Nix RM. An introduction to surface chemistry. Queen Mary, University of London.

[9] McCreey RL. Raman spectroscopy for chemical analysis. New York: John Wiley & Sons Inc. 2000.

[10] Smith E, Dent G. Modern Raman spectroscopy—a practical approach. John Wiley & Sons, Wiltshire, Great Britain, 2005.

[11] Saveant JM. Molecular catalysis of electrochemical reactions. Chemical Reviews. 2008; 108(2): 2348-2378.

[12] Li XX, Blinn K, Fang Y. Application of surface enhanced Raman spectroscopy to the study of SOFC electrode surfaces. Physical Chemistry. 2012, 14(5): 919-923.

[13] Infrared Spectroscopy: Theory. Online edition for students of organic chemistry

lab courses at the University of Colorado, Boulder, Department of Chemistry and Biochemistry (2002).

[14] Introduction to Spectroscopy. Online edition for spectroscopy introduction at Michigan State University, Department of Chemistry (2013).

[15] Keit spectrometers. FTIR spectroscopy. [Accessed 16 August 2016]; Available from: http://keit.co.uk/ftir-spectrometer-technology/.

[16] Pike Technologies. ATR theory and applications. [Accessed 20nd February 2016]; Available from: www.piketech.com/files/pdfs/ATRAN611.pdf.

[17] Huang HY, Yin QH. Fundamentals and application advances in attenuated total internal reflectance Fourier transform infrared spectroscopy (ATR-FTIR). Journal of the Graduates, Sun Yat-sen University. 2011, 32(1): 20-31.

Chapter 3

Electrochemical Study of CuO Catalyst in Ar Deoxygenated and CO_2 Saturated Solutions

3.1 CV experiment

3.1.1 CV setup

A standard three-electrode electrochemical cell was used. The electrodes were placed in a 10 mL beaker covered with Nescofilm to protect the electrolyte. A 3 mm diameter disk boron-doped-diamond (BDD) electrode was used as the working electrode (WE). A platinum wire served as counter electrode (CE) and the reference electrode (RE) was Ag/AgCl saturated with KCl. All potentials reported in this study are against Ag/AgCl electrode. The WE was polished with 0.3 μm alumina slurry, rinsed thoroughly with distilled water and dried with compressed air before placing into the electrolyte. The CE and RE were rinsed and dried before being placed into the electrolyte. A background CV measurement of the polished electrode was taken each time to ensure the electrode was free of contaminants before the WE was modified with copper oxide catalyst materials.

The aqueous electrolyte in the experiment was 0.2 M phosphate buffer solution in pH 4, pH 7 and pH 9 conditions, 0.5 M potassium bicarbonate buffer solution for pH 8 condition, 0.5 M potassium carbonate buffer solution for pH 11 condition. The electrolyte solutions were prepared using water from Millipore Milli-Q Gradient A10 water filter (18 MΩ cm at 25°C), potassium phosphate dibasic (Sigma Aldrich, 99%), potassium dihydrogen phosphate (Sigma Aldrich, 98+%), potassium bicarbonate (Sigma Aldrich, 99.7%), and potassium carbonate (Sigma Aldrich, 99%).

For control experiments measured under Ar deoxygenated solution, 10 mL of electrolyte was deoxygenated by bubbling with Ar for 20 minutes prior to each experiment. For experiments with CO_2 saturated solution, the CO_2 saturated atmosphere was formed by 20 minutes bubbling with Ar, then 20 minutes bubbling with pre-cleaned high purity CO_2 into the deoxygenated electrolyte.

CuO NP catalysts were synthesized using hydrothermal flow synthesis method by Dr. Josie Goodall. The average size of star-like NP is 50×50 nm in dimension approximately. CuO suspension was prepared by weighing 0.005 g copper oxide powder and suspending in 20 μl iso-propanol in a vial. The vial was sonicated for 15 minutes to ensure an even dispersion of the suspension liquid. 2 μl was extracted from

the suspension and drop coated onto the surface of the BDD electrode. The electrode was left to dry in normal laboratory atmosphere for 1 minute. The reproducibility of the experiment was carefully monitored. Each experiment was repeated three times with fresh electrolyte and cleaned electrode. All experiments were conducted at ambient temperature.

3.1.2 Characteristics of cyclic voltammogram

The shape of a typical cyclic voltammogram is illustrated in Figure 2-2. The electron transfer reaction in the three-electrode cell under experiment conditions is dependent on the relative concentrations of the reagent, product and solvent. In particular, for a general charge transfer reaction

$O + xe^- + yH^+ \leftrightarrow R$

in which x electrons are transferred, the Nernst equation shows that the potential (peak position at E_p in Figure 2-2) established at the electrode under equilibrium conditions is given by [1, 2, 3]

$$E = E^o + \frac{RT}{xF}\ln\frac{[O][H^+]^y}{[R]} \qquad \text{(Equation 1)}$$

where the equilibrium potential (E) of the electrode results from the standard electrode potential (E^o) of the reaction and concentrations of O, H^+ and R at the electrode surface. The Nernst Equation 1 can be rearranged into

$$E = \underbrace{E^o + \frac{RT}{xF}\ln\frac{[O]}{[R]}}_{\text{constant}} + \frac{RT}{xF}\ln[H^+]^y \qquad \text{(Equation 2)}$$

In a particular reaction and at standard temperature T=298 K, the first part of the Equation 2 is a constant number. Hence Equation 2 can be written as Equation 2'.

$$E = const + \frac{yRT}{xF}\ln[H^+] \qquad \text{(Equation 2')}$$

Equation 2' can be rewritten in the form of $\log_{10}$ [3]:

$$E = const + \frac{y}{x}\frac{RT}{F}2.3\log[H^+] \qquad \text{(Equation 3)}$$

The pH of a solution is defined as $-\log[H^+]$ [4], the Equation 3 can be rewritten as Equation 3'.

$$E = const - \underbrace{\frac{y}{x}\frac{RT}{F}2.3\,pH}_{\text{gradient}}$$

(Equation 3')

At standard temperature T=298 K, the $\frac{2.3RT}{F}$ term equals 0.0592 V [3]. Therefore, the gradient of the equation is determined by the number of electron transferred in the reaction with respect to pH value. Hence in a certain reaction from an experiment, the gradient can be obtained by plotting equilibrium potential *E* vs. solution pH. For example, at standard temperature, in one electron transfer and one proton related reaction, the gradient is 59.2 mV.

3.2 CV for pH 7 PBS in Ar deoxygenated and CO_2 saturated conditions

3.2.1 CV for pH 7 PBS in Ar deoxygenated conditions

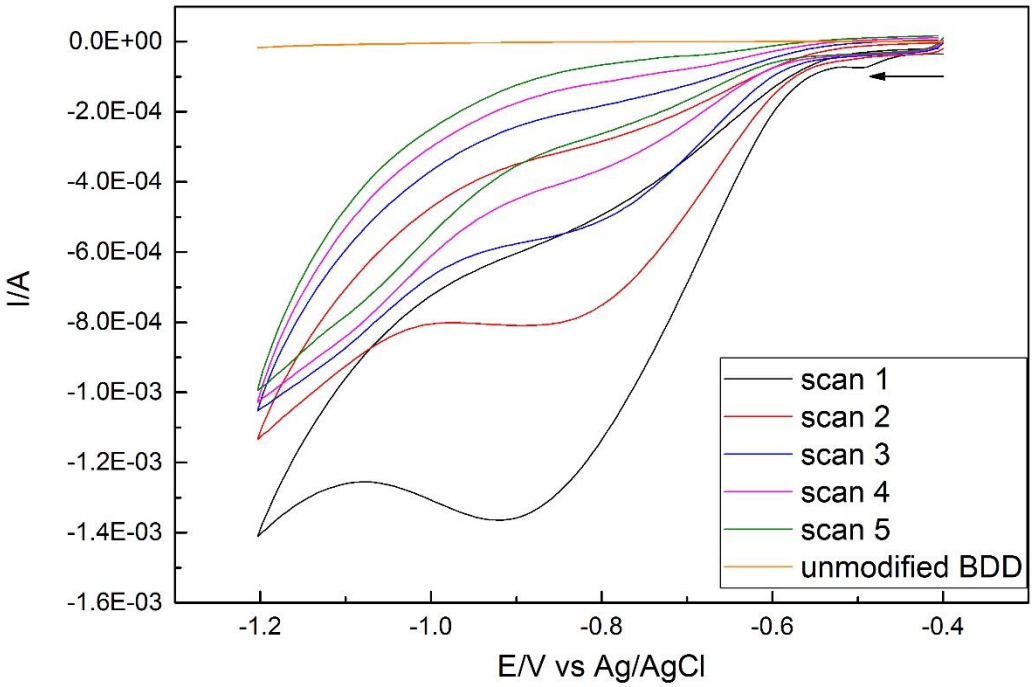

Figure 3-1. Cyclic voltammograms recorded in 0.2 M pH 7 Ar deoxygenated PBS at unmodified BDD (orange) and 5 scans modified with CuO. The potential was scanned from -0.4→-1.2→-0.4 V vs. Ag/AgCl. υ=100 $mV \cdot s^{-1}$.

Cyclic voltammograms of CuO in Ar deoxygenated solution at pH 7 are presented in Figure 3-1. The potential was cycled between -0.4 and -1.2 V. The unmodified BDD electrode shows no distinct peak during the whole cyclic sweep. This means the BDD electrode is cleaned thoroughly. For the CuO modified electrode, the reduction currents began to flow from -0.55 V in the first cycle. This may correspond to the HER. Plenty of tiny bubbles could be observed on the working electrode from this potential. The other likely reaction is the reduction of the Cu(II) centres in CuO to Cu(I) or Cu(0).

The broad cathodic peak can be observed with a maximum at -0.91 V from the first cycle, and no evidence of anodic peak on the reverse positive sweep. So it can be presumed that the reduction is irreversible in this potential range. The voltammograms show similar peaks in the subsequent sweeps, but the current magnitude decreases steadily with increasing scan number. The peak potential shifted progressively toward less cathodic potential with subsequent cycles. The decrease in current with continued cycling implies the decrease in concentration of reacting species present on the electrode surface. It can be assumed that the Cu(II) is reduced on the cathodic sweep, but the reduced Cu species that are formed cannot be oxidised in this potential range. Thus a thicker layer of Cu(I) or Cu(0) species is formed on the electrode surface with each subsequent cycle, hence the concentration of Cu(II) decreases gradually, which affects the current magnitude in the voltammograms.

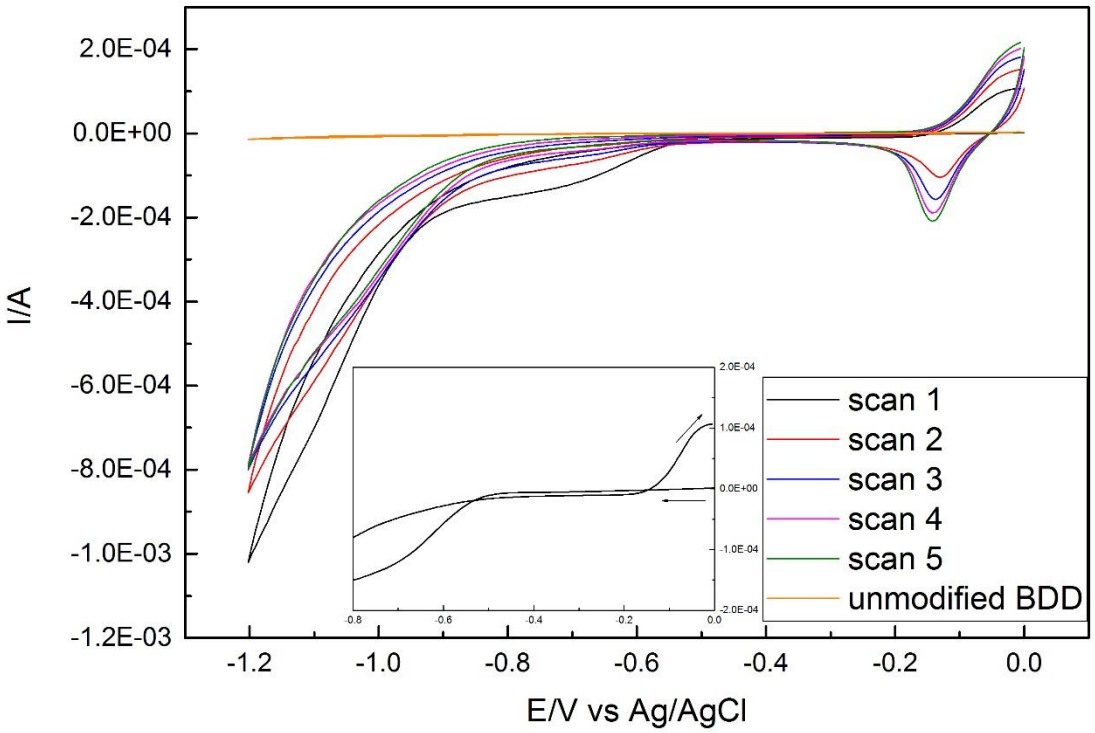

Figure 3-2. Cyclic voltammograms recorded in 0.2 M pH 7 Ar deoxygenated PBS at unmodified BDD (orange) and 5 scans modified with CuO. The potential was scanned from 0→-1.2→0 V vs. Ag/AgCl. υ=100 mV·s^{-1}. Insert figure: the first scan showing the range from 0 to -0.8 V.

Cyclic voltammograms of CuO in deoxygenated 0.2 M pH 7 PBS were recorded over a wider potential range in Figure 3-2. The cyclic potentials between 0 and -1.2 V were applied. On the first cathodic sweep, there were not any reduction peaks until -0.54 V. The current over the potential range 0 to -0.54 V appeared to close to zero (Figure 3-2 insert figure). This suggests the presence of a passivating layer [5] on the CuO surface. The passivating layer may result from the synthetic conditions and formation of a relatively non-reactive surface layer due to addition of H_2O_2 modifier and oxidant into the synthesis. Once the modifier was removed by reduction, the CuO surface is revealed and the redox peaks start to appear in the following sweep. Similar to the voltammograms in Figure 3-1, the reduction current began to flow after -0.54 V and the peak maximum at -0.80 V was observed in the first sweep. This has been assigned as Cu(II) reduction, together with HER. On the reverse positive sweep, one anodic peak appeared near 0.0 V. As can be seen in the figure, the entire oxidation peak is not

included within this scan range. This peak may be assigned to the oxidation of Cu(I) or Cu(0).

On the second negative potential sweep, another distinct cathodic peak was observed at -0.14 V. This peak may result from the reduction of Cu(II) to Cu(I). In this case, the cathodic peak at -0.80 V was due to the further reduction of Cu(I) species to Cu(0). And the anodic peak near 0.0 V can be assigned to the oxidation of Cu(0) to Cu(I) or Cu(II).

In the first cathodic scan and the second cathodic scan, the reduction of Cu(II) to Cu(I) can be observed at -0.8 V and at less negative potential at -0.14 V, respectively. Although both peaks have been assigned to the same reduction reaction, the onset potentials are quite different. This is caused by the passivation layer, which causes the cathodic peak to be observed at more negative potential [5] on the first scan. The Cu(II) formed in the anodic scan is then reduced at -0.14 V on the next cathodic sweep. Wang et al. [6] observed a very similar voltammogram of copper nanoparticle in 0.1 M pH 6±0.5 $KClO_4$. In their work one oxidation peak was observed on the reverse scan at 0.7 V vs. RHE [6]. Equation 4 [7] is used to convert the potential from RHE to Ag/AgCl reference electrode, which is used in this report.

$$E_{RHE} = E_{Ag/AgCl} + 0.059\,pH + E^{0}_{Ag/AgCl} \qquad \text{(Equation 4)}$$

At standard temperature T=298 K, $E^{0}_{Ag/AgCl}$=0.1976 V. So the oxidation peak appears at 0.12 V vs. Ag/AgCl. This is very close to our result.

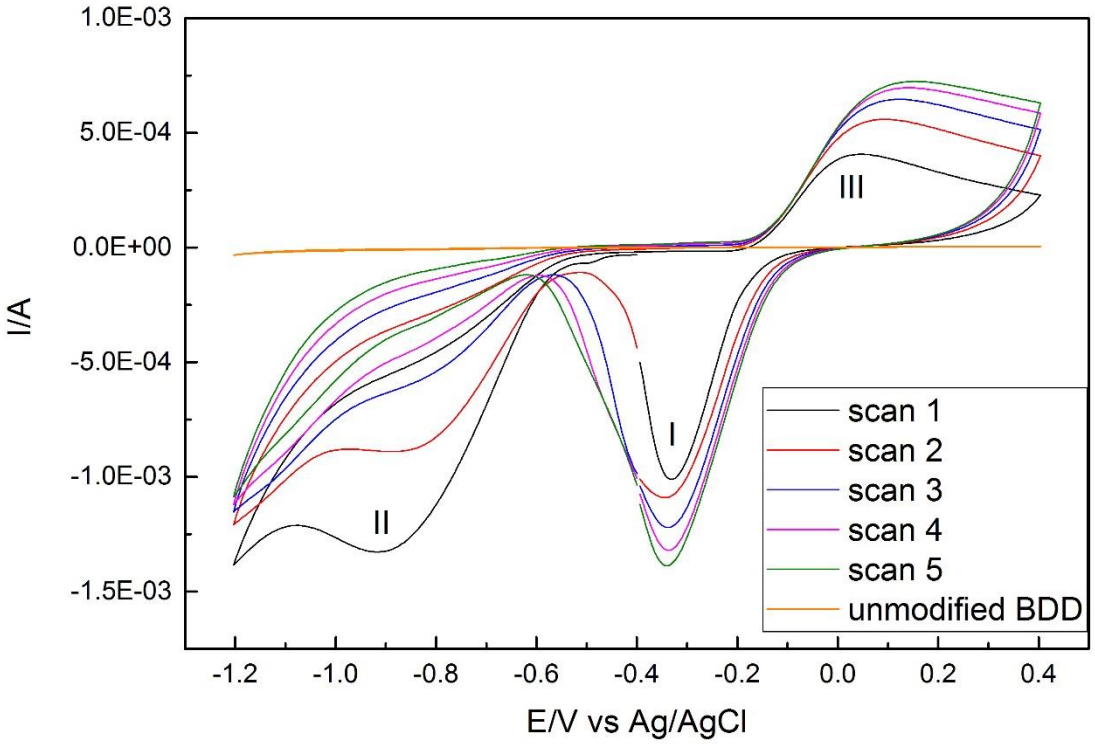

Figure 3-3. Cyclic voltammograms recorded in 0.2 M pH 7 Ar deoxygenated PBS at unmodified BDD (orange) and 5 scans modified with CuO. The potential was scanned from -0.4→-1.2→0.4→-0.4 V vs. Ag/AgCl. υ=100 mV·s^{-1}.

In figure 3-3, cyclic voltammograms of CuO in Ar deoxygenated pH 7 PBS are shown with the potential range extended further. The cyclic potential starts at -0.4 V, the first switching potential is -1.2 V, the second switching potential is 0.4 V. The shape of the first sweep is similar to the above figures. It must be noted that, on the first sweep, starting potential was selected as -0.4 V, avoiding the first reduction reaction (peak I).

The peak I appears at around -0.3 V, which is close to Strehblow's work at -0.2 V in pH 8 PBS [5], and Ambrose' work at -0.25 V in alkaline solution [8]. The peak II appears at -0.9 V. Wang [6] reported the reduction of Cu_2O to Cu at -0.85 V vs. Ag/AgCl. Han et al. [9] have investigated the electrochemical reduction of CO_2 at CuO thin films, and Cu(II) was reduced to Cu(0) at the potential of -0.874 V vs. SCE (-0.829 V vs. Ag/AgCl). One anodic peak was observed at the end of positive sweep at 0.05 V. Therefore the presence of the oxidation peak indicates that Cu(I) or Cu(0) must have been formed during reduction. The overall reactions can be summarized

below from literature [10].

I $2CuO + H_2O + 2e^- \rightarrow Cu_2O + 2OH^-$ (3-1)

II $Cu_2O + H_2O + 2e^- \rightarrow 2Cu + 2OH^-$ (3-2)

III $2Cu + H_2O \rightarrow Cu_2O + 2H^+ + 2e^-$ (3-3a)

$Cu + H_2O \rightarrow CuO + 2H^+ + 2e^-$ (3-3b)

Subsequent potential sweeps after the first cycle shown similar peaks, the current magnitude increased slightly with each cycle. This implies steady concentration of redox species present on the electrode surface.

3.2.2 CV for pH 7 PBS in CO_2 saturated conditions

To investigate the response in the presence of CO_2, CO_2 saturated solution was introduced in the following experiments. The electrolyte was deoxygenated by bubbling with Ar for 20 minutes, and then further bubbled with pre-cleaned CO_2 for 20 minutes. To ensure the reproducibility of the results, each experiment was repeated three times with fresh electrolyte and cleaned electrode.

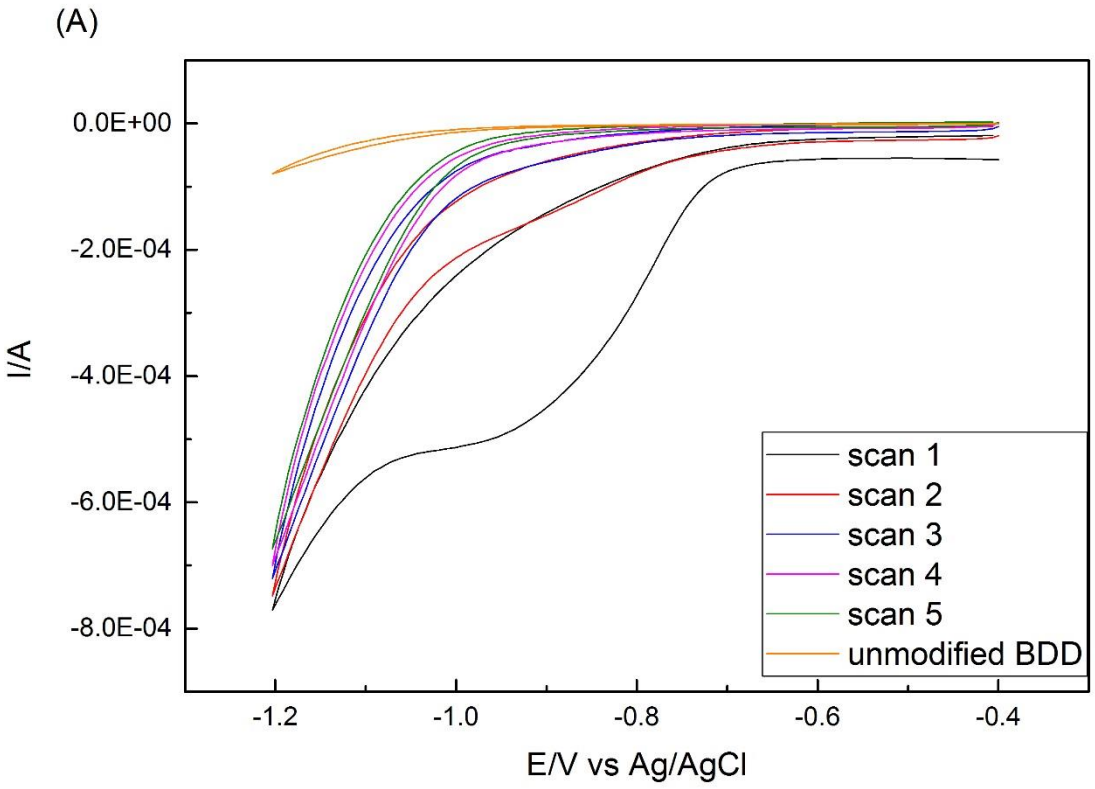

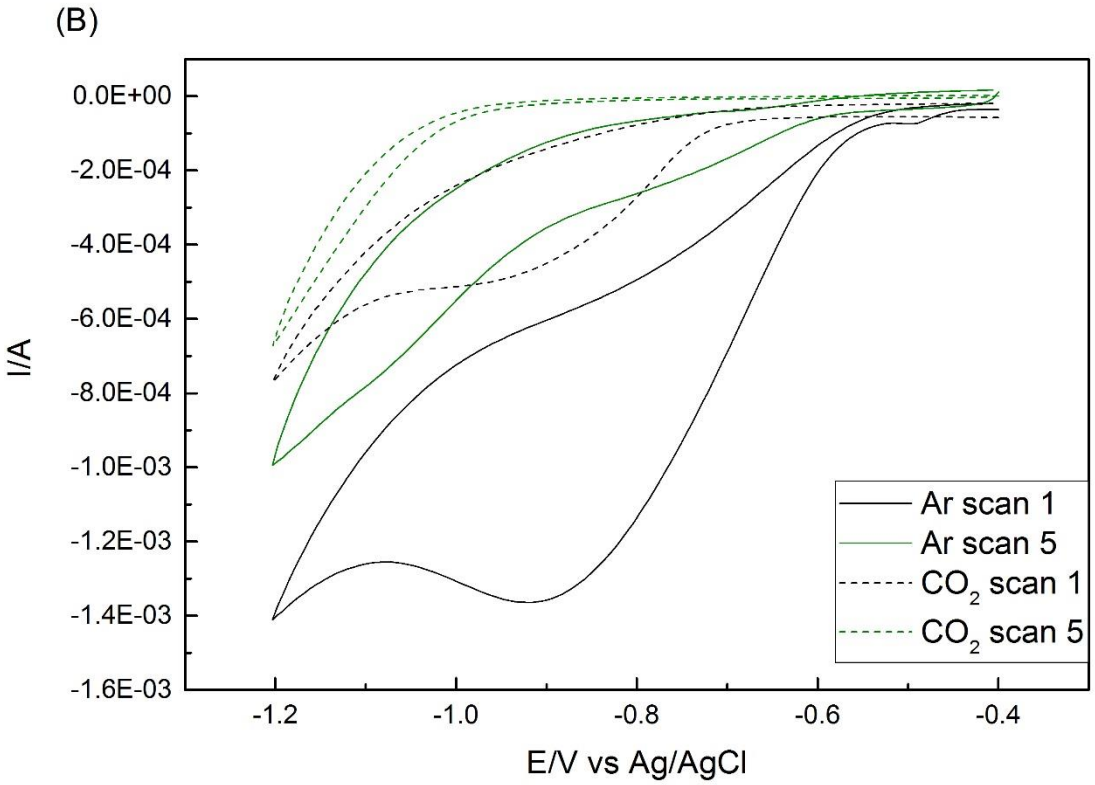

Figure 3-4. (A) Cyclic voltammograms recorded in 0.2 M pH 7 CO_2 saturated PBS at unmodified BDD (orange) and 5 scans modified with CuO. The potential was scanned from -0.4→-1.2→-0.4 V vs. Ag/AgCl. υ=100 mV·s^{-1}. (B) Cyclic voltammograms recorded in 0.2 M Ar (solid lines) and CO_2 (dashed lines) pH 7 PBS for scan 1 and 5.

Cyclic voltammograms of CuO in CO_2 saturated PBS solution are presented in Figure 3-4 (A). The unmodified BDD electrode shows no distinct peak during the potential cycle. In the first cycle with CuO modified electrode, the reduction current began to flow from -0.70 V. Since bubbles could also be observed on the electrode from this potential, it appears that HER still proceeds and is not affected by CO_2 when potential is cycled over the range -0.4 V to -1.2 V. With more negative potential applied, the reduction peak can be observed at -0.90 V. Cu(II) starts to be reduced to Cu(I) or Cu(0). As there is no oxidation peak on the reverse positive sweep, Cu(I)/Cu(0) that is formed cannot be oxidised back in this potential range. Hence the concentration of Cu(II) on the electrode surface decreases with each cycle. So the current magnitude decreases in the following sweeps. It shows very similar chemical behaviour compared with in Ar deoxygenated solution (Figure 3-1).

However the current magnitude decreases more rapidly than seen under Ar deoxygenated condition and the reduction peak cannot be clearly observed from the third cycle in CO_2 saturated solution. Another difference compared with the Ar deoxygenated solution is that the current magnitude is suppressed significantly, as shown in Figure 3-4 (B). It can be assumed that additional processes are taking place on CuO surface that result in suppression of the current. These processes must be attributed to the presence of CO_2.

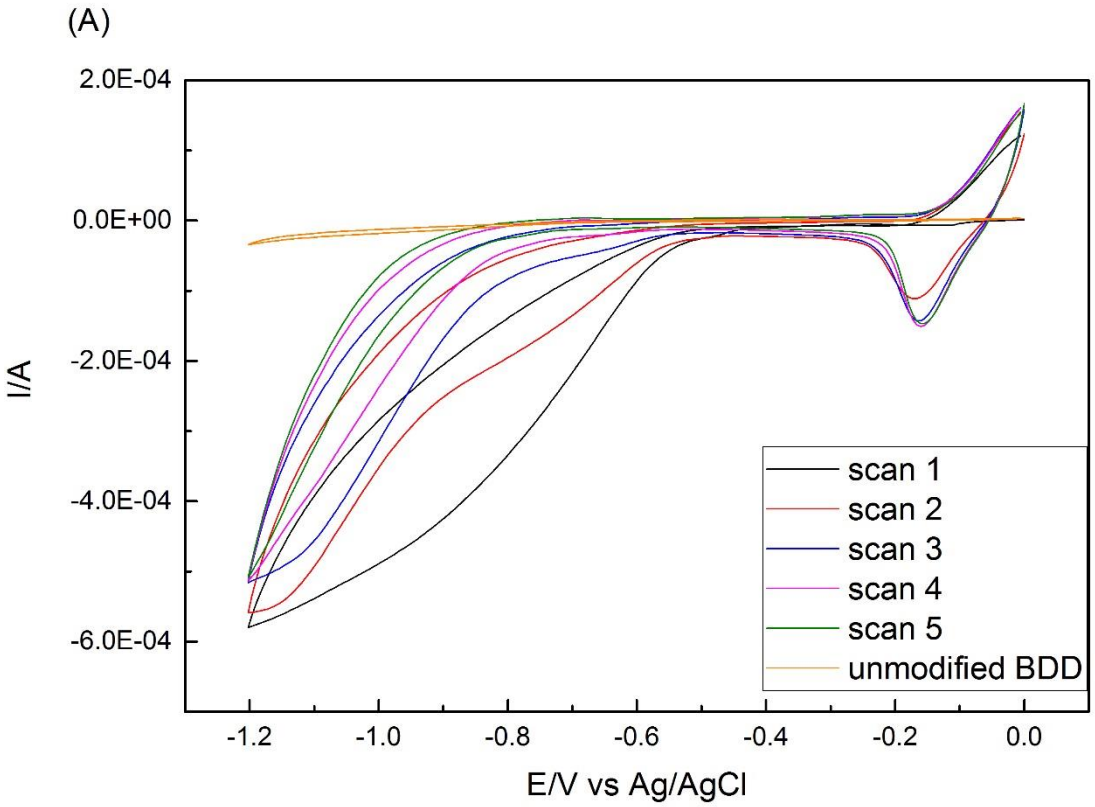

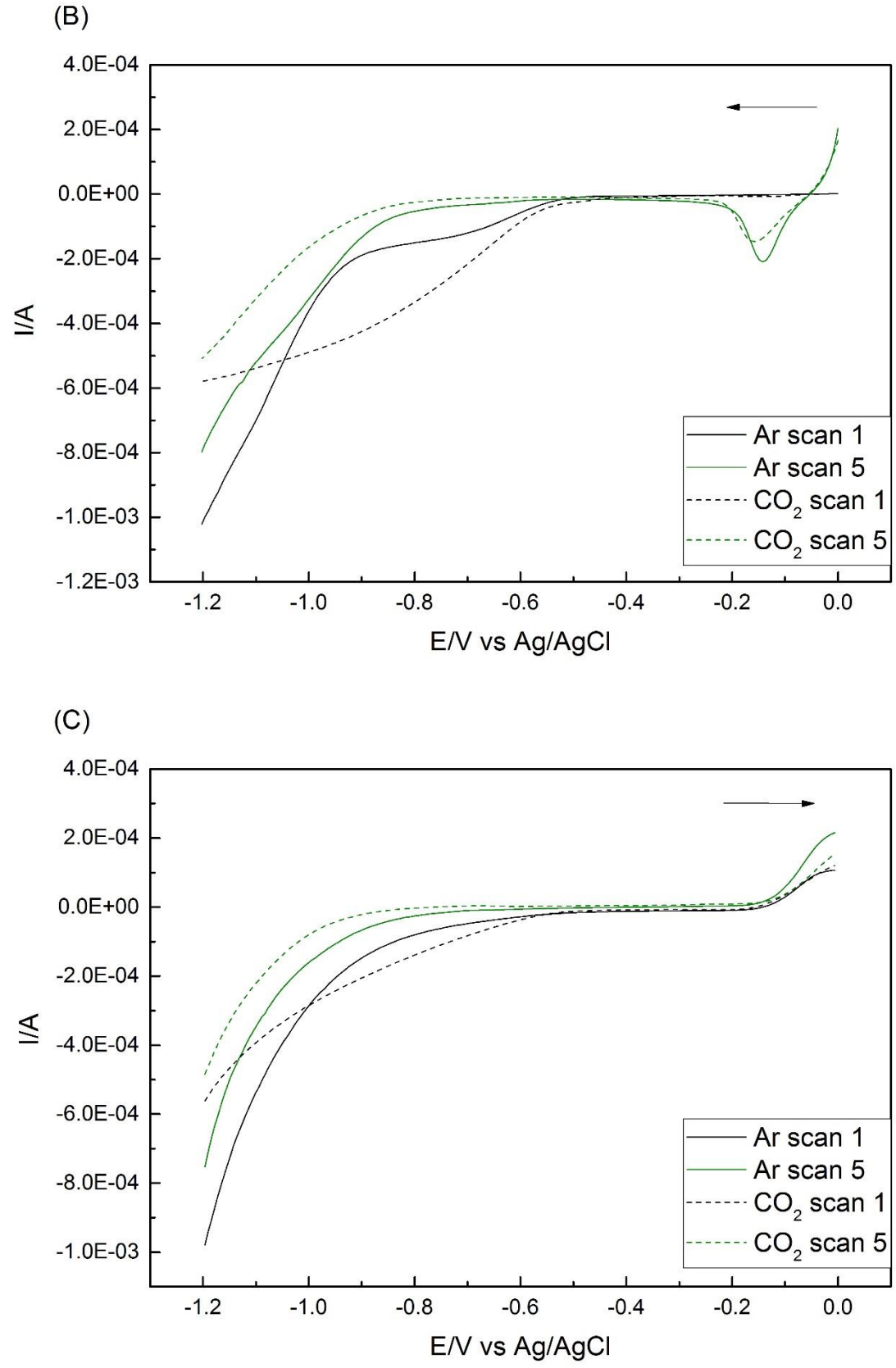

Figure 3-5. (A) Cyclic voltammograms recorded in 0.2 M pH 7 CO_2 saturated PBS at unmodified BDD (orange) and 5 scans modified with CuO. The potential was scanned

from 0→-1.2→0 V vs. Ag/AgCl. υ=100 $mV \cdot s^{-1}$. (B) Negative sweep, (C) positive sweep of cyclic voltammograms recorded in 0.2 M Ar (solid lines) and CO_2 (dashed lines) pH 7 PBS for scan 1 and 5.

Cyclic voltammograms of CuO in CO_2 saturated solution were recorded over a wider potential range between 0 and -1.2 V in Figure 3-5 (A). In the first negative sweep, there was no apparent current flow until -0.45 V because of the passivating layer discussed in the previous section. One peak at -0.80 V can be observed after activation, which could be assigned as Cu(II) reduction and HER. One oxidation peak appeared near 0.0 V on the reverse positive sweep. This peak has been assigned as oxidation of Cu(I)/Cu(0) to Cu(I) or Cu(II).

On the second negative sweep, a new reduction peak can be observed at -0.15 V. It has been assigned as reduction of Cu(II) to Cu(I). And the second reduction peak at -0.80 V is the further reduction of Cu(I) to Cu(0). So the oxidation peak near 0.0 V is the oxidation of Cu(0) to Cu(I) or Cu(II).

Comparing the cyclic voltammograms recorded in Ar deoxygenated and CO_2 saturated solutions in Figure 3-5 (B) and (C), after the first scan the current magnitude is suppressed in CO_2 saturated solution, which is consistent with the behaviour observed in narrower potential range in Figure 3-4 (B). In the first negative sweep, the current starts to flow at -0.45 V in CO_2 saturated solution, compared to -0.54 V in Ar deoxygenated solution. This indicates that an additional reduction process takes place at the CuO in the presence of CO_2. A possible explanation is that CO_2 could be adsorbed on CuO surface competing with the surface bonded H_2O or OH required for the reaction of HER. The chemical behaviour of the electrode in both solutions are similar in the positive sweep.

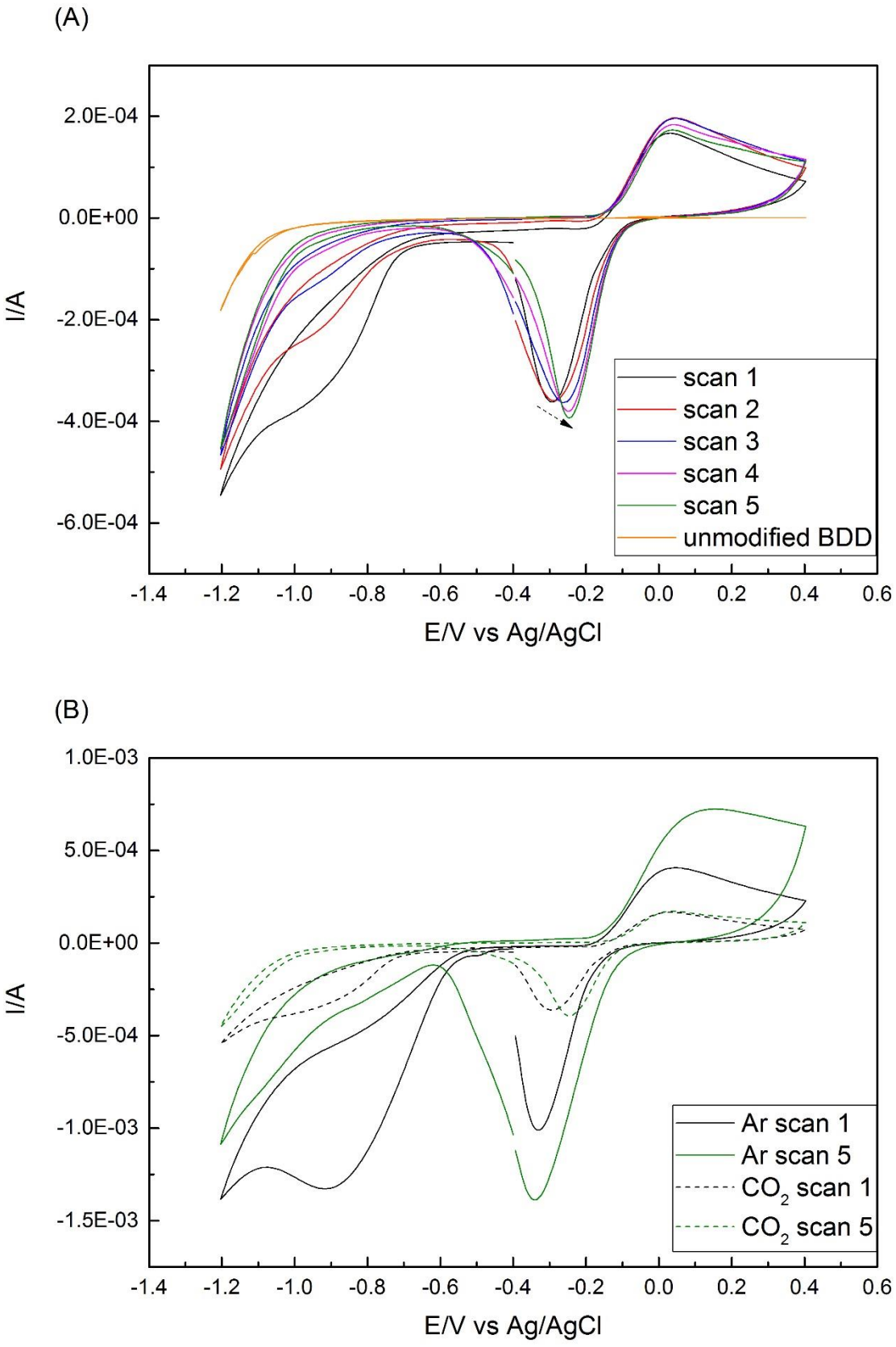

Figure 3-6. (A) Cyclic voltammograms recorded in 0.2 M pH 7 CO_2 saturated PBS at unmodified BDD (orange) and 5 scans modified with CuO. The potential was

scanned from -0.4→-1.2→0.4→-0.4 V vs. Ag/AgCl. υ=100 $mV \cdot s^{-1}$. (B) Cyclic voltammograms recorded in 0.2 M Ar (solid lines) and CO_2 (dashed lines) pH 7 PBS for scan 1 and 5.

Cyclic voltammograms of CuO in CO_2 saturated solution are recorded over a further wider potential range in Figure 3-6 (A). The potential starts at -0.4 V, cathodic sweep to -1.2 V, and switch to positive sweep to 0.4 V, then switch to cathodic sweep again till -0.4 V to finish one cyclic sweep. The first reduction peak has a positive shift from -0.29 to -0.24 V with increasing scan number. The current magnitude and minimum/maximum current of peaks are stable with cycling, which implies steady concentration of Cu(II) and Cu(I)/Cu(0) redox species present on the electrode surface with introduction of CO_2 in the solution.

Figure 3-6 (B) shows cyclic voltammograms for the first and fifth scan in Ar deoxygenated and CO_2 saturated solutions. Consistent with the above results, the current magnitude is smaller in CO_2 saturated than Ar deoxygenated solution. It is already known that there are additional processes taking place on CuO surface in presence of CO_2. This additional process could be an adsorbed layer of CO_2 or reaction intermediates on CuO surface, resulting in the decrease of current magnitude. And these also may be competitive reactions on the electrode surface. It should be noted that CO_2 dissolves to form mostly HCO_3^-, together with molecular CO_2 in this pH solution. More detail will be discussed further in the section 3.7 and 3.8.

3.3 CV for pH 4 PBS in Ar deoxygenated and CO_2 saturated conditions

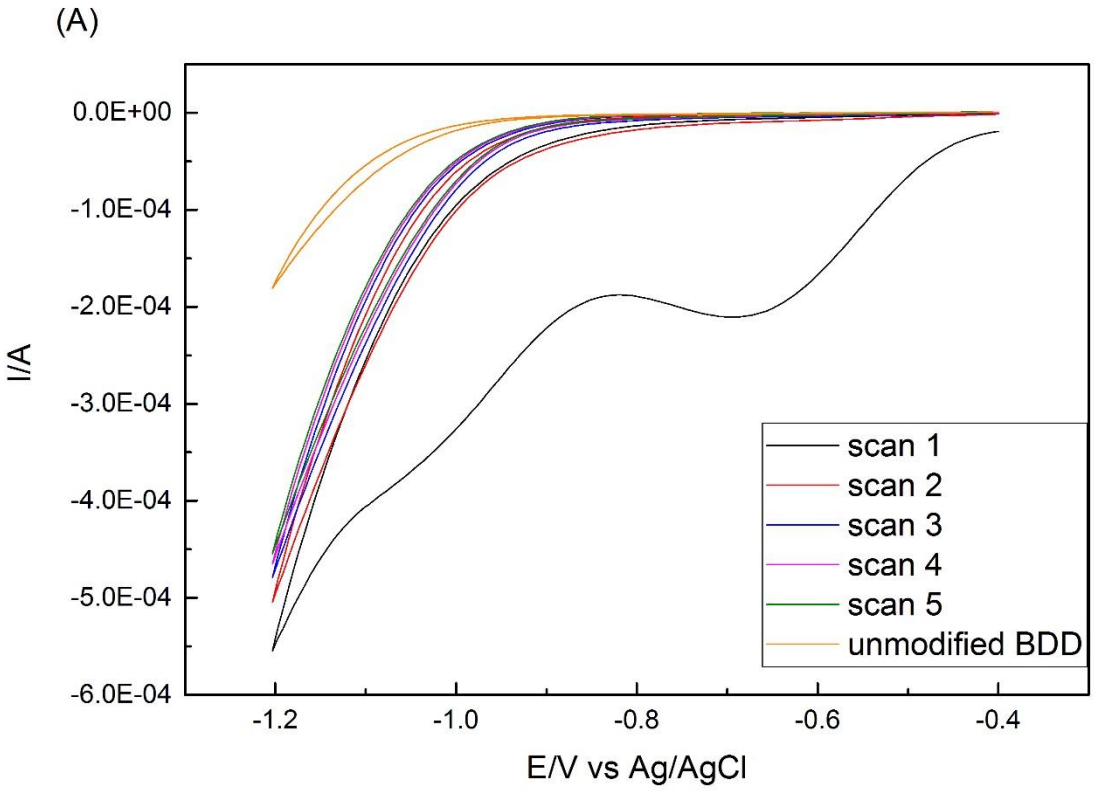

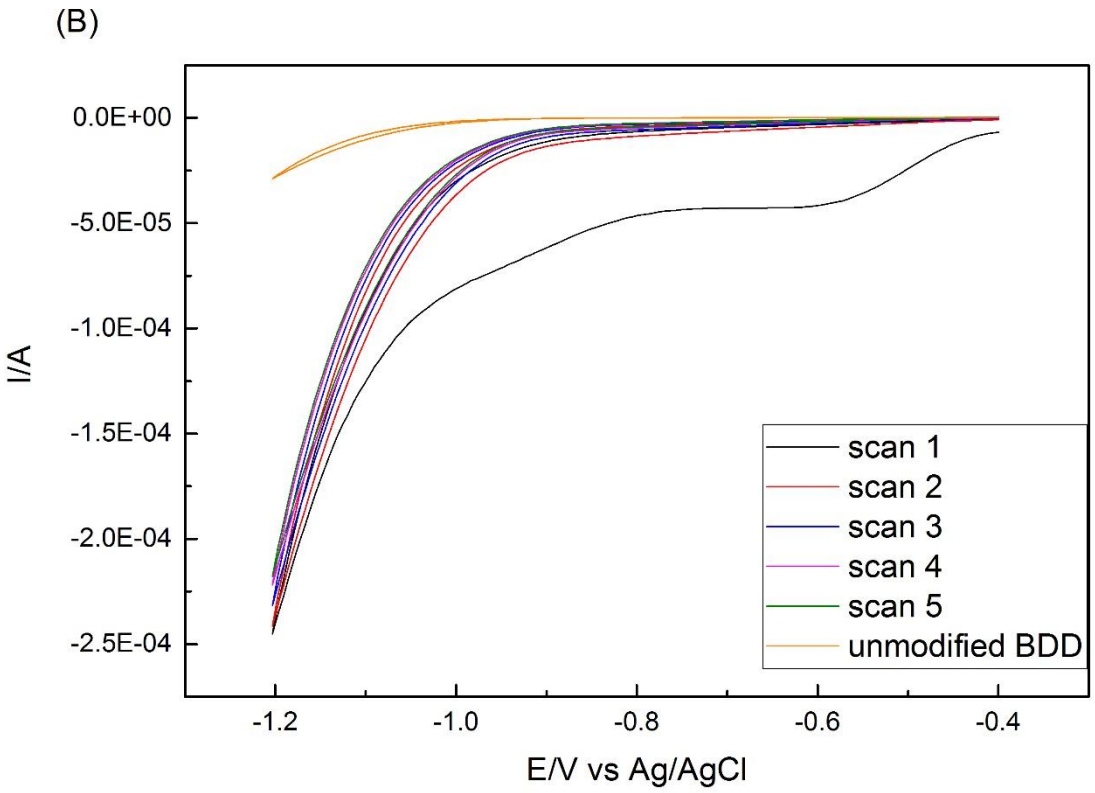

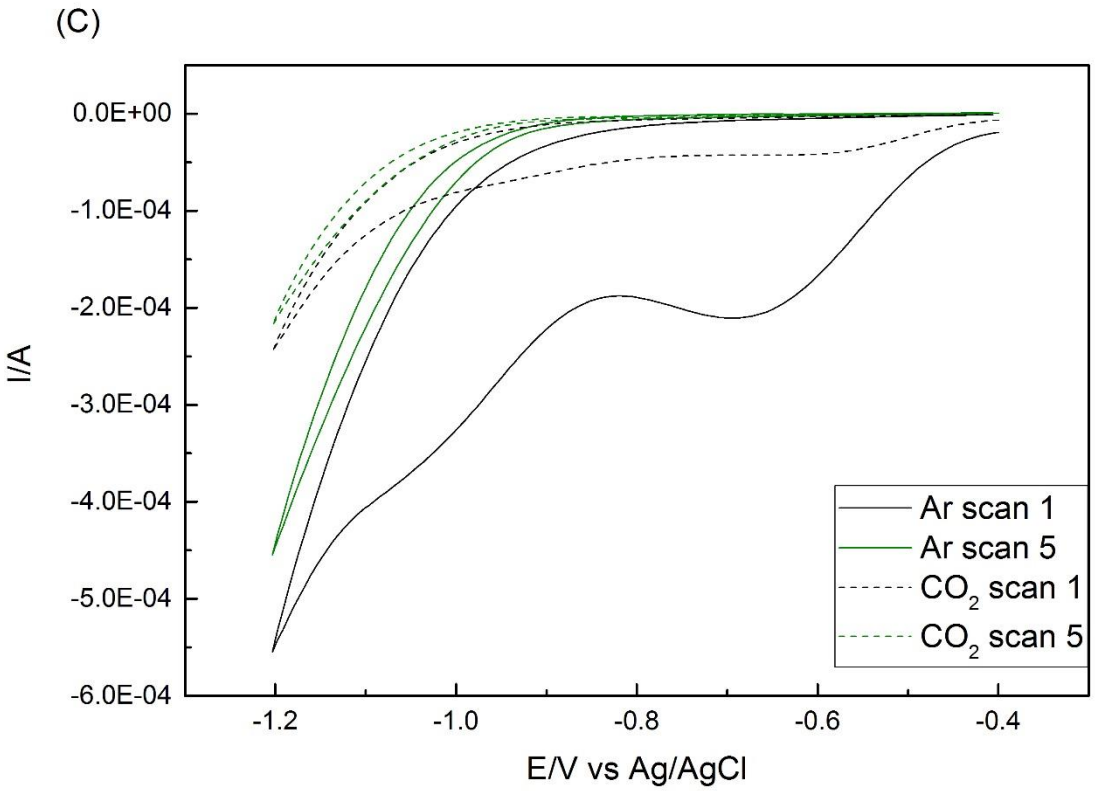

Figure 3-7. Cyclic voltammograms recorded in 0.2 M pH 4 PBS at unmodified BDD (orange) and 5 scans modified with CuO, (A) Ar deoxygenated solution, (B) CO_2 saturated solution. (C) Cyclic voltammograms recorded in 0.2 M Ar (solid lines) and CO_2 (dashed lines) pH 4 PBS for scan 1 and 5. The potential was scanned from -0.4→-1.2→-0.4 V vs. Ag/AgCl. υ=100 mV·s^{-1}.

Cyclic voltammograms of CuO in Ar deoxygenated and CO_2 saturated PBS solution are presented in Figure 3-7 (A) and (B). In Ar deoxygenated solution, the reduction current starts to increase from -0.42 V, and the reduction peak can be observed at -0.69 V in the first cycle with CuO modified electrode. As there is no oxidation peak on the reverse sweep, Cu(I)/Cu(0) cannot be oxidised to Cu(II) for the next negative sweep. The amount of Cu(II) available for reduction is therefore decreased after each cycle, so the current magnitude decreases in the following sweeps.

In CO_2 saturated solution, the current increases at around the same potential at -0.42 V, and the reduction peak is observed at less negative potential at -0.61 V. The current magnitude in CO_2 saturated solution is smaller than in Ar deoxygenated solution, as shown in Figure 3-7 (C), this is similar to the behaviour observed in pH 7 PBS solution.

(A)

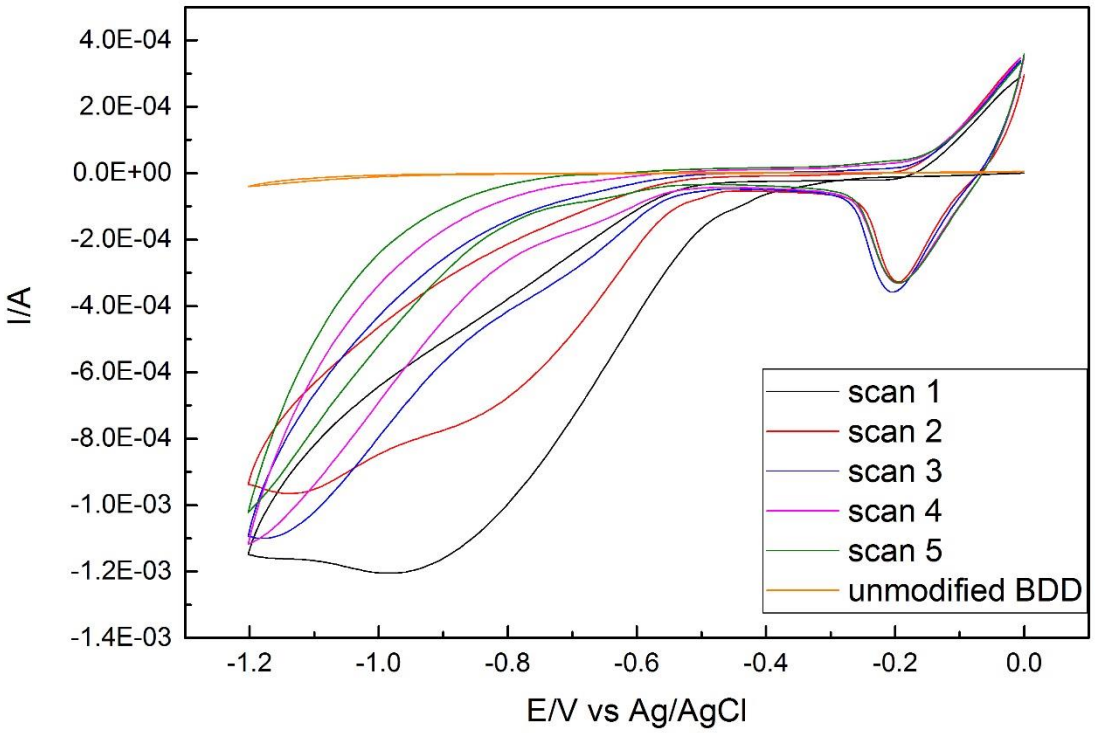
4.0E-04
2.0E-04
0.0E+00
-2.0E-04
-4.0E-04
-6.0E-04
-8.0E-04
-1.0E-03
-1.2E-03
-1.4E-03
I/A
-1.2
-1.0
-0.8
-0.6
-0.4
-0.2
0.0
E/V vs Ag/AgCl
scan 1
scan 2
scan 3
scan 4
scan 5
unmodified BDD

(B)

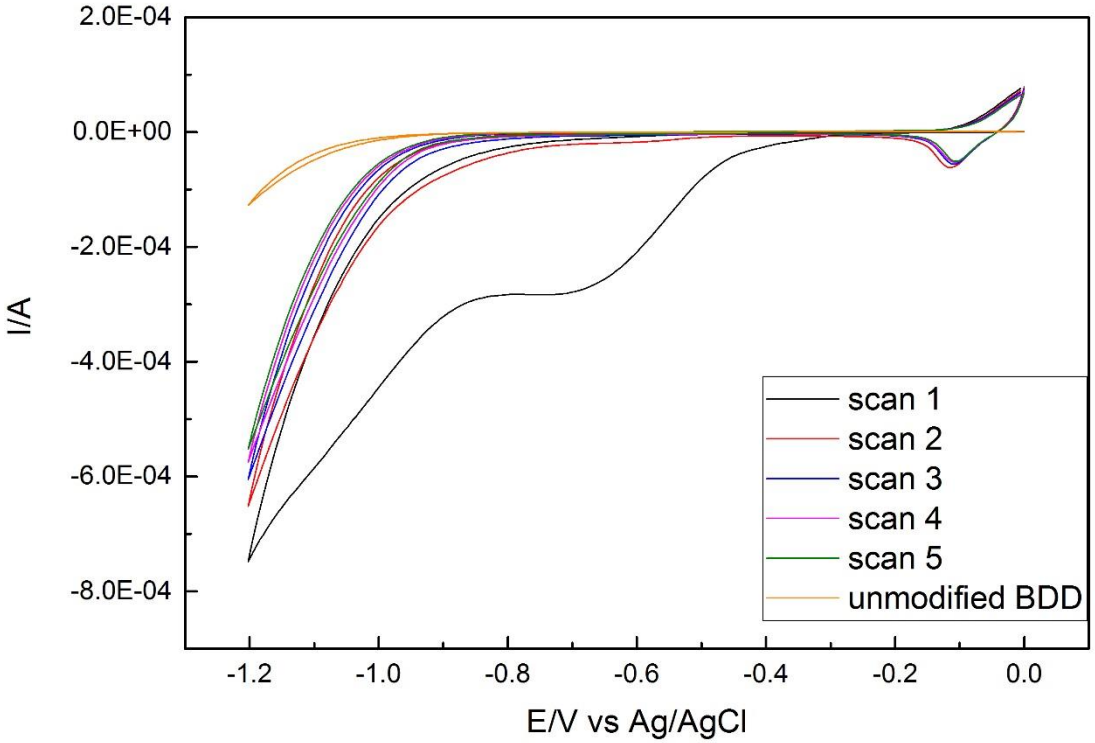
2.0E-04
0.0E+00
-2.0E-04
-4.0E-04
-6.0E-04
-8.0E-04
I/A
-1.2
-1.0
-0.8
-0.6
-0.4
-0.2
0.0
E/V vs Ag/AgCl
scan 1
scan 2
scan 3
scan 4
scan 5
unmodified BDD

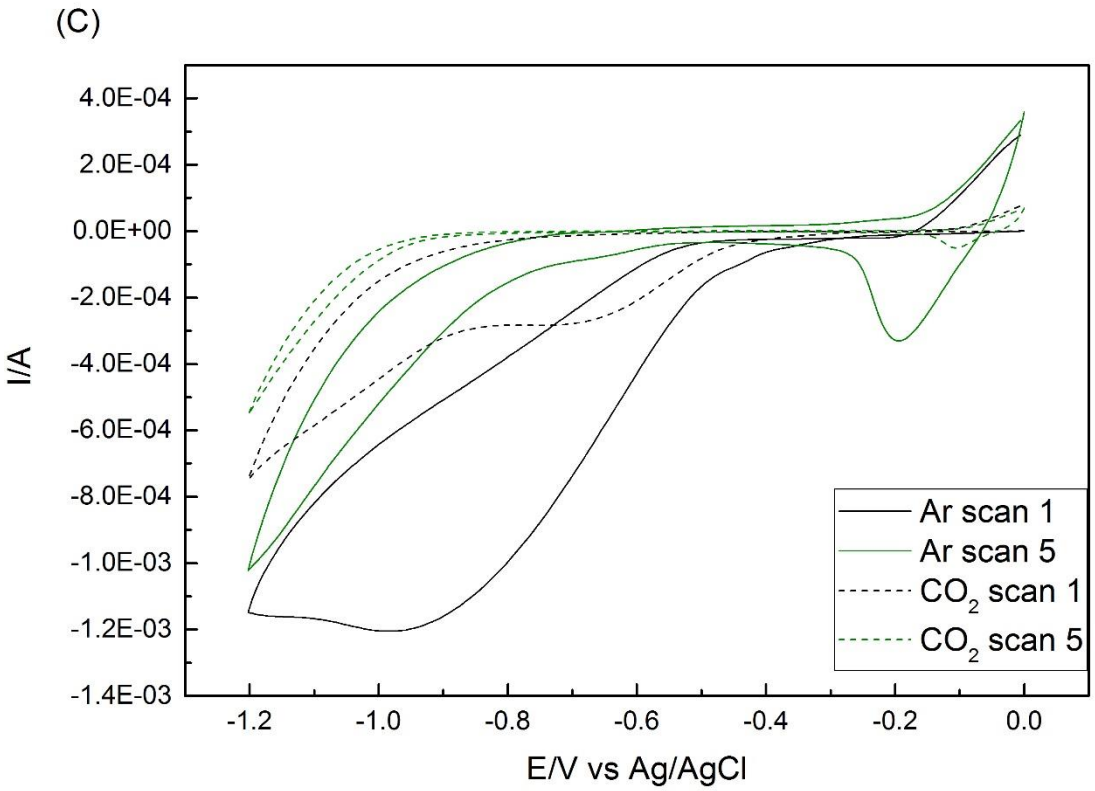

Figure 3-8. Cyclic voltammograms recorded in 0.2 M pH 4 PBS at unmodified BDD (orange) and 5 scans modified with CuO, (A) Ar deoxygenated solution, (B) CO_2 saturated solution. (C) Cyclic voltammograms recorded in 0.2 M Ar (solid lines) and CO_2 (dashed lines) pH 4 PBS for scan 1 and 5. The potential was scanned from 0→-1.2→0 V vs. Ag/AgCl. υ=100 mV·s^{-1}.

Cyclic voltammograms of CuO in Ar deoxygenated and CO_2 saturated solution is recorded with applied potential range between 0 and -1.2 V in Figure 3-8 (A) and (B). In the first negative sweep in Ar deoxygenated solution, the current magnitude starts to increase from -0.31 V, and the peak appears at -0.99 V. On reverse sweep, the oxidation peak appears near 0.0 V. On the second cycle, another reduction peak can be observed at -0.19 V.

For the cyclic voltammograms in CO_2 saturated solution, the current starts to increase from -0.30 V, two reduction peaks can be observed at -0.11 V and -0.74 V, and the oxidation peak appears around 0.0 V. Similarly to Figure 3-7 (C), in the wider range of potential, the current magnitude is smaller in CO_2 saturated solution than in Ar deoxygenated solution.

(A)

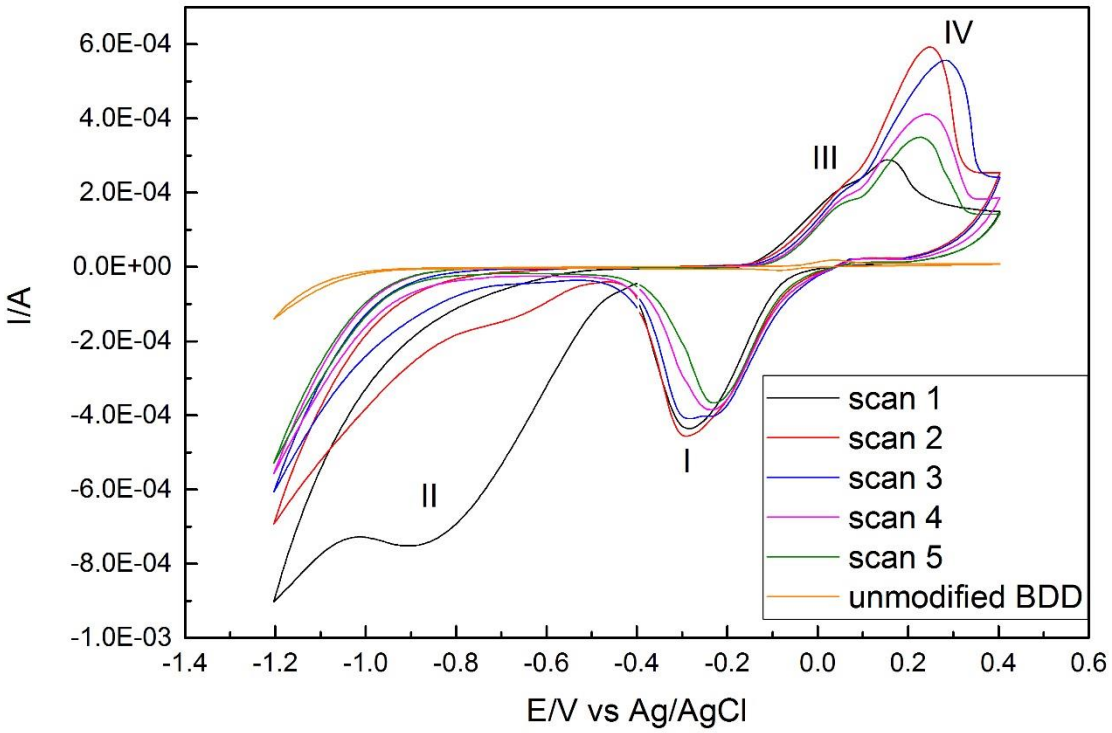
6.0E-04
4.0E-04
2.0E-04
0.0E+00
-2.0E-04
-4.0E-04
-6.0E-04
-8.0E-04
-1.0E-03
I/A
-1.4
-1.2
-1.0
-0.8
-0.6
-0.4
-0.2
0.0
0.2
0.4
0.6
E/V vs Ag/AgCl
I
II
III
IV
scan 1
scan 2
scan 3
scan 4
scan 5
unmodified BDD

(B)

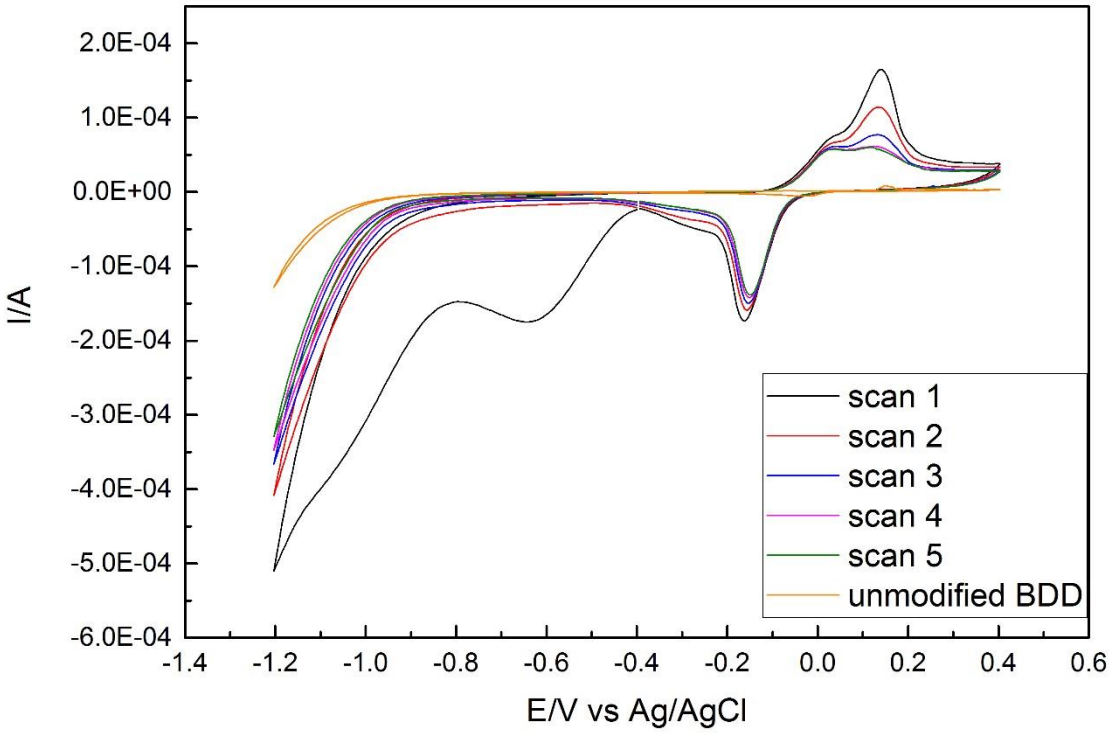
2.0E-04
1.0E-04
0.0E+00
-1.0E-04
-2.0E-04
-3.0E-04
-4.0E-04
-5.0E-04
-6.0E-04
I/A
-1.4
-1.2
-1.0
-0.8
-0.6
-0.4
-0.2
0.0
0.2
0.4
0.6
E/V vs Ag/AgCl
scan 1
scan 2
scan 3
scan 4
scan 5
unmodified BDD

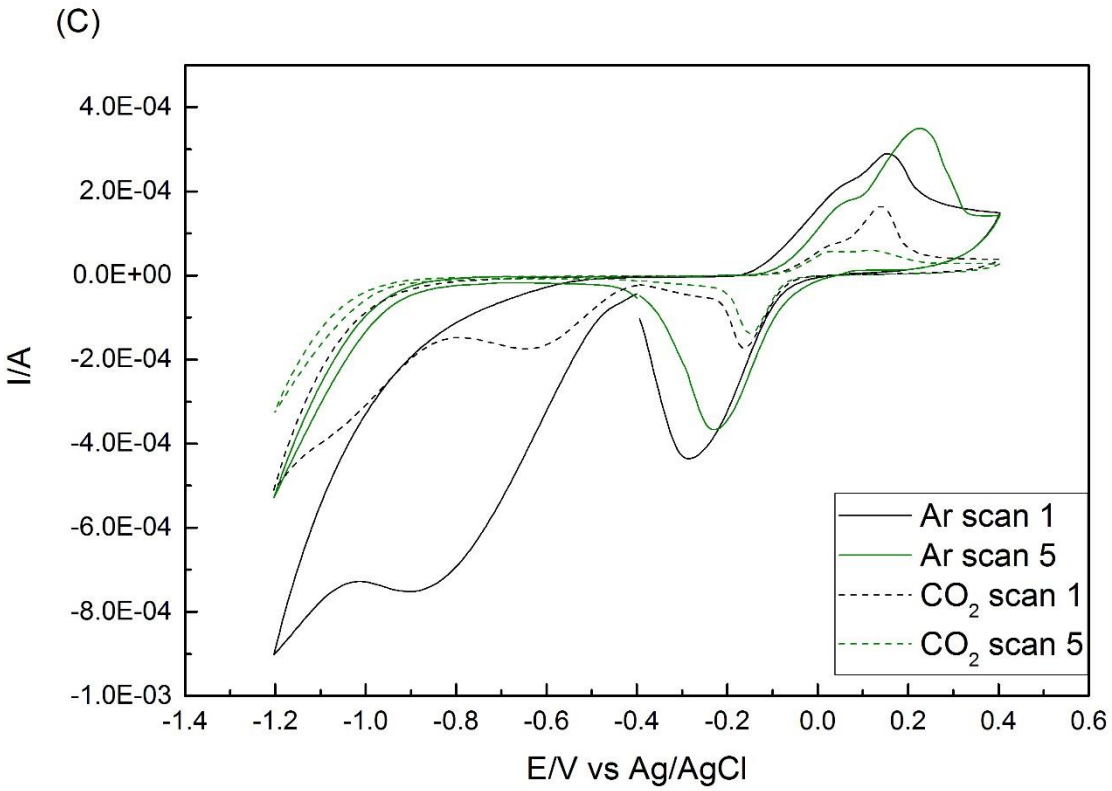

Figure 3-9. Cyclic voltammograms recorded in 0.2 M pH 4 PBS at unmodified BDD (orange) and 5 scans modified with CuO, (A) Ar deoxygenated solution, (B) CO_2 saturated solution. (C) Cyclic voltammograms recorded in 0.2 M Ar (solid lines) and CO_2 (dashed lines) pH 4 PBS for scan 1 and 5. The potential was scanned from -0.4→-1.2→0.4→-0.4 V vs. Ag/AgCl. υ=100 mV·s^{-1}.

Cyclic voltammograms were recorded with the potential range between 0.4 V and -1.2 V in Figure 3-9. The cyclic voltammogram in Ar deoxygenated solution shows reduction peak II at -0.88 V in the first negative sweep. After switching potential, two oxidation peaks at 0.04 V (peak III) and 0.15 V (peak IV) can be observed. After the second switching potential, another reduction peak I appears at -0.29 V. In the second cycle, the peak II shifts to -0.71 V, and oxidation peaks III and IV shift to 0.05 and 0.25 V. The peak I is stable at -0.29 V. Except peak II, the current magnitude of other three peaks increases in the second cycle. The oxidation peaks show positive shift in the second cycle. From the third cycle, the peaks show positive shift continually, but the current magnitude of the peaks decrease gradually. It has been assigned that peak I is the reduction of Cu(II) to Cu(I), and peak II is the further reduction of Cu(I) to Cu(0). The oxidation peak III is the oxidation of Cu(0) to Cu(I), and peak IV is the

oxidation of Cu(I) back to Cu(II), by Wilhelm et al. [11]. They suggested that the separation of peaks I and II implies a layered $Cu/Cu_2O/CuO$ electrode surface structure [11]. The reduction and oxidation reactions and potentials are influenced by pH value [11]. The reactions in acid solution can be summarized below [12, 13].

I $2CuO + 2H^+ + 2e^- \rightarrow Cu_2O + H_2O$ (3-4)

II $Cu_2O + 2H^+ + 2e^- \rightarrow 2Cu + H_2O$ (3-5)

III $2Cu + H_2O \rightarrow Cu_2O + 2H^+ + 2e^-$ (3-6)

IV $Cu_2O + H_2O \rightarrow 2CuO + 2H^+ + 2e^-$ (3-7)

The cyclic voltammogram in CO_2 saturated solution shows peak II at -0.64 V, peak III and VI at 0.02 V and 0.14V, peak I at -0.16 V in the first cycle. In CO_2 saturated condition, the magnitude of the peak current decreases from the second cycle and the potential of the peaks are stable.

Figure 3-9 (C) shows cyclic voltammograms for the first and fifth scan in Ar deoxygenated and CO_2 saturated solutions. Consistent with above results, the current magnitude is smaller in CO_2 saturated than in Ar deoxygenated solution in three different scan scales. Besides, the reduction peaks are observed at less negative potential in CO_2 saturated solution than Ar deoxygenated solution. This indicates that in pH 4 solution, CO_2 could be adsorbed on electrode surface and the additional reduction process takes place at the CuO catalyst in the presence of CO_2. In pH 4 solution, the CO_2 exists in the solution in the form of dissolved molecular CO_2.

3.4 CV for pH 9 PBS in Ar deoxygenated and CO_2 saturated conditions

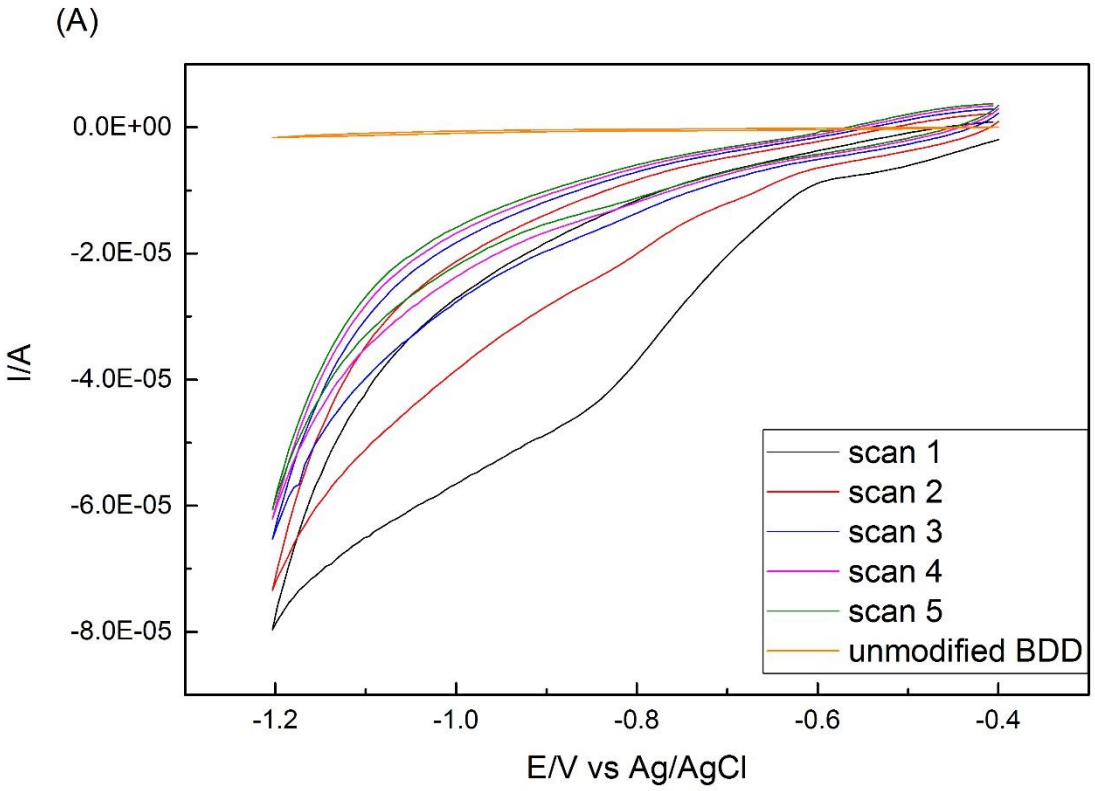

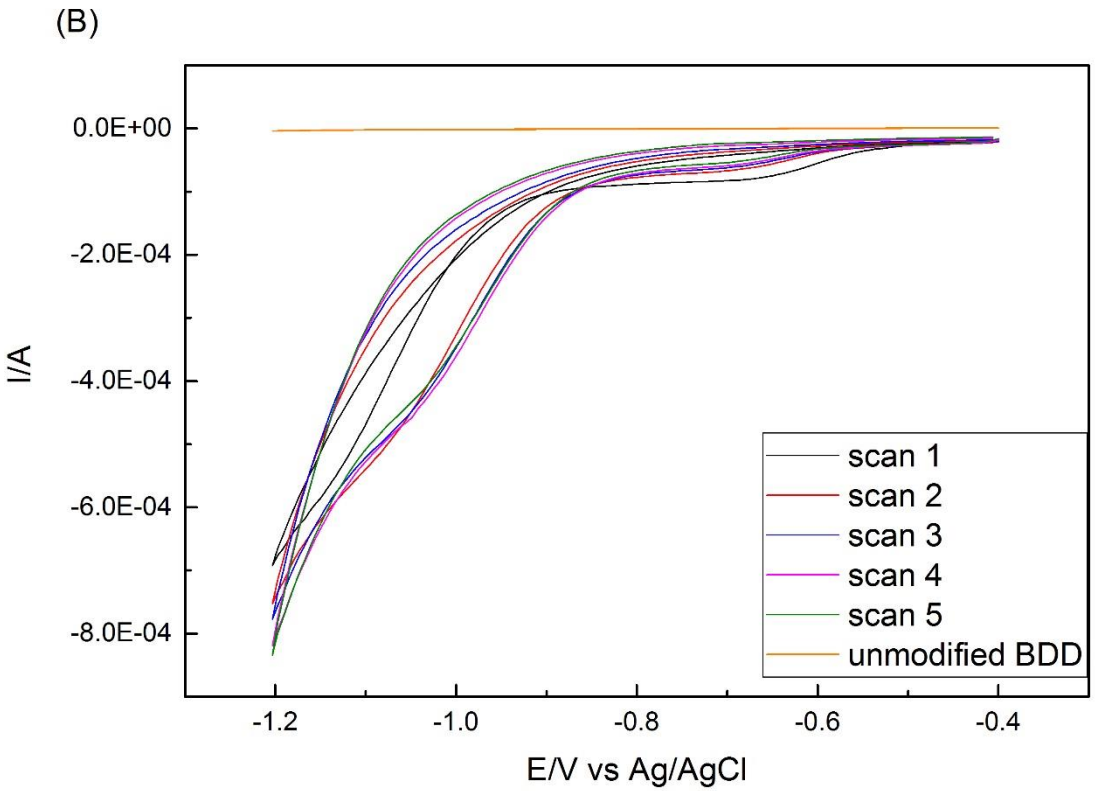

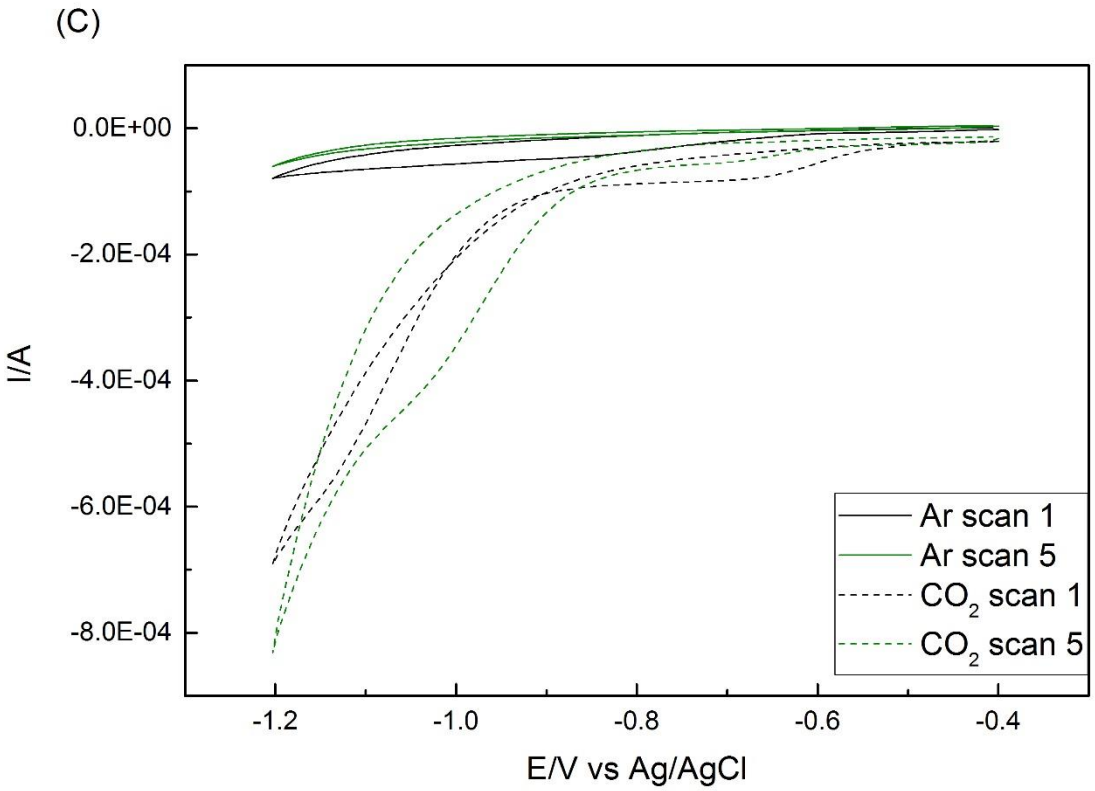

Figure 3-10. Cyclic voltammograms recorded in 0.2 M pH 9 PBS at unmodified BDD (orange) and 5 scans modified with CuO, (A) Ar deoxygenated solution, (B) CO_2 saturated solution. (C) Cyclic voltammograms recorded in 0.2 M Ar (solid lines) and CO_2 (dashed lines) pH 9 PBS for scan 1 and 5. The potential was scanned from -0.4→-1.2→-0.4 vs. Ag/AgCl. υ=100 mV·s^{-1}.

In pH 9 Ar deoxygenated solution with the potential range from -0.4 V to -1.2 V, the cyclic voltammograms in Figure 3-10 (A) show very typical reduction behaviour, with a reduction peak observed at -0.85 V in the first cycle. The reduction current decreases with increasing cycles.

In CO_2 saturated solution, as shown in Figure 3-10 (B), the first reduction peak occurs at -0.70 V. With increasing number of scans, the currents are enhanced over the potential range in general. This indicates that reduction processes involving CO_2 take place at higher pH values. But the current magnitude of the peak current is smaller than the first scan, as not enough Cu(II) can be oxidised back in the positive sweep for the following scans.

The Figure 3-10 (C) shows the first and fifth scans in Ar deoxygenated and CO_2 saturated conditions, the overall currents are larger in CO_2 saturated solution compared with in Ar deoxygenated solution. This is opposite to what has been observed in pH 4 (Figure 3-4 (B)) and pH 7 (Figure 3-7 (C)) solutions, where the current is suppressed in CO_2 saturated solution. So the current enhancement is pH value dependent. This may also depend on what dissolved species are present in CO_2 saturated solutions in different pH values.

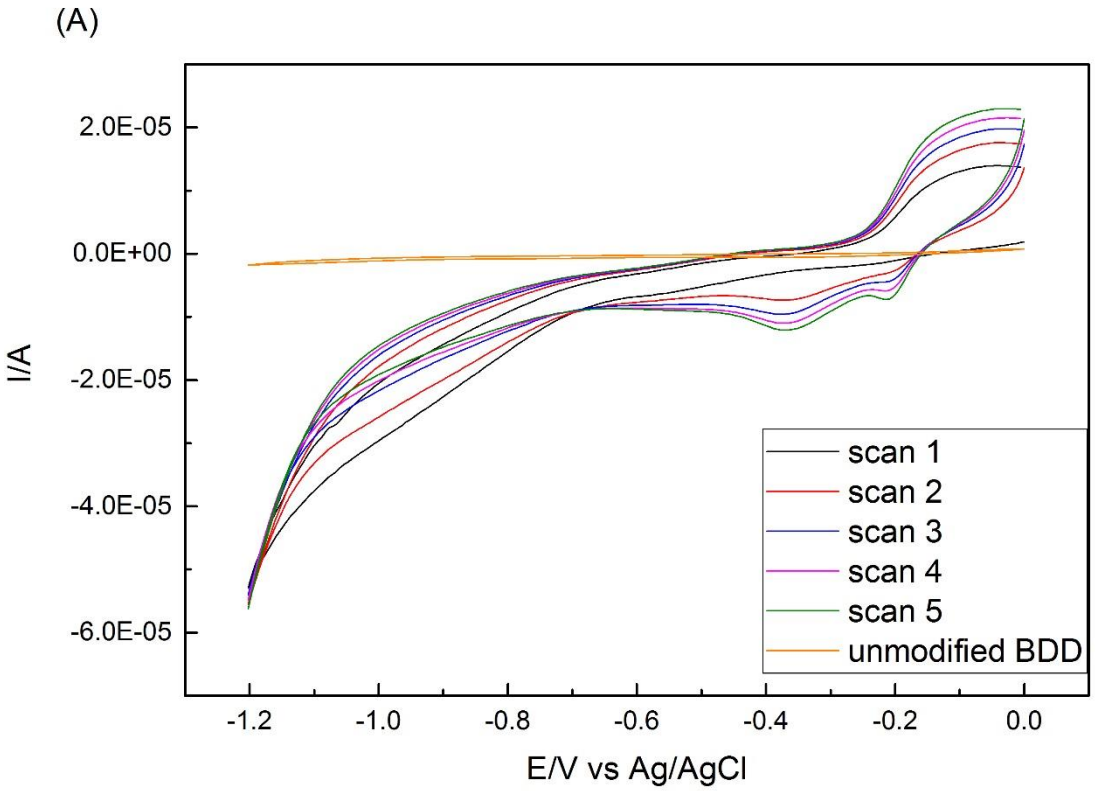

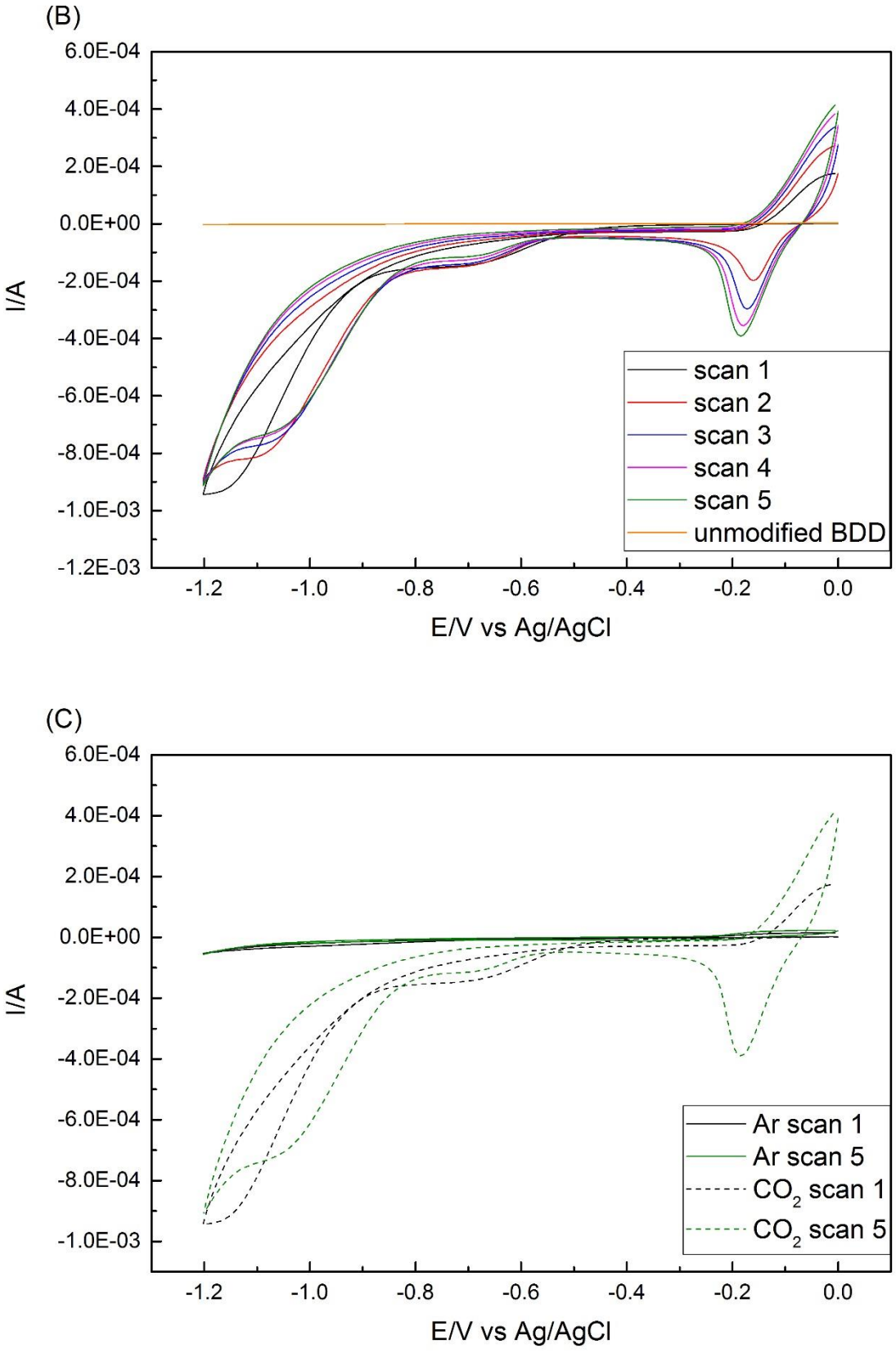

Figure 3-11. Cyclic voltammograms recorded in 0.2 M pH 9 PBS at unmodified BDD (orange) and 5 scans modified with CuO, (A) Ar deoxygenated solution, (B) CO_2

saturated solution. (C) Cyclic voltammograms recorded in 0.2 M Ar (solid lines) and CO_2 (dashed lines) pH 9 PBS for scan 1 and 5. The potential was scanned from 0→-1.2→0 V vs. Ag/AgCl. υ=100 $mV \cdot s^{-1}$.

Figure 3-11 (A) shows cyclic voltammograms of CuO in pH 9 Ar deoxygenated solution. On the first cycle, the reduction current is increased with negative potential, the peak is not obvious. From the second cycle, two reduction peaks are generated at -0.21 V and -0.36 V. And the peak current increases with increasing scans.

In CO_2 saturated solution, the reduction peak shifts from -0.16 V to -0.18 V from second to fifth scan. The other reduction peak is stable at -0.71 V. The current is increased with increasing scan numbers. As shown in Figure 3-11 (C), the current enhancement in CO_2 saturated solution is therefore further verified in wider potential range.

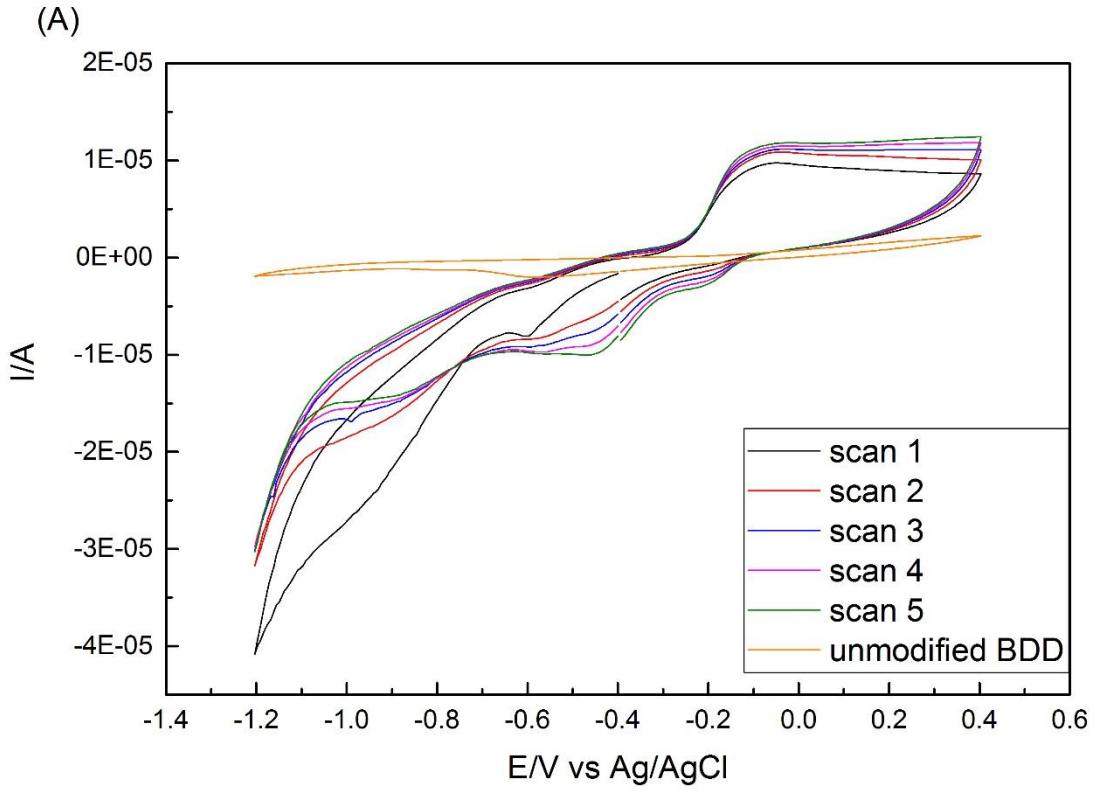

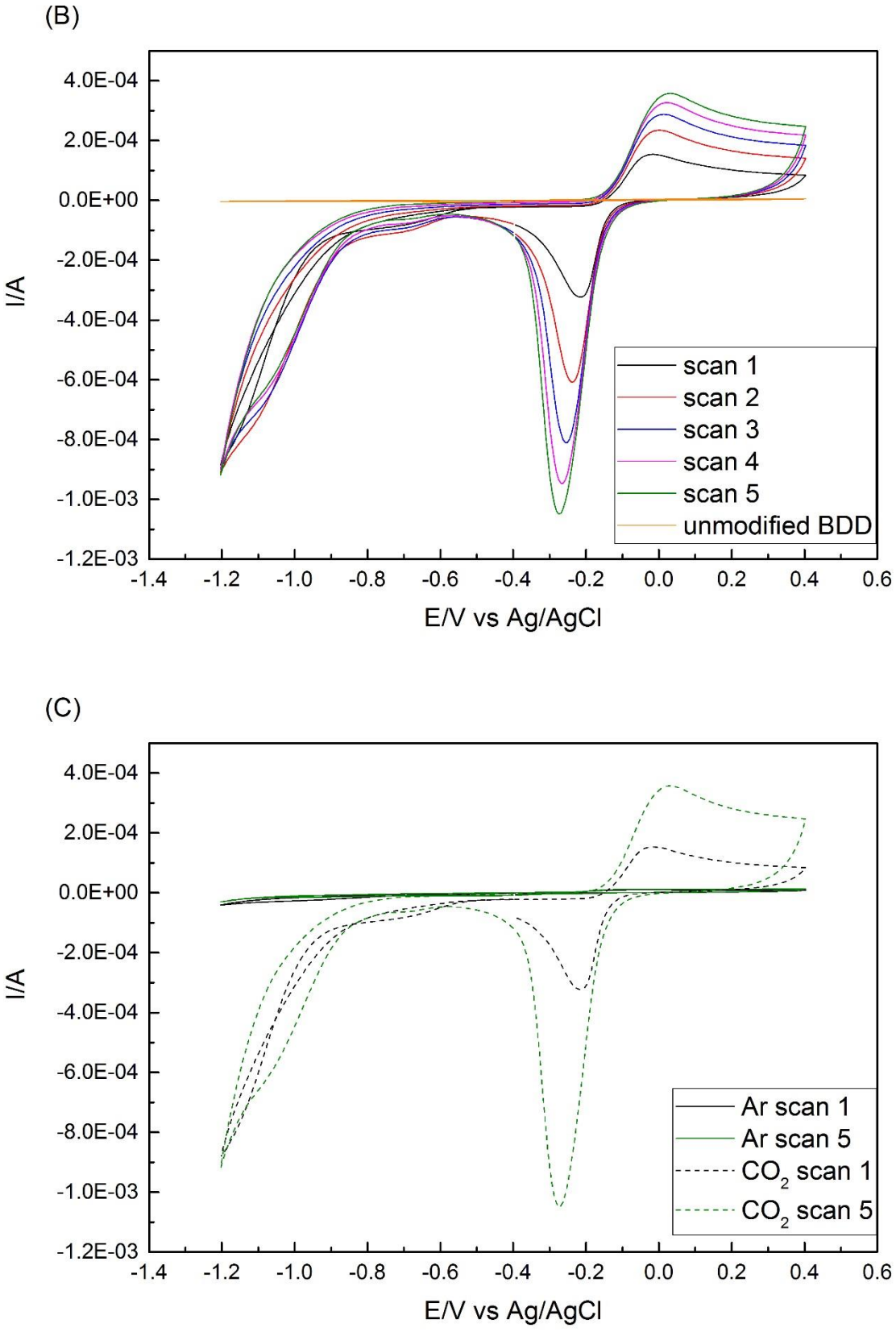

Figure 3-12. Cyclic voltammograms recorded in 0.2 M pH 9 PBS at unmodified BDD (orange) and 5 scans modified with CuO, (A) Ar deoxygenated solution, (B) CO_2

saturated solution. (C) Cyclic voltammograms recorded in 0.2 M Ar (solid lines) and CO_2 (dashed lines) pH 9 PBS for scan 1 and 5. The potential was scanned from -0.4→-1.2→0.4→-0.4 V vs. Ag/AgCl. υ=100 $mV \cdot s^{-1}$.

Cyclic voltammograms of CuO in Ar deoxygenated and CO_2 saturated solution are recorded in Figure 3-12 (A) and (B). In Ar deoxygenated solution, two reduction peaks remain stable with the peak current increasing with increasing scan number. Only one oxidation peak can be observed in this pH value around 0.0 V. In CO_2 saturated solution, the first reduction peak has slight negative shift from -0.22 V to -0.25 V. The oxidation peak has positive shift from -0.02 V to 0.02 V. The peak currents increase obviously with continued scanning.

In pH 9, CO_2 dissolves to form mostly HCO_3^- together with CO_3^{2-} in the solution. In higher pH value, the proportion of molecular CO_2 decreases. The enhancement of current may therefore relate to the increasing amount of HCO_3^- and CO_3^{2-} in the solution.

3.5 CV for pH 8 $KHCO_3$ solution in Ar deoxygenated and CO_2 saturated conditions

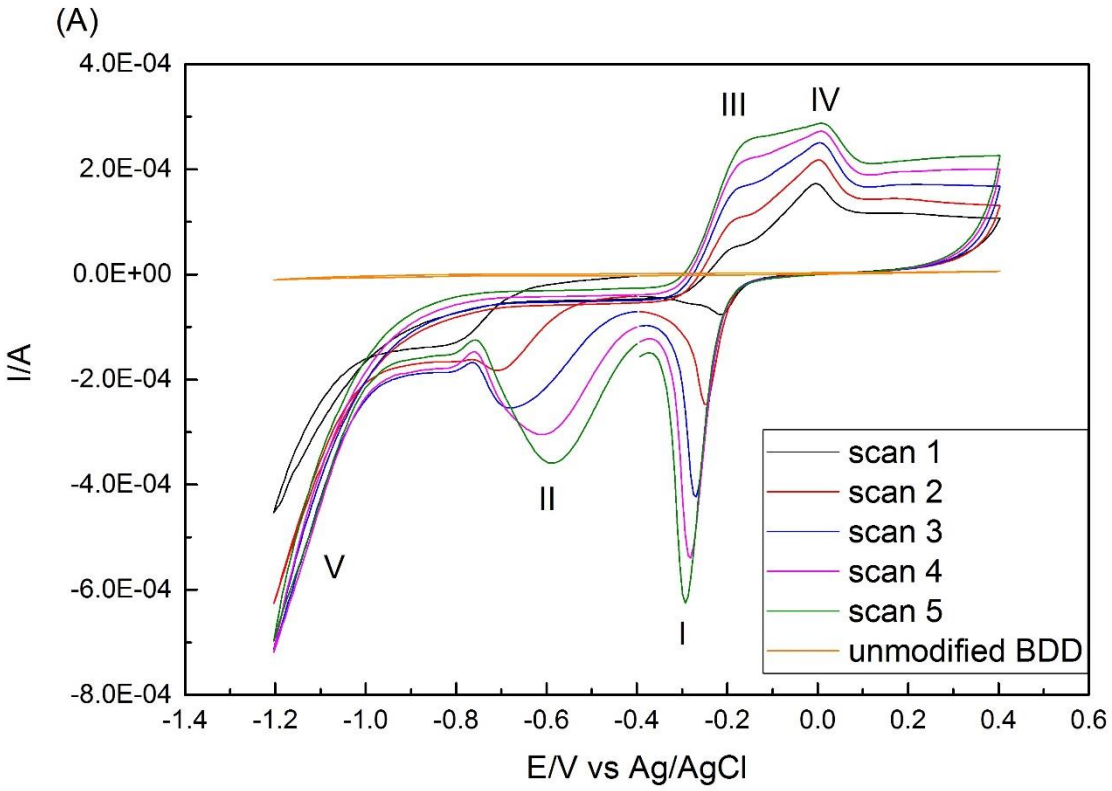

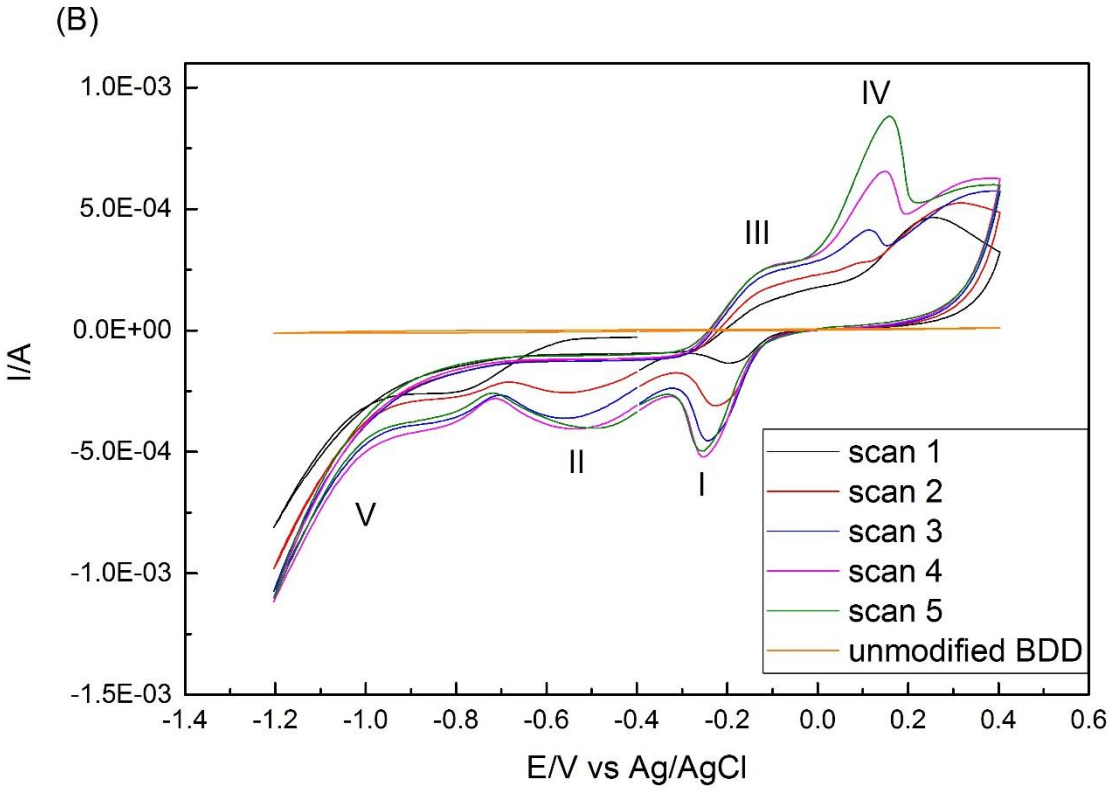

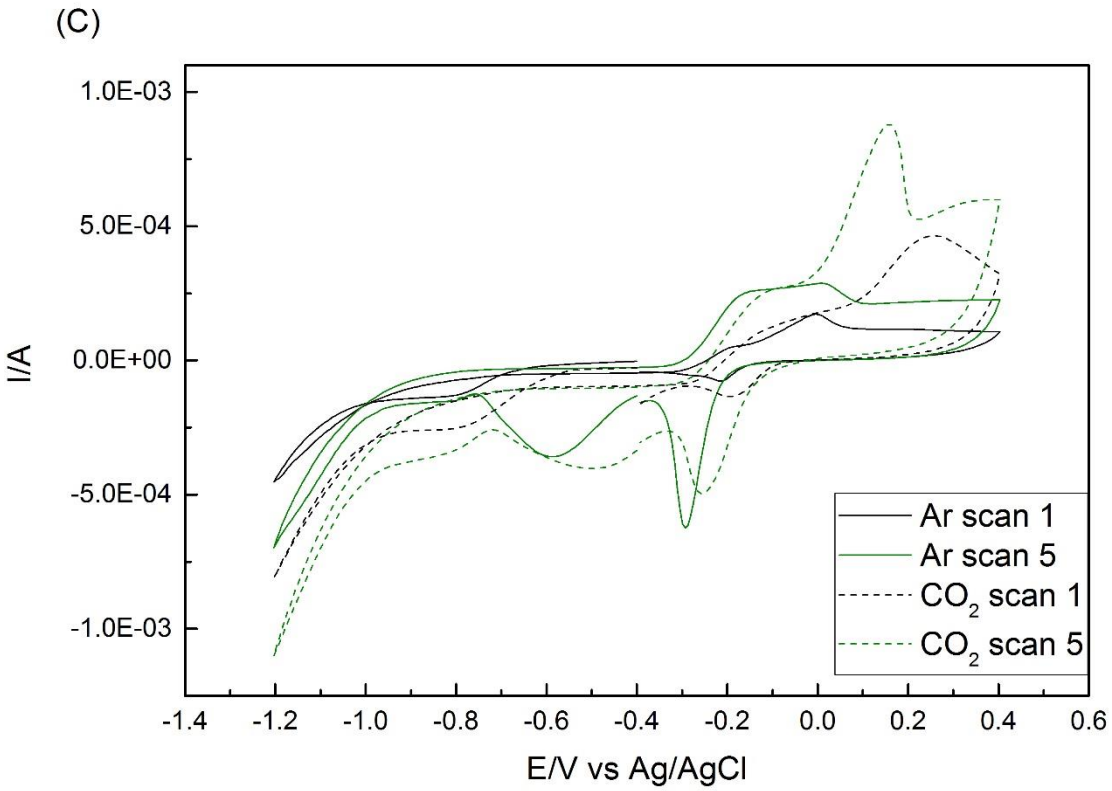

Figure 3-13. Cyclic voltammograms recorded in 0.5 M pH 8 $KHCO_3$ solution at unmodified BDD (orange) and 5 scans modified with CuO, (A) Ar deoxygenated solution, (B) CO_2 saturated solution. (C) Cyclic voltammograms recorded in 0.5 M Ar (solid lines) and CO_2 (dashed lines) pH 8 $KHCO_3$ solution for scan 1 and 5. The potential was scanned from -0.4→-1.2→0.4→-0.4 V vs. Ag/AgCl. υ=100 $mV \cdot s^{-1}$.

Cyclic voltammograms of CuO in Ar deoxygenated and CO_2 saturated $KHCO_3$ solution are presented in Figure 3-13 (A) and (B). In Ar deoxygenated solution, the reduction current starts to increase from -0.70 V in the first cycle with CuO modified electrode. The reduction peak V was assigned as HER. Two oxidation peaks III and IV can be observed at -0.20 and 0.00 V on the reverse sweep, so Cu(I)/Cu(0) was oxidised to Cu(II) for the next negative sweep. After the second switching potential at 0.40 V, two reduction peaks I and II were formed at -0.20 and -0.70 V. Combining the experiment results and previous research [11, 14], the reduction and oxidation on CuO surface can be proposed by a series of reactions, summarized as below. The exact reactions will be explained further with supporting XPS and Raman results in the following sections.

I $2CuO + H_2O + 2e^- \rightarrow Cu_2O + 2OH^-$ (3-8a)

	$2Cu(OH)_2 + 2e^- \rightarrow Cu_2O + H_2O + 2OH^-$	(3-8b)
II	$Cu_2O + H_2O + 2e^- \rightarrow 2Cu + OH^-$	(3-9)
III	$2Cu + 2OH^- \rightarrow Cu_2O + H_2O + 2e^-$	(3-10)
IV	$Cu_2O + 2OH^- \rightarrow CuO + H_2O + 2e^-$	(3-11a)
	$Cu_2O + H_2O + 2OH^- \rightarrow 2Cu(OH)_2 + 2e^-$	(3-11b)
V	$2H_2O + 2e^- \rightarrow H_2\uparrow + 2OH^-$	(3-12)

In Figure 3-13 (B), the cyclic voltammograms for CO_2 saturated solution show similar peaks. Compared with the cyclic voltammograms for Ar deoxygenated solution, higher overall current and earlier reduction current flow can be observed in CO_2 saturated solution in Figure 3-13 (C). For example, in the first scan, the reduction current increases at less negative potential at -0.60 V, compared to in Ar deoxygenated solution at -0.70 V. Similar results were found by Monnier [15] in CO_2 saturated 0.5 M KCl on TiO_2 electrode with RuO_2. Tinnemans [16] reported that the increase of the reduction current in unbuffered solutions can be contributed to the lowering pH value when the solution was saturated with CO_2. However we found this only produces small change of pH value from 8.05 (Ar deoxygenated solution) to 7.85 (CO_2 saturated solution). The high buffer capacity of 0.5 M $KHCO_3$ solution maintains the pH value during measurement. Therefore, the higher current and earlier current flow observed in CO_2 saturated solution could be attributed to direct CO_2 reduction. From the shape of the cyclic voltammograms, the reduction of CO_2 proceeds before water reduction.

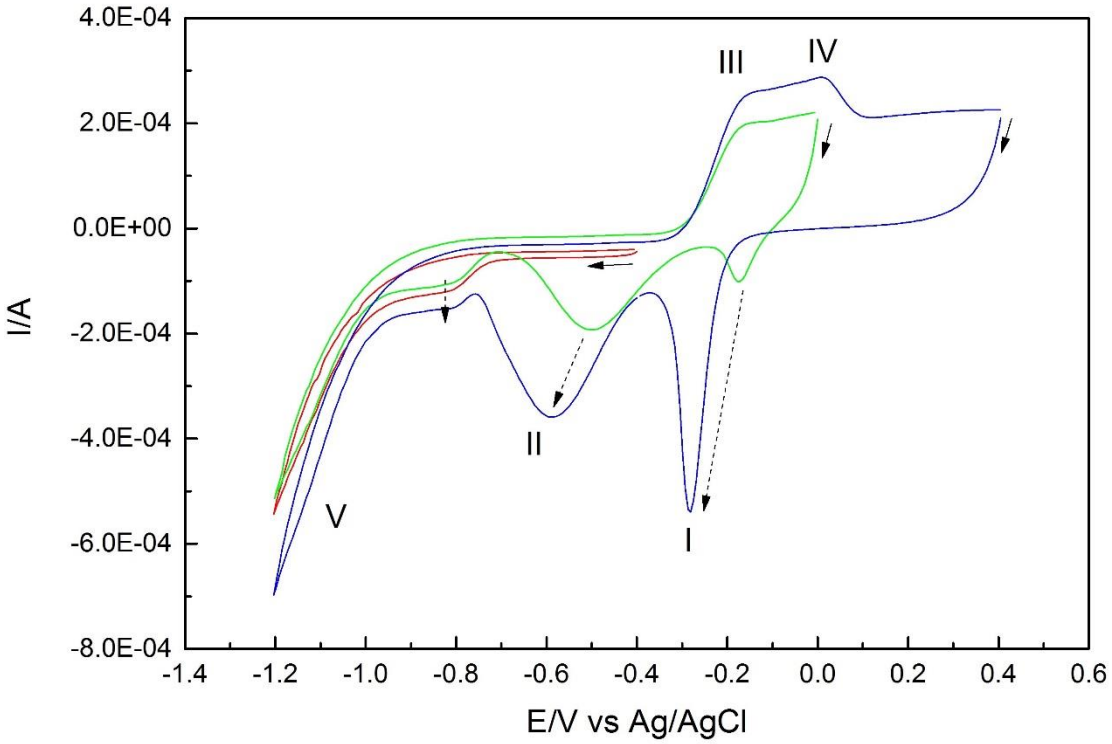

Figure 3-14. Cyclic voltammograms recorded in Ar deoxygenated 0.5 M pH 8 $KHCO_3$ solution at CuO modified BDD with fix cathodic scan limit and increased anodic scan limits. The potential was negative scanned vs. Ag/AgCl. υ=100 $mV \cdot s^{-1}$.

The reaction equations are supported by experiments with increased potential limits (-0.4 V, 0 V, 0.4 V) in successive scans illustrated in Figure 3-14. In the potential scale from -0.4 V to -1.2 V, only peak V can be observed. In the wider scan with potential scale from 0 V to -1.2 V, the reduction peaks I and II are related to oxidation peak III and IV. In the further wider scan scale from 0.4 V to -1.2 V, reduction peaks are enhanced together with oxidation peaks. The reduction peak V for HER is stable with changes in scan limits. The reduction potential for peak I (Cu(II)→Cu(I)) and II (Cu(I)→Cu(0)) shifted progressively to more negative potential as the anodic limit is increased. The two reduction peaks of copper species on the cathodic sweep suggests a layered $Cu/Cu_2O/CuO$ or $Cu(OH)_2$ electrode surface structure [11].

3.6 CV for pH 11 K_2CO_3 solution in Ar deoxygenated and CO_2 saturated conditions

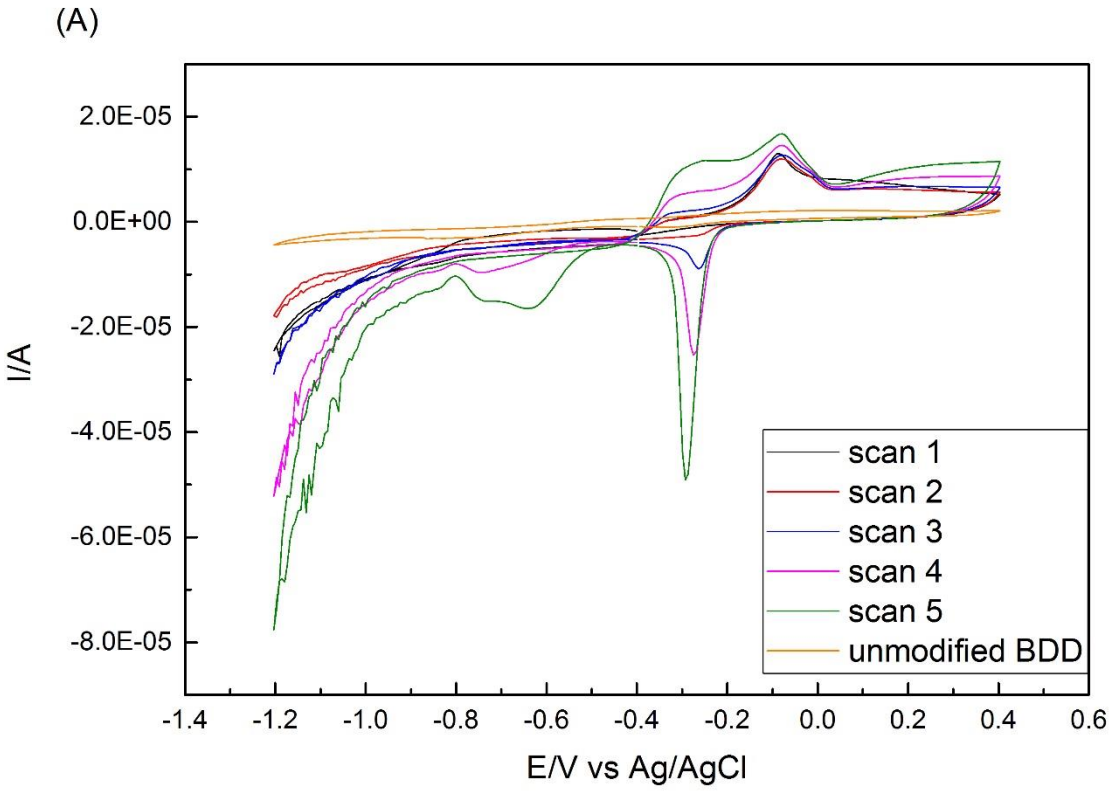

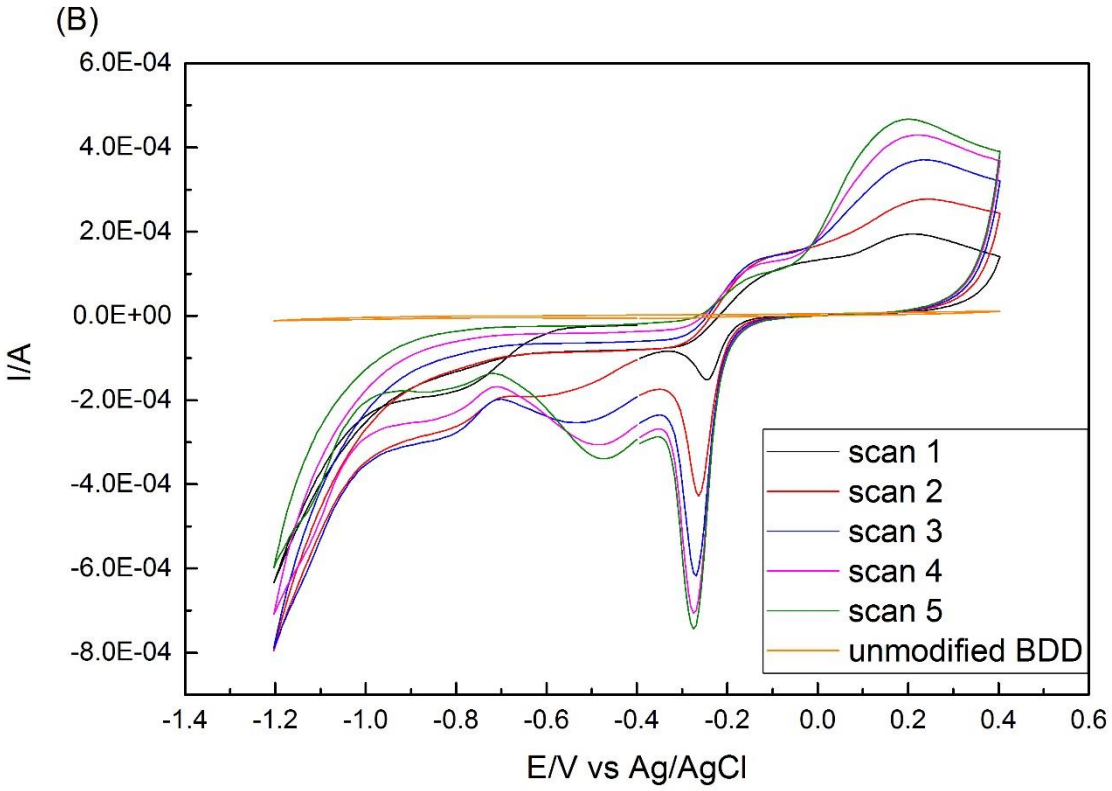

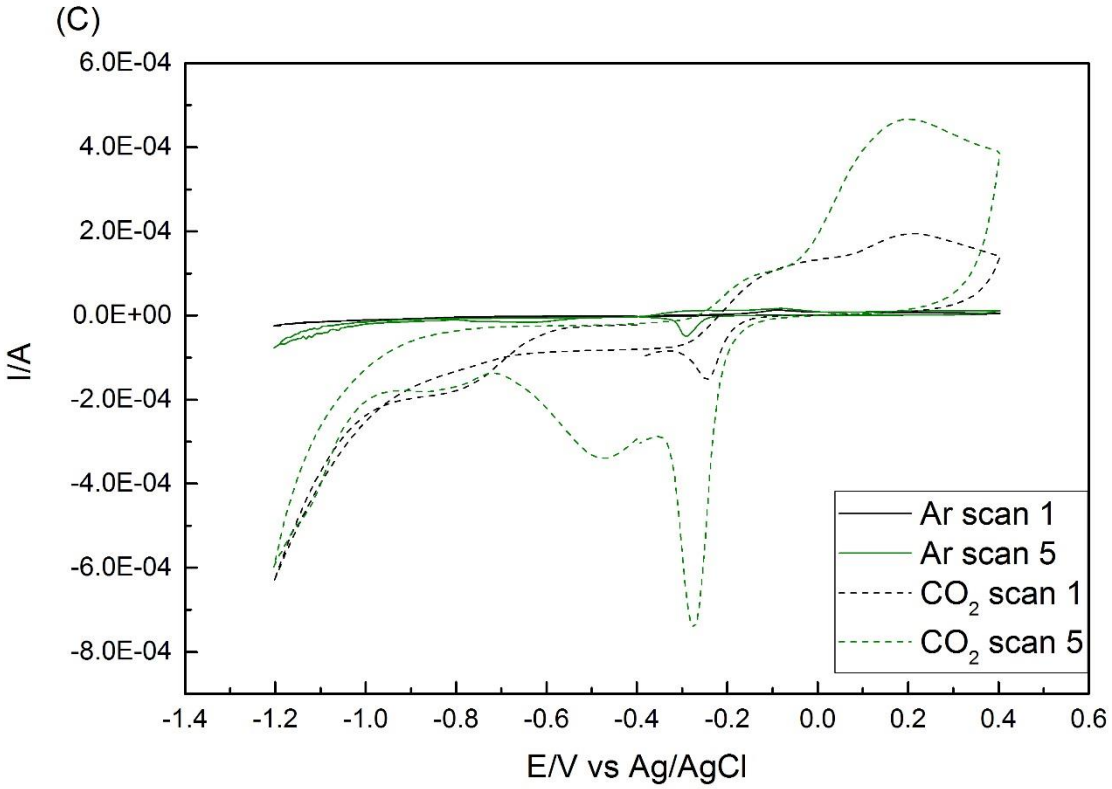

Figure 3-15. Cyclic voltammograms recorded in 0.5 M pH 11 K_2CO_3 solution at unmodified BDD (orange) and 5 scans modified with CuO, (A) Ar deoxygenated solution, (B) CO_2 saturated solution. (C) Cyclic voltammograms recorded in 0.5 M Ar (solid lines) and CO_2 (dashed lines) pH 11 K_2CO_3 solution for scan 1 and 5. The potential was scanned from -0.4→-1.2→0.4→-0.4 V vs. Ag/AgCl. υ=100 $mV \cdot s^{-1}$.

Cyclic voltammograms of CuO in pH 11 K_2CO_3 electrolyte under Ar deoxygenated and CO_2 saturated conditions are recorded in Figure 3-15 (A) and (B). In Ar deoxygenated solution, although almost showing the same peaks, the cyclic voltammograms were relatively smaller than in pH 8 $KHCO_3$ solution under same conditions.

After being saturated with CO_2, the pH value of the solution changed from 11 to 10.6, as dissolved CO_2 forms as HCO_3^- and CO_3^{2-} under the experiment conditions. After introducing CO_2 in the solution, the equilibrated condition of K^+ and CO_3^{2-} ions from electrolyte were changed with additional HCO_3^- and CO_3^{2-}. Since the current is enhanced in CO_2 saturated solution, the CO_2 dissolved species appear to promote electrode surface reactions.

3.7 Discussions

From previous studies in literature and our experiment results, the presence and absence of CO_2 in the electrolyte clearly affects the CV results. Besides, the electrochemical behaviour of copper oxide catalysts is influenced by pH values of solutions.

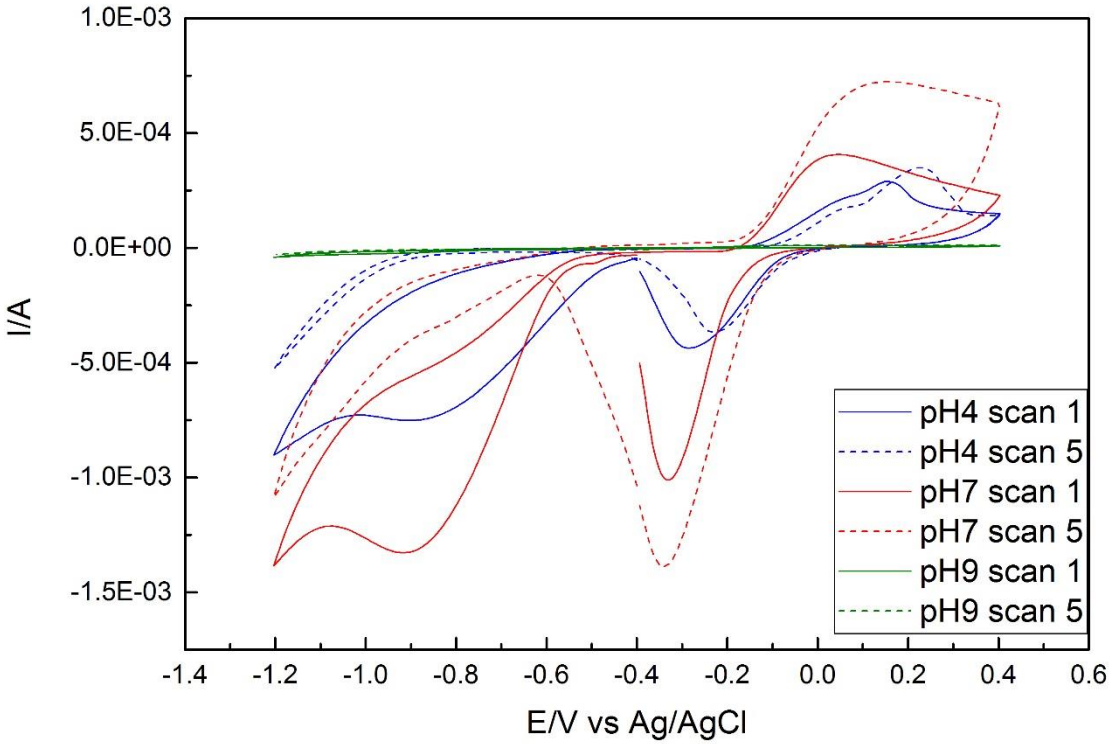

Figure 3-16. Cyclic voltammograms recorded in 0.2 M Ar deoxygenated PBS at different pHs for scan 1 (solid lines) and scan 5 (dashed lines). The potential was scanned from -0.4→-1.2→0.4→-0.4 V vs. Ag/AgCl. υ=100 mV·s^{-1}.

The cyclic voltammograms in PBS with different pH conditions are shown in Figure 3-16. In Ar deoxygenated solutions, the current response depends on pH, the current magnitude increase in the order pH 9 < pH 4 < pH 7. At the same pH value, the peak current magnitude of the fifth scan is larger than the first scan in pH 7. In pH 4 solution, there are two oxidation peaks on the reverse scan, but only one peak can be found in other two pH values.

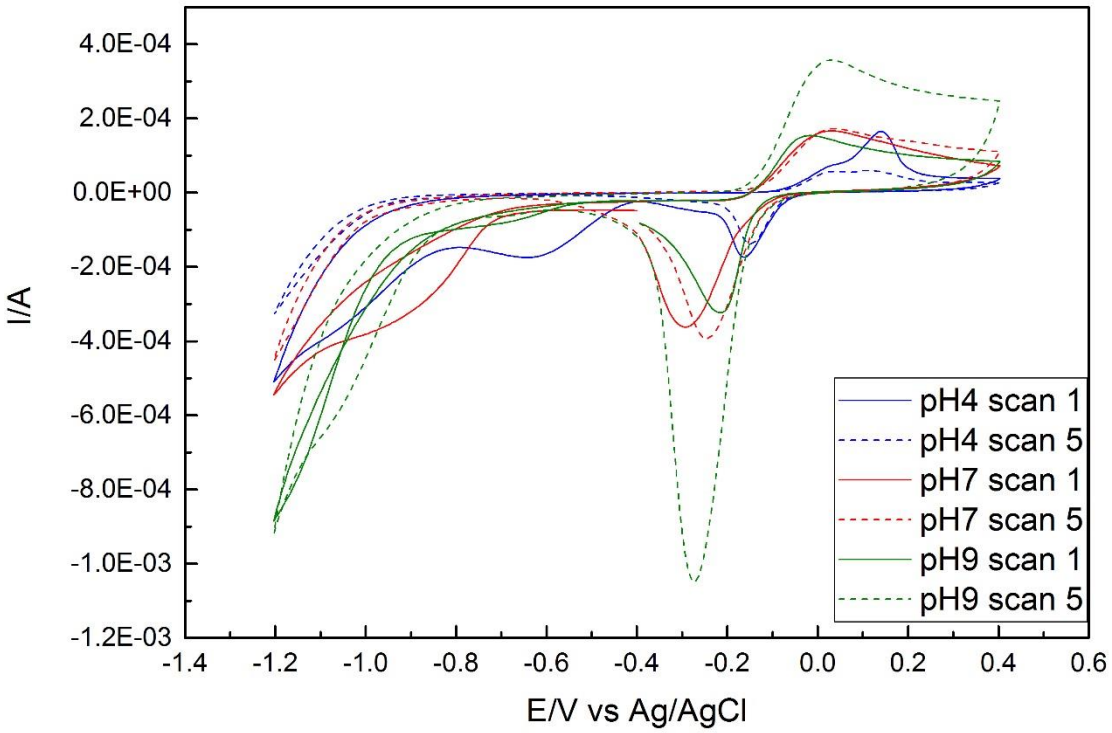

Figure 3-17. Cyclic voltammograms recorded in 0.2 M CO_2 saturated PBS at different pHs for scan 1 (solid lines) and scan 5 (dashed lines). The potential was scanned from -0.4→-1.2→0.4→-0.4 V vs. Ag/AgCl. υ=100 mV·s^{-1}.

In CO_2 saturated solutions, the overall current increases with increasing of pH values. The current magnitude of fifth scan is larger than the first scan in higher pH values. The pH dependent behaviour may relate to the form of CO_2 in different pH solutions. In pH 4 solution, CO_2 exists mostly as molecular CO_2. The current in pH 4 CO_2 saturated solution is smaller than in pH 4 Ar deoxygenated solution. This implies that molecular CO_2 does not contribute to reaction on the electrode surface. Molecular CO_2 could be adsorbed on electrode surface and block the further bonding with H_2O or OH required for the HER and reaction of the Cu species, causing the observed current decrease. In pH 7 solution, CO_2 exists as HCO_3^- with a smaller proportion of molecular CO_2. Although the current in CO_2 saturated is still smaller than in Ar deoxygenated solution, the presence of HCO_3^- enhances current compared with in pH 4 solution. This indicates that the increasing of current relates to HCO_3^- adsorption. In pH 9 solution, CO_2 dissolves as HCO_3^- and CO_3^{2-}. The current magnitude is larger in CO_2 saturated solution compared with in Ar deoxygenated solution, indicating the presence

of HCO_3^- and CO_3^{2-} promote the surface reactions.

Two other electrolytes potassium bicarbonate (pH 8) and potassium carbonate (pH 11) show two reduction peaks and two oxidation peaks during the cyclic sweep with the potential range from 0.4 V to -1.2 V. Although the electrolytes contain carbonate and bicarbonate species in both Ar deoxygenated and CO_2 saturated solution originally, CV results show different electrochemical behaviour.

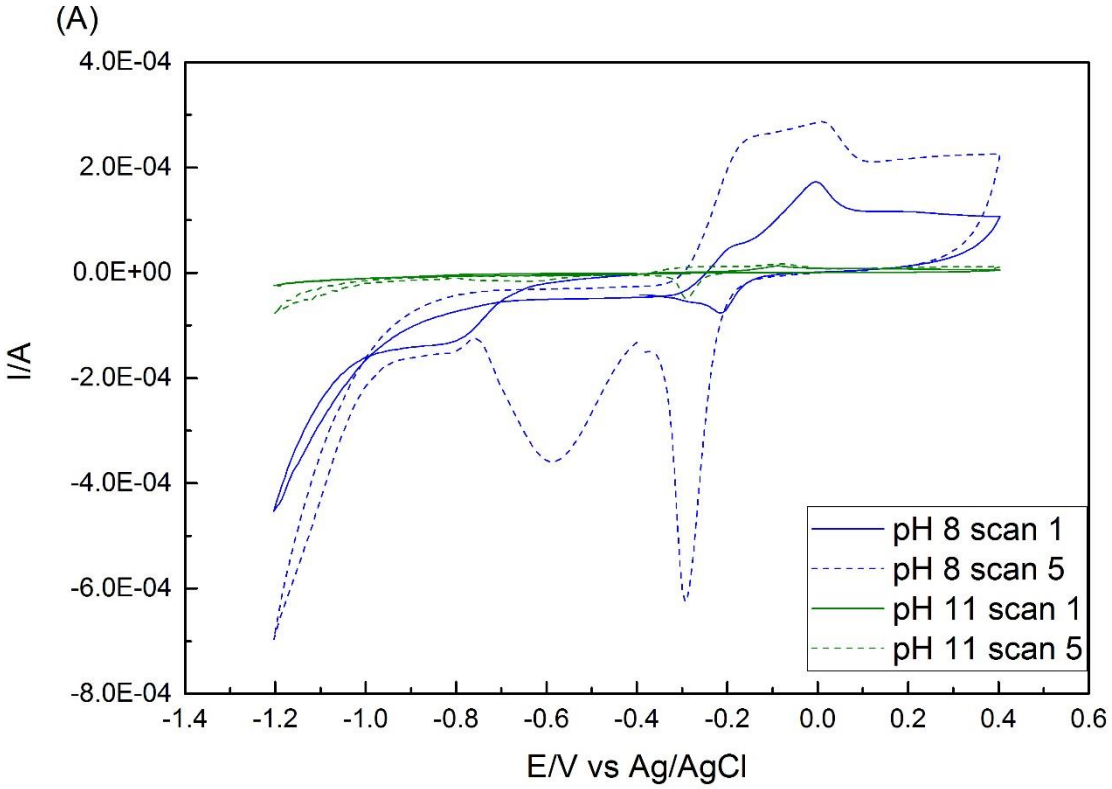

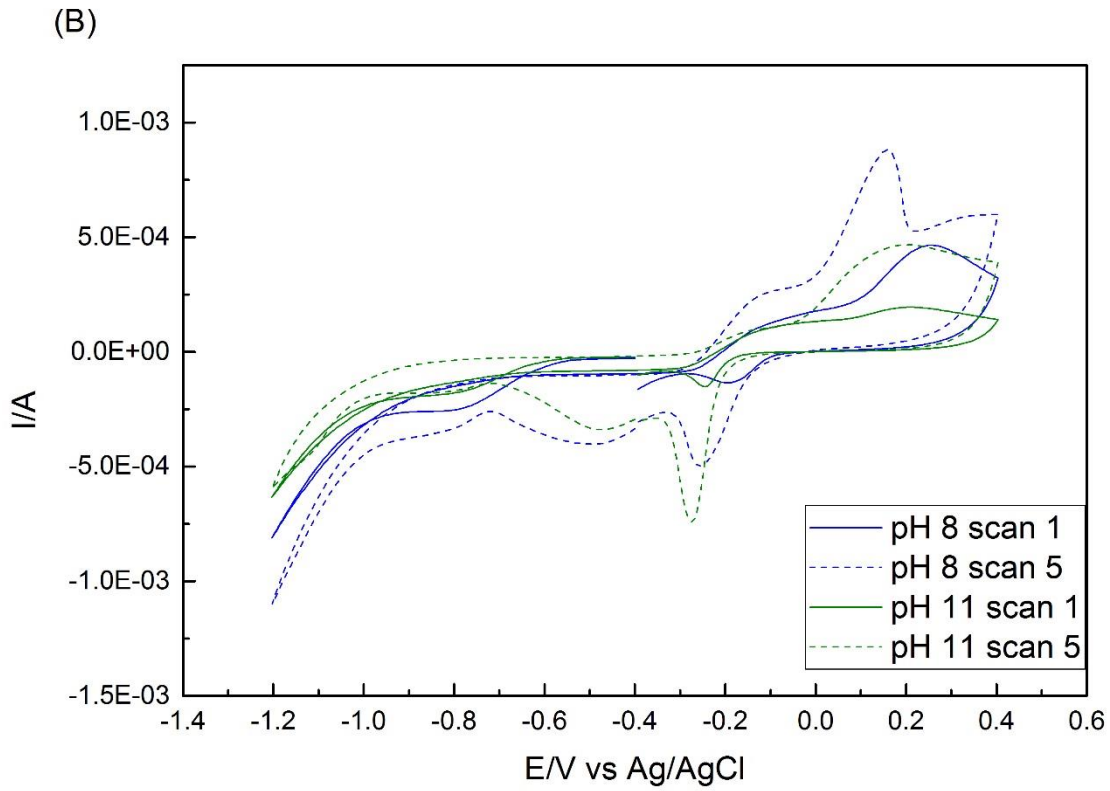

Figure 3-18. Cyclic voltammograms recorded in 0.5 M pH 8 $KHCO_3$ solution (blue lines) and pH 11 K_2CO_3 solution (green lines) for scan 1 (solid lines) and scan 5 (dashed lines), (A) Ar deoxygenated solutions, (B) CO_2 saturated solutions. The potential was scanned from -0.4→-1.2→0.4→-0.4 V vs. Ag/AgCl. υ=100 $mV \cdot s^{-1}$.

The cyclic voltammograms in $KHCO_3$ and K_2CO_3 solutions are shown in Figure 3-18. In Ar deoxygenated solutions, the current response is highly dependent on pH, the overall current magnitude for pH 8 solution is significantly larger than pH 11 in general. In the same pH values, the peak current magnitude of the fifth scan is larger than the first scan.

The overall current magnitude for both solutions in CO_2 saturated conditions is larger than in Ar deoxygenated conditions. Similar to the results in Ar deoxygenated solution, the peak current magnitude of the fifth scan is larger than the first scan.

(A)

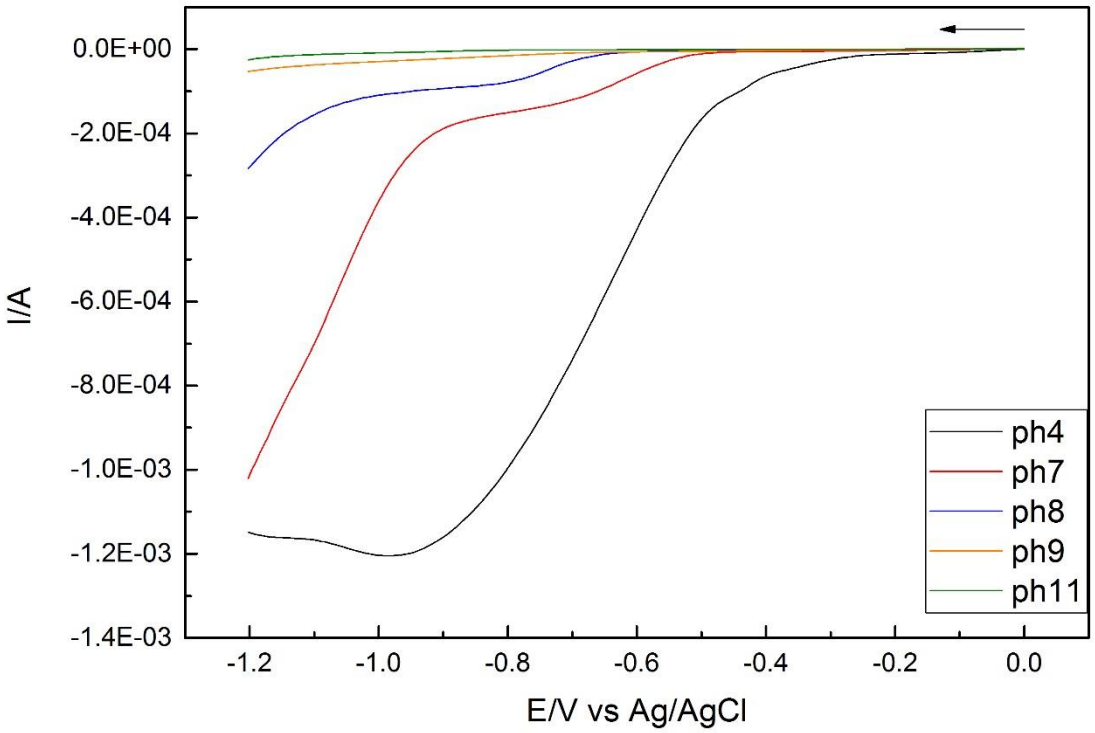
0.0E+00
-2.0E-04
-4.0E-04
-6.0E-04
-8.0E-04
-1.0E-03
-1.2E-03
-1.4E-03
I/A
-1.2
-1.0
-0.8
-0.6
-0.4
-0.2
0.0
E/V vs Ag/AgCl
ph4
ph7
ph8
ph9
ph11

(B)

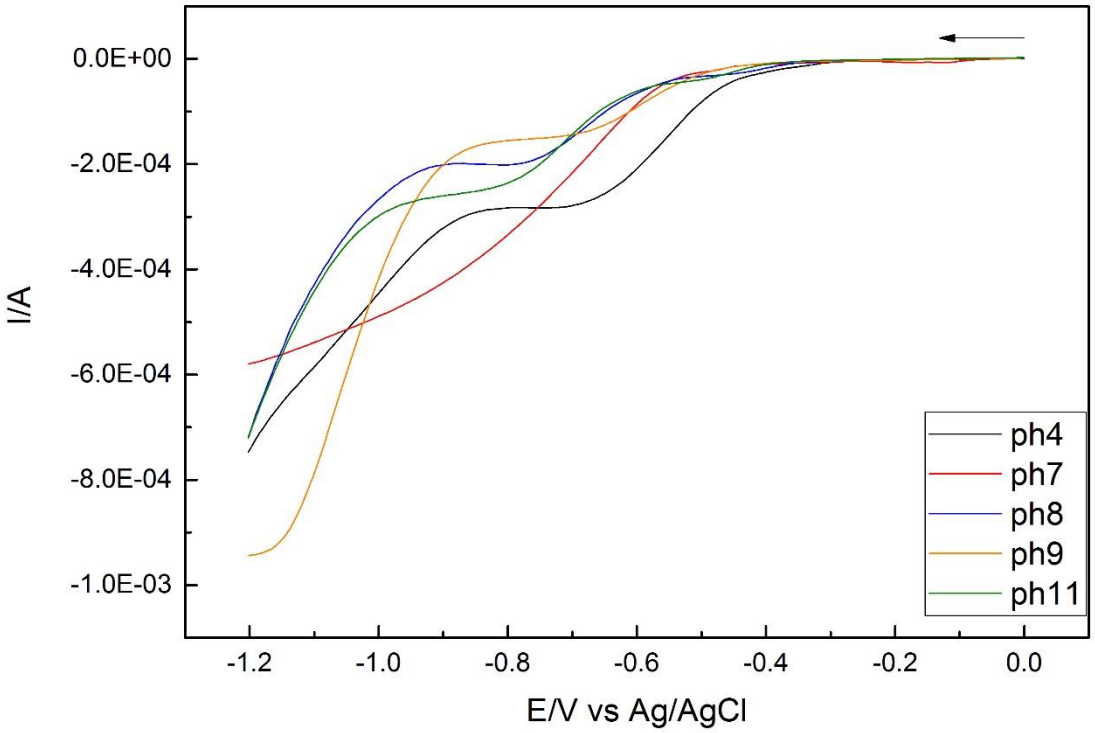
0.0E+00
-2.0E-04
-4.0E-04
-6.0E-04
-8.0E-04
-1.0E-03
I/A
-1.2
-1.0
-0.8
-0.6
-0.4
-0.2
0.0
E/V vs Ag/AgCl
ph4
ph7
ph8
ph9
ph11

Figure 3-19. Cyclic voltammograms recorded at different pHs for the first scan, (A) Ar deoxygenated solution, (B) CO_2 saturated solution. The potential was scanned backward from 0→-1.2 V vs. Ag/AgCl. υ=100 $mV \cdot s^{-1}$.

The cyclic voltammograms in different pH conditions are shown in Figure 3-19. It is obvious from Figure 3-19 (A) that with the increasing of pH values, the currents start to flow at more negative potential. The current magnitude of the cathodic scans are suppressed with increasing pH values. The electrochemical behaviour of catalyst is highly dependent on pH values. In CO_2 saturated solutions, except in pH 4 condition, the current starts to flow around -0.40 V, and the current onset potentials are not correlative with increasing pH values.

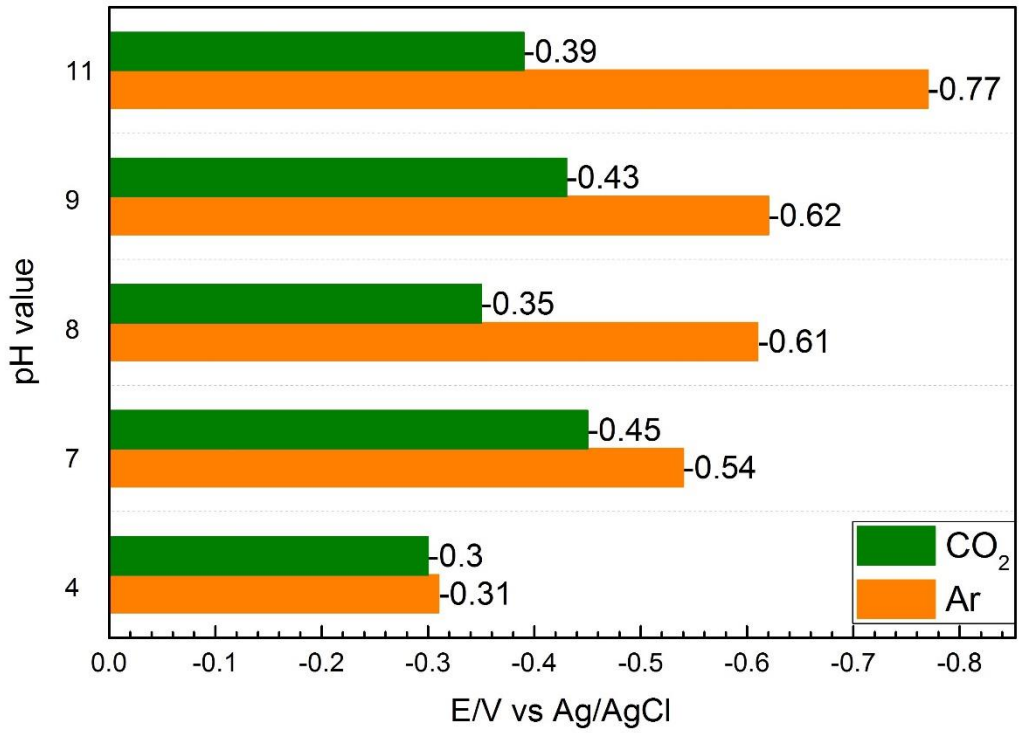

Figure 3-20. The current onset potential recorded for different pHs for the first cathodic scan. The potential was scanned backward from 0→-1.2 V vs. Ag/AgCl. υ=100 $mV \cdot s^{-1}$.

The results of current onset potential are summarized in Figure 3-20. For five different pH conditions, the currents start to flow at less negative potential in CO_2 saturated solutions than in Ar deoxygenated solutions. The more negative potential for current

onset indicates a higher potential is required for the catalyst to start to become active.

Section 3.1.2 illustrates the gradient of the Nernst equation (Equation 1 to 3') is determined by the number of electron transferred in the reaction with respect to pH value. In order to clarify the CuO reduction reaction represented by peak I, the gradient of Equation 3' can be used to analyse by the potential and solution pH.

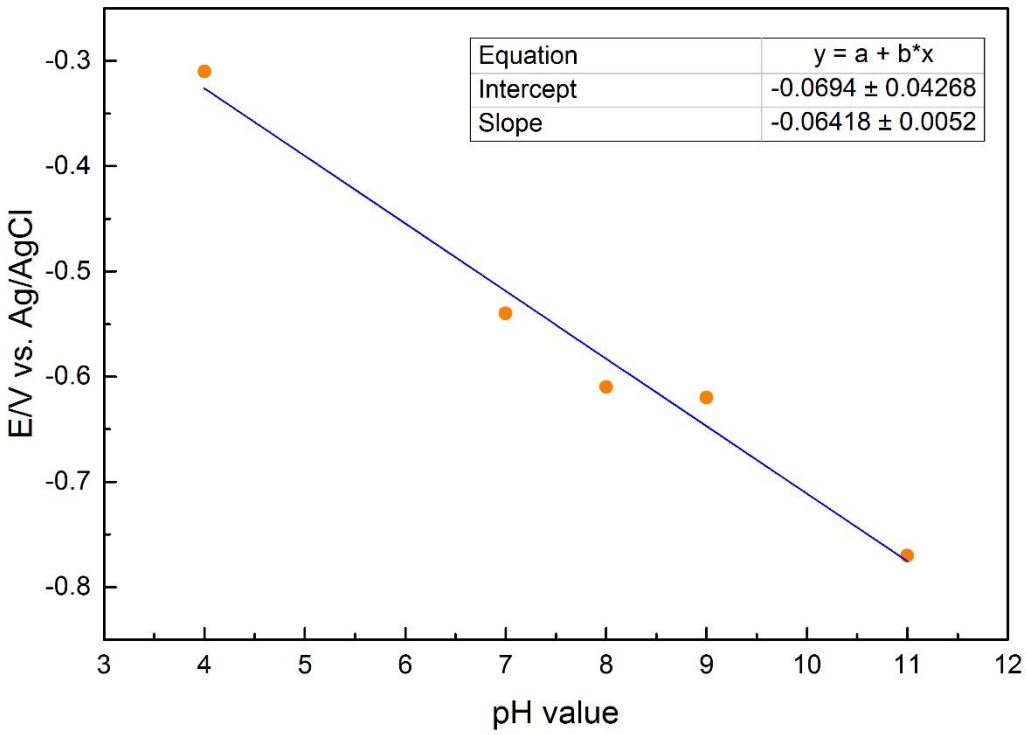

Figure 3-21. The linear fitting of the current onset potential recorded for the first cathodic scan with respect to pH values.

Figure 3-21 plots the current onset potential in Ar deoxygenated solution for the first cathodic scan with respect to pH values. The data is linear fitted to the form $y=-0.0694-0.0642x$. The error of intercept and slope are 0.043 and 0.005, respectively. According to the discussion in section 3.1.2, the predicted slope for a reaction with equal number of electrons and protons transferred is 0.0592 V. The experimental result is 0.0642, which is quite close to the theoretical value 0.0592. The calculation result for the first cathodic scan shows that this reaction takes place with ratio of electron and proton of 1:1 [17]. This reaction should be the reduction of Cu(II) to Cu(I) and shows the predicted pH dependence related to earlier equations (Equation 3-1, 3-4, 3-8) and

discussions. However this trend (59 mV gradient) is not observed in CO_2 saturated solutions. The presence of CO_2 makes the reduction of Cu(II) less sensitive to the solution conditions, such as pH values and the type of buffer solutions.

Table 3-1. The peaks potentials recorded for different pHs for the fifth scan. The potential was scanned from 0.4→-1.2→0.4 V vs. Ag/AgCl. υ=100 mV·s^{-1}.

pH	Peak I		Peak II		Peak III		Peak IV	
	Ar	CO_2	Ar	CO_2	Ar	CO_2	Ar	CO_2
4	-0.23 V	-0.15 V	-0.85 V	-0.64 V	0.06 V	0.03 V	0.22 V	0.13 V
7	-0.34 V	-0.25 V	-0.88 V	-0.88 V	0.15 V	0.03 V	/	/
8	-0.29 V	-0.26 V	-0.58 V	-0.50 V	-0.16 V	-0.11 V	0.01 V	-0.16 V
9	-0.22 V	-0.27 V	-0.87 V	-0.69 V	-0.03 V	0.03 V	/	/
11	-0.29 V	-0.27 V	-0.63 V	-0.48 V	-0.20 V	-0.13 V	-0.08 V	0.20 V

Table 3-1 summarized peaks potentials in different pH values. For three different PBS conditions, peak IV can only be observed in pH 4 solutions, but not in pH 7 and 9 solutions. So the peak splitting takes place in acid solution rather in higher pH value solutions. But peak IV was recorded in $KHCO_3$ and K_2CO_3 solutions, where the pH value is even higher than PBS solution. So the catalyst behaviour also influenced by electrolyte species. Figure 3-22 illustrates the peaks potentials in detail.

(A)

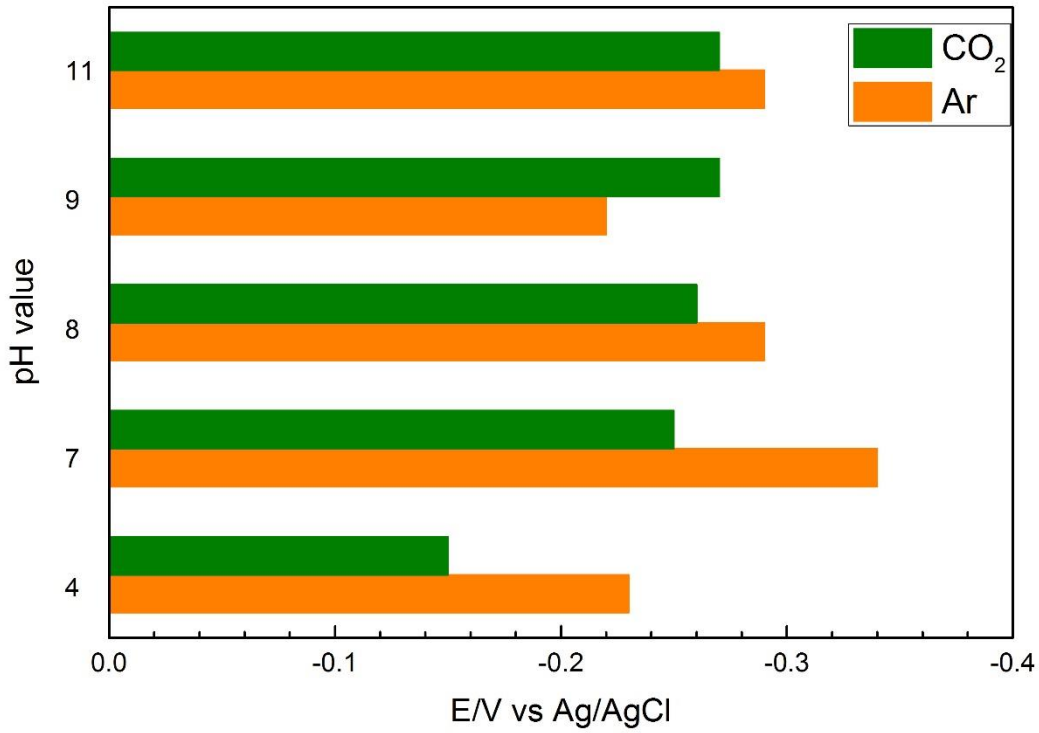
CO2
Ar
11
9
8
7
4
pH value
0.0
-0.1
-0.2
-0.3
-0.4
E/V vs Ag/AgCl

(B)

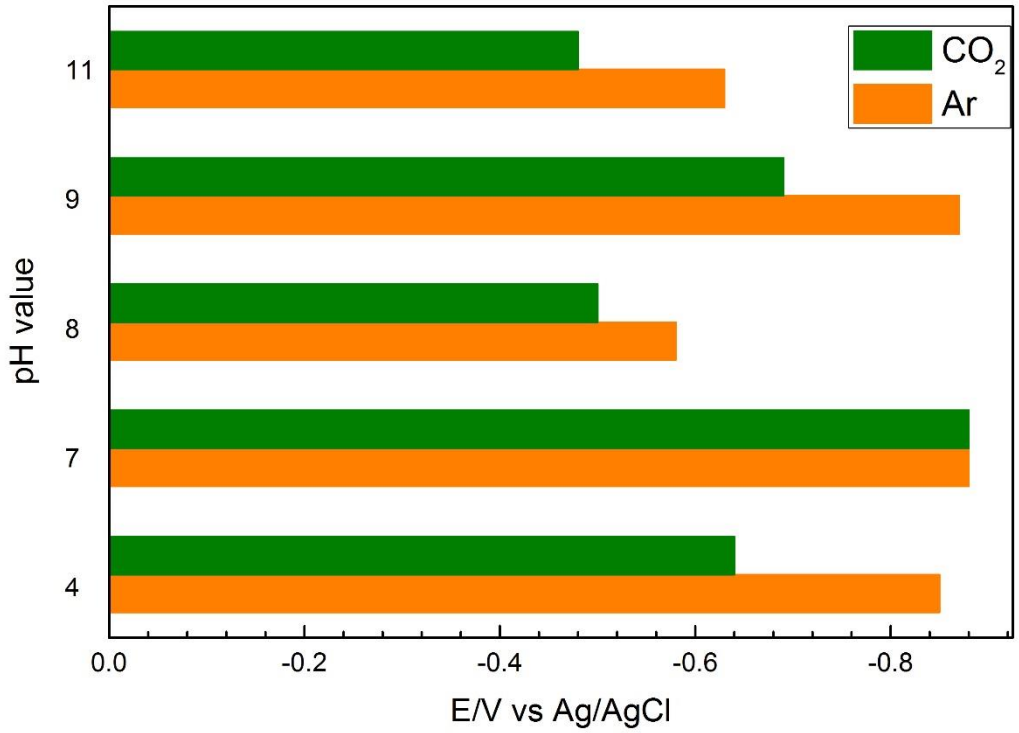
CO2
Ar
11
9
8
7
4
pH value
0.0
-0.2
-0.4
-0.6
-0.8
E/V vs Ag/AgCl

Figure 3-22. The peaks potentials recorded for different pHs for the fifth cathodic scan, (A) peak I, (B) peak II. The potential was scanned backward from 0.4→-1.2 V vs. Ag/AgCl. υ=100 mV·s^{-1}.

Figure 3-22 shows the potentials for peak I and II in different solutions. Peak I is assigned as Cu(II) reduction to Cu(I). Except pH 9 solution, the potential for peak I in CO_2 saturated conditions is less negative than in Ar deoxygenated conditions. This indicates that when CO_2 is introduced in the solution, it needs less overpotential for Cu(II) to be reduced to Cu(I). In CO_2 saturated solutions, the peak I is generated at more negative potential with increasing of pH values. So it needs less overpotential in acid solution. Peak II is assigned as Cu(I) reduction to Cu(0). The potentials for peak II in Ar deoxygenated conditions are more negative than in CO_2 saturated conditions in all five different solutions. Similar to the discussions mentioned above, the relationship between peak potentials and pH values is not clear in CO_2 saturated conditions. Although the reactions are pH dependent, the positions of peak I and II do not show a simple linear relationship with pH value, which can be observed for cathodic onset potential as seen in Figure 3-21. The experimental data suggested the complex correlation among thermodynamic, kinetic and mass transfer in the reactions [17].

In different electrolytes, both current flow onset potentials and reduction peaks potentials are less negative in CO_2 saturated conditions than in Ar deoxygenated conditions. It has been discussed that all electrolytes have high buffer capacity, the pH values changed only slightly with and without CO_2. So the different electrochemical behaviour is attributed to the introduced CO_2.

3.8 Summary

The catalyst behaviour depends on pH value and presence and absence of CO_2 in the solution. The results of electrochemical measurement have been discussed in relation to these two parameters.

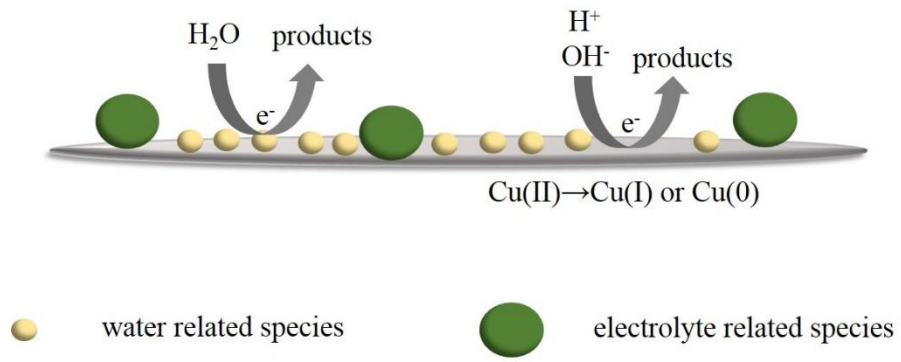

Figure 3-23. Schematic of reactions on electrode at negative potential in Ar deoxygenate solution.

The catalyst behaviour at negative potential in Ar deoxygenated solution can be illustrated in Figure 3-23. In Ar deoxygenated solutions, the electrode surface is covered with water related species and electrolyte related species. With the application of negative potential, Cu(II) is reduced to Cu(I) or Cu(0), and water is split due to HER.

When we introduce CO_2 in the system, the current magnitude is suppressed in pH 4 and pH 7 solutions, but enhanced in pH 8, pH 9 and pH 11 solutions compared with in Ar deoxygenated solutions in same pH values. This may be caused by dissolved CO_2 giving rise to different species in different pH value solutions.

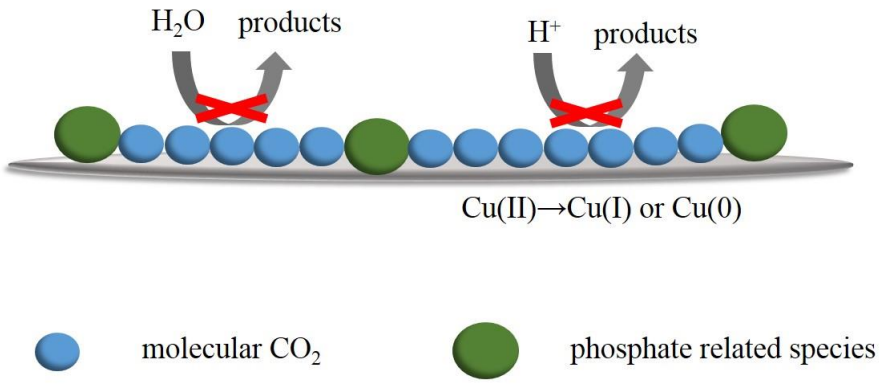

Figure 3-24. Schematic of reactions on electrode at negative potential in 0.2 M pH 4 CO_2 saturated PBS.

Figure 3-24 shows the schematic of reactions on electrode at negative potential in pH

4 CO_2 saturated solution. In pH 4 solution, CO_2 dissolves to molecular CO_2 and molecular CO_2 could be adsorbed and covered on the electrode surface. This will block the bonding with water related species required for the HER and the reduction of CuO on electrode surface. In this case, the current magnitude of the overall voltammogram is much smaller than in pH 4 Ar deoxygenated solution. This indicates that molecular CO_2 is not involved in the reaction.

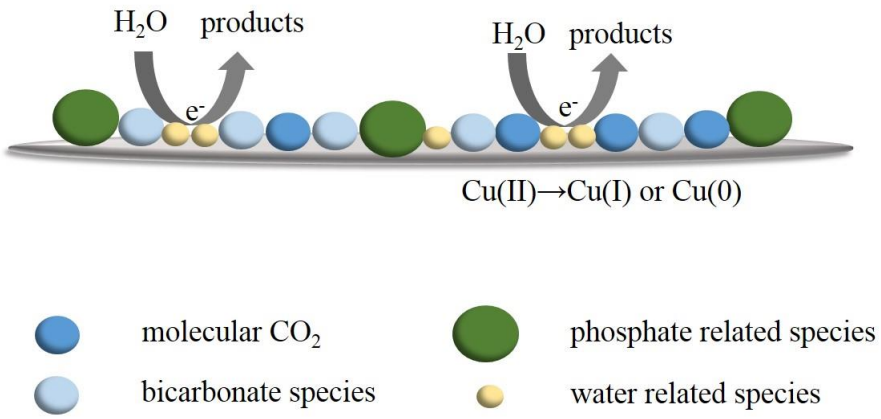

Figure 3-25. Schematic of reactions on electrode at negative potential in 0.2 M pH 7 CO_2 saturated PBS.

Figure 3-25 shows the schematic of reactions on electrode at negative potential in 0.2 M pH 7 CO_2 saturated solution. CO_2 dissolves to HCO_3^- and small proportion of molecular CO_2. The current magnitude in CO_2 saturated solution is still smaller than in pH 7 Ar deoxygenated solution. However the presence of HCO_3^- enhances current magnitude compared with in pH 4 CO_2 saturated solution. This indicates that the increasing current magnitude relates to less molecular CO_2 adsorption.

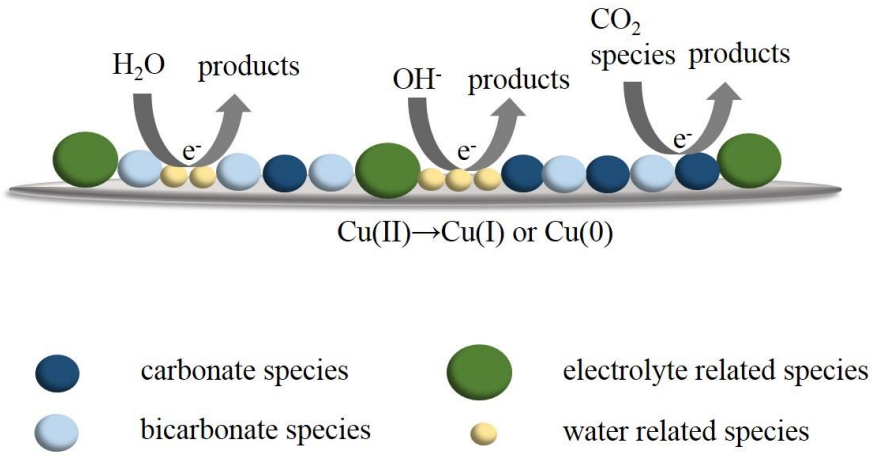

Figure 3-26. Schematic of reactions on electrode at negative potential in pH 8 and above CO_2 saturated solutions.

Figure 3-26 shows the schematic of reactions on electrode at negative potential in pH 8 and above CO_2 saturated solutions. From pH 8 solution, the CO_2 dissolves to HCO_3^- and CO_3^{2-}. With the increasing pH value, the proportion of CO_3^{2-} increases and HCO_3^- decreases. In the solution with higher pH values (pH 8, pH 9, pH 11), the current magnitude enhances compared with in Ar deoxygenated solutions in the same pH value. This indicates the presence of HCO_3^- and CO_3^{2-} promote the electrode surface reaction, and the enhanced current may be due to CO_2 related reaction, for example reduction of carbonate or bicarbonate to give formic acid or other products.

The electrochemical studies of CuO modified electrode with cycled potentials reveal that the behaviour of the catalyst is dependent on the pH value and the presence and absence of CO_2 in the system. In Ar deoxygenated solutions, the electrode surface is surrounded with water and electrolyte related species. With the application of negative potential, Cu(II) is reduced to Cu(I) or Cu(0), together with HER. In CO_2 saturated solutions, the electrode surface adsorbs different CO_2 related species in different pH conditions. The current magnitude is suppressed in pH 4 and pH 7, but enhanced in pH 8, 9 and 11 CO_2 saturated solutions compared with in Ar deoxygenated solutions in same pH values. The pH 4 PBS conditions shows most suppression compared with other conditions.

The reactions have been assigned through experimental cyclic voltammograms and

literature. The CV results give information about electron transfer, but cannot prove the exact reactions. Hence, these results will be discussed further in light of supporting spectroscopic data in the following chapters.

References

[1] Fisher AC. Electrode Dynamics. Oxford university press; 1996. p. 3-4.

[2] Detailed derivation of the Nernst equation. [Accessed 14 July 2016]; Available from: http://www.doitpoms.ac.uk/tlplib/pourbaix/nersnt_detailed.php.

[3] Nernst Equation. 18 October 2015. [Accessed 14 July 2016]; Available from: http://chemwiki.ucdavis.edu/Core/Analytical_Chemistry/Electrochemistry/Nernst_Equation

[4] Application of the Nernst Equation. 3 June 2007. [Accessed 14 July 2016]; Available from: http://www.chem1.com/acad/webtext/elchem/ec5.html

[5] Strehblow HH, Titze B. The investigation of the passive behaviour of copper in weakly acid and alkaline solutions and the examination of the passive film by ESCA and ISS. Electrochimica Acta. 1980 Jun 1;25(6):839-50.

[6] Tang W, Peterson AA, Varela AS, Jovanov ZP, Bech L, Durand WJ, Dahl S, Nørskov JK, Chorkendorff I. The importance of surface morphology in controlling the selectivity of polycrystalline copper for CO_2 electroreduction. Physical Chemistry Chemical Physics. 2012;14(1):76-81.

[7] Saito R, Miseki Y, Sayama K. Highly efficient photoelectrochemical water splitting using a thin film photoanode of $BiVO_4/SnO_2/WO_3$ multi-composite in a carbonate electrolyte. Chemical Communications. 2012;48(32):3833-5.

[8] Ambrose J, Barradas RG, Shoesmith DW. Investigations of copper in aqueous alkaline solutions by cyclic voltammetry. Journal of Electroanalytical Chemistry and Interfacial Electrochemistry. 1973 Sep 25;47(1):47-64.

[9] Han WK, Choi JW, Hwang GH, Hong SJ, Lee JS, Kang SG. Fabrication of Cu nano particles by direct electrochemical reduction from CuO nano particles. Applied Surface Science. 2006 Feb 15;252(8):2832-8.

[10] Hori Y. Electrochemical CO_2 reduction on metal electrodes. In Modern aspects of electrochemistry 2008 (pp. 89-189). Springer New York.

[11] Wilhelm SM, Tanizawa Y, Liu CY, Hackerman N. A photo-electrochemical

investigation of semiconducting oxide films on copper. Corrosion Science. 1982 Dec 31;22(8):791-805.

[12] Wang X, Hanson JC, Frenkel AI, Kim JY, Rodriguez JA. Time-resolved studies for the mechanism of reduction of copper oxides with carbon monoxide: complex behavior of lattice oxygen and the formation of suboxides. The Journal of Physical Chemistry B. 2004 Sep 9;108(36):13667-73.

[13] Estrella M, Barrio L, Zhou G, Wang X, Wang Q, Wen W, Hanson JC, Frenkel AI, Rodriguez JA. In Situ Characterization of $CuFe_2O_4$ and Cu/Fe_3O_4 Water-Gas Shift Catalysts. The Journal of Physical Chemistry C. 2009 Jul 17;113(32):14411-7.

[14] Marchiano SL, Elsner CI, Arvia AJ. The anodic formation and cathodic reduction of cuprous oxide films on copper in sodium hydroxide solutions. Journal of Applied Electrochemistry. 1980 May 1;10(3):365-77.

[15] Monnier A, Augustynski J, Stalder C. On the electrolytic reduction of carbon dioxide at TiO_2 and TiO_2-Ru Cathodes. Journal of Electroanalytical Chemistry and Interfacial Electrochemistry. 1980 Sep 25;112(2):383-5.

[16] Tinnemans AH, Koster TP, Thewissen DH, De Kreuk CW, Mackor A. On the electrolytic reduction of carbon dioxide at TiO_2 and other titanates. Journal of Electroanalytical Chemistry and Interfacial Electrochemistry. 1983 Mar 25;145(2):449-56.

[17] Cramer WA, Knaff DB, editors. Energy transduction in biological membranes: a textbook of bioenergetics. Springer Science & Business Media; 2012 Dec 6. p. 3-6, 43, 124.

Chapter 4

XPS and Raman Spectroscopic Studies of CuO Catalyst in Ar Deoxygenated and CO_2 Saturated Solutions

4.1 XPS study

XPS is a surface sensitive technique with analysis depths of about 3-10 nm [1], used for the characterisation of surface elemental compositions and elemental oxidation states of solid materials. The presence of peaks at particular energies indicates the presence of a specific element. Therefore the characteristic peaks in the spectrum can be used to identify chemical elements for a sample [1]. The intensity of XPS is related to the concentration of the element within the sampled region [2], and sensitivity factor which is different for each element. So the peak intensity is proportional to the elemental surface composition.

The exact binding energy of an electron also depends on the oxidation states of the atom, and local chemical and physical environment [2]. These factors will give rise to small shifts in the peak position in the spectrum [2]. In practice, when multiple oxidation states of one element are detected in an analysis, the peaks can be deconvoluted into sub-peaks caused by the chemical shifts. The area under the characteristic sub-peaks can be used to calculate the composition of the detected oxidation states of the element [3].

4.1.1 XPS setup

To prepare samples for ex situ XPS analysis, a three-electrode setup was used. Experimental cell and conditions were similar to CV experiments. Glassy carbon rods (vitreous carbon, 3 mm diameter, Sigma Aldrich) served as working electrodes. The rod was polished with 0.3 μm alumina slurry, sonicated for 20 minutes and cleaned with distilled water. Then the rod was placed in a dessicator for 10 hours before using. The CuO catalysts were dip coated onto the rod. A fresh carbon rod and electrolyte were used in each experiment.

The experiments were carried out at selected potentials of -0.4 V, -0.8 V, -1.2 V. Cyclic sweeps (1 cycle and 10 cycles) were also carried out under the same conditions. The CuO modified electrode was held at the chosen potential for 15 minutes before being removed from solution, dried in a dessicator for 1 hour and stored in a vial. XPS analysis was then carried out using these samples.

The XPS experiments were performed by Thermo scientific K-Alpha surface analysis X-ray photoelectron spectrometer system, using Al K alpha X-rays (1486.6 eV), the spot size of 400 microns, 3 random spots were selected for every electrode rod.

4.1.2 Characteristics of XPS spectrum

The analysis involves simulating synthetic spectra (peak fitting) in order to match or fit the experimental data. Peak fitting begins with subtraction of the background to reveal the true intensities of the peaks. Once the background is fitted, simulated peaks can be deconvoluted by common parameters, such as peak position, full-width-half-maximum, and peak area [4]. To be more specific, the intensity, *I*, of a photoelectron peak from a homogeneous solid is given by [4, 5]

$$I = JC\sigma\xi T\lambda \qquad \text{(Equation 5)}$$

where *J* is the photon flux, *C* is the concentration of the element/ion-of-interest in the solid, σ is the ionization cross-section, ξ is the spectrometer angular acceptance, *T* is the spectrometer transmission function, and λ is the inelastic mean free path (IMFP). The Equation 5 can be rearranged to

$$C = \frac{I}{J\sigma\xi T\lambda} = \frac{I}{JF} \qquad \text{(Equation 6)}$$

The term $F = \sigma\xi T\lambda$, is called the atomic sensitivity factor, which incorporates the terms associated with the spectrometer and specimen. The atomic fraction of one element (*X*) in a two oxidation states system (*A*-*B*) can be determined using the following expression [4, 5]

$$Atomic\%A = \frac{I_A / F_A}{I_A / F_A + I_B / F_B} \qquad \text{(Equation 7)}$$

In the following XPS experiments,

(1) Peak fitting will be performed using the CasaXPS processing software (version 2.3.16);

(2) Shirley type is used as the model background type for the quantitative analysis;

(3) National Institute of Standards and Technology XPS Database [6], XPS References Pages [7] and other literature were used to assign experimental peaks.

4.1.3 XPS for pH 7 PBS in Ar deoxygenated conditions

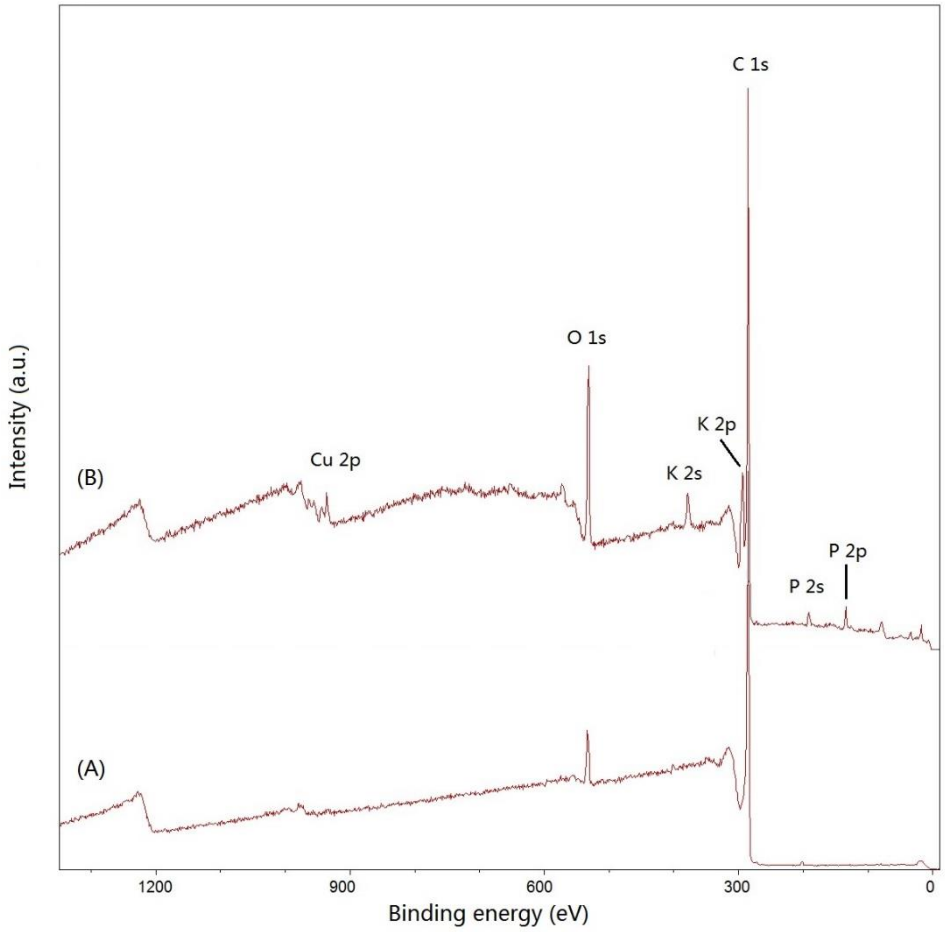

Figure 4-1. Ex situ XPS wide scan survey for all elements. (A) The electrode was cleaned and dried in dessicator for 1 hour; (B) The electrode was dip coated with CuO and placed in the cell with 0.2 M pH 7 Ar deoxygenated PBS for 15 minutes without potential, and removed from solution, dried in dessicator for 1 hour.

The wide scan survey XPS spectra are shown in Figure 4-1. The clean electrode in Figure 4-1 (A) generates two peaks for C 1s and O 1s at 283.5 and 532.1 eV [6]. Figure 3-7 (B) is the spectrum from the electrode coated with sample and placed in the cell for 15 minutes without potential. It showed the presence of C (1s 283.5 eV), O (1s 532.1 eV), Cu (2p 935.7 eV), K (2s 377.7 eV, 2p 293.5eV), P (2s 191.0 eV, 2p 134.3 eV) [6, 7]. The impurities of elements K and P came from the phosphate buffer electrolyte.

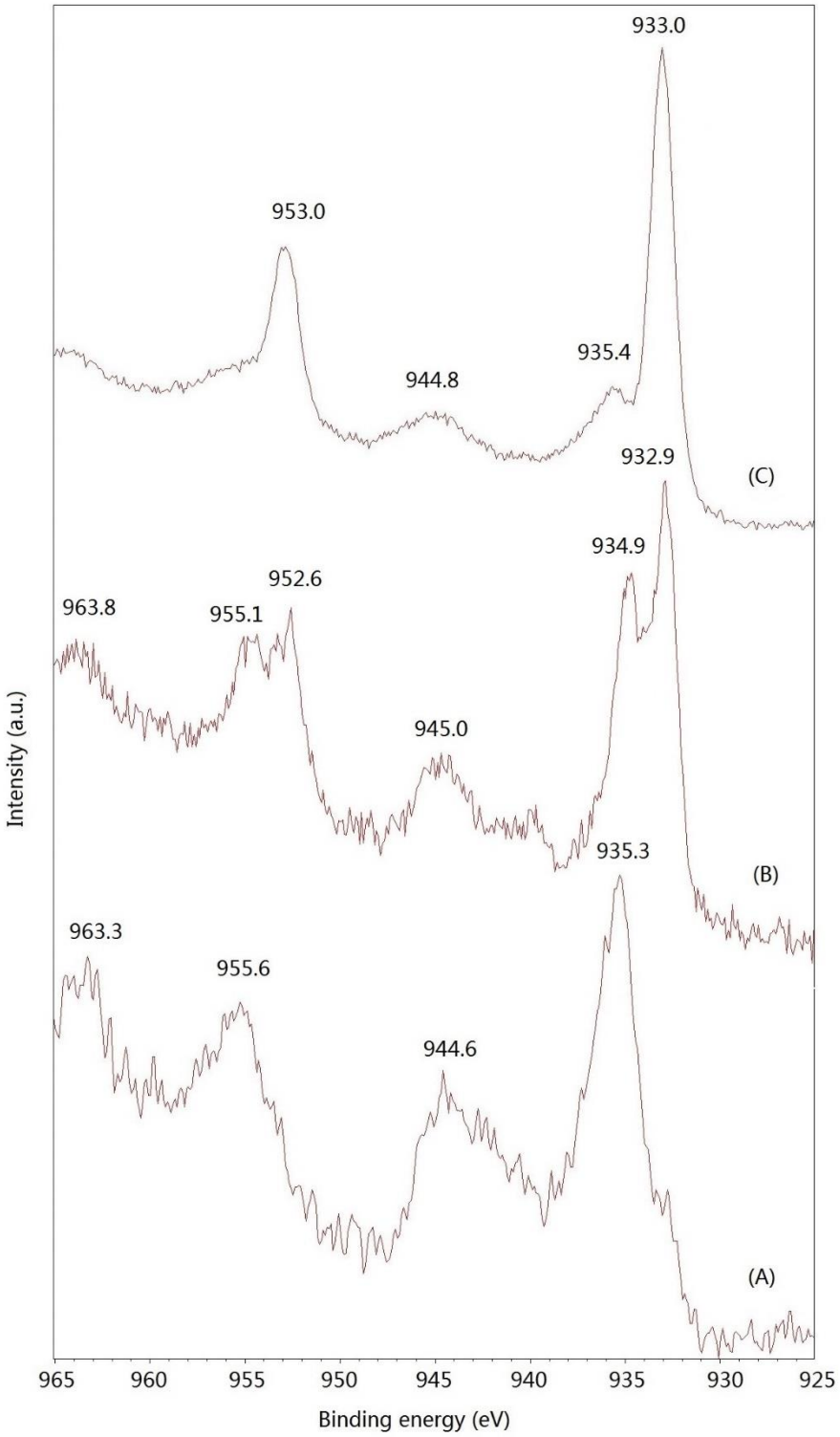

Figure 4-2. High resolution Cu 2p XPS spectra for the electrode after applying potential in 0.2 M pH 7 Ar deoxygenated PBS at (A) -0.4 V; (B) -0.8 V; (C) -1.2 V.

Figure 4-2 shows the high resolution Cu 2p XPS spectra for the electrode after applying potential at -0.4 V (A), -0.8 V (B) and -1.2 V (C). The result for the -0.4 V rod shows Cu(II) $2p_{3/2}$ peak at 935.3 eV and Cu(II) $2p_{1/2}$ peak at 955.6 eV, together

with well-defined Cu(II) $2p_{3/2}$ and $2p_{1/2}$ satellite peaks at 944.6 and 963.3 eV, respectively [6, 7]. At this potential, the sample on electrode is CuO only.

For the -0.8 V rod, the spectrum shows the Cu(II) $2p_{3/2}$ and $2p_{1/2}$ peak at 934.9 and 955.1 eV, and the presence of Cu(I) or Cu(0) $2p_{3/2}$ peak at 932.9 eV, $2p_{1/2}$ peak at 952.6 eV [6-9]. The satellite peaks for Cu(II) appear at 945.0 and 963.8 eV. The presence of the satellites structure is due to charge transfer transitions from O^{2-} ions into unfilled valence level of the Cu(II) ion [8]. Cu(I) has a filled ground state configuration, so no satellites can be seen [8]. This indicates some of the Cu(II) species were reduced to Cu(I)/Cu(0), and Cu(I)/Cu(0) species are now present on the electrode surface. It is not clear whether the peaks at 932.9 and 952.6 eV are attributed to metallic copper or Cu_2O because the Cu 2p binding energy and peak width of these two species are very similar [8]. The shape of the spectrum is still dominated by Cu(II), the intensity of the peaks of Cu(I)/Cu(0) are relatively low. The proportion of Cu(I)/Cu(0) species is no more than 40% calculated from the spectrum. This implies that small amount of CuO is reduced on the surface to the form of Cu_2O or Cu.

At the more negative potential at -1.2 V, a Cu_2O/Cu surface layer is formed on the electrode, as evidenced by the large Cu(I)/Cu(0) $2p_{3/2}$ peak centred at 933.0 eV, and $2p_{1/2}$ peak at 953.0 eV. Cu(II) shows a small peak at 935.4 eV, together with a hump at 944.8 eV as the characteristic $2p_{3/2}$ satellite peak.

As seen in section 3.2.1 cyclic voltammetry in pH 7 Ar deoxygenated PBS, the first negative scan in the cyclic voltammogram Figure 3-3 shows that, Cu(II) begins to be reduced from about -0.8 V under these conditions. The XPS spectra are consistent with the electrochemistry results as they show Cu(I)/Cu(0) peaks at 932.5 and 952.5 eV after holding at -0.8 V. This means the reduction of Cu(II) to Cu(I) or Cu(0) begins at about -0.8 V.

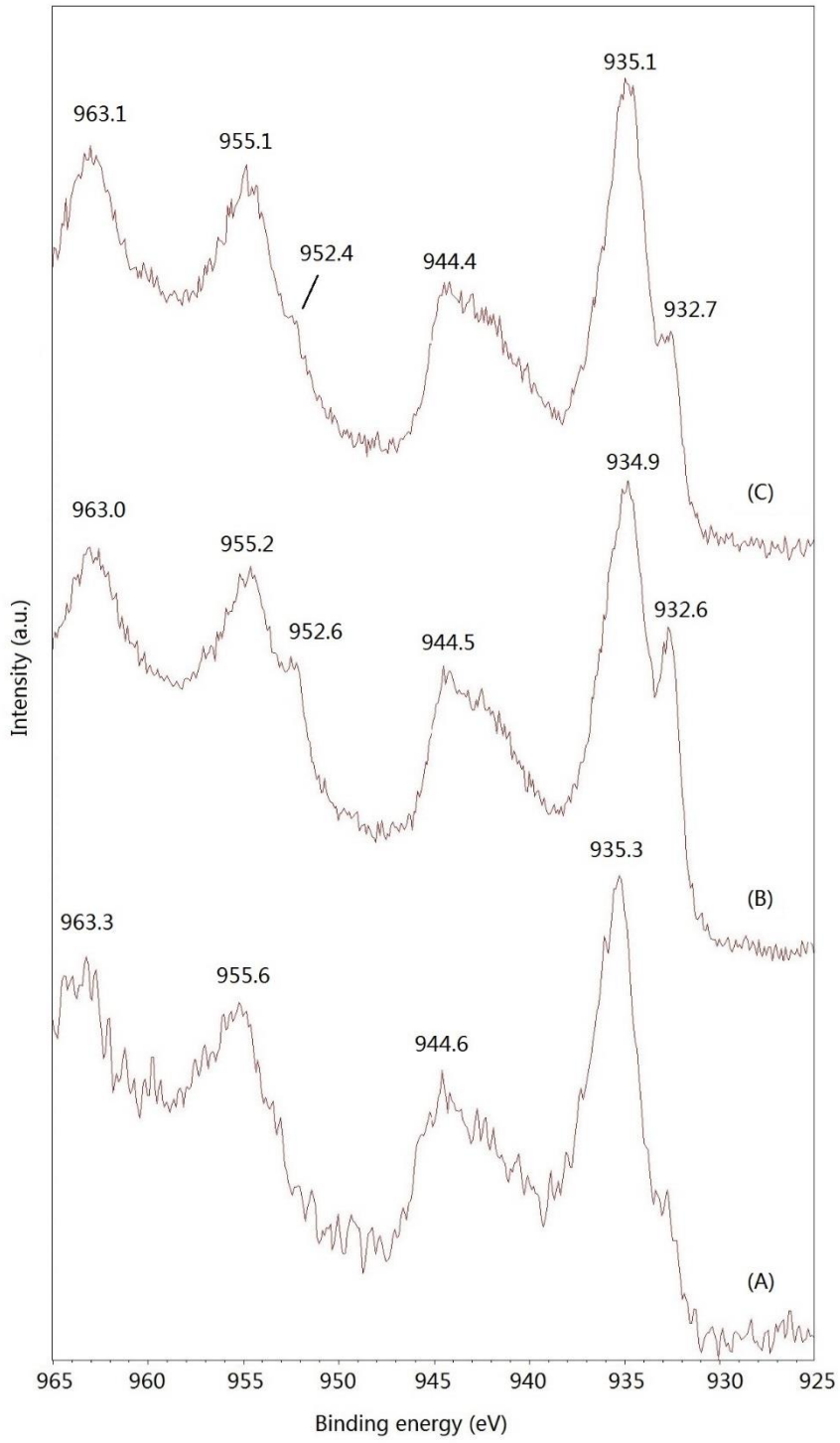

Figure 4-3. High resolution Cu 2p XPS spectra for the electrode in 0.2 M pH 7 Ar deoxygenated PBS after: (A) holding 15 minutes at -0.4 V; (B) 1 cycle; (C) 10 cycles. For (B) and (C) the potential was scanned from 0→-1.2→0.4→0 V vs. Ag/AgCl. υ=100 mV·s^{-1}.

Figure 4-3 shows the high resolution Cu 2p XPS spectra for the electrode after holding

at -0.4 V, after 1 full cyclic sweep and after 10 cycles. The cyclic potential starts at 0 V, the first switching potential is -1.2 V, the second switching potential is 0.4 V, and ends at 0 V. The potential cycle enables the reduction reaction at -1.2 V and oxidation reaction at 0.4 V of CuO catalyst. Then the potential cycle finishes at 0 V, before the next reduction reaction starts. Therefore, the oxidation state of copper species after a full reduction-oxidation cycle can be compared with the pre-reaction catalyst. For the electrode after applied potential at -0.4 V for 15 minutes, it shows a Cu(II) $2p_{3/2}$ peak at 935.3 eV and Cu(II) $2p_{1/2}$ peak at 955.6 eV, and satellite peaks at 944.6 and 963.3 eV. Similar to the above discussion, the electrode surface contains CuO only.

After application of 1 potential cycle, the spectrum shows a dominant Cu(II) $2p_{3/2}$ peak at 934.9 eV, and $2p_{1/2}$ peak at 955.2 eV, and satellite peaks at 944.5 and 963.0 eV. Besides, there are small Cu(I)/Cu(0) shoulders for $2p_{3/2}$ and $2p_{1/2}$ at 932.6 and 952.6 eV. This means after one completed cycle where the CuO is first reduced and then oxidised, most but not all of the Cu returns to the Cu(II) oxidation state.

After 10 cycles, the Cu(II) $2p_{3/2}$ peak shifts to 935.1 eV, $2p_{1/2}$ peaks at 955.1 eV, and the well-defined satellite peaks centre at 944.4 and 963.1 eV. The shoulders for Cu(I)/Cu(0) are smaller at 932.7 and 952.4 eV. It is apparent after 10 cycles, the electrochemically active Cu(II) layer is reduced and oxidised associated with continued cycling potential. Catalyst NPs are not poisoned or deactivated. After 10 cycles, the NPs are still present mainly as Cu(II) species. There is a steady concentration of redox species present on the electrode surface. This indicates catalyst stability with respect to potential cycling over the potential ranges used in this experiment.

4.1.4 XPS for pH 7 PBS in CO_2 saturated conditions

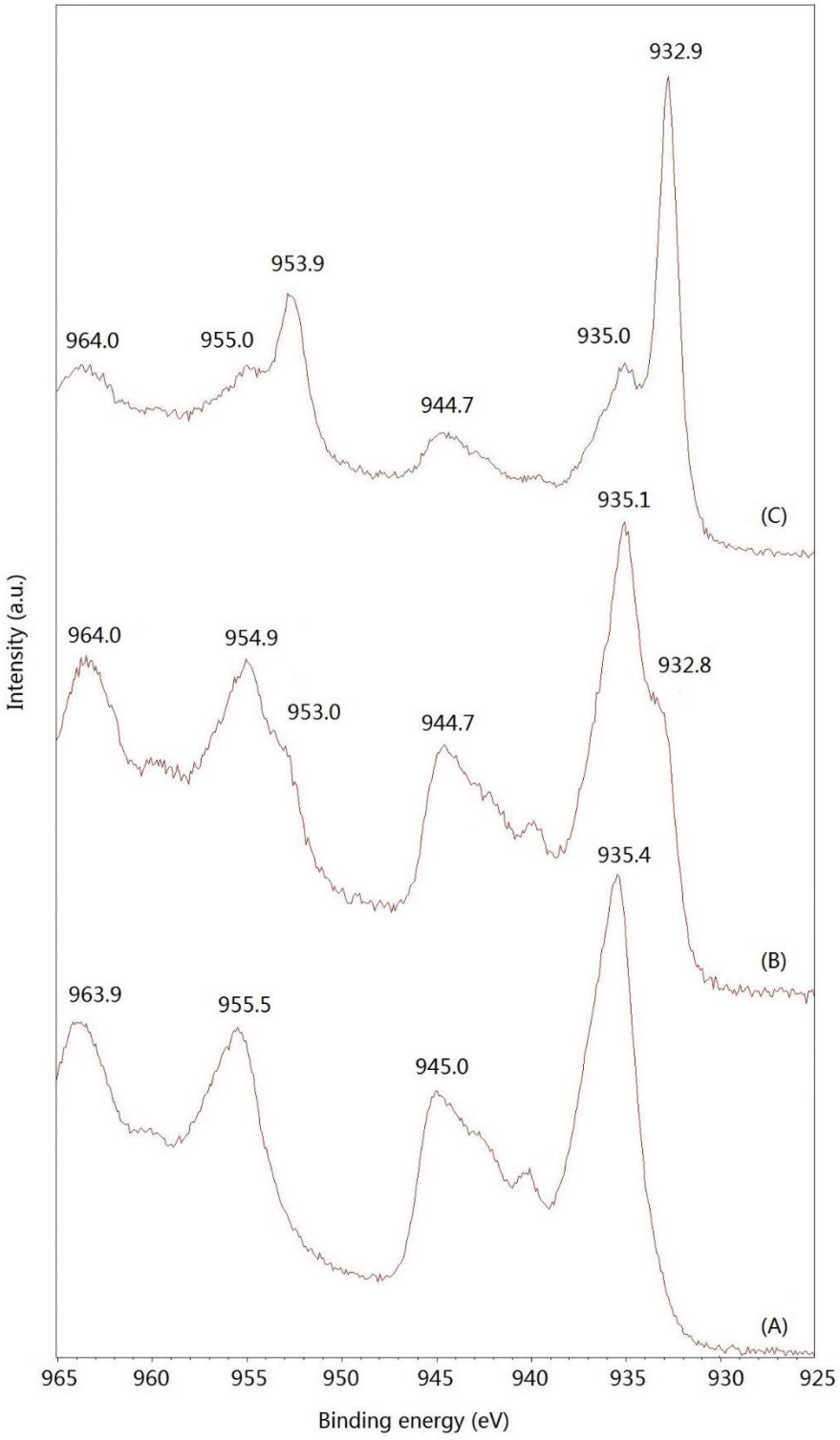

Figure 4-4. High resolution Cu 2p XPS spectra for the electrode after applying potential in 0.2 M pH 7 CO_2 saturated PBS at (A) -0.4 V; (B) -0.8 V; (C) -1.2 V.

Figure 4-4 shows the high resolution Cu 2p XPS spectra for the electrode after

applying potential in CO_2 saturated solution. The -0.4 V rod spectrum shows typical Cu(II) 2p peaks. The Cu(II) $2p_{3/2}$ peak appears at 935.4 eV and $2p_{1/2}$ peak at 955.5 eV. The corresponding satellite peaks are generated at 945.0 and 963.9 eV for Cu(II) $2p_{3/2}$ and $2p_{1/2}$, respectively. At this potential, the sample on the electrode is CuO only. This is identical to the spectrum in Ar deoxygenated solution at the same potential.

The results of the -0.8 V rod show the dominant Cu(II) $2p_{3/2}$ peak at 935.1 eV, $2p_{1/2}$ peak at 954.9 eV, together with the presence of Cu(I) or Cu(0) $2p_{3/2}$ and $2p_{1/2}$ peak at 932.8 and 953.0 eV. The satellite peaks for Cu(II) $2p_{3/2}$ and $2p_{1/2}$ appear at 944.7 and 964.0 eV. Although this is a similar spectrum to that obtained in Ar deoxygenated solution, the proportion of Cu(II) and Cu(I)/Cu(0) is different, shown in Table 4-1. In CO_2 saturated conditions, the intensity of the main peak and satellite peaks of Cu(II) are relatively higher than in Ar deoxygenated conditions. It implies that in CO_2 saturated solution less Cu(II) is converted to Cu(I)/Cu(0) on the electrode surface than in Ar deoxygenated conditions at -0.8 V.

Table 4-1. Peak position and percentage of Cu $2p_{3/2}$ on electrode in different conditions. Calculated from the high resolution Cu 2p spectra in Figure 4-2 and 4-4.

Sample	Cu(II) $2p_{3/2}$		Cu(I)/Cu(0) $2p_{3/2}$	
Figure 4-2	Peak position	Composition	Peak position	Composition
Figure 4-4	eV	at%	eV	at%
Ar deoxygenated	934.9	60	932.9	40
CO_2 saturated	935.1	81	932.8	19

Almost all Cu(II) is reduced at -1.2 V, resulting in the main Cu(I)/Cu(0) $2p_{3/2}$ peak at 932.9 eV, and $2p_{1/2}$ peak at 953.9 eV. Cu(II) generates small peaks at 935.0 and 955.0 eV, together with hump at 944.7 and 964.0 eV as the characteristic 2p satellite peaks.

In section 3.2.2 cyclic voltammetry in pH 7 CO_2 saturated PBS, it was found that the first negative scan in cyclic voltammogram Figure 3-6 (A) shows that Cu(II) is reduced from -0.75 V, which is a less negative potential than the cyclic voltammogram in Ar deoxygenated condition. However the XPS spectra shows smaller Cu(I)/Cu(0) peaks at 932.8 and 953.0 eV after holding potential at -0.8 V. This means the reduction of

Cu(II) to Cu(I)/Cu(0) was less effective in CO_2 saturated conditions. It is discussed in section 3.7 that the decrease in magnitude of reduction currents may be attributed to CO_2 adsorption. Since CO_2 dissolves to molecular CO_2 and HCO_3^- in pH 7 solution, and less Cu(II) is reduced, the current magnitude is smaller in CO_2 saturated conditions than in Ar deoxygenated conditions from cyclic voltammogram Figure 3-6 (B). In this case the Cu 2p XPS spectra are consistent with the cyclic voltammogram results for less reduction of Cu(II) taking place.

Figure 4-5 shows the high resolution Cu 2p XPS spectra for the electrode in CO_2 saturated solution after holding at -0.4 V, after 1 full cyclic sweep and after 10 cycles. The potential was applied as $0 \rightarrow -1.2 \rightarrow 0.4 \rightarrow 0$ V for cyclic sweep. For the electrode after holding the potential at -0.4 V for 15 minutes, it shows a Cu(II) $2p_{3/2}$ peak at 935.4 eV and Cu(II) $2p_{1/2}$ peak at 955.5 eV, and satellite peaks at 945.0 and 963.9 eV. The electrode surface contains CuO only after applied potential.

After application of 1 potential cycle, the spectrum shows dominant Cu(I)/Cu(0) $2p_{3/2}$ peak at 933.1 eV, and $2p_{1/2}$ peak at 952.9 eV. Besides, there are small Cu(II) shoulders for $2p_{3/2}$ and $2p_{1/2}$ at 935.0 and 955.4 eV, and satellite peaks for $2p_{3/2}$ at 944.4, $2p_{1/2}$ at 963.6 eV. This means after one complete cycle, the CuO is first reduced but not completely oxidised back to Cu(II) oxidation state.

After 10 cycles, the spectrum is still dominated by Cu(I)/Cu(0) peaks, but the shoulder of the Cu(II) peaks are more distinct than in the spectrum recorded for Ar deoxygenated conditions. This implies that after introduction of CO_2, electron transfer processes involving the change in catalyst oxidation state are slower than in Ar deoxygenated solution. It also needs to be noted that the proportion of Cu(II) on the electrode surface gains steadily after 10 cycles, indicating the catalyst material is not completely poisoned or deactivated. However when CO_2 is present in solution, recovery of the CuO species by oxidation appears to be inhibited.

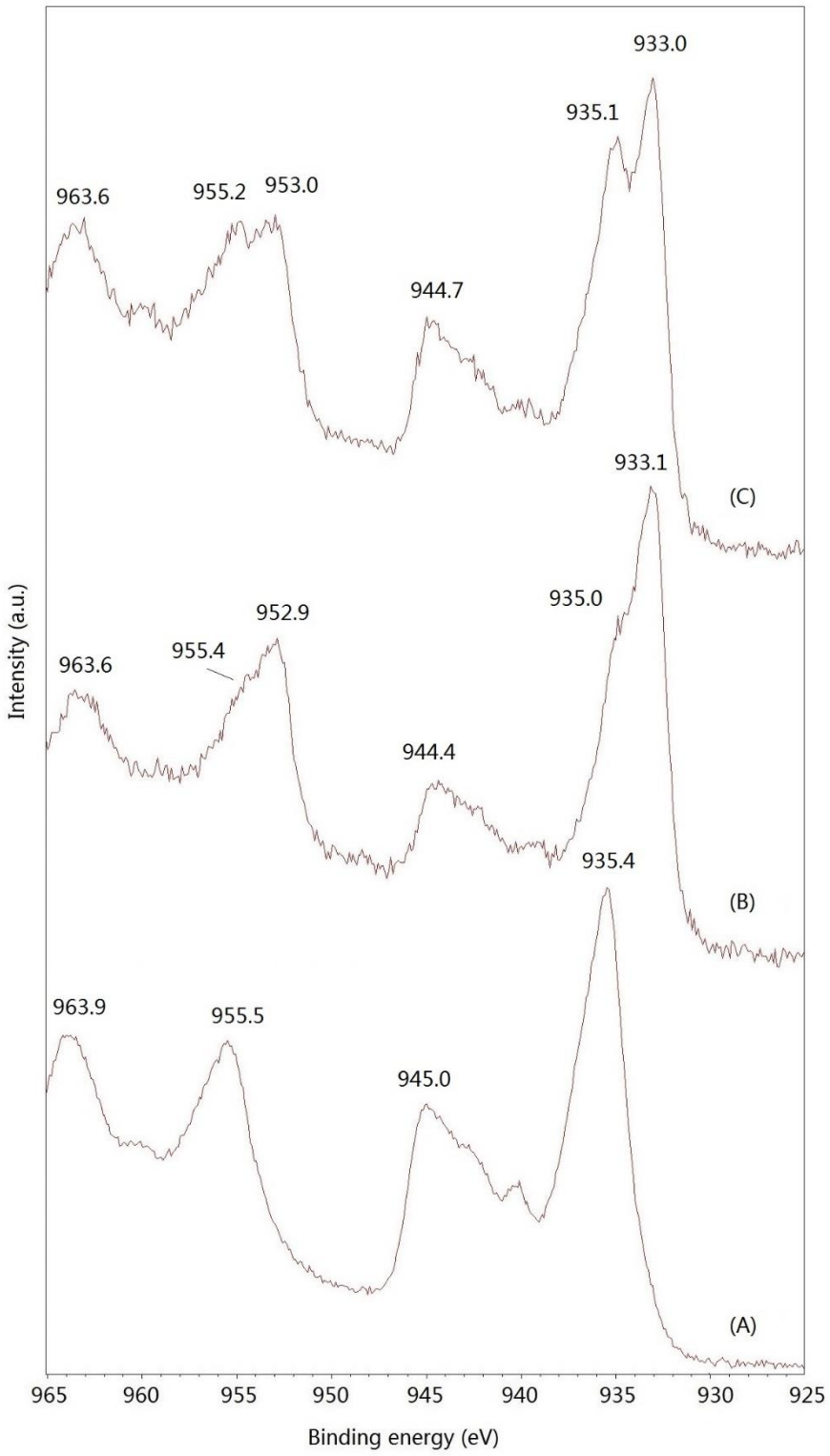

Figure 4-5. High resolution Cu 2p XPS spectra for the electrode in 0.2 M pH 7 CO_2 saturated PBS after: (A) holding 15 minutes at -0.4 V; (B) 1 cycle; (C) 10 cycles. For (B) and (C) the potential was scanned from 0→-1.2→0.4→0 V vs. Ag/AgCl. υ=100 $mV \cdot s^{-1}$.

4.1.5 XPS for pH 4 PBS in Ar deoxygenated conditions

Table 4-2. Peak position and percentage of Cu $2p_{3/2}$ on electrode after various treatment in pH 4 Ar deoxygenated PBS. Calculated from the high resolution Cu 2p spectra in Figure A-1.

Sample		Cu(II) $2p_{3/2}$		Cu(I)/Cu(0) $2p_{3/2}$	
Figure A-1		Peak position eV	Composition at%	Peak position eV	Composition at%
(C)	-1.2 V	934.9	18	932.6	82
(B)	-0.8 V	935.4	46	932.8	54
(A)	-0.4 V	935.5	100	/	0

Figure A-1 (figure in Appendix) shows the high resolution Cu 2p XPS spectra in pH 4 Ar deoxygenated solution for the electrode after various applying potentials. Table 4-2 shows the calculated composition of Cu(II) and Cu(I)/Cu(0) with respect to Cu $2p_{3/2}$ results from Figure A-1. The -0.4 V rod shows Cu(II) $2p_{3/2}$ peak at 935.5 eV, satellite peak at 944.9 eV and Cu(II) $2p_{1/2}$ peak at 955.7 eV, and satellite peak and 963.8 eV. At this potential, the sample on electrode is CuO only.

For the -0.8 V rod, the spectrum show the Cu(II) $2p_{3/2}$ and $2p_{1/2}$ peak at 935.4 and 955.1 eV, and the Cu(I) or Cu(0) $2p_{3/2}$ peak at 932.8 eV, $2p_{1/2}$ peak at 952.7 eV. The satellite peaks for Cu(II) appear at 944.6 and 963.5 eV. This indicates some Cu(I)/Cu(0) species present on the electrode surface, from the reduction of Cu(II) species.

At more negative potential at -1.2 V, a Cu_2O/Cu layer has formed on the electrode, as evidenced by the large Cu(I)/Cu(0) $2p_{3/2}$ peak dominant at 932.6 eV, and $2p_{1/2}$ peak at 952.5 eV. Cu(II) shows small shoulder at 934.9 eV, together with a hump at 944.6 eV as the characteristic $2p_{3/2}$ satellite peak, and Cu(II) $2p_{1/2}$ peak at 954.9 eV with satellite peak at 963.5 eV.

Table 4-3. Peak position and percentage of Cu $2p_{3/2}$ on electrode after various treatment in pH 4 Ar deoxygenated PBS. Calculated from the high resolution Cu 2p spectra in Figure A-2.

Sample		Cu(II) $2p_{3/2}$		Cu(I)/Cu(0) $2p_{3/2}$	
Figure A-2		Peak position	Composition	Peak position	Composition
		eV	at%	eV	at%
(C)	10 cycles	935.9	84	932.7	16
(B)	1 cycle	935.2	87	932.8	13
(A)	-0.4 V	935.5	100	/	0

Figure A-2 shows the high resolution Cu 2p XPS spectra for the electrode in pH 4 Ar deoxygenated solution after holding at -0.4 V, after 1 full cyclic sweep and after 10 cycles. The potential was applied as 0→-1.2→0.4→0 V for cyclic sweep. Table 4-3 calculated the composition of Cu(II) and Cu(I)/Cu(0) with respect to Cu $2p_{3/2}$ results from Figure A-2. For the electrode after applied holding potential at -0.4 V for 15 minutes, it shows a Cu(II) $2p_{3/2}$ peak at 935.5 eV and Cu(II) $2p_{1/2}$ peak at 955.7 eV, and satellite peaks at 944.9 and 963.8 eV, respectively. The electrode surface contains CuO only after applied potential at -0.4 V.

After applied of 1 potential cycle, the spectrum shows sharp Cu(II) $2p_{3/2}$ and $2p_{1/2}$ peaks at 935.2 and 955.1 eV, and satellite peaks for $2p_{3/2}$ at 944.6, $2p_{1/2}$ at 963.6 eV. Also a small Cu(I)/Cu(0) $2p_{3/2}$ peak at 932.8 eV can be observed. This means after one complete cycle, the CuO is first reduced to Cu(I)/Cu(0) then re-oxidised back to Cu(II), but not all of the Cu centres return to the Cu(II) oxidation state. So it can be observed from XPS spectrum that the existing of Cu(I)/Cu(0) peak after one cycle.

After 10 cycles, the spectrum is almost back to the original spectrum of CuO as shown in Figure A-2 (A), but with a barely distinct shoulder for Cu(I)/Cu(0) at 932.7 eV. The small Cu(I)/Cu(0) peak after 10 cycles implies thorough reduction and oxidation between Cu(II) and Cu(I)/Cu(0) with respect to potential cycling over the potential range used in this experiment.

4.1.6 XPS for pH 4 PBS in CO_2 saturated conditions

Table 4-4. Peak position and percentage of Cu $2p_{3/2}$ on electrode after various treatment in pH 4 CO_2 saturated PBS. Calculated from the high resolution Cu 2p spectra in Figure A-3.

Sample		Cu(II) $2p_{3/2}$		Cu(I)/Cu(0) $2p_{3/2}$	
Figure A-3		Peak position eV	Composition at%	Peak position eV	Composition at%
(C)	-1.2 V	935.1	29	932.8	71
(B)	-0.8 V	935.3	85	933.2	15
(A)	-0.4 V	935.4	100	/	0

Figure A-3 shows the high resolution Cu 2p XPS spectra for the electrode after applying potential in pH 4 CO_2 saturated PBS solution. The -0.4 V rod spectrum shows typical Cu(II) 2p peaks. The Cu(II) $2p_{3/2}$ peak appears at 935.4 eV and $2p_{1/2}$ peak at 955.3 eV. The corresponding satellite peaks are generated at 945.1 and 963.8 eV for Cu(II) $2p_{3/2}$ and $2p_{1/2}$, respectively. The results show the sample on the electrode is CuO, which is same as in Ar deoxygenated solution.

The spectrum of the -0.8 V rod shows the Cu(I) or Cu(0) $2p_{3/2}$ and $2p_{1/2}$ peak at 933.2 and 953.5 eV, together with the presence of Cu(II) $2p_{3/2}$ peak at 935.3 eV, $2p_{1/2}$ peak at 955.2 eV. The satellite peaks for Cu(II) $2p_{3/2}$ and $2p_{1/2}$ appear at 945.0 and 963.7 eV. The spectrum implies that Cu(II) is partly converted to Cu(I)/Cu(0) on electrode surface.

Not all of the Cu(II) species were reduced to Cu(I)/Cu(0) on the electrode surface after applied potential at -1.2 V for 15 minutes. The main peak in the spectrum is generated by Cu(I)/Cu(0) peaks, together with Cu(II) and its satellite peaks. The reduction of Cu(II) is not complete in CO_2 saturated pH 4 solution.

Table 4-5. Peak position and percentage of Cu $2p_{3/2}$ on electrode after various treatment in pH 4 CO_2 saturated PBS. Calculated from the high resolution Cu 2p spectra in Figure A-4.

Sample		Cu(II) $2p_{3/2}$		Cu(I)/Cu(0) $2p_{3/2}$	
Figure A-4		Peak position eV	Composition at%	Peak position eV	Composition at%
(C)	10 cycles	935.3	59	932.9	41
(B)	1 cycle	935.4	76	932.7	24
(A)	-0.4 V	935.4	100	/	0

Figure A-4 shows the high resolution Cu 2p XPS spectra for the electrode in CO_2 saturated solution after holding at -0.4 V, after 1 full cyclic sweep and after 10 cycles. The potential was applied as 0→-1.2→0.4→0 V for cyclic sweep. For the electrode after applied holding potential at -0.4 V for 15 minutes, it shows a Cu(II) $2p_{3/2}$ peak at 935.4 eV and Cu(II) $2p_{1/2}$ peak at 955.3 eV, and satellite peaks at 945.1 and 963.8 eV. The electrode surface contains CuO only after applied potential.

The spectrum shows both Cu(II) ($2p_{3/2}$ at 935.4 eV, satellite peak at 944.5 eV, and $2p_{1/2}$ at 955.8 eV, satellite peak at 963.8 eV) and Cu(I)/Cu(0) ($2p_{3/2}$ peak at 932.7 eV, $2p_{1/2}$ peak at 952.6 eV) after application of one potential cycle. Combined with the result for the -1.2 V rod, after one complete cycle, the CuO is first reduced (not complete) then oxidised to Cu(II) oxidation state (also not complete) on the electrode surface.

After 10 cycles, apparently larger Cu(I)/Cu(0) peaks can be observed. The proportion of Cu(I)/Cu(0) increased with number of cycles is due to the fact that not all Cu(I)/Cu(0) is oxidised back to Cu(II) in each cycle. After repeated addition of remaining Cu(I)/Cu(0), more Cu(I)/Cu(0) species can be observed in the spectrum.

4.1.7 XPS for pH 9 PBS in Ar deoxygenated conditions

Table 4-6. Peak position and percentage of Cu $2p_{3/2}$ on electrode after various treatment in pH 9 Ar deoxygenated PBS. Calculated from the high resolution Cu 2p spectra in Figure A-5.

Sample		Cu(II) $2p_{3/2}$		Cu(I)/Cu(0) $2p_{3/2}$	
Figure A-5		Peak position eV	Composition at%	Peak position eV	Composition at%
(C)	-1.2 V	935.0	34	932.9	66
(B)	-0.8 V	934.7	71	932.5	29
(A)	-0.4 V	934.9	100	/	0

Figure A-5 shows the high resolution Cu 2p XPS spectra for the electrode after applying potential at -0.4 V (A), -0.8 V (B) and -1.2 V (C). Results for the -0.4 V rod show Cu(II) $2p_{3/2}$ peak at 934.9 eV and $2p_{1/2}$ peak at 954.9 eV, with Cu(II) $2p_{3/2}$ and $2p_{1/2}$ satellite peaks at 944.3 and 963.0 eV, respectively. At this potential, the sample on electrode surface is CuO only.

The -0.8 V rod spectrum shows the Cu(I)/Cu(0) $2p_{3/2}$ peak at 932.5 eV, $2p_{1/2}$ peak at 952.5 eV, with the presence of Cu(II) $2p_{3/2}$ and $2p_{1/2}$ peak at 934.7 and 955.4 eV. The satellite peaks for Cu(II) appear at 944.6 and 963.0 eV. Some of the Cu(II) species were reduced to Cu(I)/Cu(0) on the electrode surface.

At more negative potential at -1.2 V, as the proportion of the Cu(I)/Cu(0) increased, a Cu_2O/Cu layer was formed on the electrode surface, as evidenced by the large Cu(I)/Cu(0) $2p_{3/2}$ peak generated at 932.9 eV, and $2p_{1/2}$ peak at 952.9 eV. Cu(II) shows small peak as $2p_{3/2}$ at 935.0 eV, together with a hump at 944.7 eV as the characteristic $2p_{3/2}$ satellite peak, and $2p_{1/2}$ at 954.4 eV, with satellite peak at 963.8 eV.

Table 4-7. Peak position and percentage of Cu $2p_{3/2}$ on electrode after various treatment in pH 9 Ar deoxygenated PBS. Calculated from the high resolution Cu 2p spectra in Figure A-6.

Sample		Cu(II) $2p_{3/2}$		Cu(I)/Cu(0) $2p_{3/2}$	
Figure A-6		Peak position eV	Composition at%	Peak position eV	Composition at%
(C)	10 cycles	934.7	75	932.8	25
(B)	1 cycle	934.9	88	933.0	12
(A)	-0.4 V	934.9	100	/	0

The Figure A-6 shows the high resolution Cu 2p XPS spectra for the electrode in pH 9 Ar deoxygenated solution after holding at -0.4 V for 15 minutes, after 1 full cyclic sweep and after 10 cycles. The cyclic potential starts at 0 V, the first switching potential is -1.2 V, the second switching potential is 0.4 V, and ends at 0 V. For the electrode after applied potential at -0.4 V for 15 minutes, it shows a Cu(II) $2p_{3/2}$ peak at 934.9 eV and Cu(II) $2p_{1/2}$ peak at 954.9 eV, and satellite peaks at 944.3 and 963.0 eV. Similar to the above discussion, the electrode surface contains CuO only.

After application of 1 potential cycle, the spectrum shows Cu(II) $2p_{3/2}$ and $2p_{1/2}$ at 934.9 and 954.6 eV, with satellite peaks at 944.3 and 963.1 eV. Small amount of Cu(I)/Cu(0) composition for $2p_{3/2}$ peak can be calculated centred at 933.0 eV. This means after one completed cycle, although not all of the CuO is reduced to Cu(I)/Cu(0) (seen as Figure A-5 (C)), the reduced Cu(I)/Cu(0) is mostly oxidised back to Cu(II) oxidation state.

After 10 cycles, the Cu(II) $2p_{3/2}$ peak appears at 934.7 eV, $2p_{1/2}$ peaks at 954.3 eV, and the well-defined satellite peaks centre at 944.8 and 963.2 eV. It is apparent in the 10 cycles, the electrochemically active Cu(II) layer is reduced and oxidised with continued cycling potential. The spectrum presents high stability as a catalyst material in the experiment conditions.

4.1.8 XPS for pH 9 PBS in CO_2 saturated conditions

Table 4-8. Peak position and percentage of Cu $2p_{3/2}$ on electrode after various treatment in pH 9 CO_2 saturated PBS. Calculated from the high resolution Cu 2p spectra in Figure A-7.

Sample		Cu(II) $2p_{3/2}$		Cu(I)/Cu(0) $2p_{3/2}$	
Figure A-7		Peak position eV	Composition at%	Peak position eV	Composition at%
(C)	-1.2 V	/	0	932.7	100
(B)	-0.8 V	934.6	77	932.7	23
(A)	-0.4 V	933.6	100	/	0

Figure A-7 shows the high resolution Cu 2p XPS spectra for the electrode after applying potential in CO_2 saturated solution. The -0.4 V rod spectrum shows typical Cu(II) 2p peaks. At this potential, only CuO is detected on the electrode surface.

The spectrum of the -0.8 V rod shows the Cu(I)/Cu(0) $2p_{3/2}$ and $2p_{1/2}$ peak at 932.7 and 952.8 eV, together with the presence of Cu(II) $2p_{3/2}$ peak at 934.6 eV, $2p_{1/2}$ peak at 954.6 eV. The satellite peaks for Cu(II) $2p_{3/2}$ and $2p_{1/2}$ appear at 944.1 and 962.8 eV.

Only Cu(I)/Cu(0) $2p_{3/2}$ peaks at 932.7 eV, and $2p_{1/2}$ peak at 952.5 eV were obtained in the spectrum after applied potential at -1.2 V for 15 minutes. This implies the reduction of Cu(II) to Cu(I)/Cu(0) was complete in pH 9 solution under CO_2 saturated condition.

Table 4-9. Peak position and percentage of Cu $2p_{3/2}$ on electrode after various treatment in pH 9 CO_2 saturated PBS. Calculated from the high resolution Cu 2p spectra in Figure A-8.

Sample		Cu(II) $2p_{3/2}$		Cu(I)/Cu(0) $2p_{3/2}$	
Figure A-8		Peak position eV	Composition at%	Peak position eV	Composition at%
(C)	10 cycles	934.8	85	932.9	15
(B)	1 cycle	934.2	84	933.1	16
(A)	-0.4 V	933.6	100	/	0

Figure A-8 shows the high resolution Cu 2p XPS spectra for the electrode in pH 9 CO_2 saturated solution. For the electrode after applied holding potential at -0.4 V for 15 minutes, it shows Cu(II) $2p_{3/2}$ peak at 933.6 eV and Cu(II) $2p_{1/2}$ peak at 953.6 eV, and satellite peaks at 944.1 and 962.8 eV. The electrode surface contains CuO only after applied potential.

After application of 1 potential cycle, large Cu(II) peaks can be observed. This means in 1 complete cycle, the reduction and oxidation of CuO takes place almost thoroughly in higher pH value.

After 10 cycles, the spectrum is still dominant by Cu(II) peaks. This implies that after introduction of CO_2, the catalysts have same Cu oxidation state as in Ar deoxygenated solution (Figure A-6). Although the catalysts show very high electrochemical activity and stability in pH 9 solution in both Ar deoxygenated and CO_2 saturated solutions, it is not clear whether CO_2 is involved in the electron transfer and/or the further reduction reactions, since the CuO behaviour is similar in these two conditions.

4.1.9 XPS for pH 8 $KHCO_3$ solution in Ar deoxygenated conditions

Table 4-10. Peak position and percentage of Cu $2p_{3/2}$ on electrode after various treatment in pH 8 Ar deoxygenated $KHCO_3$ solution. Calculated from the high resolution Cu 2p spectra in Figure A-9.

Sample		Cu(II) $2p_{3/2}$		Cu(I)/Cu(0) $2p_{3/2}$	
Figure A-9		Peak position eV	Composition at%	Peak position eV	Composition at%
(D)	1 cycle	934.4	85	932.7	15
(C)	-1.2 V	/	0	932.8	100
(B)	-0.8 V	934.0	56	932.7	44
(A)	-0.4 V	934.3	100	/	0

Figure A-9 shows the high resolution Cu 2p XPS spectra in pH 8 Ar deoxygenated $KHCO_3$ solution for the electrode after various applying potentials. The calculation of Cu $2p_{3/2}$ percentage is summarized in Table 4-10. Result for the Figure A-9 (A), (B), (C) present the reduction process from Cu(II) to Cu(I)/Cu(0). For the -1.2 V rod, the

spectra shows only Cu(I)/Cu(0) can be detected on electrode surface. After application of one potential cycle, most of the Cu(I)/Cu(0) was oxidised back to Cu(II). The XPS results are consistent with CV data.

4.1.10 XPS for pH 8 $KHCO_3$ solution in CO_2 saturated conditions

Table 4-11. Peak position and percentage of Cu $2p_{3/2}$ on electrode after various treatment in pH 8 CO_2 saturated $KHCO_3$ solution. Calculated from the high resolution Cu 2p spectra in Figure A-10.

Sample		Cu(II) $2p_{3/2}$		Cu(I)/Cu(0) $2p_{3/2}$	
Figure A-10		Peak position eV	Composition at%	Peak position eV	Composition at%
(D)	1 cycle	934.4	73	932.5	27
(C)	-1.2 V	934.6	12	932.5	88
(B)	-0.8 V	934.7	82	932.4	18
(A)	-0.4 V	934.7	100	/	0

Figure A-10 shows the high resolution Cu 2p XPS spectra for the electrode in pH 8 CO_2 saturated solution after holding at -0.4 V, -0.8 V, -1.2 V and after 1 full cyclic sweep. The reduction ratio of Cu(II) at -0.8 V is smaller than in Ar deoxygenated solution at same potential. Besides, at -1.2 V, residual Cu(II) can be detected from spectrum. The reduction of Cu(II) was not complete in CO_2 saturated conditions.

4.1.11 XPS for pH 11 K_2CO_3 solution in Ar deoxygenated conditions

Table 4-12. Peak position and percentage of Cu $2p_{3/2}$ on electrode after various treatment in pH 11 Ar deoxygenated K_2CO_3 solution. Calculated from the high resolution Cu 2p spectra in Figure A-11.

Sample		Cu(II) $2p_{3/2}$		Cu(I)/Cu(0) $2p_{3/2}$	
Figure A-11		Peak position eV	Composition at%	Peak position eV	Composition at%
(D)	1 cycle	934.4	73	932.7	27
(C)	-1.2 V	934.6	17	932.7	83
(B)	-0.8 V	934.6	89	932.8	11

(A)	-0.4 V	934.7	100	/	0

Figure A-11 shows the high resolution Cu 2p XPS spectra in pH 11 Ar deoxygenated K_2CO_3 solution for the electrode after various applying potentials. Table 4-12 calculated the composition of Cu(II) and Cu(I)/Cu(0) with respect to Cu $2p_{3/2}$ results from Figure A-11. The -0.4 V rod spectrum shows only Cu(II) 2p peaks. The spectrum of the -0.8 V rod shows the dominant Cu(II) peaks together with small proportion of Cu(I)/Cu(0) $2p_{3/2}$ peak at 932.8 eV. After application of -1.2 V for 15 minutes, sharp of Cu(I)/Cu(0) $2p_{3/2}$ peak at 932.7 eV, and $2p_{1/2}$ peak at 952.3 eV were obtained. After application of 1 potential cycle, the spectrum shows Cu(II) $2p_{3/2}$ and $2p_{1/2}$ main peaks and satellite peaks clearly. This means large amount of Cu(II) were oxidised back from Cu(I)/Cu(0).

4.1.12 XPS for pH 11 K_2CO_3 solution in CO_2 saturated conditions

Table 4-13. Peak position and percentage of Cu $2p_{3/2}$ on electrode after various treatment in pH 11 CO_2 saturated K_2CO_3 solution. Calculated from the high resolution Cu 2p spectra in Figure A-12.

Sample		Cu(II) $2p_{3/2}$		Cu(I)/Cu(0) $2p_{3/2}$	
Figure A-12		Peak position	Composition	Peak position	Composition
		eV	at%	eV	at%
(D)	1 cycle	934.5	47	932.5	53
(C)	-1.2 V	934.5	17	932.6	83
(B)	-0.8 V	934.1	73	932.5	27
(A)	-0.4 V	933.8	100	/	0

Figure A-12 shows the high resolution Cu 2p XPS spectra in pH 11 CO_2 saturated K_2CO_3 solution for the electrode after various applying potentials. Table 4-13 calculated the composition of Cu(II) and Cu(I)/Cu(0) with respect to Cu $2p_{3/2}$ results from Figure A-12. The -0.4 V rod spectrum shows only Cu(II) 2p peaks. After applied holding potential at -0.8 V, the spectrum is dominated by Cu(II) peaks, and Cu(I)/Cu(0) $2p_{3/2}$ peak can be observed at 932.5 eV. The spectrum of the -1.2 V rod shows distinct Cu(I)/Cu(0) $2p_{3/2}$ peak at 932.6 eV, $2p_{1/2}$ peak at 952.2 eV, and Cu(II) $2p_{3/2}$ shoulder centred at 934.5 eV. The other Cu(II) 2p peaks were not clear in the spectrum. After

application of 1 potential cycle, the spectrum shows both Cu(II) and Cu(I)/Cu(0) $2p_{3/2}$ and $2p_{1/2}$ peaks and satellite peaks together. This means the presence of Cu(I)/Cu(0) on the electrode surface, so oxidation back to Cu(II) was not complete.

4.1.13 Discussions

Five pH values and two types of buffer solutions were used in these experiments. The XPS spectra of the high resolution Cu 2p show significant influence of the choice of pH values and solution types with and without CO_2 in the system on the resulting oxidation state of copper species.

After holding potential for 15 minutes at -0.4 V, the spectra show only Cu(II) characteristic peaks in all pH conditions. This is consistent with CV results, the catalysts need more overpotential to start the reduction reaction.

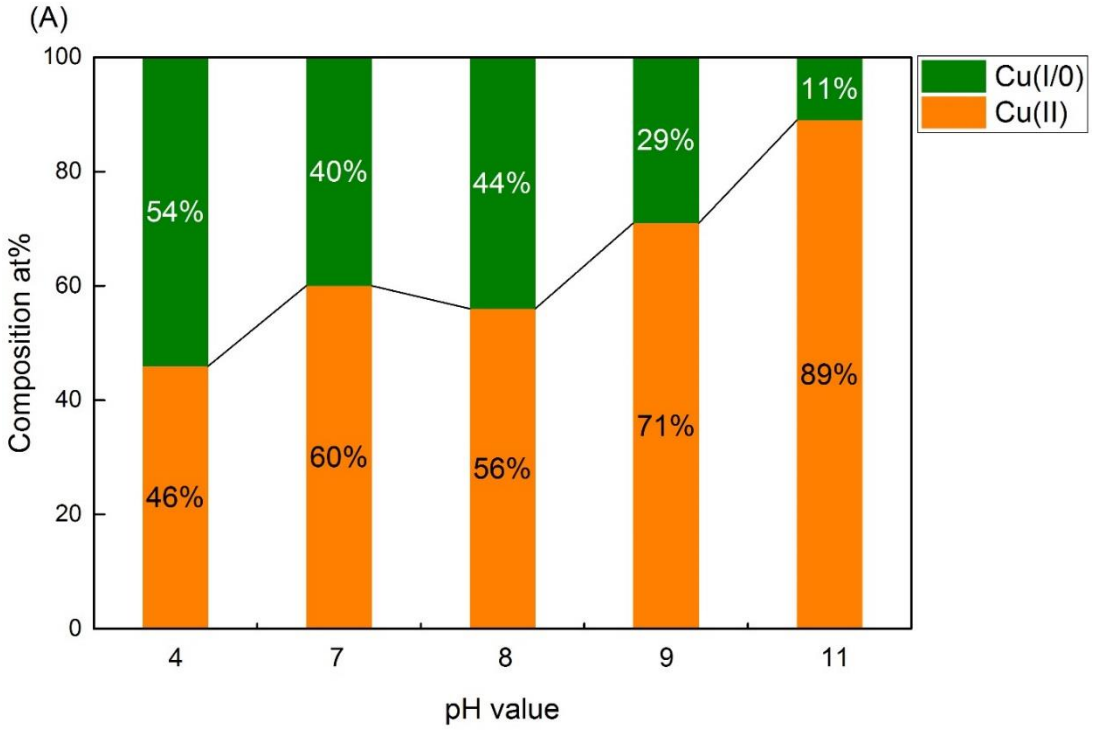

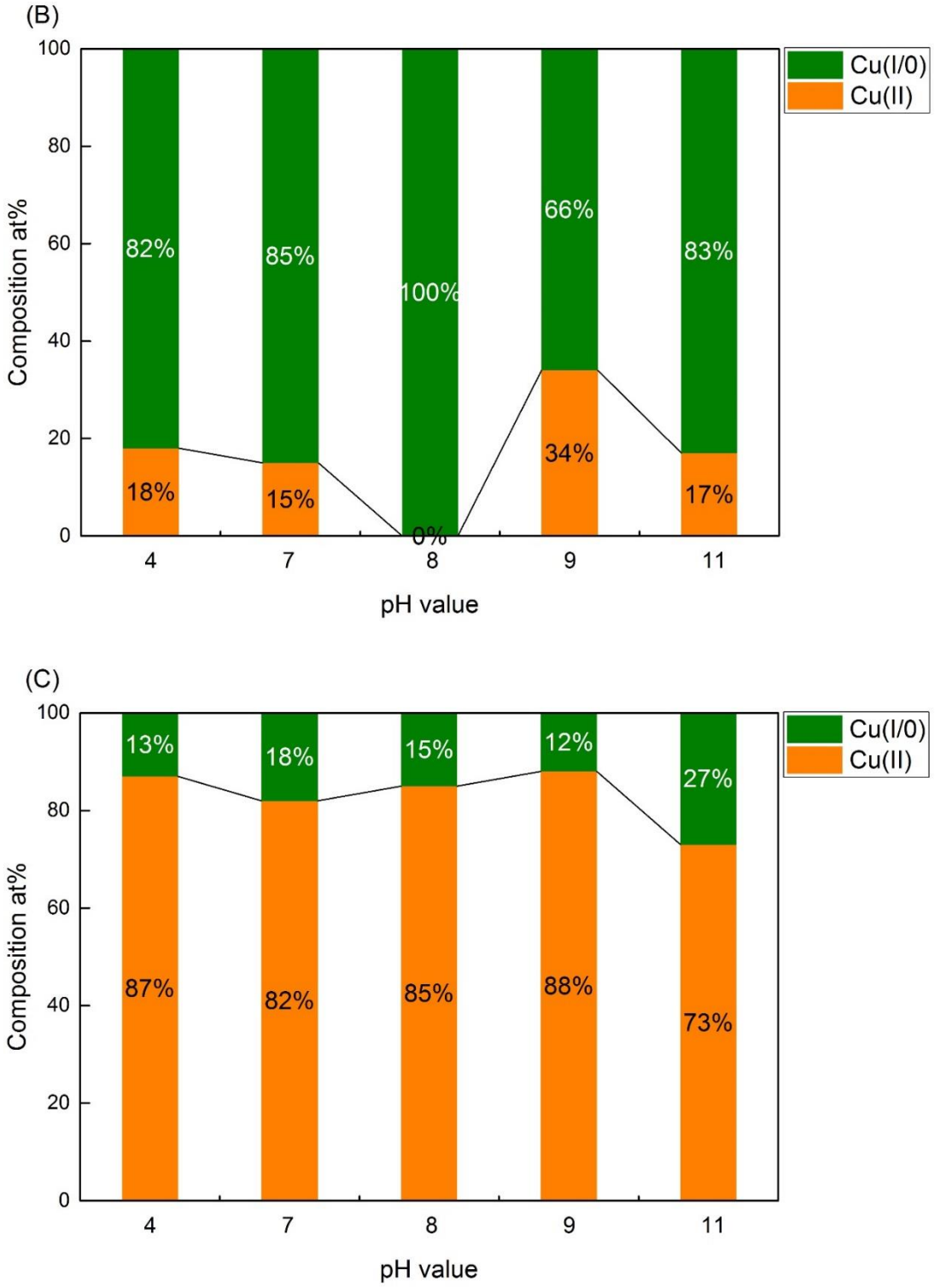

Figure 4-6. The composition of Cu(II) and Cu(I)/Cu(0) with respect to Cu $2p_{3/2}$ XPS spectra for different pHs in Ar deoxygenated solutions after: (A) holding 15 minutes at -0.8 V; (B) holding 15 minutes at -1.2 V; (C) 1 cycle. For (C) the potential was scanned from 0→-1.2→0.4→0 V vs. Ag/AgCl. υ=100 mV·s^{-1}.

Figure 4-6 shows the composition of Cu species in five different solutions. The proportion of Cu(II) and Cu(I) or Cu(0) species is calculated via the high resolution Cu $2p_{3/2}$ XPS spectra. In Ar deoxygenated solutions, after holding potential for 15 minutes at -0.8 V, the proportion of Cu(II) decreases with the decreasing of pH value in general. This is consistent with CV results, where more negative potentials are required for reduction as pH increases. This means less Cu(II) is reduced in higher pH solutions as more overpotential is required to start the reaction. The inverted trend between pH 7 and pH 8 may be caused by the different type of the buffer solution used in the experiments (pH 7 phosphate buffer solution, pH 8 bicarbonate buffer solution).

After holding potential for 15 minutes at -1.2 V, more Cu(II) is reduced to Cu(I)/Cu(0), compared with the results at -0.8 V for each solution. For the pH 8 $KHCO_3$ solution, the XPS spectrum shows Cu(I)/Cu(0) peaks only. It means in the $KHCO_3$ solution, the Cu(II) reduction is complete.

Under all conditions after application of 1 potential cycle, not all of Cu(II) is oxidised back from Cu(I)/Cu(0), which was formed at negative potentials. The spectrum from the pH 11 solution shows 73% of Cu(II) after 1 cyclic sweep, which is the lowest number among five solutions. This means the stability of catalyst to potential cycling can be influenced by pH value. The stability of the catalyst is one primary concern, hence the higher pH value may not be the suitable condition for the experiments.

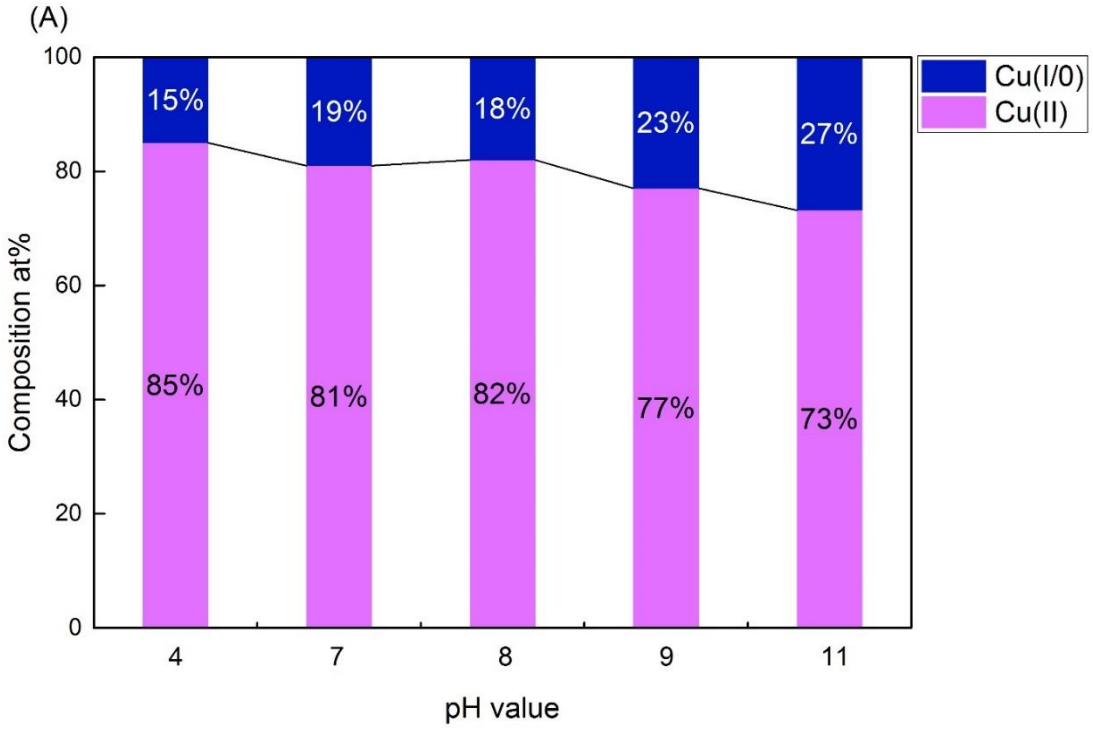
(A)
Cu(I/0)
Cu(II)
Composition at%
pH value
15%
19%
18%
23%
27%
85%
81%
82%
77%
73%

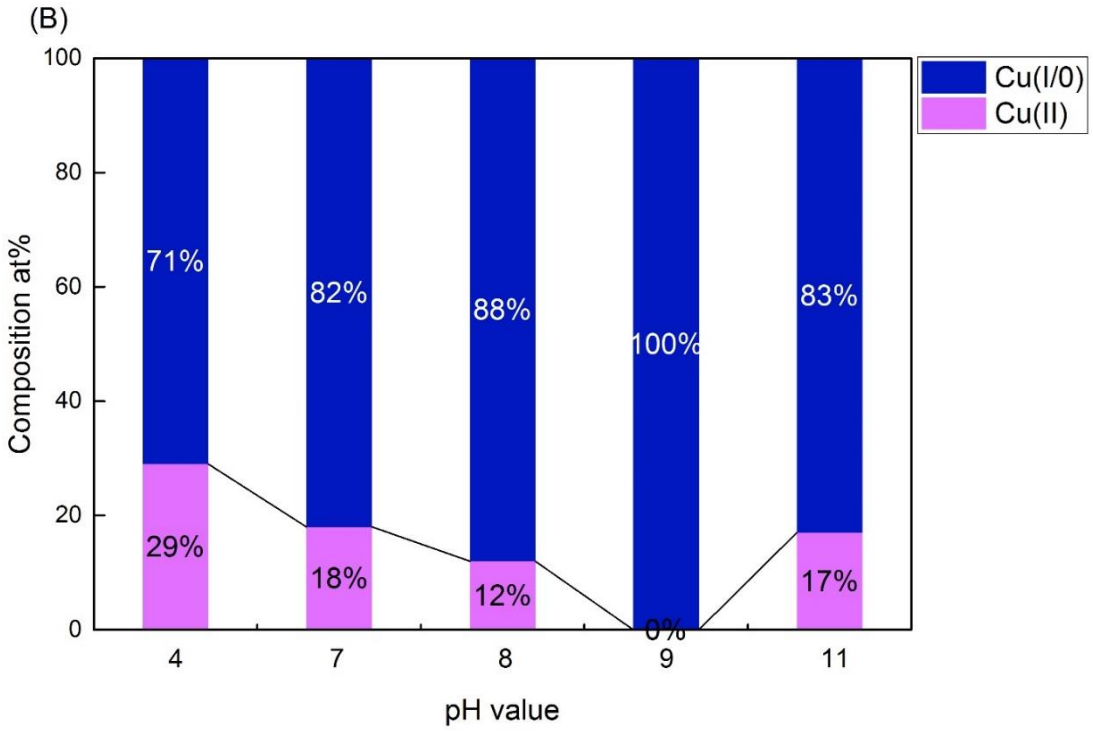
(B)
Cu(I/0)
Cu(II)
Composition at%
pH value
71%
82%
88%
100%
83%
29%
18%
12%
0%
17%

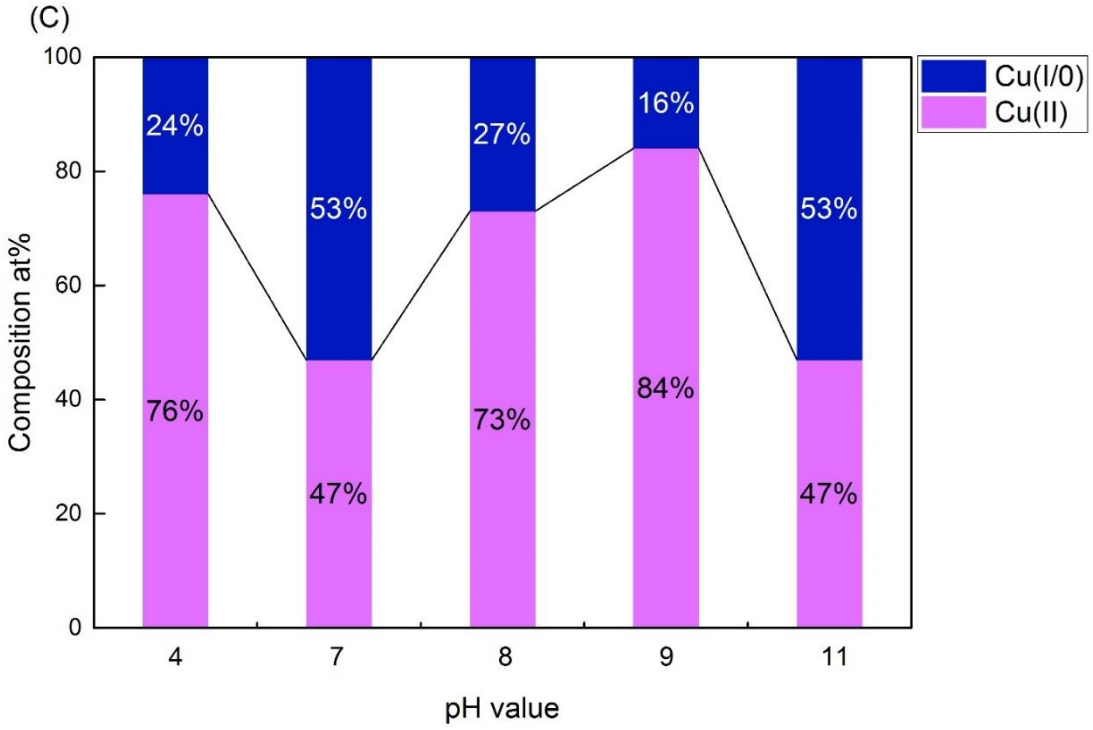

Figure 4-7. The composition of Cu(II) and Cu(I)/Cu(0) with respect to Cu $2p_{3/2}$ XPS spectra for different pHs in CO_2 saturated solutions after: (A) holding 15 minutes at -0.8 V; (B) holding 15 minutes at -1.2 V; (C) 1 cycle. For (C) the potential was scanned from 0→-1.2→0.4→0 V vs. Ag/AgCl. υ=100 $mV \cdot s^{-1}$.

The composition of Cu species in five different solutions in CO_2 saturated conditions are summarized in Figure 4-7. The proportion is calculated using the high resolution Cu $2p_{3/2}$ XPS spectra. After holding potential at -0.8 V for 15 minutes, the proportion of Cu(II) decreases slightly with the increasing of pH value. This means in CO_2 saturated solutions, more Cu(II) is reduced in higher pH solutions. As seen in section 3.7, Figure 3-19 & 20 show that less negative currents were required for reduction of CuO in the presence of CO_2 compared with the Ar deoxygenated conditions. The XPS spectra also show that at the same potential, the proportion of Cu(II) is higher in CO_2 saturated conditions in the four lower pH solutions (pH 4, 7, 8, 9) than in Ar deoxygenated conditions. This indicates that less Cu(II) is reduced in CO_2 saturated solution than in Ar deoxygenated solution at same pH values, which means Cu(II) reduction reaction occurs less effectively in CO_2 saturated solution. It has been discussed in section 3.8 that the current magnitude is enhanced in higher pH value (pH 8, 9, 11) in CO_2 saturated solutions than in Ar deoxygenated solutions. So it can be

concluded that the charge passed on the electrode may not all participate in Cu(II) reduction, since the current onset is observed at less negative potential. The XPS spectra support the conclusion from CV results: in CO_2 saturated solution, the current magnitude is increased, but less Cu(II) reduction reaction takes place, so some of the charge passed may be attributed to CO_2 related reactions in pH 8 and 9 solutions.

After holding potential for 15 minutes at -1.2 V, a significant amount of Cu(II) is reduced to Cu(I)/Cu(0), compared with the results at -0.8 V for each solutions. For three different PBS: pH 4, pH 7 and pH 9, the proportion of Cu(II) decreases with the increasing pH value. This means in higher pH value solution, the Cu(II) reduction occurs thoroughly. But this rule is not applied for potassium carbonate and bicarbonate solutions, where more Cu(II) was detected after treatment in pH 11 solution than in pH 8 solution.

After application of 1 potential cycle, not all of Cu(II) is oxidised back from Cu(I)/Cu(0), which is similar to Ar deoxygenated conditions. But no clear trend can be obtained for the proportion of Cu(II) in CO_2 saturated conditions. For $KHCO_3$ and K_2CO_3 solutions, the proportion of Cu(II) decreases with the increasing pH value. So the lower pH value shows better stability of the catalyst after cyclic sweep. The pH 9 PBS conditions shows best stability among three PBS conditions.

The results of XPS measurements are consistent with CV results in general. It shows the proportion between different oxidation states of Cu species. However we cannot distinguish between Cu(I) and Cu(0) using XPS technique. Hence it is not clear whether the increased proportion of Cu(I)/Cu(0) is attributed by more Cu(II) reduction reaction to Cu(I) or Cu(I) reduction reaction to Cu(0). It can be concluded from CV results and XPS spectra, in general, less Cu(II) is reduced at same pH conditions in CO_2 saturated solutions than Ar deoxygenated solutions. In the cases where the current magnitude is enhanced in CO_2 saturated solution, the additional charge must be involved with some CO_2 related reduction reactions.

4.2 Raman spectroscopic study

XPS is surface sensitive technique, providing analysis of the chemical composition of the top few monolayers of the sample. Raman is expected to give more information about the bulk material, with the analysis depth of 1-5 μm in confocal mode [10, 11]. It is reported that the intensity is related to the grain size and crystal structure [10]. Stronger and sharper Raman peaks are observed which also shift to longer wavenumbers with highly ordered crystal and increasing/decreasing grain size [10].

4.2.1 Raman setup

A three-electrode setup was used to prepare samples for ex situ Raman spectroscopy. Experimental cell and conditions were similar to XPS experiments. The glassy carbon rod was cleaned using the same method as described before. The CuO NPs were dip-coated onto the rod. A fresh carbon rod and electrolyte were used in each experiment.

The experiments were carried out at selected potentials of -0.4 V, -0.8 V, -1.2 V. Cyclic sweeps (1 cycle and 10 cycles) were also carried out in the same conditions as described in the XPS sections. The electrode was held at the chosen potential for 15 minutes before being removed from solution, dried in dessicator for 1 hour and stored in a vial.

The Raman experiments were performed using a Renishaw inVia Raman Microscope with 514.5 nm laser, at least 3 random spots were selected for each electrode rod.

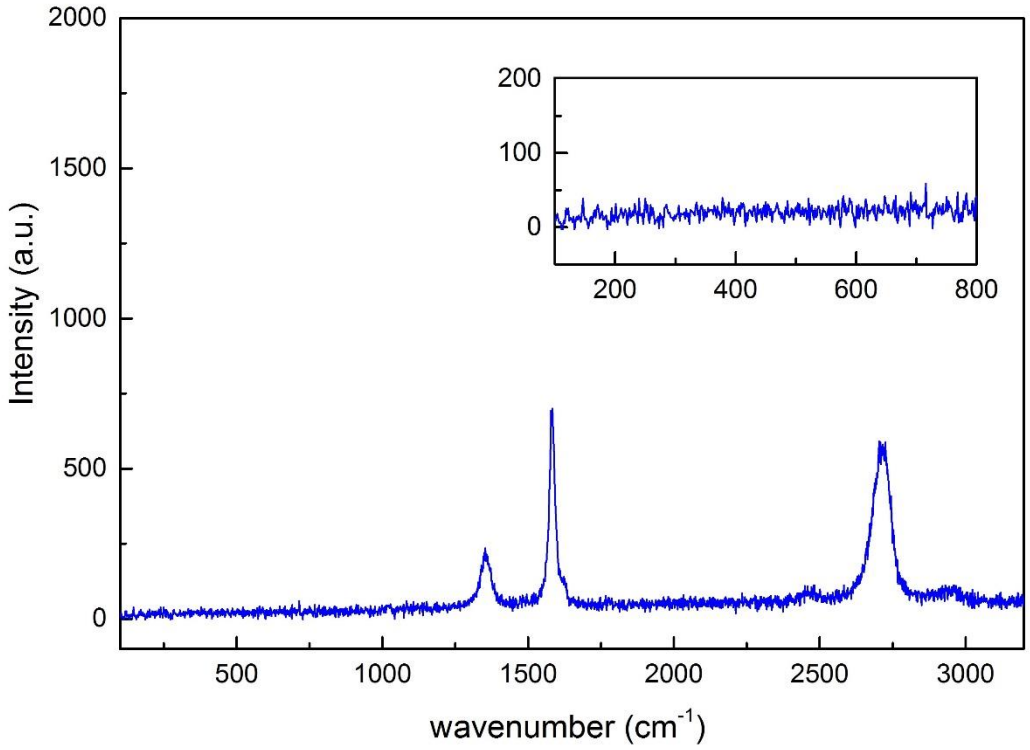

Figure 4-8. Wide scan Raman spectrum for the clean glassy carbon electrode. Insert figure: the same spectrum from 100 to 800 cm^{-1} wavenumber.

Figure 4-8 shows the Raman spectrum for clean glassy carbon rod. Three sharp peaks at 1352, 1583, and 2708 cm^{-1} are contributed by C-C vibrations from the glassy carbon rod [12]. The insert figure shows flat and featureless spectrum between 100 and 800 cm^{-1} wavenumber. The copper related species normally generate peaks in this range. So the glassy carbon rod is a suitable substrate for the Raman measurements in the experiments conditions.

4.2.2 Raman for pH 7 PBS in Ar deoxygenated conditions

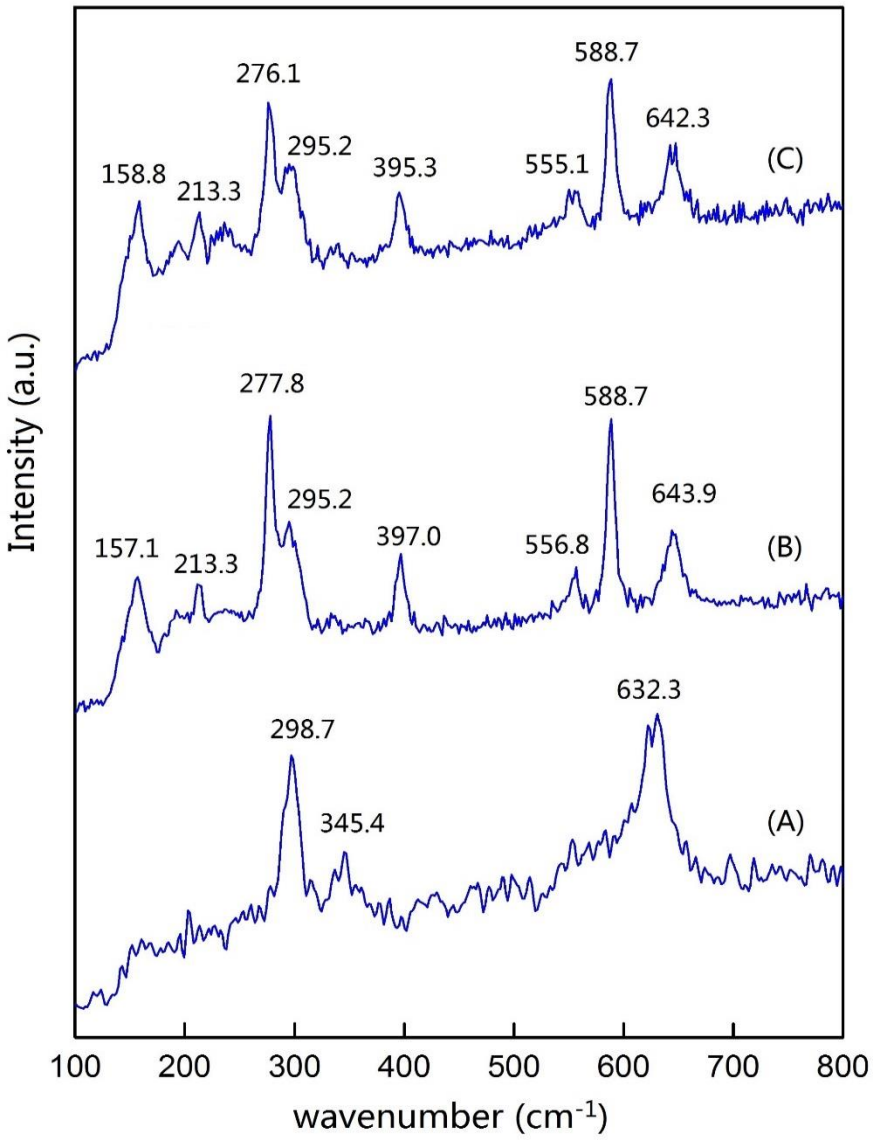

Figure 4-9. Raman spectra for the electrode after applying potential in pH 7 Ar deoxygenated PBS at (A) -0.4 V; (B) -0.8 V; (C) -1.2 V.

The spectra recorded after selected holding potential at -0.4 V, -0.8 V, -1.2 V are presented in Figure 4-9. For the sample after holding potential for 15 minutes at -0.4 V, three peaks at 298.7, 345.4 and 632.3 cm^{-1} were attributed to CuO A_g, B^1_g, B^2_g optical modes, respectively [13]. The experimental CuO Raman shifts can be assigned by literature summarized in Table 4-14. Combing the result with XPS spectrum in pH 7 Ar deoxygenated PBS at same potential, it indicates at both the surface and in the bulk of the samples, only CuO exists at the beginning of the experiment.

Table 4-14. Raman shifts of copper oxide CuO from different literature sources.

Raman shift cm^{-1}			Reference
299	354	632	Figure 4-9
296	346	631	14
273	321	606	15
288-295	330-342	621-628	16
303	350	636	17
301	348	633	18
282	330	616	19

After application of more negative potential at -0.8 V, several weak peaks appear corresponding to Cu_2O modes. The peak at 157.1 cm^{-1} is attributed to Raman scattering from symmetry Γ^-_{15} phonon [20, 21]. The peak at 213.3 cm^{-1} is assigned to two Γ^-_{12} phonons [22, 23]. The sharp peak at 277.8 cm^{-1} may correspond to the A^2_u mode [13, 24]. The 397 cm^{-1} corresponds to multiphonon process [24]. The experimental Cu_2O Raman shifts can be assigned by literatures summarized in Table 4-15. Three CuO peaks shift to 295.2, 397.0, and 643.9 cm^{-1}. The presence of Cu_2O peaks indicates the reduction of Cu(II) takes place not only on the electrode surface as shown in XPS, it also happens in the bulk of the sample.

Table 4-15. Raman shifts of cuprous oxide Cu_2O from different literature sources.

Raman shift cm^{-1}						Reference
157	213	278	/	557	589	Figure 4-9
155	220	309	433	523	629	25
/	218	/	/	523	623	26
150	/	/	/	528	623	27
150	220	/	415	520	630	28

There is not much change between -0.8 V and -1.2 V in Figure 4-8. Peaks contributed from Cu_2O and CuO mode still can be observed. This means that in the surface and bulk of the catalyst material, Cu(II) was not completely reduced to Cu(0) by the end of reduction sweep. Similar to the XPS spectra Figure 4-2, not all of Cu(II) is reduced, around 85% of surface Cu(II) was converted to Cu(I)/Cu(0).

It is well known that vibrations or rotations are essential to change the polarizability of the molecule or material, which is the source of the Raman activity [10]. Since metals are infinitely polarizable, it is hard to see how the vibration of the atoms in the crystal lattice could cause a change in the polarizability [29]. So metals do not have Raman response in general. Hence regions of metallic copper Cu(0) could not show Raman bands. Therefore for the samples, it is not clear whether Cu(II) is reduced to Cu(0) as evidence for this would not be available from Raman spectra.

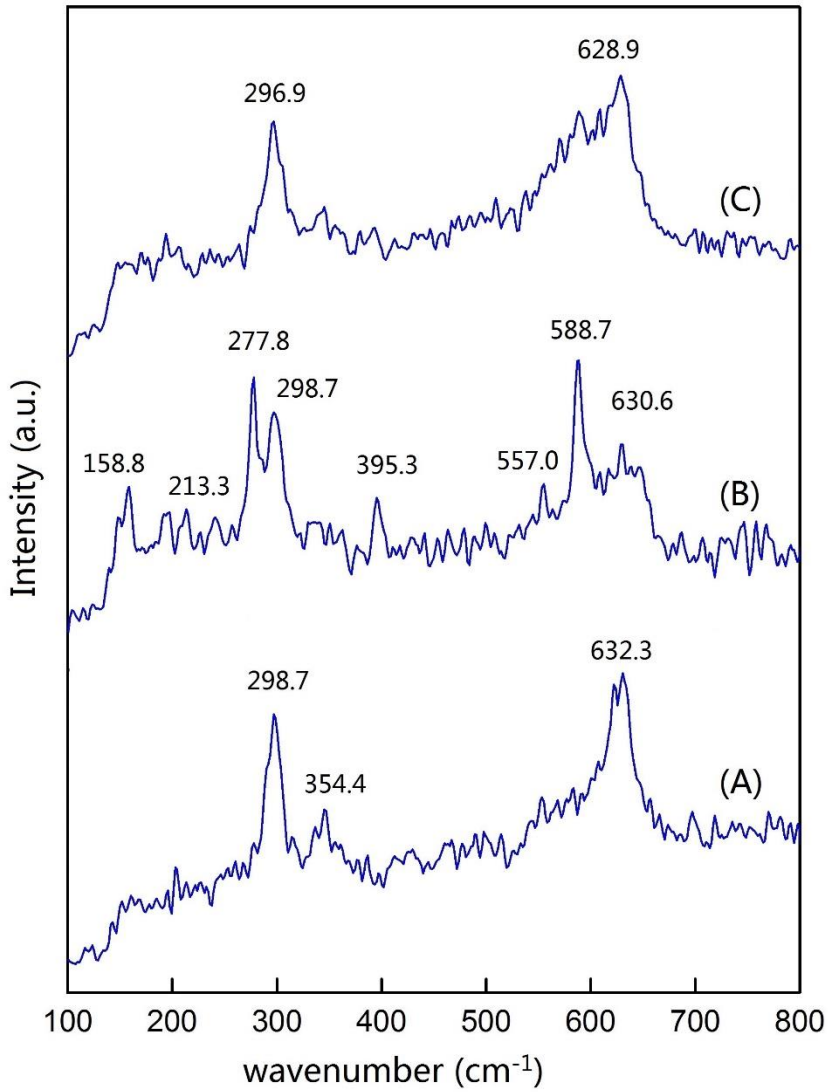

Figure 4-10. Raman spectra for the electrode in pH 7 Ar deoxygenated PBS after: (A) holding 15 minutes at -0.4 V; (B) 1 cycle; (C) 10 cycles. For (B) and (C) the potential was scanned from 0→-1.2→0.4→0 V vs. Ag/AgCl. υ=100 mV·s^{-1}.

The Figure 4-10 shows the Raman spectra for the electrode holding potential at -0.4 V (A), after 1 full cyclic sweep (B) and after 10 cycles (C). The cyclic potential starts at

0 V, the first switching potential is -1.2 V, the second switching potential is 0.4 V, and ends at 0 V. For the sample after holding potential for 15 minutes at -0.4 V, three peaks at 298.7, 345.4 and 632.3 cm^{-1} are attributed to CuO.

After one cyclic potential applied, the spectrum shows a combined peaks of CuO and Cu_2O related modes. After 10 cycles, the spectrum is again dominated by CuO modes. The presence of peaks at 296.9 and 628.9 cm^{-1} are attributed to the CuO. The Cu_2O peaks no longer exist.

The Raman spectra support the XPS results in Figure 4-2 & 3, and indicate that in the first negative sweep, both electrode surface and bulk material are involved in the reaction. However the reduction of Cu(II) is not complete, as shown by CuO existing at -1.2 V on the electrode surface in Figure 4-2 (C) and in bulk material in Figure 4-9 (C). At the end of first cycle, the reduction and oxidation are not complete in bulk, so both CuO and Cu_2O can be observed. It has been discussed in CV section 3.3 that the current magnitude increased with continued cyclic potential and then reaches a steady value, this implies steady concentration of redox species involve in the reaction after continued cycling. This reveals that the redox-active layer is first generated in the top few monolayers, then extends further into the bulk material with several potential cycles. When the current magnitude reaches its steady value, a consistent thickness redox-active surface layer is formed. Hence, after 10 cycles, active CuO can be reduced-oxidised completely.

4.2.3 Raman for pH 7 PBS in CO_2 saturated conditions

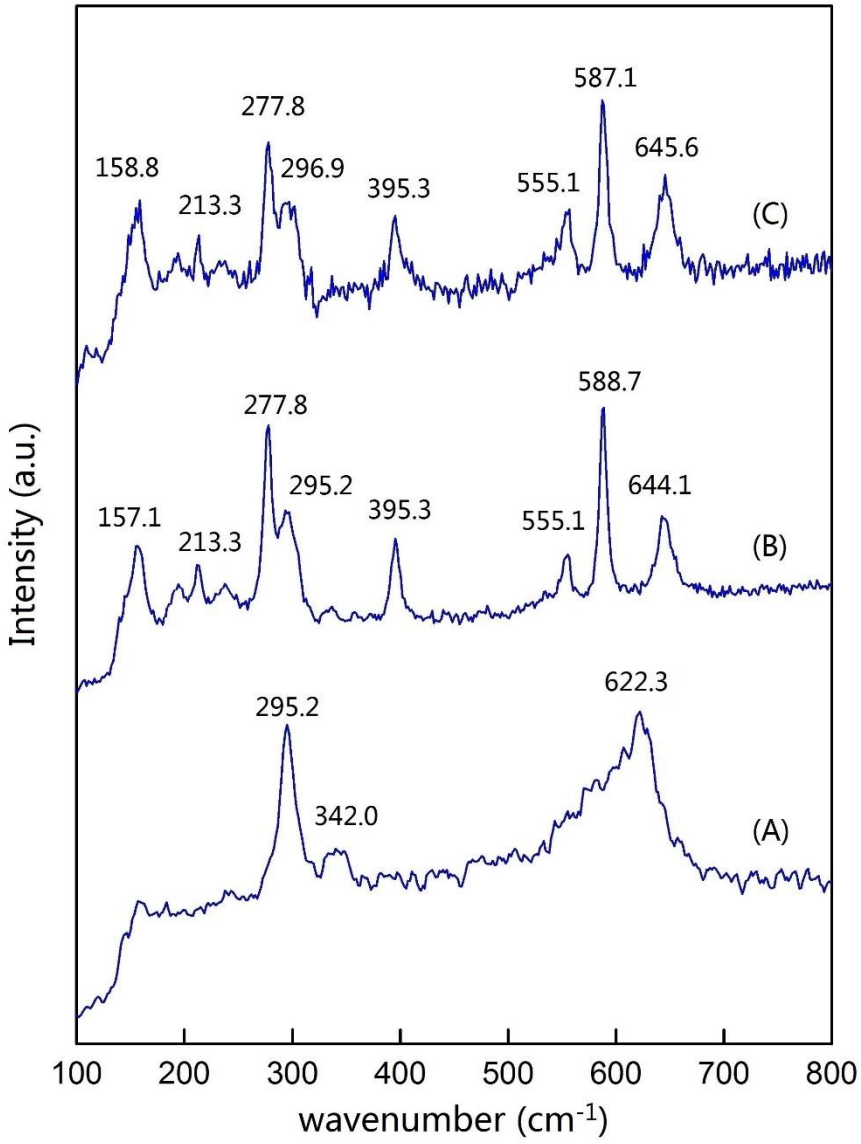

Figure 4-11. Raman spectra for the electrode after applying potential in pH 7 CO_2 saturated PBS at (A) -0.4 V; (B) -0.8 V; (C) -1.2 V.

Figure 4-11 shows the Raman spectra recorded after selected holding potential at -0.4 V, -0.8 V and -1.2 V. For the sample after holding potential for 15 minutes at -0.4 V, three peaks at 295.2, 342.0 and 622.3 cm^{-1} were attributed to CuO modes. The spectrum implies no CuO is reduced at -0.4 V in the bulk of samples.

After applied potential at -0.8 V, the presence of peaks at 157.1, 213.3, 277.8, 555.1, 588.7 cm^{-1} are associated to Cu_2O mode. The dominant of intense Cu_2O peaks

indicates the reduction of Cu(II) takes place in the bulk of the sample as well.

Similar to the spectrum in Ar deoxygenated conditions, there is not much change between -0.8 V and -1.2 V in Figure 4-9. Peaks contributed from CuO mode: 296.9, 395.3, and 645.6 cm^{-1}, still can be observed. This indicates that in the bulk of the material, Cu(II) was not reduced completely by the end of reduction sweep.

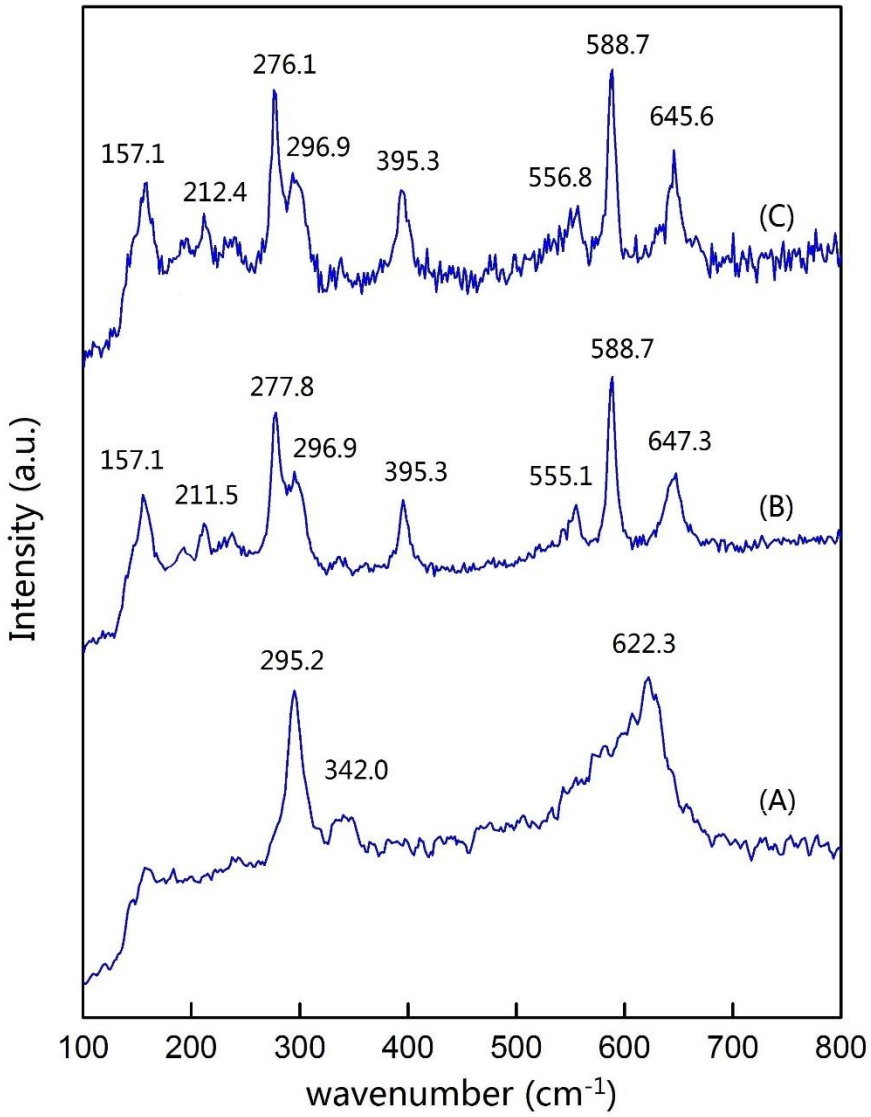

Figure 4-12. Raman spectra for the electrode in pH 7 CO_2 saturated PBS after: (A) holding 15 minutes at -0.4 V; (B) 1 cycle; (C) 10 cycles. For (B) and (C) the potential was scanned from 0→-1.2→0.4→0 V vs. Ag/AgCl. υ=100 $mV \cdot s^{-1}$.

The Raman spectra recorded after holding potential for 15 minutes at -0.4 V, after 1 full cyclic sweep and after 10 cycles are shown in Figure 4-12. The potential was

applied as 0→-1.2→0.4→0 V for cyclic sweep. For the sample after holding potential for 15 minutes at -0.4, three peaks at 295.2, 342.0 and 622.3 cm^{-1} were attributed to CuO.

After 1 cyclic potential applied, the spectrum was generated by peaks for CuO and Cu_2O related modes together. The spectrum shows not much change after 10 cycles, it is dominated by intense Cu_2O mode.

The Raman spectra give similar results compared with the XPS spectra in Figure 4-4 & 5. From Raman and XPS spectra, Cu(II) and Cu(I)/Cu(0) related peaks can be observed together at most negative potential at -1.2V. This implies not all of Cu(II) is reduced to Cu(I)/Cu(0) at -1.2 V. And after cyclic potential, not all of the formed Cu(I)/Cu(0) is oxidised back to Cu(II). This behaviour is attributed to the presence of CO_2 in the system.

4.2.4 Raman for pH 4 PBS in Ar deoxygenated conditions

Table 4-16. Raman shifts and compounds of copper oxide species on electrode after various treatment in pH 4 Ar deoxygenated PBS. Summarized from Raman spectra Figure A-13.

Sample		Raman shift cm^{-1}	Compounds
(C)	-1.2 V	150.0, 200.2, 216.8, 295.1, 397.0, 573.6, 590.4, 643.9	CuO Cu_2O
(B)	-0.8 V	157.7, 209.1, 298.0, 341.5, 561.0, 590.4, 630.6	CuO Cu_2O
(A)	-0.4 V	298.7, 341.9, 628.9	CuO

Figure A-13 shows spectra for the electrode after applied potential at -0.4 V, -0.8 V, -1.2 V in pH 4 Ar deoxygenated solution. Table 4-16 summarizes the Raman shifts in the spectra. For the sample after holding potential for 15 minutes at -0.4 V, three peaks marked by red stars corresponded to CuO in Figure A-13. The CuO material present is therefore formed uniformly on the electrode surface (seen as Figure A-1 (A)) and in the bulk of the material after applied potential at -0.4 V. With applied potential at -0.8 V, several weak peaks were attributed to Cu_2O mode, marked by green stars. After application of more negative potential of -1.2 V, the intensity of Cu_2O peaks increases

and CuO peaks decreases. More Cu(II) is reduced to Cu(I) at negative potential. The presence of both Cu_2O and CuO peaks indicates the reduction of Cu(II) was not complete in the bulk of the catalyst material.

Table 4-17. Raman shifts and compounds of copper oxide species on electrode after various treatment in pH 4 Ar deoxygenated PBS. Summarized from Raman spectra Figure A-14.

Sample		Raman shift cm^{-1}	Compounds
(C)	10 cycles	158.8, 211.5, 277.8, 293.5, 397.0, 555.1, 588.7, 645.6	CuO Cu_2O
(B)	1 cycle	157.1, 213.3, 277.8, 297.0, 397.0, 555.1, 588.7, 645.6	CuO Cu_2O
(A)	-0.4 V	298.7, 341.9, 628.9	CuO

The Figure A-14 shows the Raman spectra for the electrode holding potential at -0.4 V (A), after 1 full cyclic sweep (B), and after 10 cycles (C), in pH 4 Ar deoxygenated solution. Table 4-17 summarizes the Raman shifts and corresponding compounds from the spectra. The cyclic potential starts at 0 V, the first switching potential is -1.2 V, the second switching potential is 0.4 V, and ends at 0 V. After one potential cycle is applied, the spectrum shows a combined peaks of CuO and Cu_2O related modes. After 10 cycles, the spectrum is not changed much. This indicates the composition of the copper oxide material becomes relatively stable after the continued cycle.

In CV section 3.3, two oxidation peaks can be observed in pH 4 solution. XPS and Raman results are consistent with CV data in general. The equation 3-4 to 3-7 represent the copper species changed within the potential range.

4.2.5 Raman for pH 4 PBS in CO_2 saturated conditions

Table 4-18. Raman shifts and compounds of copper oxide species on electrode after various treatment in pH 4 CO_2 saturated PBS. Summarized from Raman spectra Figure A-15.

Sample	Raman shift cm^{-1}	Compounds

(C)	-1.2 V	162.3, 215.0, 296.9, 338.5, 597.1, 627.3	CuO Cu_2O
(B)	-0.8 V	296.9, 341.9, 625.6	CuO
(A)	-0.4 V	295.2, 340.2, 622.3	CuO

Figure A-15 shows the Raman spectra recorded after selected holding potential at -0.4 V, -0.8 V and -1.2 V in pH 4 CO_2 saturated solution. Table 4-18 summarizes the Raman shifts from the spectra. Only CuO related peaks can be observed in first two spectra. This indicates that the bulk material is not involved in the Cu(II) reduction reaction at these negative potentials, or the amount is too small to be detected. It might be explained that with CO_2 introduced in the system, the surface material undergoes with some competitive reactions besides the Cu(II) reduction reaction. In this case the Cu(II) reduction reaction could not go further from electrode surface to the bulk, so no Cu_2O mode can be observed in the bulk material. But at the more negative potential, several weak peaks of the Cu_2O mode can be observed. This is consistent with XPS spectra.

Table 4-19. Raman shifts and compounds of copper oxide species on electrode after various treatment in pH 4 CO_2 saturated PBS. Summarized from Raman spectra Figure A-16.

Sample		Raman shift cm^{-1}	Compounds
(C)	10 cycles	155.3, 213.3, 277.8, 293.5, 395.3, 555.1, 588.7, 640.6	CuO Cu_2O
(B)	1 cycle	218.6, 296.9, 340.2, 607.2, 627.3	CuO Cu_2O
(A)	-0.4 V	295.2, 340.2, 622.3	CuO

Figure A-16 shows the Raman spectra for the electrode holding potential at -0.4 V for 15 minutes (A), after 1 full cyclic sweep (B), and after 10 cycles (C), in pH 4 CO_2 saturated solution. The potential was applied as $0 \rightarrow -1.2 \rightarrow 0.4 \rightarrow 0$ V for cyclic sweep (B) and (C). It has been discussed above that bulk material may not be involved in the Cu(II) reduction at -0.8 V but some CuO was reduced at -1.2 V. So after one potential cycle is applied, the spectrum was dominated by peaks for CuO mode and several peaks with low intensity of Cu_2O mode. The spectrum shows higher intensity of Cu_2O peaks together with CuO peaks after 10 potential cycles. This shows that repeated cycling is required to produce enough Cu_2O to be detected. These results show that

the presence of CO_2 in solution dramatically slows down the rate of CuO reduction to Cu_2O.

4.2.6 Raman for pH 9 PBS in Ar deoxygenated conditions

Table 4-20. Raman shifts and compounds of copper oxide and hydroxide species on electrode after various treatment in pH 9 Ar deoxygenated PBS. Summarized from Raman spectra Figure A-17.

Sample		Raman shift cm^{-1}	Compounds
(C)	-1.2 V	178.2, 279.6, 751.7	$Cu(OH)_2$ Cu_2O
(B)	-0.8 V	300.4, 345.4, 605.5, 628.9	CuO Cu_2O
(A)	-0.4 V	293.5, 348.8, 623.9	CuO

Figure A-17 shows spectra for the electrode after applied potential at -0.4 V, -0.8 V, -1.2 V in pH 9 Ar deoxygenated solution. After holding potential for 15 minutes at -0.8 V, a barely detectable amount of Cu(II) was reduced to Cu(I). After application of more negative potential at -1.2 V, two new peaks at 178.2 and 751.7 cm^{-1} can be observed. These peaks marked by blue stars were attributed to $Cu(OH)_2$ mode [25]. One Cu_2O mode peak exists and the CuO peaks disappeared. It indicates in higher pH solution, Cu(II) species may exist as $Cu(OH)_2$, so the reduction of Cu(II) was not complete in the bulk of the catalyst material.

Table 4-21. Raman shifts and compounds of copper oxide and hydroxide species on electrode after various treatment in pH 9 Ar deoxygenated PBS. Summarized from Raman spectra Figure A-18.

Sample		Raman shift cm^{-1}	Compounds
(C)	10 cycles	189.9, 335.0, 589.2, 745.8	$Cu(OH)_2$ Cu_2O
(B)	1 cycle	151.8, 178.2, 294.6, 348.8	CuO Cu_2O $Cu(OH)_2$
(A)	-0.4 V	293.5, 348.8, 623.9	CuO

The Figure A-18 shows the Raman spectra for the electrode holding potential at -0.4 V (A), after 1 full cyclic sweep (B), and after 10 cycles (C), in pH 9 Ar deoxygenated solution. The cyclic potential for (B) and (C) starts at 0 V, the first switching potential is -1.2 V, the second switching potential is 0.4 V, and ends at 0 V. After one cyclic

potential applied, the spectrum shows CuO, $Cu(OH)_2$, and Cu_2O related modes. The intensity of CuO peaks are larger than the other two peaks. So after 1 potential cycle, Cu(II) was re-oxidised back, but existed as CuO and $Cu(OH)_2$. After 10 cycles, the spectrum show larger intensity of $Cu(OH)_2$ and Cu_2O peaks. The Raman peak at 335.0 cm^{-1} may relate to $Cu(OH)_2$. In alkaline solution, the Cu(II) reformed as $Cu(OH)_2$.

4.2.7 Raman for pH 9 PBS in CO_2 saturated conditions

Table 4-22. Raman shifts and compounds of copper oxide species on electrode after various treatment in pH 9 CO_2 saturated PBS. Summarized from Raman spectra Figure A-19.

Sample		Raman shift cm^{-1}	Compounds
(C)	-1.2 V	296.9, 340.2, 585.4, 620.6	CuO Cu_2O
(B)	-0.8 V	297.0, 343.6, 628.9	CuO
(A)	-0.4 V	295.2, 340.2, 625.6	CuO

Figure A-19 shows the Raman spectra recorded after selected holding potential at -0.4 V, -0.8 V and -1.2 V in pH 9 CO_2 saturated solution. The spectra for the electrode after applied potential at -0.4 V and -0.8 V present CuO related peaks only, and the spectrum for the sample after holding potential at -1.2 V shows small Cu_2O peak. This is similar to the spectra in pH 4 CO_2 saturated conditions. This indicates that the bulk material is not involved in the Cu(II) reduction reaction at -0.8 V in CO_2 saturated solution, and Cu(II) is reduced at more negative potential.

Table 4-23. Raman shifts and compounds of copper oxide species on electrode after various treatment in pH 9 CO_2 saturated PBS. Summarized from Raman spectra Figure A-20.

Sample		Raman shift cm^{-1}	Compounds
(C)	10 cycles	150.0, 215.0, 640.6	CuO Cu_2O
(B)	1 cycle	296.9, 343.6, 628.9	CuO
(A)	-0.4 V	295.2, 340.2, 625.6	CuO

Figure A-20 shows the Raman spectra for the electrode holding potential at -0.4 V for 15 minutes (A), after 1 full cyclic sweep (B), and after 10 cycles (C), in pH 9 CO_2

saturated solution. The potential was applied as 0→-1.2→0.4→0 V for cyclic sweep (B) and (C). After one cyclic potential is applied, the spectrum was generated by peaks for CuO mode. It has been discussed above that bulk material is involved in the Cu(II) reduction at very negative potential, so a small amount of Cu_2O was formed. After application of 1 cyclic potential, the Cu_2O may oxidise back to CuO. The spectrum shows several Cu_2O and CuO peaks after 10 cyclic potential applied, increased amount of bulk materials is reduced but not re-oxidised with repeated cycling.

4.2.8 Raman for pH 8 $KHCO_3$ solution in Ar deoxygenated conditions

Table 4-24. Raman shifts and compounds of copper oxide and hydroxide species on electrode after various treatment in pH 8 Ar deoxygenated $KHCO_3$ solution. Summarized from Raman spectra Figure A-21.

Sample		Raman shift cm^{-1}	Compounds
(D)	1 cycle	151.8, 213.3, 338.5, 405.6, 554.6, 588.8, 758.3	CuO Cu_2O $Cu(OH)_2$
(C)	-1.2 V	151.8, 213.3, 558.8, 589.6, 761.6	$Cu(OH)_2$ Cu_2O
(B)	-0.8 V	151.8, 213.3, 338.5, 405.6, 642.3, 761.6	CuO Cu_2O $Cu(OH)_2$
(A)	-0.4 V	295.2, 344.4, 635.6	CuO

Figure A-21 shows the Raman spectra recorded after selected holding potential at -0.4 V, -0.8 V, -1.2 V, and 1 full cyclic sweep in pH 8 Ar deoxygenated solution. The spectrum for the electrode after applied potential at -0.8 V shows CuO, Cu_2O and $Cu(OH)_2$ related modes. And the spectrum for the sample after holding potential at -1.2 V shows Cu_2O and $Cu(OH)_2$ peaks. This is similar to the spectra in pH 9 Ar deoxygenated conditions. After 1 cyclic potential applied, the spectrum shows CuO, $Cu(OH)_2$, and Cu_2O related modes. The intensity of $Cu(OH)_2$ peaks are larger than that of the -0.8 V sample. It implies that the Cu(II) oxidised form is $Cu(OH)_2$ rather than CuO under these conditions.

As seen in CV section 3.5, the CuO firstly reduced to Cu_2O (peak I Equation 3-8a), then further reduced. In the anodic sweep, the reduced species firstly oxidised via peak III, then oxidised to CuO (peak IV Equation 3-11a) and $Cu(OH)_2$ (peak IV Equation 3-11b). In the continued cycling, the $Cu(OH)_2$ is involved in the reduction reaction (peak I Equation 3-8b).

4.2.9 Raman for pH 8 $KHCO_3$ solution in CO_2 saturated conditions

Table 4-25. Raman shifts and compounds of copper oxide and hydroxide species on electrode after various treatment in pH 8 CO_2 saturated $KHCO_3$ solution. Summarized from Raman spectra Figure A-22.

Sample		Raman shift cm^{-1}	Compounds
(D)	1 cycle	295.2, 627.3	CuO
(C)	-1.2 V	148.2, 213.3, 541.6, 640.0	CuO Cu_2O
(B)	-0.8 V	295.2, 340.2, 625.6	CuO $Cu(OH)_2$
(A)	-0.4 V	296.9, 350.5, 625.6	CuO

Figure A-22 shows the Raman spectra recorded after selected holding potential at -0.4 V, -0.8 V, -1.2 V and 1 full cyclic sweep in pH 8 CO_2 saturated solution. The spectrum for the electrode after applied potential at -0.8 V presented $Cu(OH)_2$ related peak. And the spectrum for the sample after holding potential at -1.2 V showed Cu_2O peaks. This means that Cu(II) in $Cu(OH)_2$ was reduced to Cu_2O and/or Cu. After 1 cyclic potential applied, the spectrum was generated by peaks for CuO mode. After application of 1 potential cycle, the Cu_2O and maybe Cu was oxidised back to CuO. This is different from the spectrum in Ar deoxygenated solution with same pH value, which implies CuO catalyst has different chemical behaviour with the presence of CO_2 in electrolyte.

4.2.10 Discussions

It can be observed from the Raman spectra that the CuO is reduced to Cu_2O, then oxidised back to CuO in pH 4 and pH 7 solutions. In higher pH value solution, pH 8 and pH 9, some of the CuO is reduced to Cu_2O at negative potential and then oxidised to $Cu(OH)_2$ after 1 cyclic potential. The Raman spectra give evidence that the corresponding reaction equations are influenced by different pH solutions, which have

been proposed in the CV section. The Raman spectra also show the different reduction behaviour in Ar deoxygenated solutions and CO_2 saturated solutions. To be more specific, at -0.8 V, Cu_2O related bands can be observed in all pH solutions in Ar deoxygenated conditions, but not in CO_2 saturated conditions (except in pH 7). This is consistent with XPS results — less Cu(II) is reduced in CO_2 saturated solution than in Ar deoxygenated solution with same pH values at -0.8 V. So the Raman spectra are influenced by pH values and presence and absence of CO_2 in solution.

4.3 Summary

The results of ex situ XPS and Raman spectroscopies after electrocatalysis measurements show different information of CuO modified electrode, since the analysis depth is 3-10 nm for XPS measurement, and 1-5 μm for Raman measurement. The XPS results show the change of surface composition, while the Raman spectra show the composition of both surface and bulk of the material. In the first potential cycling, the ratio of Cu oxidation states is different between the XPS and Raman spectra. With continued application of potential, the reactions extend from surface to bulk material, and the XPS and Raman spectra show more consistency with the observed changes in the Cu oxidation states.

The XPS spectra show less Cu(II) is reduced in CO_2 saturated solution than in Ar deoxygenated solution at same pH values, which means Cu(II) reduction reaction occurs less effectively in CO_2 saturated solution. The charge passed on the electrode may not all participate in Cu(II) reduction, since the current onset is observed at less negative potential in CO_2 saturated solutions. Hence in pH 8, 9 and 11 solutions, some of the charge passed may be attributed to CO_2 related reactions. In these solutions, the proportion of Cu(II) decreases with the increasing pH value after cycled potential. So the lower pH value shows better stability of the catalyst after cyclic sweeps. The results of Raman spectra show the corresponding reaction equations are influenced by different pH solutions. CuO is reduced to Cu_2O, and oxidised back to CuO in pH 4 and 7 solutions, while oxidised to $Cu(OH)_2$ after one cyclic potential in pH 8 and 9 solutions.

References

[1] Van der Heide P. X-ray photoelectron spectroscopy: an introduction to principles and practices. John Wiley & Sons; 2011 Nov 1. p. 1-7.

[2] Nix RM. An introduction to surface chemistry. Queen Mary, University of London online resource. September 2013. [Accessed 20 July 2016]; Available from: www.chem.qmul.ac.uk/surfaces/scc/scat5_3.htm.

[3] Hofmann S. Auger-and X-ray photoelectron spectroscopy in materials science: a user-oriented guide. Springer Science & Business Media; 2012 Oct 25. p. 44.

[4] University of Illinois at Chicago. X-ray photoelectron spectroscopy: theory and practice. Fall 2014. [Accessed 20 July 2016]; Available from: physicsweb.phy.uic.edu/581/XPS%20Lecture%20Fall%2014.pdf.

[5] Palgrave R. Features of a photoemission spectrum. XPS summer school. University College London. 30 July 2015.

[6] National Institute of Standards and Technology XPS Database. 15 September 2012. [Accessed 10 March 2016]; Available from: ttp://srdata.nist.gov/xps/main_search_menu.aspx.

[7] X-ray Photoelectron Spectroscopy (XPS) Reference Pages. 2015. [Accessed 10 March 2016]; Available from: http://www.xpsfitting.com/.

[8] Hernandez J, Wrschka P, Oehrlein GS. Surface chemistry studies of copper chemical mechanical planarization. Journal of the Electrochemical Society. 2001 Jul 1;148(7):G389-97.

[9] Thermo Scientific XPS. 2016. [Accessed 10 March 2016]; Available from: http://xpssimplified.com/elements/copper.php

[10] Chalmers JM, Edwards HG, Hargreaves MD. Infrared and Raman spectroscopy in forensic science. John Wiley & Sons; 2012 Mar 5. p. 12-13, 47-50.

[11] EAG Laboratories. 2016. [Accessed 15 March 2016]; Available from: http://www.eag.com/raman/.

[12] Soukup L, Gregora I, Jastrabik L, Koňáková A. Raman spectra and electrical conductivity of glassy carbon. Materials Science and Engineering: B. 1992 Jan 15;11(1-4):355-7.

[13] Kauffman DR, Ohodnicki PR, Kail BW, Matranga C. Selective electrocatalytic activity of ligand stabilized copper oxide nanoparticles. The Journal of Physical Chemistry Letters. 2011 Jul 28;2(16):2038-43.

[14] Debbichi L, Marco de Lucas MC, Pierson JF, Kruger P. Vibrational properties of CuO and Cu_4O_3 from first-principles calculations, and Raman and infrared spectroscopy. The Journal of Physical Chemistry C. 2012 May 2;116(18):10232-7.
[15] Wang W, Liu Z, Liu Y, Xu C, Zheng C, Wang G. A simple wet-chemical synthesis and characterization of CuO nanorods. Applied Physics A. 2003 Mar 1;76(3):417-20.
[16] Xu JF, Ji W, Shen ZX, Li WS, Tang SH, Ye XR, Jia DZ, Xin XQ. Raman spectra of CuO nanocrystals. Journal of Raman Spectroscopy. 1999 May 1;30(5):413-5.
[17] Chen XK, Irwin JC, Franck JP. Evidence for a strong spin-phonon interaction in cupric oxide. Physical Review B. 1995 Nov 1;52(18):R13130.
[18] Kliche G, Popovic ZV. Far-infrared spectroscopic investigations on CuO. Physical Review B. 1990 Dec 1;42(16):10060.
[19] Rashad M, Rüsing M, Berth G, Lischka K, Pawlis A. CuO and Co3O4 Nanoparticles: synthesis, Characterizations, and Raman Spectroscopy. Journal of Nanomaterials. 2013 Jan 1;2013:82.
[20] Mao Y, He J, Sun X, Li W, Lu X, Gan J, Liu Z, Gong L, Chen J, Liu P, Tong Y. Electrochemical synthesis of hierarchical Cu_2O stars with enhanced photoelectrochemical properties. Electrochimica Acta. 2012 Feb 15;62:1-7.
[21] Compaan A, Cummins HZ. Resonant Quadrupole-Dipole Raman Scattering at the 1S Yellow Exciton in Cu_2O. Physical Review Letters. 1973 Jul 2;31(1):41.
[22] Eisermann S, Kronenberger A, Laufer A, Bieber J, Haas G, Lautenschläger S, Homm G, Klar PJ, Meyer BK. Copper oxide thin films by chemical vapor deposition: Synthesis, characterization and electrical properties. Physica Status Solidi (a). 2012 Mar 1;209(3):531-6.
[23] Yu PY, Shen YR, Petroff Y, Falicov L. Resonance Raman Scattering at the Forbidden Yellow Exciton in Cu_2O. Physical Review Letters. 1973 Feb 12;30(7):283.
[24] Dawson P, Hargreave MM, Wilkinson GR. The dielectric and lattice vibrational spectrum of cuprous oxide. Journal of Physics and Chemistry of Solids. 1973 Dec 31;34(12):2201-8.
[25] McCann LI, Trentelman K, Possley T, Golding B. Corrosion of ancient Chinese bronze money trees studied by Raman microscopy. Journal of Raman spectroscopy. 1999 Feb 1;30(2):121-32.

[26] Deng Y, Handoko AD, Du Y, Xi S, Yeo BS. In Situ Raman Spectroscopy of Copper and Copper Oxide Surfaces during Electrochemical Oxygen Evolution Reaction: Identification of CuIII Oxides as Catalytically Active Species. ACS Catalysis. 2016 Mar 11;6(4):2473-81.

[27] Niaura G. Surface-enhanced Raman spectroscopic observation of two kinds of adsorbed OH^- ions at copper electrode. Electrochimica Acta. 2000 Jul 14;45(21):3507-19.

[28] Singhal A, Pai MR, Rao R, Pillai KT, Lieberwirth I, Tyagi AK. Copper (I) oxide nanocrystals–one step synthesis, characterization, formation mechanism, and photocatalytic properties. European Journal of Inorganic Chemistry. 2013 May 6;2013(14):2640-51.

[29] Maniv T. Raman side-bands in the reflectivity from metals due to surface impurities. Le Journal de Physique Colloques. 1983 Dec 1;44(C10):C10-321.

Chapter 5

ATR-FTIR Spectroscopic Study of CuO Catalyst in Ar Deoxygenated and CO_2 Saturated Solutions

It is clear from the electrochemical and spectroscopic investigations in chapter 3 and 4 that the CuO catalyst shows different electrochemical behaviour in different pH value solutions. How the CO_2 related species are involved and reduced on the electrode cannot be determined using cyclic voltammetry and ex situ measurements. In situ IR measurement can monitor certain species adsorbed on the electrode surface under selected applied potential, hence in situ spectroelectrochemical experiments were designed and carried out.

5.1 ATR-FTIR setup

A three-electrode setup was used for in situ IR spectroelectrochemical experiments. The electrochemical cell was positioned on top of a Bruker Tensor 27 spectrometer fitted with a room temperature DLaTGS detector at 4 cm^{-1} resolution and a diamond prism operating with one reflection as the internal reflection element. Multistep amperometry measurements were used to record the current at the electrode surface via PSTrace software. The three electrodes and experimental conditions were similar to CV experiments. A Y-shape metal holder was used to support the whole cell and fix electrodes in place. The BDD electrode was polished with 0.3 μm alumina slurry and cleaned with distilled water before using. Counter electrode and reference electrode were rinsed and dried before being inserted into the cell.

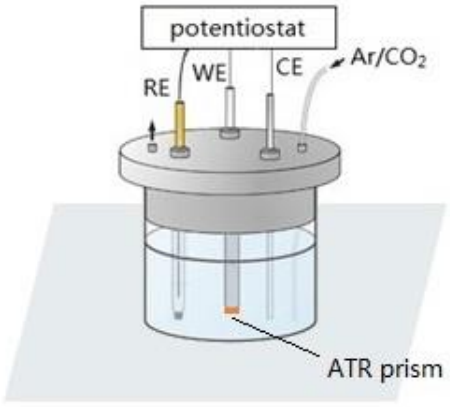

Figure 5-1. Schematic diagram of in situ electrochemical ATR-FTIR cell.

1 mL of electrolyte was pipetted into the cell, the BDD WE modified with CuO sample by drop coating was positioned directly in contact with the ATR prism, CE and RE

were placed in the cell, shown in Figure 5-1. All FTIR spectra were recorded in full wavenumbers over 400-4000 cm^{-1} in absorbance mode.

At the beginning of each measurement, a background spectrum was recorded. The background spectrum is 100 spectra of the clean and unmodified working electrode with no CuO catalyst and no applied potential in electrolyte. Then the sample spectrum was collected with the background spectra subtracted. The absorbance spectra presented throughout this chapter are the result of subtraction of the background spectrum.

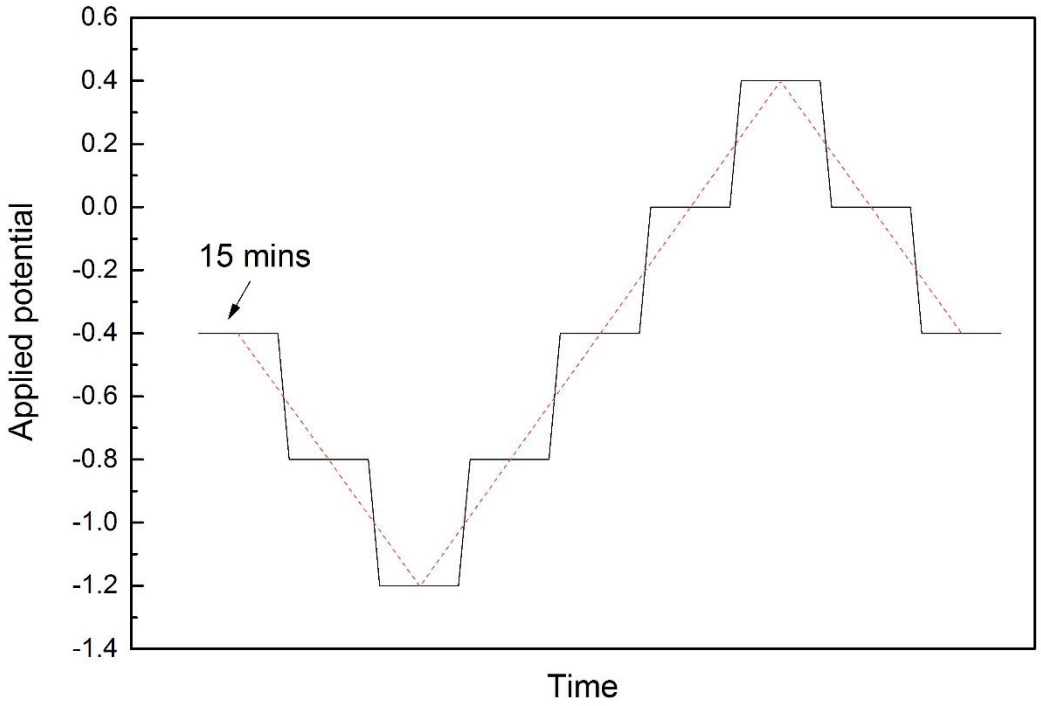

Figure 5-2. The actual applied potential vs. time in multistep amperometry measurement (black solid line) to mimic one full cyclic sweep (red dashed line). The potential was scanned from -0.4→-1.2→0.4→-0.4 V vs. Ag/AgCl.

The potential steps applied in multistep amperometry measurements are shown in Figure 5-2. Each potential step was held for 15 minutes. Before the step potential, a conditioning step of -0.4 V was applied for 5 seconds. A spectrum measurement was taken every 5 minutes, 3 FTIR spectra were collected during each potential step. A control measurement was performed where no potential was applied to the system and FTIR spectra were recorded for 2.5 hours, which is the time taken to collect the spectra using the potential step programme shown in Figure 5-2.

5.2 FTIR for pH 7 PBS in Ar deoxygenated conditions

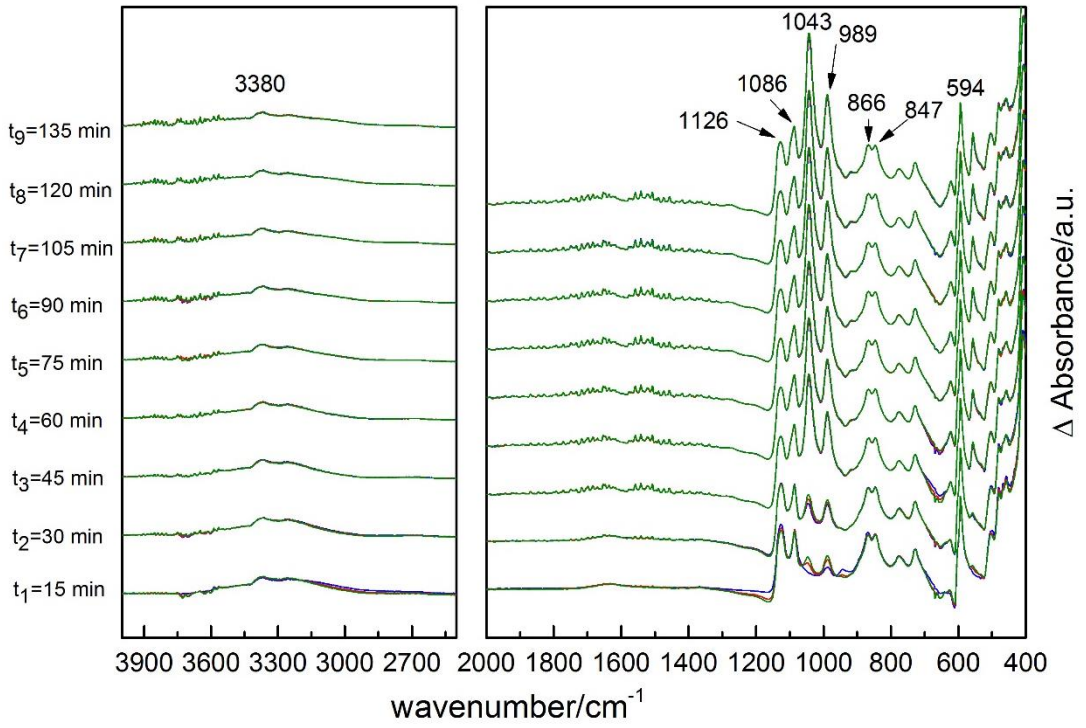

Figure 5-3. In situ FTIR absorbance difference spectra of CuO on BDD electrode in pH 7 Ar deoxygenated PBS with no applied potentials. The spectra were grouped in every 15 minutes, which is same time in each potential step: t_1=15 min, t_2=30 min, t_3=45 min, t_4=60 min, t_5=75 min, t_6=90 min, t_7=105 min, t_8=120 min, t_9=135 min. Blue, red and green line represent the first, middle and final scans.

A control measurement was carried out using CuO modified WE without applied potential during the experiment with the background spectra subtracted. Figure 5-3 shows the control experiment for the in situ FTIR measurement with no applied potentials in pH 7 Ar deoxygenated conditions. The absorbance bands were recorded at 594, 847, 866, 989, 1043, 1086, 1126 and 3380 cm^{-1}. 594 cm^{-1} is attributed to the metal-oxygen stretching of CuO [1, 2]. The electrolyte related phosphate species peaks are present at 847, 866, 989, 1043, 1086 and 1126 cm^{-1} bands [3]. The absorption bands of different phosphate species are summarized in Table 5-1.

Table 5-1. FTIR bands of different phosphate species from different literature sources.

Chemical group	Absorption bands (cm^{-1})	Reference
$H_3PO_4^0$	1172, 1005, 889	4
$H_2PO_4^-$	1159, 1077, 940, 875	4
	1291, 1165, 1074, 956	5
	1300, 1104, 1072, 1059, 824	6
HPO_4^{2-}	1078, 990, 850	4
	1077, 985, 859	5
PO_4^{3-}	1011	4
	1040	7

The broad peak at around 3380 cm^{-1} wavenumbers on the higher wavenumber region can be assigned as surface adsorbed water [8, 9]. Some increase and decrease in absorbance can be observed compared with the first spectrum. Since there is no potential applied during the measurement, any changes observed in these spectra are caused by changes to surface adsorption with time. Despite the intensities of some bands increasing, the wavenumber of the IR bands remain stable. So the increase and decrease of some IR bands implies that some time is required for the adsorbed species to achieve an equilibrium.

When potential was applied, the changes in the sample spectra are generated by surface reactions occurring as a result of applied potentials. In absorbance mode, an increase in absorbance indicates an increase in species which is adsorbed on electrode surface at that wavenumber, and decreasing absorbance indicates a decrease in concentration of species which is adsorbed at that wavenumber.

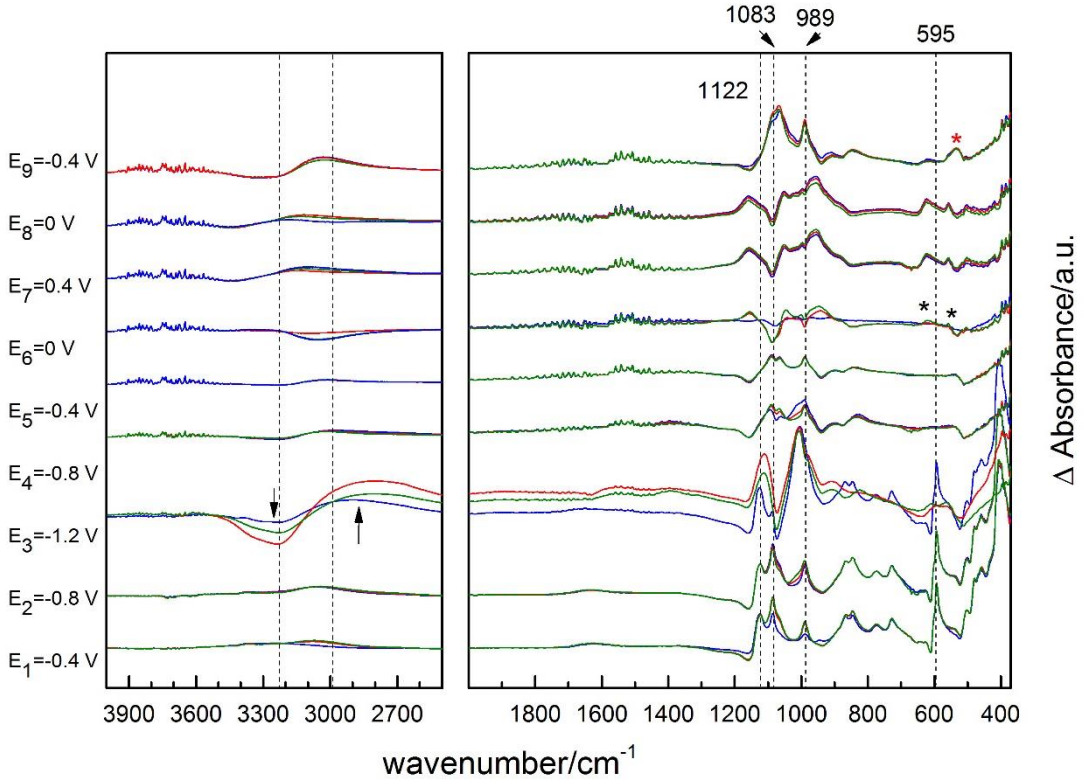

Figure 5-4. In situ FTIR absorbance difference spectra of CuO on BDD electrode in pH 7 Ar deoxygenated PBS with applied potentials. Potential steps applied: E_1=-0.4 V, E_2=-0.8 V, E_3=-1.2 V, E_4=-0.8 V, E_5=-0.4 V, E_6=0 V, E_7=0.4 V, E_8=0 V, E_9=-0.4 V. Each potential step held for 15 minutes, FTIR spectrum collected every 5 minutes, which is 3 scans in each potential stage. Blue, red and green line represent the first, middle and final scans.

FTIR absorbance spectra of CuO on BDD electrode in pH 7 PBS under Ar deoxygenated with applied potentials are presented in the Figure 5-4. Three spectra were measured for each potential step. Blue, red and green line represent the first, second and third spectrum, respectively. Spectra are split to two wavenumber ranges 400-2000 cm^{-1} and 2500-4000 cm^{-1}. The low wavenumber range contains information about phosphates and CuO related bands. The high wavenumber range contains information about water.

On applying potential at E_1=-0.4 V, absorbance increases were recorded at 3080, 1122, 1083, 989 and 595 cm^{-1}. 595 cm^{-1} has been assigned as Cu-O stretching mode. 1126, 1087, 989 cm^{-1} bands can be assigned to adsorption of phosphate related species onto

the CuO surface. Phosphate bands will be discussed in detail in the following sections in this chapter. 3080 cm^{-1} corresponds to surface bonded water species on the electrode surface [8, 10].

At E_2=-0.8 V, the intensities of the IR bands remain unchanged except the water band around 3230 and 3080 cm^{-1}, corresponding to surface adsorbed water and surface bonded water. The IR band around 3230 cm^{-1} is the water band adsorbed at the electrode surface but not bonded. The other water band at 3080 cm^{-1} is -OH band resulting from surface bonded water. The IR absorbance band at 3080 cm^{-1} increases and the band around 3230 decreases. It was speculated in chapter 3 that HER starts around this potential. Hence the decrease in absorbance at 3230 cm^{-1} wavenumber may be attributed to the HER [11]. This would result to the loss of surface adsorbed water on electrode surface, and therefore decrease of the absorbance intensity at 3230 cm^{-1}.

On the end of the cathodic sweep at E_3=-1.2 V, the peaks assigned as phosphate species show different changes. A significant increase in two peaks at 1122 and 989 cm^{-1} were observed, while the 989 cm^{-1} band shifts slightly to 1006 cm^{-1} at this potential. However, the absorbance band at 1083 cm^{-1} decreases at the same time. At the higher wavenumber region, the change of water bands appears more obviously than at previous potentials. An increase in absorbance intensity at 3000 cm^{-1} together with a huge decrease at 3230 cm^{-1} is attributed to water dissociation at this negative potential. The CuO peak at 595 cm^{-1} is clearly obtained in the first scan at this potential (blue line when E_3=-1.2 V). But this peak is missing in the following two scans at the same potential (red and green line when E_3=-1.2 V). This implies that at -1.2 V, Cu(II) is reduced to lower oxidation states with the resulting loss of the Cu-O stretch at this wavenumber. The second and third spectra at -1.2 V do not show any copper related bonding in the finger print region. The FTIR response is based on the change in the dipole moment of the molecule caused by vibrational modes [12]. Metals of course have vibrational modes but do not absorb infrared light because the vibrational frequencies of the metal bonds are beyond the measuring range of conventional FTIR spectrometer (700-6000 cm^{-1}) [13]. So metallic Cu does not have IR response in our study. It has been discussed in Figure 4-2 (C), 85% of the Cu(II) is reduced to Cu(I)/Cu(0), so the XPS spectrum is dominated by Cu(I)/Cu(0). XPS did not allow us to distinguish between the Cu(I) and Cu(0) oxidation states. However the loss of the

IR Cu(II)-O stretch without gain of Cu(I)-O stretch indicates that Cu(II) is reduced to Cu(0). In this case, Cu(II) is reduced to Cu(0) from FTIR spectra. The IR spectrum for the electrode after holding potential at -1.2 V is therefore consistent with the ex situ spectroscopic measurements in chapter 4 but provides more specific information on Cu oxidation state.

Not much change is observed in absorbance results after switching the potential to E_4=-0.8 V and E_5=-0.4 V. The peak assigned as Cu-O stretching mode disappears after the most negative potential, but we cannot find the corresponding peaks for the reduced copper species in the spectra. This may be caused by IR-inactive Cu(0) species dominating the electrode surface.

When potential applied is E_6=0.0 V, a reverse in absorbance intensities was observed at both high and low wavenumber. In phosphate bands region, 1083 and 989 cm^{-1} decrease and 1122 cm^{-1} is indistinctive, which indicates desorption of previously adsorbed phosphates on electrode surface. This is accompanied with loss of surface bonded water band region at 3000 cm^{-1}, and slight increase in the 3230 cm^{-1} band. This implies the cessation of water splitting and restructuring of surface adsorbed water at the electrode surface. The 595 cm^{-1} band is still indistinct. But two peaks at 624 and 557 cm^{-1} appear from the second spectrum at 0.0 V, marked by black stars, can be assigned as Cu(II)-O vibrations [14, 15]. This means that from -1.2 V to 0 V, Cu(0) is oxidised back to Cu(II). From CV Figure 3-3, peak III represents the oxidation of Cu(0)/Cu(I) to Cu(II), which is consistent with the FTIR spectra. The Cu-O bonding on electrode surface is modified by potential, as the Cu(II)-O peaks are at different wavenumbers from the peak at E_1=-0.4 V. Gupta and Darr examined the surface morphology of CuO nanoparticles before and after electrolysis by SEM [16]. The results of CuO SEM images show significant changes to the morphology and surface roughness after electrolysis and the size of the NPs grows from 20 nm to 50 nm [16]. It has been studied by others that change of surface morphology reflects to change of IR intensities and wavenumbers [17]. Hence the change of IR bands of Cu(II)-O stretch relates to the change of surface morphology of re-oxidised CuO particles.

At the most positive potential of E_7=0.4 V, two peaks of CuO at 624 and 557 cm^{-1} increase. More Cu(II) is oxidised back at more positive potential. There is not much

change in the spectra when potential is swept from 0.4 V to 0 V. The desorption of phosphates on CuO surface continued till -0.4 V, a similar increase in absorbance bands observed previously at the beginning of the applied potential E_1 occurred. A new peak at 534 cm^{-1} (marked by red star in Figure 5-4 E_9=-0.4V) might be the Cu(I)-O band [18] relating to the new formed Cu_2O. The CV Figure 3-3 shows peak I around this potential, which represent the reduction of Cu(II) to Cu(I). The FTIR spectra are therefore consistent with CV result. This is the end of first cycle and the beginning of the second cycle, which shows the reproducibility of the surface activity.

5.3 FTIR for pH 7 PBS in CO_2 saturated conditions

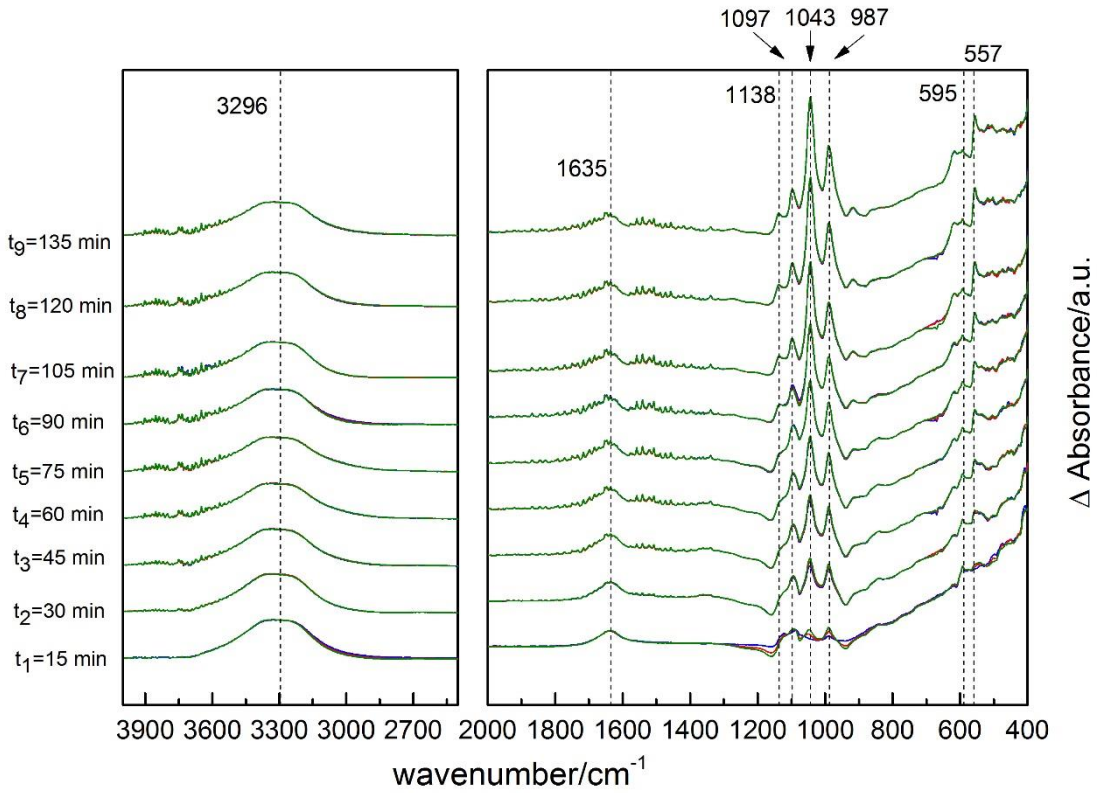

Figure 5-5. In situ FTIR absorbance difference spectra of CuO on BDD electrode in pH 7 CO_2 saturated PBS with no applied potentials. The spectra were grouped in every 15 minutes, which is same time in each potential step: t_1=15 min, t_2=30 min, t_3=45 min, t_4=60 min, t_5=75 min, t_6=90 min, t_7=105 min, t_8=120 min, t_9=135 min. Blue, red and green line represent the first, middle and final scans.

Figure 5-5 shows the control experiments for the in situ FTIR measurement with no

applied potentials in pH 7 CO_2 saturated conditions. Spectra were split to 400-2000 cm^{-1} and 2500-4000 cm^{-1} wavenumber ranges. In the first 3 spectra, a small gain in absorbance was recorded at 595, 987, 1043, 1097, 1138, 1635 and 3296 cm^{-1}. 595 cm^{-1} has been assigned as Cu(II)-O stretches. The IR band at 557 cm^{-1} increases during the experiment, which is also generated by CuO as discussed previously. The same phosphate species peaks as observed in Ar deoxygenated conditions are presented at 987, 1097 and 1138 cm^{-1} bands. According to Table 5-1, the IR band at 987 cm^{-1} is attributed to HPO_4^{2-} [4, 19]. The IR band at 1138 cm^{-1} is assigned as $H_2PO_4^-$ [4]. The IR band at 1097 cm^{-1} is generated by either HPO_4^{2-} or $H_2PO_4^-$ [4-6], and will be discussed in the following sections. One new absorbance peak at 1043 cm^{-1} is attributed to PO_4^{3-} [7]. The peak appearing at 1635 cm^{-1} is due to the C=O stretching mode [20], which is from dissolved CO_2 in the solution. The broad peak at around 3300 cm^{-1} wavenumbers on the higher wavenumber region of spectra has been assigned as surface adsorbed water. Some increase and decrease in absorbance can be observed compared the first spectrum with the second and third spectra. So the increase and decrease of some IR bands implies it needs time for electrode surface to reach equilibrium.

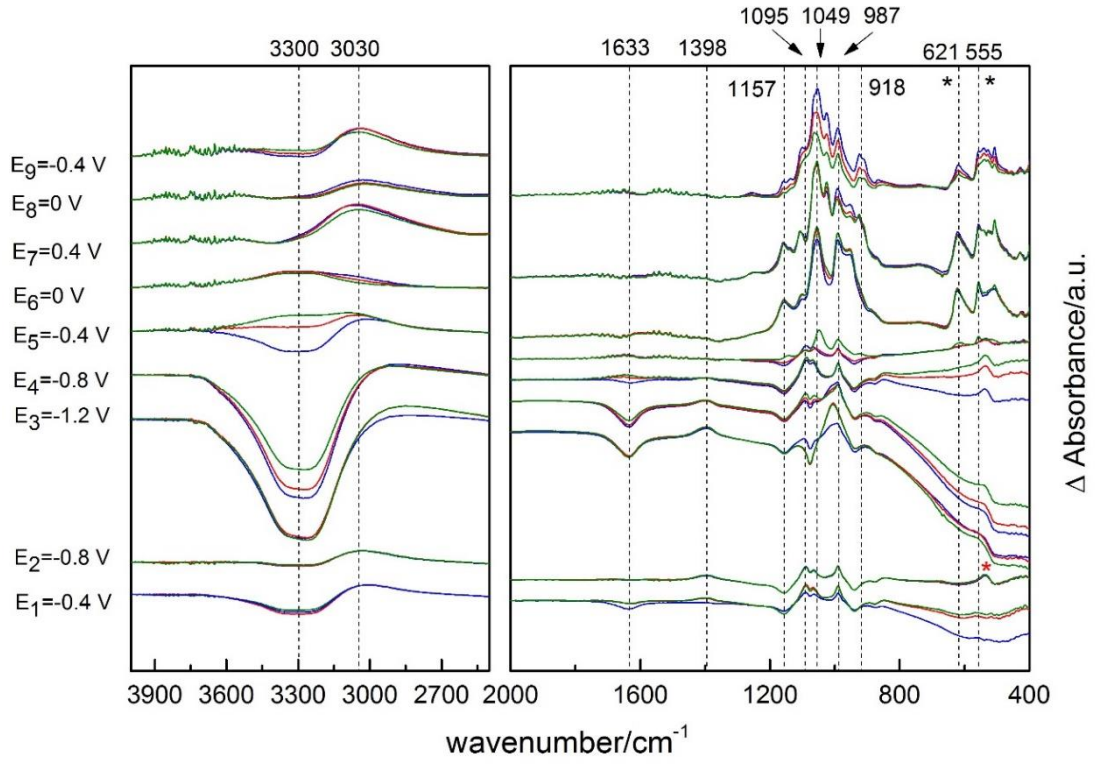

Figure 5-6. In situ FTIR absorbance difference spectra of CuO on BDD electrode in pH 7 CO_2 saturated PBS with applied potentials. Potential steps applied: E_1=-0.4 V,

E_2=-0.8 V, E_3=-1.2 V, E_4=-0.8 V, E_5=-0.4 V, E_6=0 V, E_7=0.4 V, E_8=0 V, E_9=-0.4 V. Each potential step held for 15 minutes, FTIR spectrum collected every 5 minutes, which is 3 scans in each potential stage. Blue, red and green line represent the first, middle and final scans.

Figure 5-6 shows the FTIR absorbance difference spectra of CuO on BDD electrode with applied potentials in pH 7 CO_2 saturated conditions. At E_1=-0.4 V, the absorbance bands were recorded at 987, 1049, 1095, 1157, 1398, 1633, 3030 and 3300 cm^{-1}. The IR band at 987, 1049, 1095, 1157 cm^{-1} are attributed to phosphate species. The peak appearing at 1633 and 1398 cm^{-1} is due to CO_2 related species [20, 21] from dissolved CO_2 in the solution. The broad bands at around 3300 and 3030 cm^{-1} wavenumbers have been assigned as water bands. With applied potential, there are decreases in absorbance at 1633 and increases at 1398 cm^{-1}. The changes may relate to two different carbonate species adsorbed on electrode surface, such as CO_3^{2-} and HCO_3^-.

At E_2=-0.8 V, the absorbance band at 534 cm^{-1} marked by red star relates to Cu_2O. This peak appears throughout all of the spectra till E_5=-0.4 V, which indicates the CuO is reduced to Cu_2O. In Ar deoxygenated conditions, Cu_2O peak cannot be observed until E_9=-0.4 V at the beginning of the second scan. Compared with the spectra in pH 7 Ar deoxygenated solution at E_2=-0.8 V, the CuO reduction takes place at less negative potential, similar to the result in cyclic voltammogram Figure 3-6. This is consistent with the XPS spectra for these electrodes under the same conditions. Not many changes in absorbance intensities were recorded in other IR bands.

With applied potential of E_3=-1.2 V, the water band at 3300 cm^{-1} shows significant decrease, attributed to onset of water reduction. The Cu_2O band at 534 cm^{-1} does not disappear at -1.2 V, which means the Cu_2O reduction to Cu is not complete. It has been discussed competitive processes undergo on electrode with the presence of carbonate and/or bicarbonate species in the system. Therefore the existence of Cu_2O band may relate to the applied potential and the adsorbed CO_2 related species.

After switching potential, the loss of the surface adsorbed water band at 3300 cm^{-1} becomes less apparent with less negative potential from E_4=-0.8 V to E_5=-0.4 V. The peak assigned as Cu_2O becomes smaller at E_6=0 V, and two new peaks at 555 and 621

cm^{-1} (marked by black stars) are presented from the third scan (green line). These peaks are attributed to the newly formed CuO. So the Cu(I) and/or Cu(0) formed at negative potential is oxidised to Cu(II) at positive potential.

At E_7=0.4 V, the CuO peaks increase intensively at 621 and 555 cm^{-1}. This means a large amount of Cu and/or Cu_2O were oxidised to CuO. The IR band at 3030 cm^{-1} increased. At positive potential, the electrode bonded water increases on the surface. Not many changes in IR bands are observed after the second switching potential. At the end of the first cycle, water bands have similar absorbance intensity compared with the beginning of the experiment. Besides, the distinct CuO bands that appear after the sample is re-oxidised at positive potential shows the reproducibility and surface activity of the catalyst material in the experimental conditions.

5.4 FTIR for pH 4 PBS in Ar deoxygenated conditions

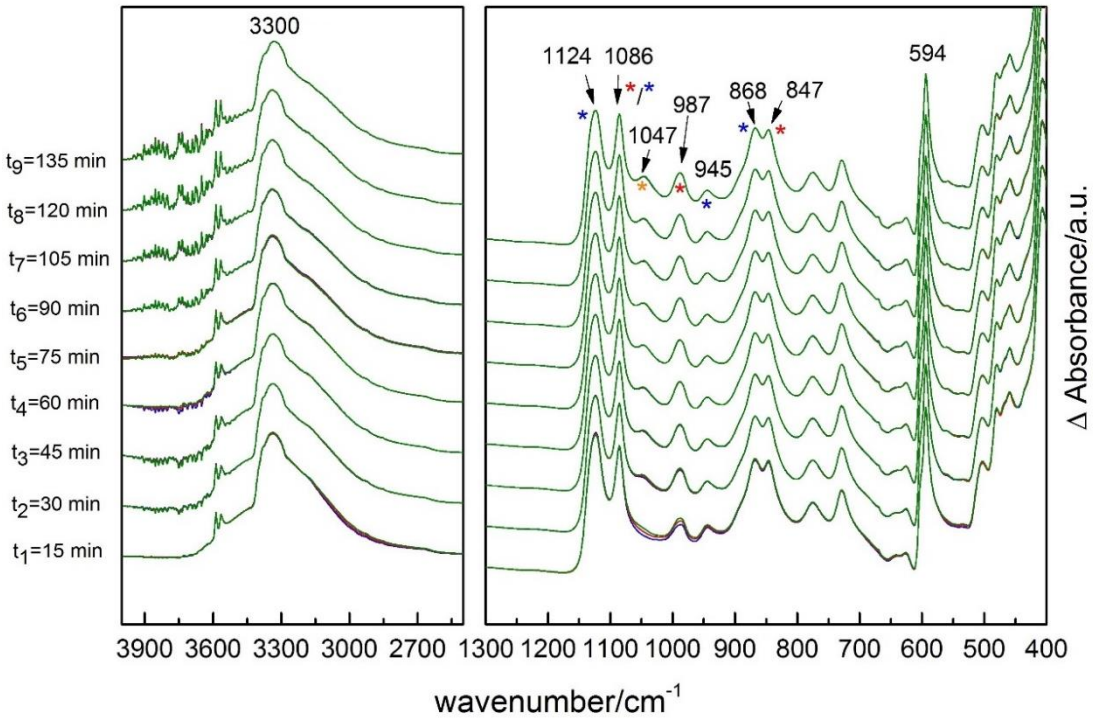

Figure 5-7. In situ FTIR absorbance difference spectra of CuO on BDD electrode in pH 4 Ar deoxygenated PBS with no applied potentials. The spectra were grouped in every 15 minutes, which is same time in each potential step: t_1=15 min, t_2=30 min,

t_3=45 min, t_4=60 min, t_5=75 min, t_6=90 min, t_7=105 min, t_8=120 min, t_9=135 min. Blue, red and green line represent the first, middle and final scans.

Control experiments for the in situ FTIR measurement in pH 4 Ar deoxygenated solution were carried out with no applied potentials. An unmodified electrode with no potential in electrolyte was recorded as a background spectrum. The results of the control experiment are presented in Figure 5-7. Since time is the only variable in this control experiment, any changes observed in spectra are caused by time parameter. In the first three spectra, slight increase and decrease in absorbance bands can be observed around 1000 cm^{-1} over time. This means the electrode surface adsorb and/or desorb some species in this absorbance region, which indicates that it takes time for the electrode surface to reach an equilibrium state. The other peaks stay quite stable throughout the experiment, except one peak at 1047 cm^{-1} grew over time.

In the lower wavenumber region, several peaks recorded from 1250-800 cm^{-1} range can be assigned to adsorption of phosphate species on the CuO surface. The absorbance band at 594 cm^{-1} is attributed to CuO. In the higher wavenumber region, the broad band at 3300 cm^{-1} is water band, corresponding to surface adsorbed water.

To be more specific, 3 different kind of phosphate species are present in buffer solution, PO_4^{3-}, HPO_4^{2-}, and $H_2PO_4^-$. The IR band at 1047 cm^{-1}, marked by orange star, is attributed to PO_4^{3-} [7]. The absorbance peaks at 1086, 987, and 847 cm^{-1}, marked by red star, is assigned as HPO_4^{2-} [4] The peaks at 1124, 1086, 945, and 868 cm^{-1}, marked by blue star, is assigned as $H_2PO_4^-$ [4]. The peak at 1086 cm^{-1} wavenumber has been marked twice. It is hard to assign at this stage, because the HPO_4^{2-} and $H_2PO_4^-$ species have similar wavenumber in this region, but will be discussed in the following sections.

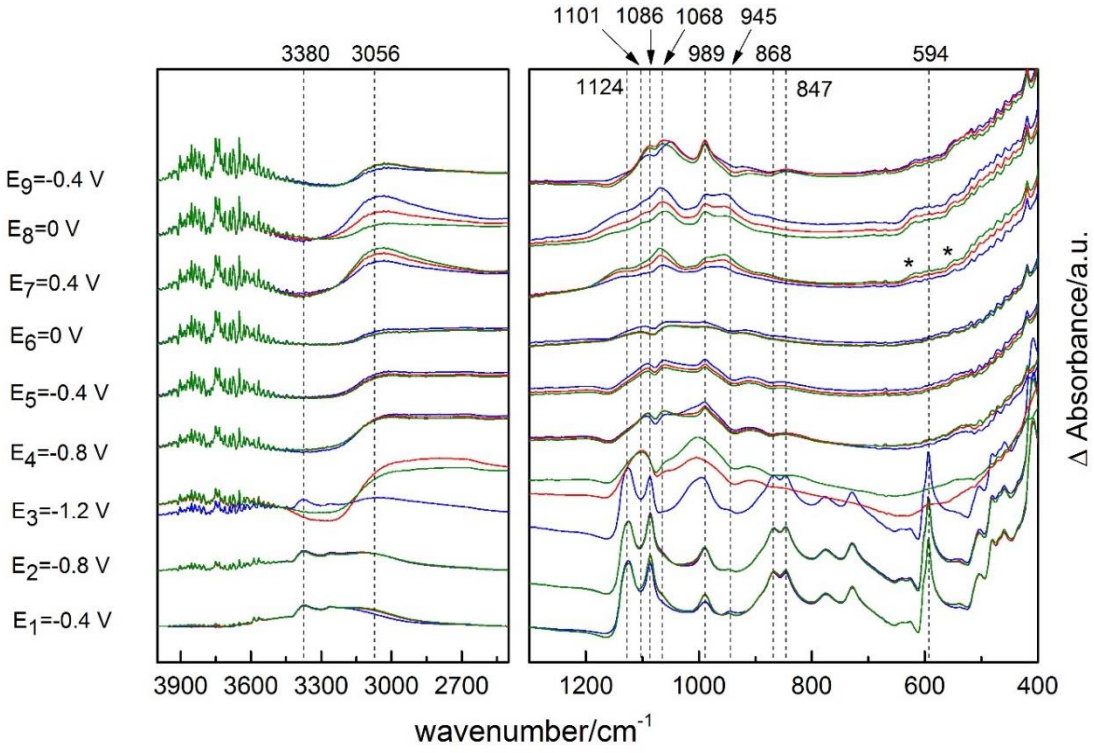

Figure 5-8. In situ FTIR absorbance difference spectra of CuO on BDD electrode in pH 4 Ar deoxygenated PBS with applied potentials. Potential steps applied: E_1=-0.4 V, E_2=-0.8 V, E_3=-1.2 V, E_4=-0.8 V, E_5=-0.4 V, E_6=0 V, E_7=0.4 V, E_8=0 V, E_9=-0.4 V. Each potential step held for 15 minutes, FTIR spectrum collected every 5 minutes, which is 3 scans in each potential stage. Blue, red and green line represent the first, middle and final scans.

FTIR absorbance difference spectra of CuO on BDD electrode in pH 4 Ar deoxygenated solution with applied potentials are presented in the Figure 5-8. Spectra were split to two wavenumber ranges 400-1300 cm^{-1} and 2500-4000 cm^{-1}.

On applying potential E_1=-0.4 V, absorbance peak were recorded at 3380, 1124, 1086, 989, 868, 847, and 594 cm^{-1}. IR band at 3380 cm^{-1} corresponds to surface adsorbed water. Absorbance peaks at 1124, 1086, 945 and 868 cm^{-1} are contributed by $H_2PO_4^-$. IR peaks at 989 and 847 cm^{-1} are assigned as HPO_4^{2-} peaks. The peak at 594 cm^{-1} can be assigned as CuO.

At E_2=-0.8 V, the intensities of the IR bands remain unchanged. With applied potential at E_3=-1.2 V, the spectra show obvious changes. The first scan, marked by blue line,

is not changed much from that at -0.8 V, while the huge difference can be observed on the second and third spectrum. In the higher wavenumber region, the absorbance band at 3300 cm^{-1} decreased along with increased absorbance intensity at 3050 cm^{-1} from the second scan, which is attributed to water dissociation at this potential. In the lower wavenumber region, the IR bands at 1101 and 1068 cm^{-1} appear. The absorbance peak at 989 shifts to 1005 cm^{-1}. IR peaks 1124, 1086, 868 and 847 cm^{-1} were no longer present. This means that the previous adsorbed $H_2PO_4^-$ was desorbed, and electrode adsorbed HPO_4^{2-} and PO_4^{3-} on the surface. The adsorption and desorption of phosphate bands implies that at different potential, the electrode adsorbs different phosphate species. The IR band at 1124 and 1086 cm^{-1} changed concurrently, so the 1086 cm^{-1} along with the 1124 cm^{-1} band are attributed to $H_2PO_4^-$ rather than HPO_4^{2-}. The IR band of Cu-O stretching mode at 594 cm^{-1} is clearly observed on the first spectrum but disappeared in the following two spectra. As no Cu_2O band can be observed in the spectra, this implies that Cu(II) is reduced to Cu(0).

At E_4=-0.8 V and E_5=-0.4 V, the intensity difference was smaller between two water bands in the high wavenumber region. The intensity of HPO_4^{2-} peaks at 1101 cm^{-1} decreased, and the IR band at 1005 shifts back to 989 cm^{-1}. The HPO_4^{2-} species is therefore no longer adsorbed on electrode surface at higher potentials. Although small, the PO_4^{3-} peak remain stable at these potentials. At E_6=0 V, the intensity difference was even smaller for the two water bands. All IR peaks in the lower wavenumber region are indistinct at zero potential.

At positive potential E_7=0.4 V, the absorbance band at 3056 cm^{-1} increased and 3300 cm^{-1} decreased over time at same potential, which means more adsorbed water are bonded on electrode surface at positive potential. The IR peaks for phosphate species appeared at 1124, 1068, 989 and 945 cm^{-1}. The relative intensity of 1068 cm^{-1} band for PO_4^{3-} peak is the highest among other peaks. Two new peaks at 615 and 552 cm^{-1} band, marked by black stars, become distinctive at this potential. This might be Cu(II)-O species formed through re-oxidation of Cu(0).

When the potential was decreased to E_8=0 V, the intensity of surface bonded water band decreased with spectrum number. The peaks at 1124, 1068, 989 and 945 cm^{-1} also decrease with increasing time. So the electrode desorbed three phosphate species

when the electrode is applied from 0.4 V to 0.0 V.

At E_9=-0.4 V, the water bands are not changed. The intensity of the IR peaks for three phosphate species increased, but the relative intensity was smaller than at applied potential E_1. The IR bands for Cu(II) disappeared, indicating it might be reduced to Cu(I)/Cu(0).

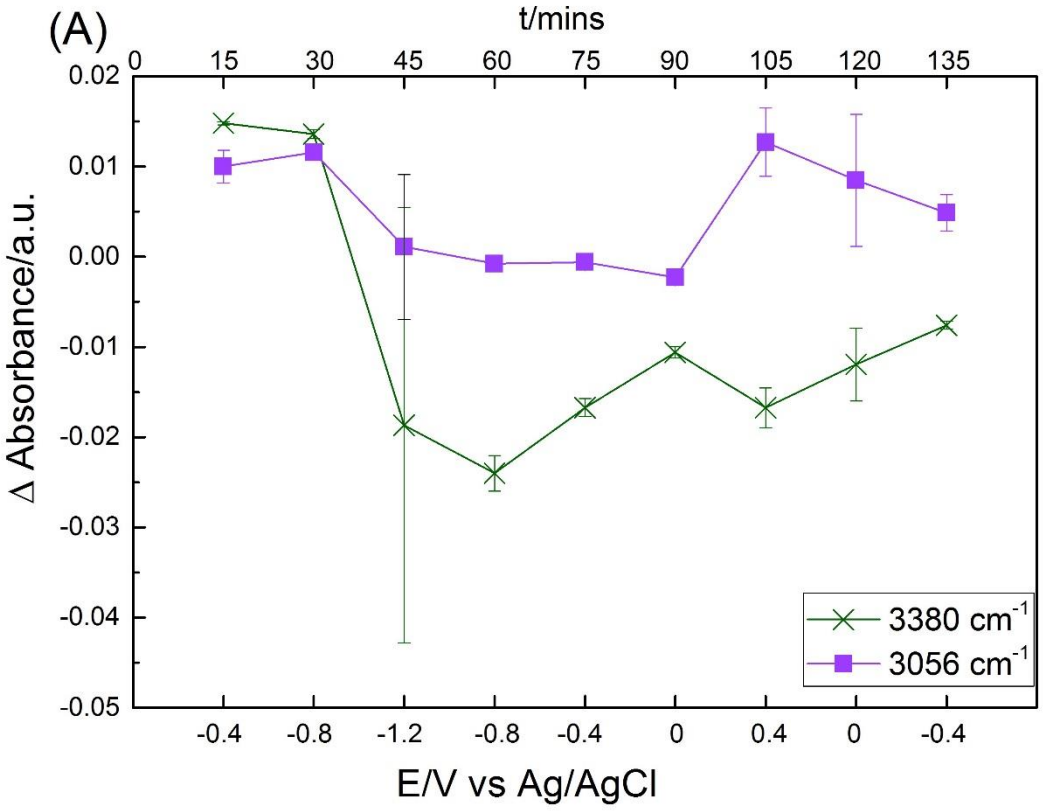

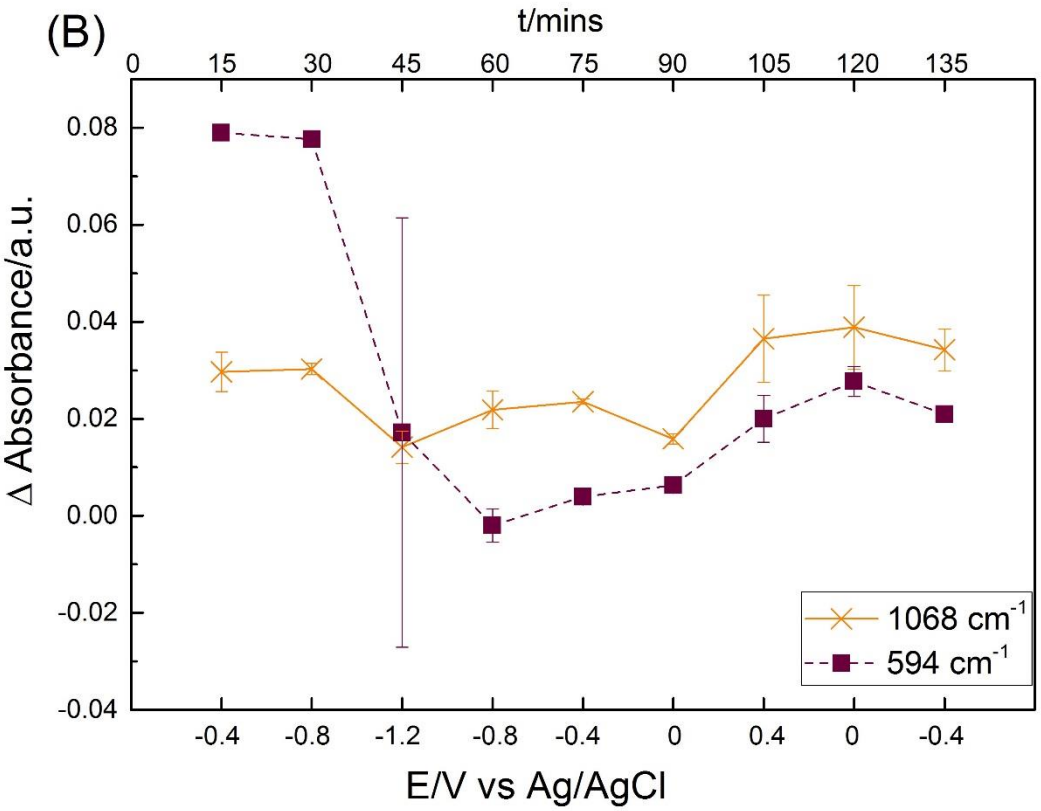
(B)
t/mins
0
15
30
45
60
75
90
105
120
135
0.08
0.06
0.04
0.02
0.00
-0.02
-0.04
Δ Absorbance/a.u.
-0.4
-0.8
-1.2
-0.8
-0.4
0
0.4
0
-0.4
E/V vs Ag/AgCl
1068 cm-1
594 cm-1

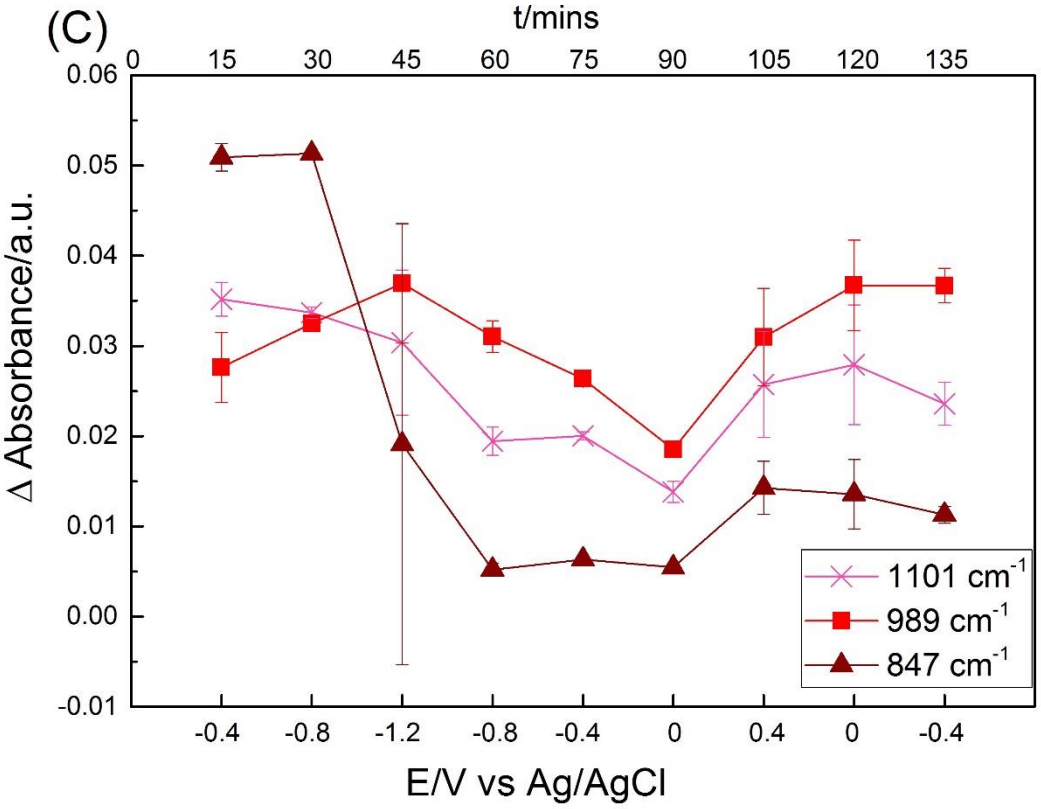
(C)
t/mins
0
15
30
45
60
75
90
105
120
135
0.06
0.05
0.04
0.03
0.02
0.01
0.00
-0.01
Δ Absorbance/a.u.
-0.4
-0.8
-1.2
-0.8
-0.4
0
0.4
0
-0.4
E/V vs Ag/AgCl
1101 cm-1
989 cm-1
847 cm-1

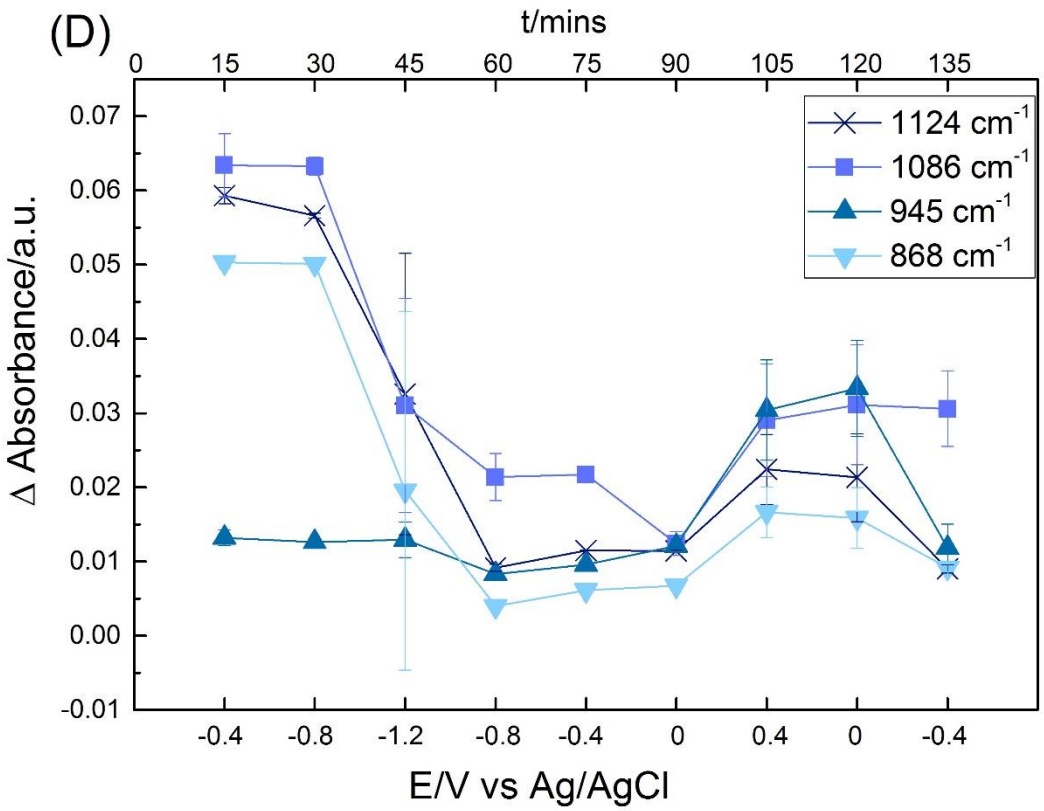

Figure 5-9. The intensity of the IR peaks as a function of time and potential plot from in situ FTIR absorbance difference spectra of CuO on BDD electrode in pH 4 Ar deoxygenated PBS. (A) water bands, (B) the orange line represents PO_4^{3-}, the brown dashed line represents Cu(II)O, (C) HPO_4^{2-} bands, (D) $H_2PO_4^-$ bands.

To discuss the dependency of the IR bands which were described above, Figure 5-9 shows how the intensity of different IR bands changes with applied potentials in Ar deoxygenated solution. The four figures were grouped by species. The 5-8 (A) shows the IR bands at 3380 and 3056 cm^{-1}, the intensity of two peaks reflect the surface adsorbed water and surface bonded water. In the negative sweep from -0.4 V to -1.2 V, the two water bands decreased together, but the electrode surface lost more adsorbed water, since the HER takes place at negative potential. After switching potential, the trend of two bands is negatively correlated with each other in general. After one cycle, the relative intensity of surface bonded water did not reduce much, but surface adsorbed water decreased obviously.

The solid lines in Figure 5-9 (B, C, D) give intensity details for phosphate species. The Figure 5-9 (B) shows the IR bands at 1068 cm^{-1}, related to PO_4^{3-}, (C) shows the IR

bands at 1101, 989, 847 cm^{-1}, related to HPO_4^{2-}, and (D) shows the IR bands at 1124, 1086, 945, and 868 cm^{-1}, related to $H_2PO_4^-$. The trends for different absorbance peaks in one specific species are correlated in general. In the negative sweep from -0.4 V to -1.2 V, with the highest starting absorbance intensity, $H_2PO_4^-$ decreased sharply companied by the other two phosphate species. After switching potential, $H_2PO_4^-$ and HPO_4^{2-} still decreased with forward potential, but the intensity of PO_4^{3-} had a small increase. When the applied potential was E_6= 0 V, the electrode surface desorbed almost all phosphate species.

The dashed line in Figure 5-9 (B) represents the copper species 594 cm^{-1} band, corresponding to Cu(II)-O stretches. The IR peak did not change from -0.4 V to -0.8 V, then decreased steadily at lower potential. This is caused by CuO being reduced to Cu_2O and/or Cu at around -0.8 V, consistent with the CV data. The intensity of this peak stays near zero till around E_6=0.0 V, when Cu(I) could be oxidised back to Cu(II), the IR band increased at positive potentials, then decreased again at negative potentials.

5.5 FTIR for pH 4 PBS in CO_2 saturated conditions

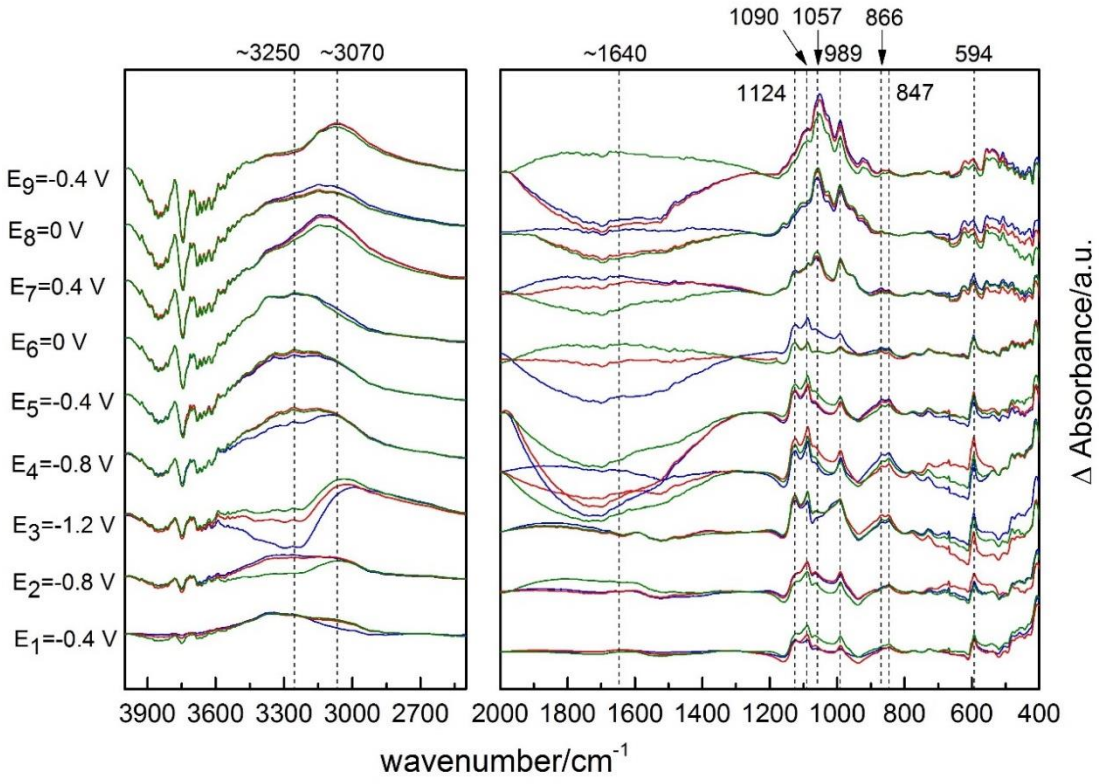

Figure 5-10. In situ FTIR absorbance difference spectra of CuO on BDD electrode in pH 4 CO_2 saturated PBS with applied potentials. Potential steps applied: E_1=-0.4 V, E_2=-0.8 V, E_3=-1.2 V, E_4=-0.8 V, E_5=-0.4 V, E_6=0 V, E_7=0.4 V, E_8=0 V, E_9=-0.4 V. Each potential step held for 15 minutes, FTIR spectrum collected every 5 minutes, which is 3 scans in each potential stage. Blue, red and green line represent the first, middle and final scans.

Figure 5-10 shows the FTIR absorbance difference spectra of CuO on BDD electrode with applied potentials in CO_2 saturated conditions. Spectra were split to 400-2000 cm^{-1} and 2500-4000 cm^{-1} wavenumber ranges. At E_1=-0.4 V, the absorbance bands were recorded at 3300, 1124, 1090, 989, 866, 847 and 594 cm^{-1}. The broad peak at around 3300 cm^{-1} band in the higher wavenumber region has been assigned as surface adsorbed water. The IR bands of phosphate bands are similar to that in Ar deoxygenated conditions, which can be assigned as adsorbed $H_2PO_4^-$ and HPO_4^{2-} on electrode surface. But the intensity of these bands are weaker in CO_2 saturated condition. The absorbance band at 594 cm^{-1} has been assigned as Cu(II)-O.

At E_2=-0.8 V, a broad peak at around 1640 cm^{-1} can be observed. This peak corresponds to C=O stretching mode from adsorbed CO_2 related species. In pH 4 solution, CO_2 is dissolved mostly as molecular CO_2 in the solution. The intensity of absorbance peaks for phosphate species (1124, 1090, 989, 866 and 847 cm^{-1}) were stable.

With the applied potential at E_3=-1.2 V, the increase at 3070 cm^{-1} and decrease at 3250 cm^{-1} band can be observed clearly. This is associated with HER at negative potential. The adsorbed CO_2 related species peak was not influenced at this potential. The intensity of phosphate species absorbance bands increased at lower potential.

After switching potential, at E_4=-0.8 V, no more HER takes place, so the 3250 cm^{-1} band increases again. The absorbance band at 1640 cm^{-1} decreases with increasing scan number, which means the electrode surface loses CO_2 related species. The adsorbed CO_2 related species may be desorbed, or may be converted to other species. A new peak at 1057 cm^{-1} grows gradually with forward potential, it has been assigned as PO_4^{3-}. The other peaks remain stable.

At E_5=-0.4 V, the water bands are not changed much. The electrode surface shows loss of CO_2 related species, as the absorbance in this region is lower than the background. But the amount lost is smaller with increasing spectrum number.

At zero potential E_6=0 V, the CO_2 related species band tend to back to the baseline with increasing number of spectra. Other phosphate bands also tend to become indistinct at zero potential. When the applied potential is stepped negative from E_7=0.4 V to E_9=-0.4 V, the electrode adsorbs phosphate species again, as the absorbance of the phosphate bands increases. The intensity of 1057 cm^{-1} band becomes dominant in this region. Also, the 989 and 1086 cm^{-1} bands are increased significantly. At this potential, the electrode adsorbs PO_4^{3-} and HPO_4^{2-} prior to $H_2PO_4^-$. The peak at 594 cm^{-1} disappears at positive potential, other changes for copper species were not clear in these spectra.

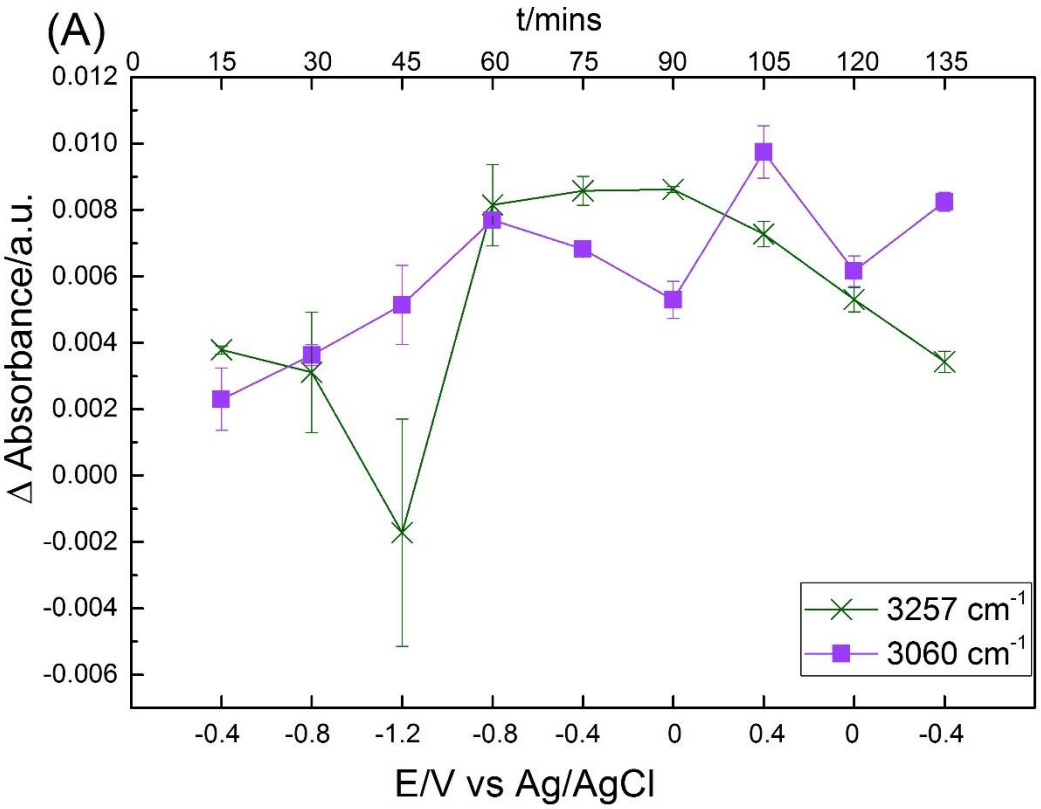

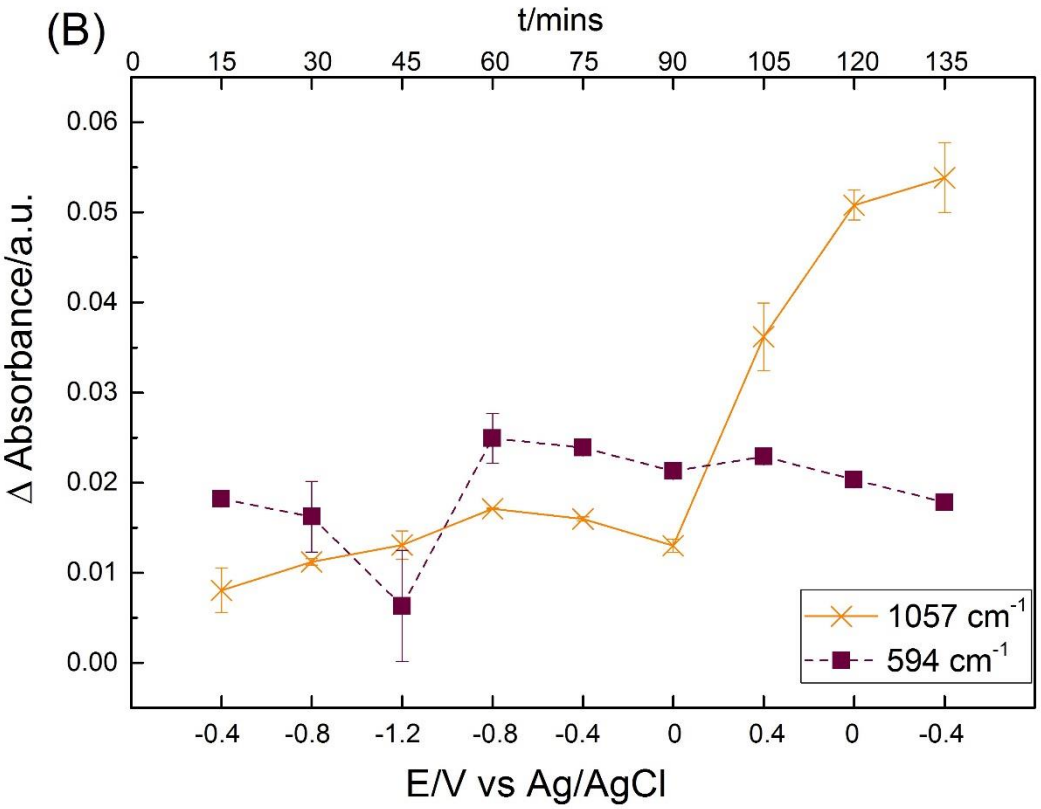
(B)
t/mins
0
15
30
45
60
75
90
105
120
135
0.06
0.05
0.04
0.03
0.02
0.01
0.00
Δ Absorbance/a.u.
1057 cm-1
594 cm-1
-0.4
-0.8
-1.2
-0.8
-0.4
0
0.4
0
-0.4
E/V vs Ag/AgCl

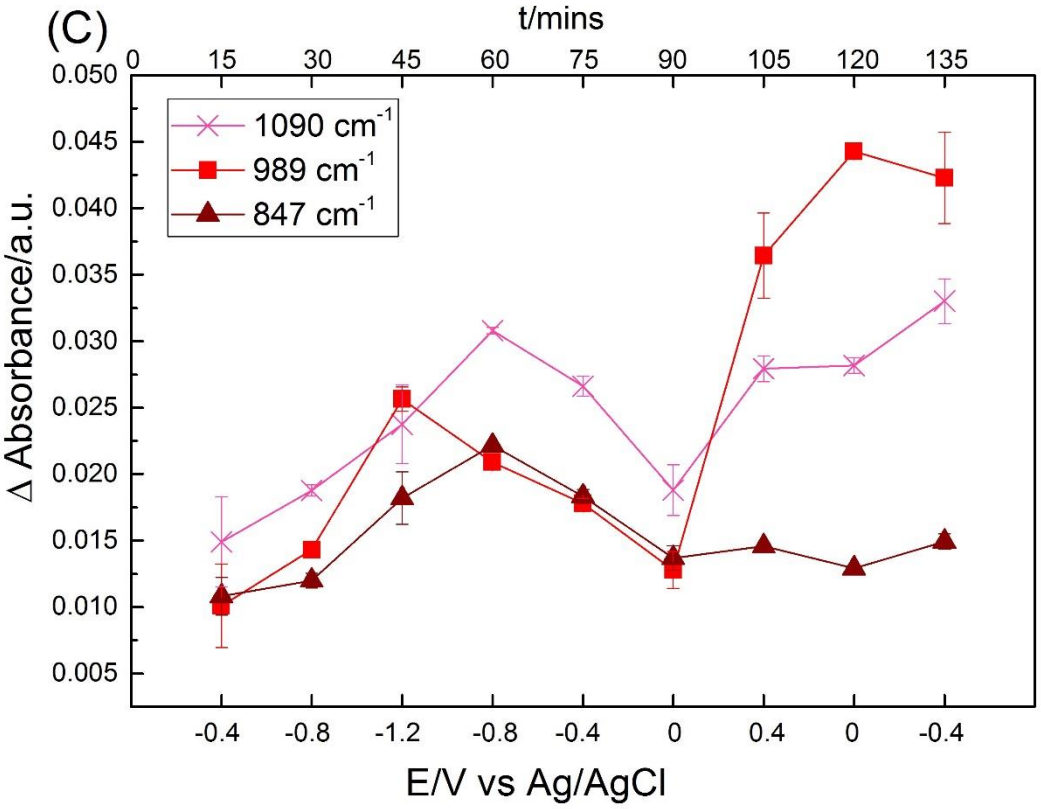
(C)
t/mins
0
15
30
45
60
75
90
105
120
135
0.050
0.045
0.040
0.035
0.030
0.025
0.020
0.015
0.010
0.005
Δ Absorbance/a.u.
1090 cm-1
989 cm-1
847 cm-1
-0.4
-0.8
-1.2
-0.8
-0.4
0
0.4
0
-0.4
E/V vs Ag/AgCl

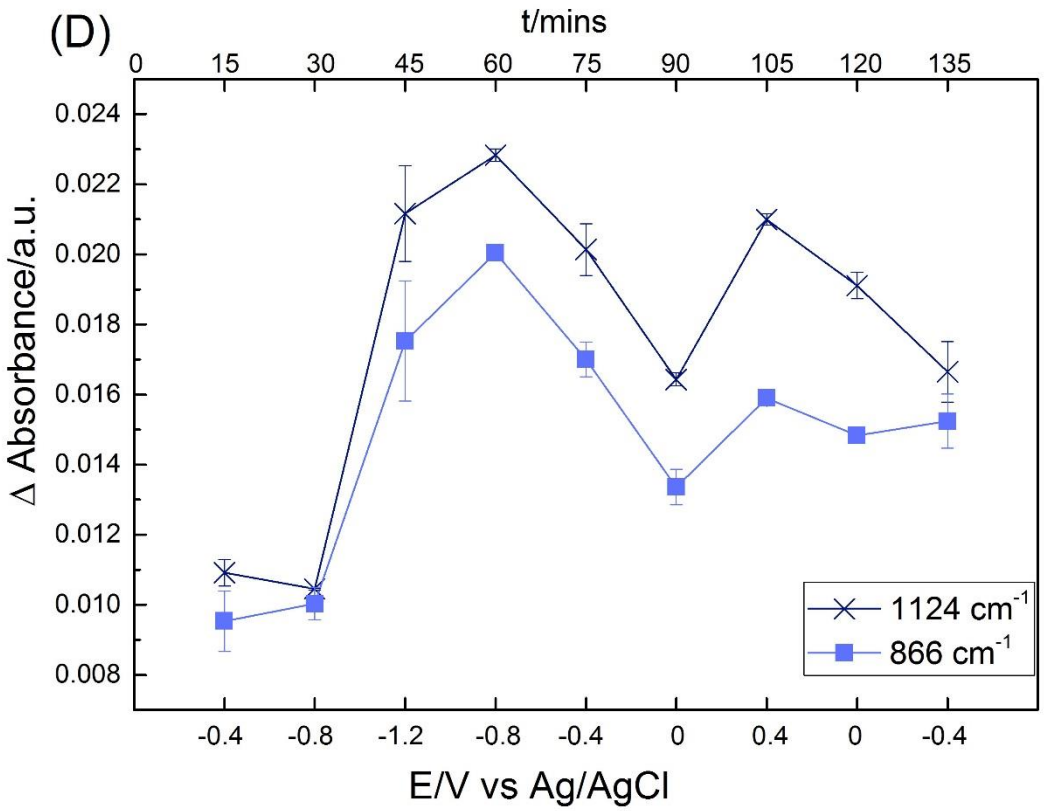

Figure 5-11. The intensity of the IR peaks as a function of time and potential plot from in situ FTIR absorbance difference spectra of CuO on BDD electrode in pH 4 CO_2 saturated PBS. (A) water bands, (B) the orange line represents PO_4^{3-}, the brown dashed line represents Cu(II)-O, (C) HPO_4^{2-} bands, (D) $H_2PO_4^-$ bands.

Figure 5-11 shows the intensity of different IR bands over time with applied potentials in CO_2 saturated solutions. Figure 5-11 (A) shows the IR bands at around 3260 and 3060 cm^{-1}, for the surface adsorbed water and surface bonded water, respectively. The 3260 cm^{-1} band decreased from -0.4 V to -1.2 V, which means the electrode surface lost the surface adsorbed water, caused by the HER. After switching potential, the 3260 cm^{-1} band increased, which implies the water splitting could not take place at higher potential. The trend of 3060 cm^{-1} band is not correlated to the 3260 cm^{-1} band at all. This is different to the relationship in Ar deoxygenated solution. Although the HER is similar under Ar deoxygenated and CO_2 saturated condition from FTIR spectra (Figure 5-9 (A) and 5-11 (A), green line), the relative intensity of the absorbance band is around one order of magnitude smaller in CO_2 saturated conditions than in the Ar deoxygenated conditions. The bonding with CO_2 related species may influence the absorbance of hydroxides under CO_2 saturated solution.

The solid lines in Figure 5-11 (B, C, D) show the information for phosphate species. The Figure 5-11 (B) shows the PO_4^{3-} IR bands at 1057 cm^{-1}, (C) shows the HPO_4^{2-} IR bands at 1090, 989, 847 cm^{-1}, and (D) shows the $H_2PO_4^-$ IR bands at 1124, 866 cm^{-1}. The trends for different absorbance peaks for one specific species (HPO_4^{2-} and $H_2PO_4^-$) are correlated in general as well. The intensity of PO_4^{3-} band increased regardless of potential. In the negative sweep -0.4→-1.2→-0.8 V, the intensities of HPO_4^{2-} and $H_2PO_4^-$ increased together. This is opposite to the Ar deoxygenated condition, where the IR bands of two species decreased at the same potential range in Figure 5-9. But it needs to be noted that at the beginning, in CO_2 saturated conditions, the magnitude of relative intensity of HPO_4^{2-} and $H_2PO_4^-$ species is around 5 times smaller than that in Ar deoxygenated conditions at E_1=-0.4 V. The difference in phosphate intensity may be caused by the competitive bonding between CO_2 related species and phosphate species. In CO_2 saturated conditions with potential applied of -0.4→-1.2→-0.8 V, the IR band of CO_2 related species decreases, allowing phosphate species to bond with electrode surface. Hence the increase in the phosphate absorbance bands is observed. The schematic progress for the adsorbed species on electrode surface is shown as Figure 5-12.

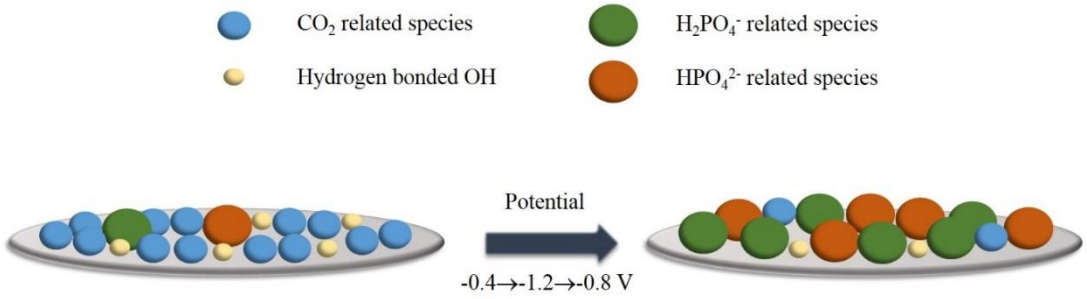

Figure 5-12. Schematic progress for adsorbed species on electrode surface with applied potential from E_1=-0.4 V to E_4=-0.8 V in pH 4 CO_2 saturated PBS.

The dashed line in Figure 5-11 (B) plots of the Cu(II) IR band at 594 cm^{-1}. It shows the IR peak did not change much from -0.4 V to -0.8 V, then decreased at lower potential. The downward trend of the 594 cm^{-1} band means the Cu(II) was reduced to Cu(I)/Cu(0). This is similar to behaviour observed in Ar deoxygenated solution.

5.6 FTIR for pH 9 PBS in Ar deoxygenated conditions

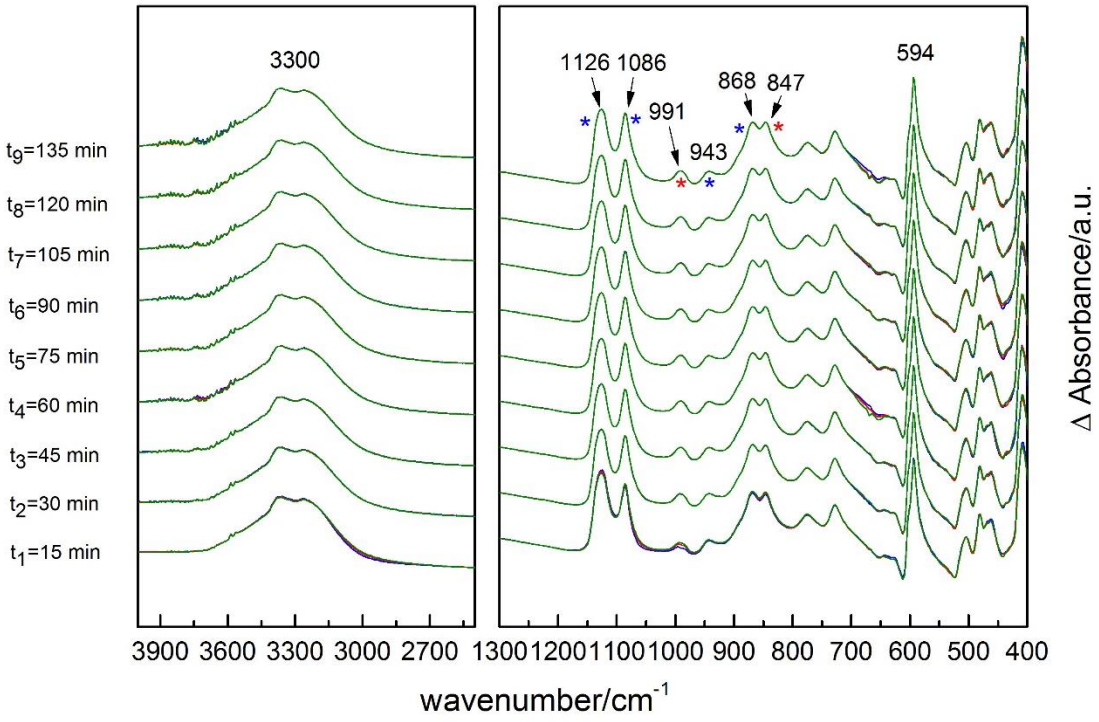

Figure 5-13. In situ FTIR absorbance difference spectra of CuO on BDD electrode in pH 9 Ar deoxygenated PBS with no applied potentials. The spectra were grouped in every 15 minutes, which is same time in each potential step: t_1=15 min, t_2=30 min, t_3=45 min, t_4=60 min, t_5=75 min, t_6=90 min, t_7=105 min, t_8=120 min, t_9=135 min. Blue, red and green line represent the first, middle and final scans.

Figure 5-13 shows the in situ FTIR spectra in pH 9 PBS under Ar deoxygenated conditions with no potential applied during the measurement. Spectra were split to two wavenumber ranges 400-1300 cm^{-1} and 2500-4000 cm^{-1}. The background scan was measured with unmodified BDD electrode. The electrode then was cleaned and coated with catalyst for the following measurement. There is more difference in the first three spectra compared with the rest of the spectra in the phosphate absorbance bands, suggesting it takes time for the electrode surface to become equilibrated with the solution.

In the higher wavenumber region, the spectra show the absorbance band in 3300 cm^{-1}, related to surface adsorbed water. In the lower wavenumber region, two different phosphate species HPO_4^{2-} and $H_2PO_4^-$ can be observed. The IR peak at 991 and 847

cm^{-1}, marked by red star, are assigned as HPO_4^{2-}. The peaks at 1126, 1086, 943, and 868 cm^{-1}, marked by blue star, are assigned as $H_2PO_4^-$. No PO_4^{3-} peak can be distinguished in pH 9 solution in this control experiment. The IR band at 594 cm^{-1} is attributed to CuO. The intensity and position of the IR peaks in this control experiment stay stable over time.

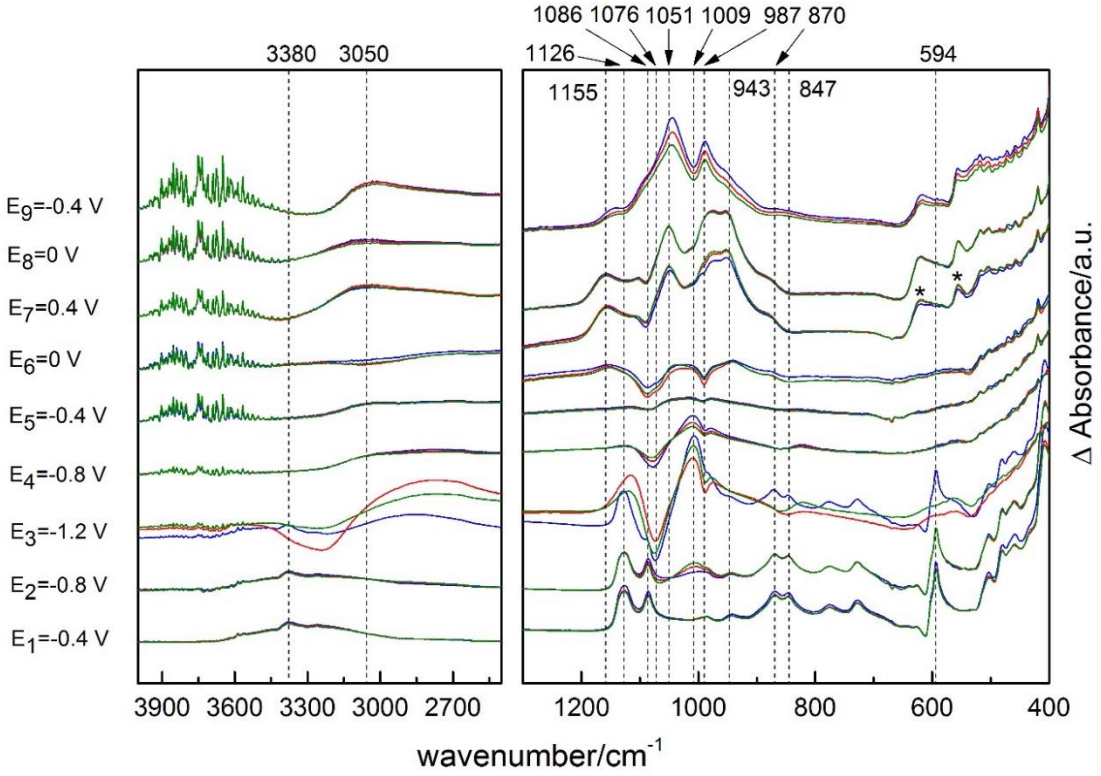

Figure 5-14. In situ FTIR absorbance difference spectra of CuO on BDD electrode in pH 9 Ar deoxygenated PBS with applied potentials. Potential steps applied: E_1=-0.4 V, E_2=-0.8 V, E_3=-1.2 V, E_4=-0.8 V, E_5=-0.4 V, E_6=0 V, E_7=0.4 V, E_8=0 V, E_9=-0.4 V. Each potential step held for 15 minutes, FTIR spectrum collected every 5 minutes, which is 3 scans in each potential stage. Blue, red and green line represent the first, middle and final scans.

Figure 5-14 presents the FTIR absorbance difference spectra in pH 9 PBS under Ar deoxygenated conditions with applied potentials. At E_1=-0.4 V, absorbance peak were recorded at 3380, 1126, 1086, 987, 943, 870, 847, and 594 cm^{-1}. IR band at 3380 cm^{-1} corresponds to surface adsorbed water. Absorbance peaks at 1126, 1086, 943 and 870 cm^{-1} are contributed by $H_2PO_4^-$. IR peaks at 987 and 847 cm^{-1} are assigned as HPO_4^{2-} peaks. The peak at 594 cm^{-1} can be assigned as CuO.

At E_2=-0.8 V, the IR band at 1009 cm^{-1} increased with number of scans. This peak can be assigned as $H_3PO_4^0$ band [4]. The intensities of the other IR bands remain unchanged.

With applied potential at E_3=-1.2 V, the spectra show obvious changes. In the higher wavenumber region, the absorbance band at 3380 cm^{-1} decreased along with increase in absorbance intensity at 3030 cm^{-1} from the second scan, which is attributed to water dissociation at this potential. In the lower wavenumber region, the IR band at 1086, 1076, 987, 943, 870 and 847 cm^{-1} decreased from the second scan and are no longer present in the end of this potential stage. The IR band at 1126 cm^{-1} remains unchanged, and the 1009 cm^{-1} band increased. This means that the previous adsorbed $H_2PO_4^-$ (1086, 943, 870 cm^{-1}) and HPO_4^{2-} (1076, 987, 847 cm^{-1}) were desorbed, and electrode adsorbed relatively more $H_3PO_4^0$ (1009 cm^{-1}) on the surface. Cu(II) peak at 594 cm^{-1} can be clearly observed on the first spectrum but disappeared in the following two spectra. This implies that Cu(II) is reduced to Cu(I)/Cu(0).

At E_4=-0.8 V, the intensity difference was less intensive between two water bands at 3380 and 3030 cm^{-1}. The intensity of HPO_4^{2-} peaks at 1076, 987 cm^{-1} decreased along with the increased $H_3PO_4^0$ absorbance bands at 1009 cm^{-1}. The peaks attributed from $H_2PO_4^-$ species cannot be observed at this potential compared with the background scan.

At E_5=-0.4 V, the spectra were flat and featureless. This implies that the absorbance species on the electrode surface are almost same as the background scan.

At E_6=0 V, the absorbance bands at 1086, 1076 and 987 decreased lower than the background level. This reveals that HPO_4^{2-} has been lost from the surface. Other IR peaks were indistinctive at zero potential.

At positive potential E_7=0.4 V, the absorbance band at 3030 cm^{-1} increased and 3380 cm^{-1} decreased, which means more surface adsorbed water bonded on electrode surface. The IR peaks for phosphate species appeared at 1155, 1051, 987 and 943 cm^{-1}. The 1051 cm^{-1} can be assigned as PO_4^{3-} peak. Two new peaks at 619 and 555 cm^{-1} band, marked by black star, might be the re-oxidised CuO from Cu(0).

Not many changes were obtained with applied potential at E_8=0 V. At E_9=-0.4 V, the IR peaks for phosphate species were dominated by 1147 and 987 cm^{-1} bands. Different to the adsorbed phosphate at same potential of E_1=-0.4 V, the main adsorbed species are PO_4^{3-} and HPO_4^{2-} at E_9=-0.4 V. The intensity of IR bands for Cu(II) decreased with the number of scans suggesting it might be reduced again.

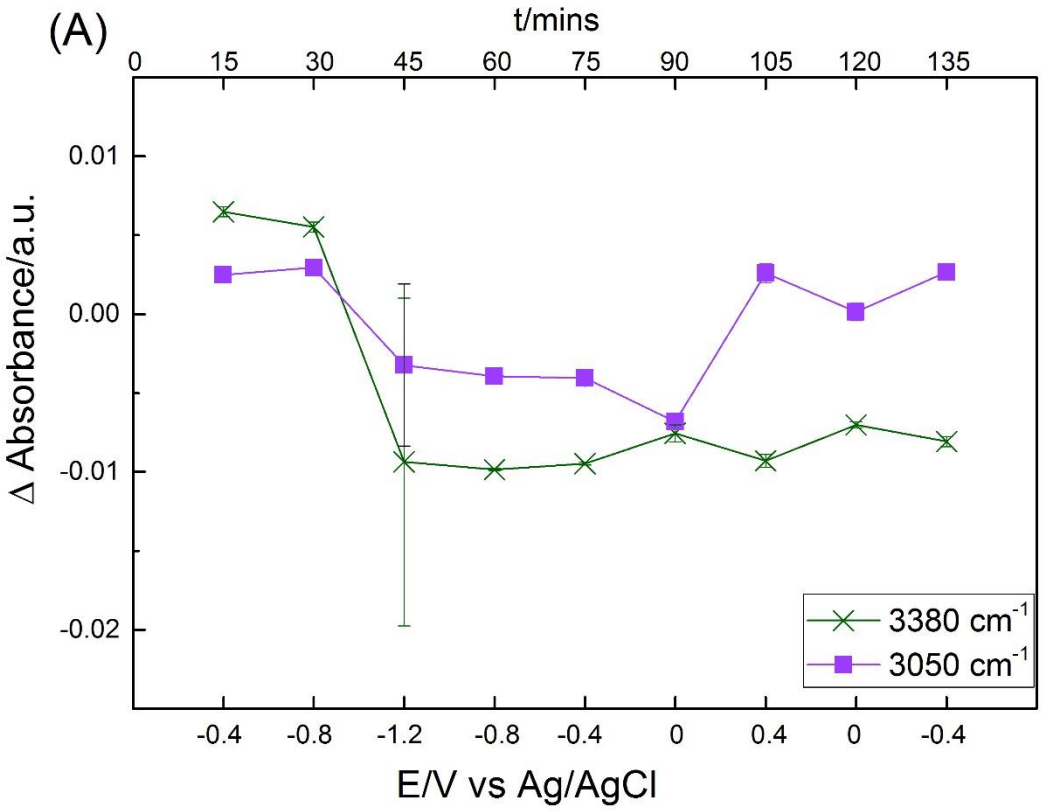

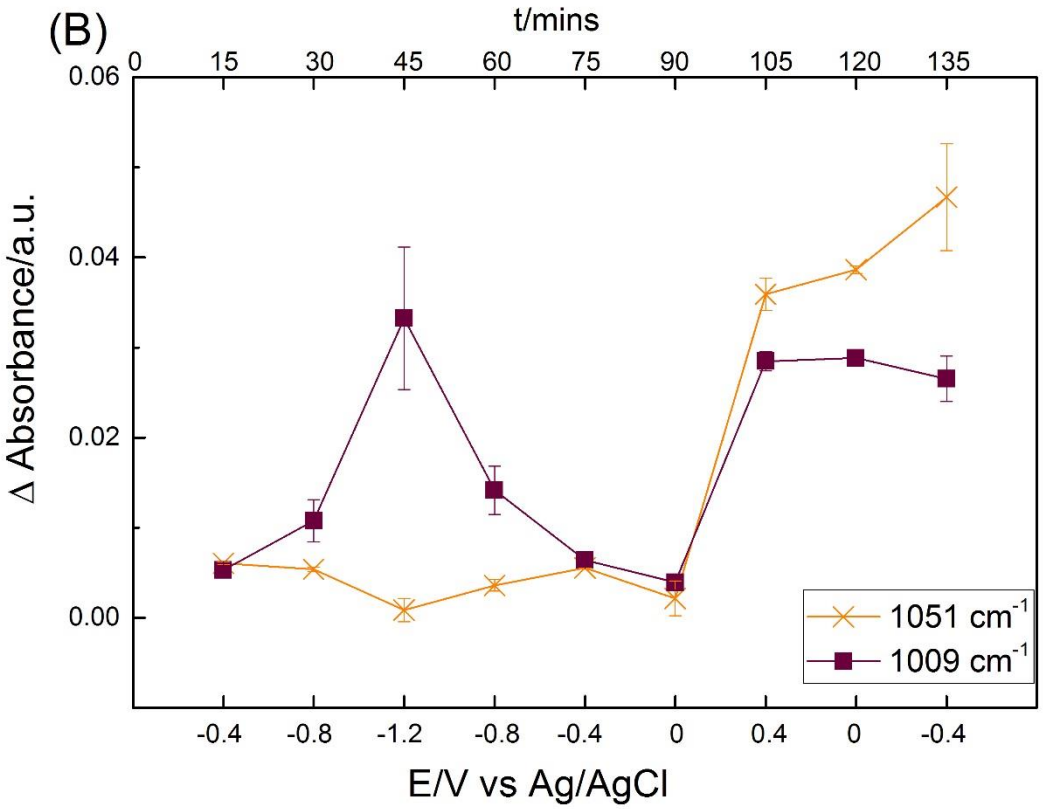
(B)
t/mins
0
15
30
45
60
75
90
105
120
135
0.06
0.04
0.02
0.00
Δ Absorbance/a.u.
1051 cm-1
1009 cm-1
-0.4
-0.8
-1.2
-0.8
-0.4
0
0.4
0
-0.4
E/V vs Ag/AgCl

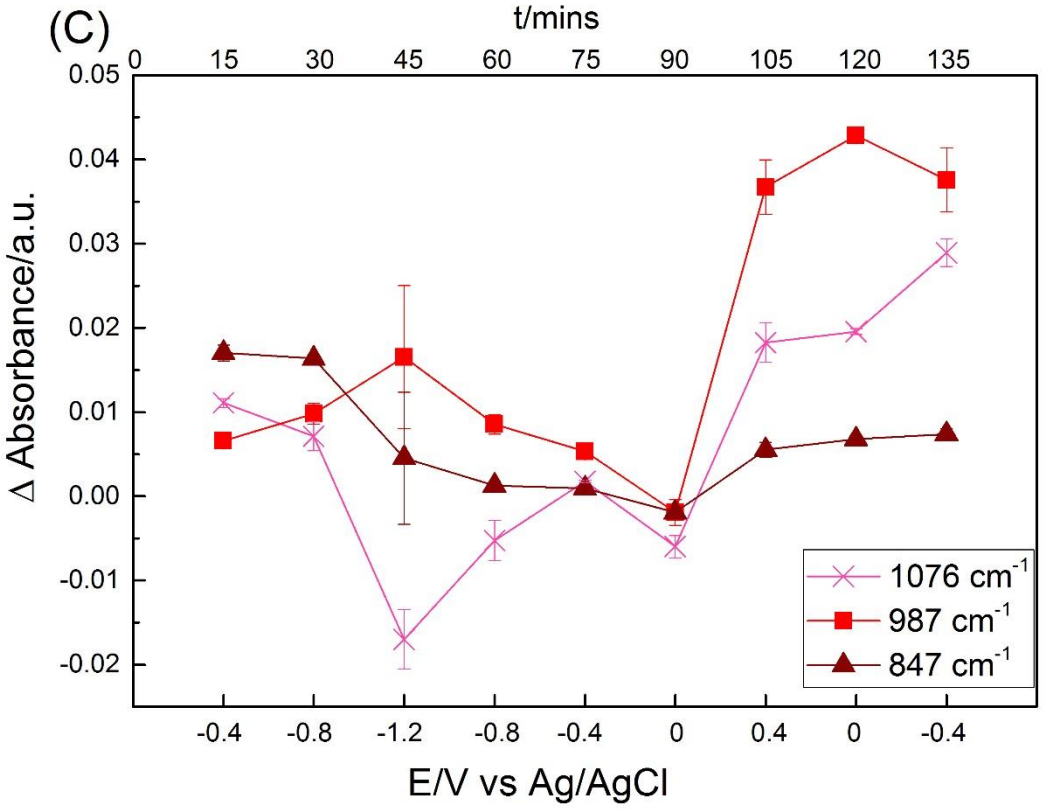
(C)
t/mins
0
15
30
45
60
75
90
105
120
135
0.05
0.04
0.03
0.02
0.01
0.00
-0.01
-0.02
Δ Absorbance/a.u.
1076 cm-1
987 cm-1
847 cm-1
-0.4
-0.8
-1.2
-0.8
-0.4
0
0.4
0
-0.4
E/V vs Ag/AgCl

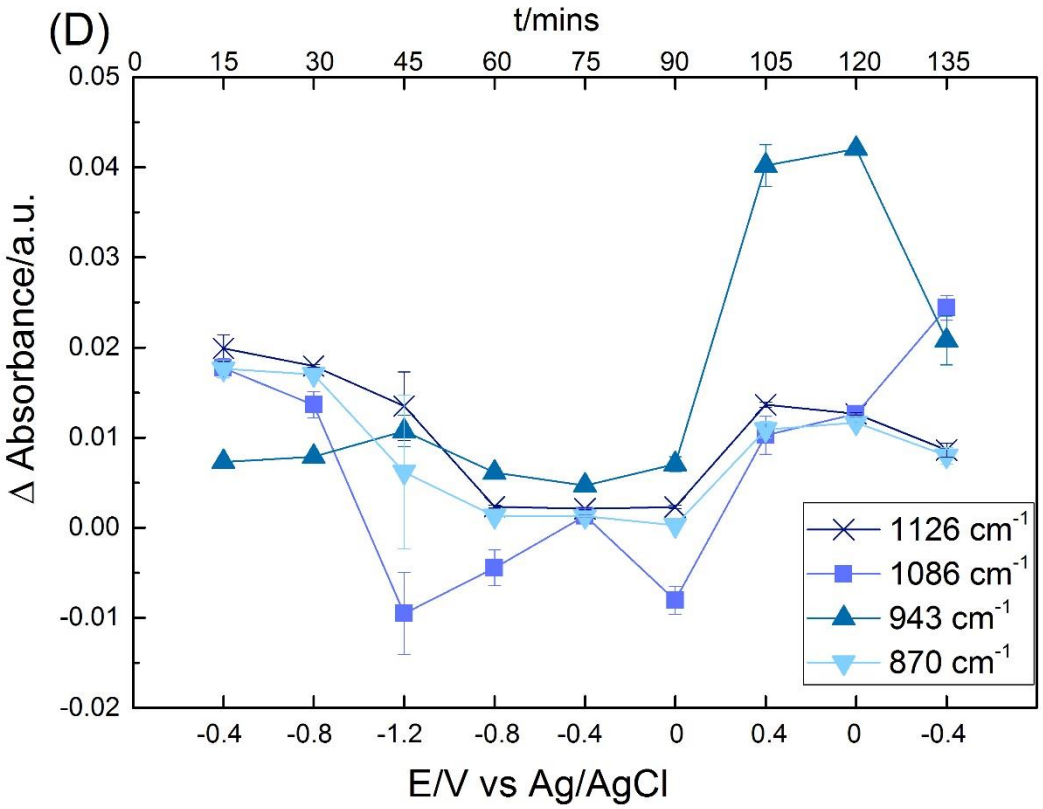

Figure 5-15. The intensity of the IR peaks as a function of time and potential plot from in situ FTIR absorbance difference spectra of CuO on BDD electrode in pH 9 Ar deoxygenated PBS. (A) water bands, (B) the orange line represents PO_4^{3-}, the brown line represents HPO_4^{0}, (C) HPO_4^{2-} bands, (D) $H_2PO_4^{-}$ bands.

Figure 5-15 presents the dependency of the IR bands by plotting the intensity of different IR bands as a function of time and applied potentials in Ar deoxygenated solution. Figure 5-15 (A) shows the absorbance bands at 3380 and 3050 cm^{-1}, the intensity of two peaks reflect the surface adsorbed water and bonded water. In negative sweep from -0.4 V to -1.2 V, the two water bands decreased together. Because of the HER, the electrode surface lost more surface adsorbed water. After switching potential, the trend of two bands is negative correlated with each other in general. After one cycle, the relative intensity of surface bonded water did not reduce much, but a huge decrease can be observed in surface adsorbed water.

The remaining three figures in Figure 5-15 give intensity details for phosphate species. The Figure 5-15 (B) shows the IR band at 1051 cm^{-1}, related to PO_4^{3-}, the band at 1009 cm^{-1}, related to $H_3PO_4^{0}$, (C) shows the IR bands at 1076, 987, 847 cm^{-1}, related to

HPO_4^{2-}, and (D) shows the IR bands at 1126, 1086, 943, and 870 cm^{-1}, related to $H_2PO_4^-$. The trends for different absorbance peaks in one specific species are correlated in general. In the negative sweep from -0.4 V to -1.2 V, the intensity of PO_4^{3-}, HPO_4^{2-}, $H_2PO_4^-$ absorbance peaks decrease overall, and the IR peak for $H_3PO_4^0$ increases oppositely. With the applied potential at E_6=0 V, the electrode surface desorbed almost all phosphate species.

5.7 FTIR for pH 9 PBS in CO_2 saturated conditions

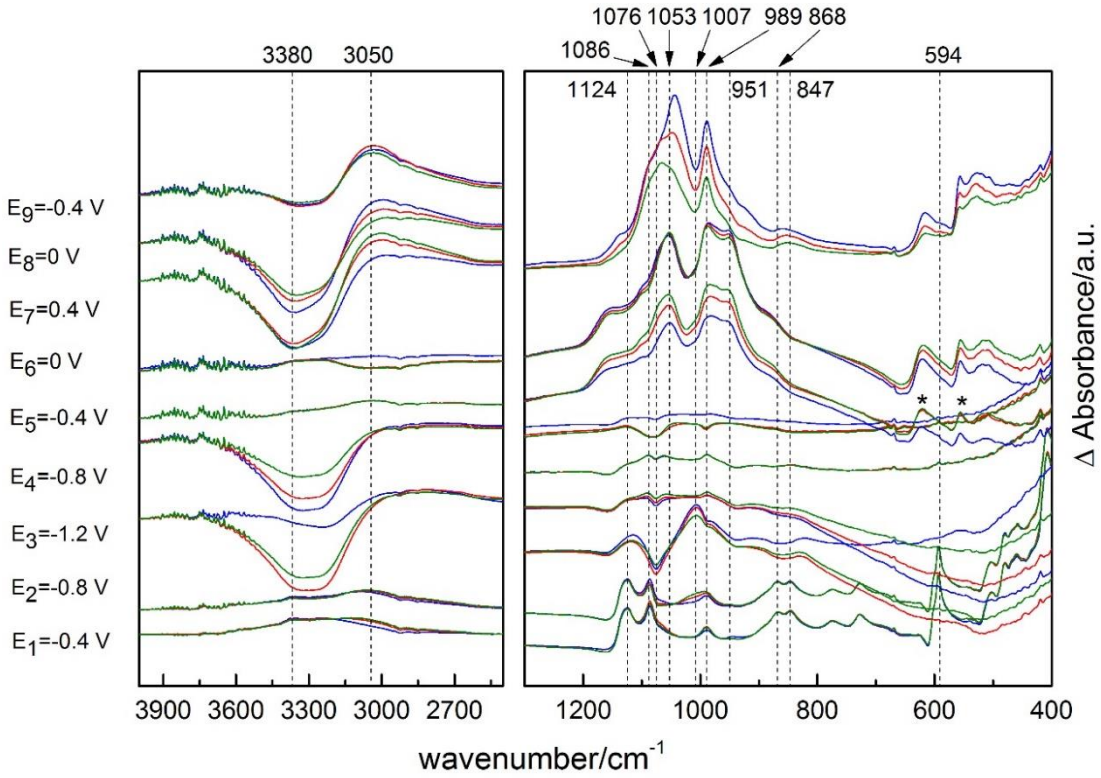

Figure 5-16. In situ FTIR absorbance difference spectra of CuO on BDD electrode in pH 9 CO_2 saturated PBS with applied potentials. Potential steps applied: E_1=-0.4 V, E_2=-0.8 V, E_3=-1.2 V, E_4=-0.8 V, E_5=-0.4 V, E_6=0 V, E_7=0.4 V, E_8=0 V, E_9=-0.4 V. Each potential step held for 15 minutes, FTIR spectrum collected every 5 minutes, which is 3 scans in each potential stage. Blue, red and green line represent the first, middle and final scans.

Figure 5-16 shows the FTIR absorbance difference spectra of CuO on BDD electrode with applied potentials in CO_2 saturated conditions. Spectra were split to 400-1300

cm^{-1} and 2500-4000 cm^{-1} wavenumber ranges. The phosphate, water and copper bands in CO_2 saturated condition have similar changing trend compared with in Ar deoxygenated conditions with applied potential.

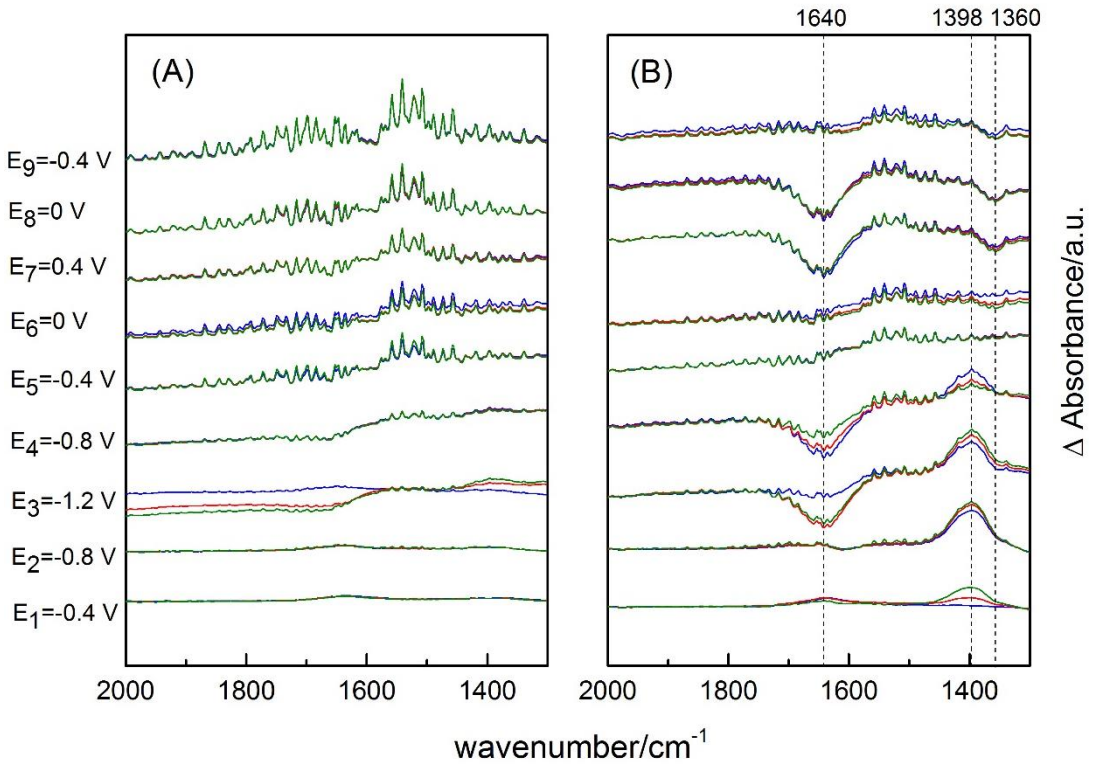

Figure 5-17. In situ FTIR absorbance difference spectra of CuO on BDD electrode in pH 9 PBS with applied potentials, (A) Ar deoxygenated solution, (B) CO_2 saturated solution. Potential steps applied: E_1=-0.4 V, E_2=-0.8 V, E_3=-1.2 V, E_4=-0.8 V, E_5=-0.4 V, E_6=0 V, E_7=0.4 V, E_8=0 V, E_9=-0.4 V. Each potential step held for 15 minutes, FTIR spectrum collected every 5 minutes, which is 3 scans in each potential stage. Blue, red and green line represent the first, middle and final scans.

Figure 5-17 compares the absorbance spectra in Ar deoxygenated solution and CO_2 saturated solution in 1300-2000 cm^{-1} region with applied potentials. In pH 9 solution, the CO_2 exists in the form of CO_3^{2-} and HCO_3^-. In Ar deoxygenated solution, the spectra in the 1300-2000 cm^{-1} region stay unchanged over applied potential during the experiments.

In CO_2 saturated solution, several peaks can be observed. The IR peak appeared at 1640 cm^{-1} was attributed to the C=O stretching mode. However, the water absorbance

band typically appears at ~1640 cm^{-1} as well. In Ar deoxygenated conditions, there is little absorbance change at 1640 cm^{-1} despite changes being observed for water bands in the 3380 and 3050 cm^{-1} regions (see Figure 5-14), hence we do not attribute changes of 1640 cm^{-1} band to water. The peak at 1398 cm^{-1} can be assigned as adsorbed CO_3^{2-}. The peak appearing from E_7=0.4 V at 1360 cm^{-1} was attributed to C···O stretching mode [20]. Compared with literature [20, 22] the 1640 and 1360 cm^{-1} peaks were contributed by HCO_3^- species, and the 1398 cm^{-1} by CO_3^{2-} species.

The electrode surface adsorbs increased CO_3^{2-} with more negative potential from -0.4 V to -1.2 V. The HCO_3^- absorbance bands have opposite trend compared to CO_3^{2-} band at negative potential. Hence the electrode adsorbs CO_3^{2-} and desorbs HCO_3^- at negative potentials of -0.4→-1.2→-0.8 V. After E_4=-0.8 V, no CO_3^{2-} is adsorbed on the electrode surface. The electrode surface continues to desorb HCO_3^- at positive potential of E_7=0.4 V. It can be concluded that the electrode selectively adsorbs different CO_2 related species at particular potentials.

5.8 FTIR for pH 8 $KHCO_3$ solution in Ar deoxygenated conditions

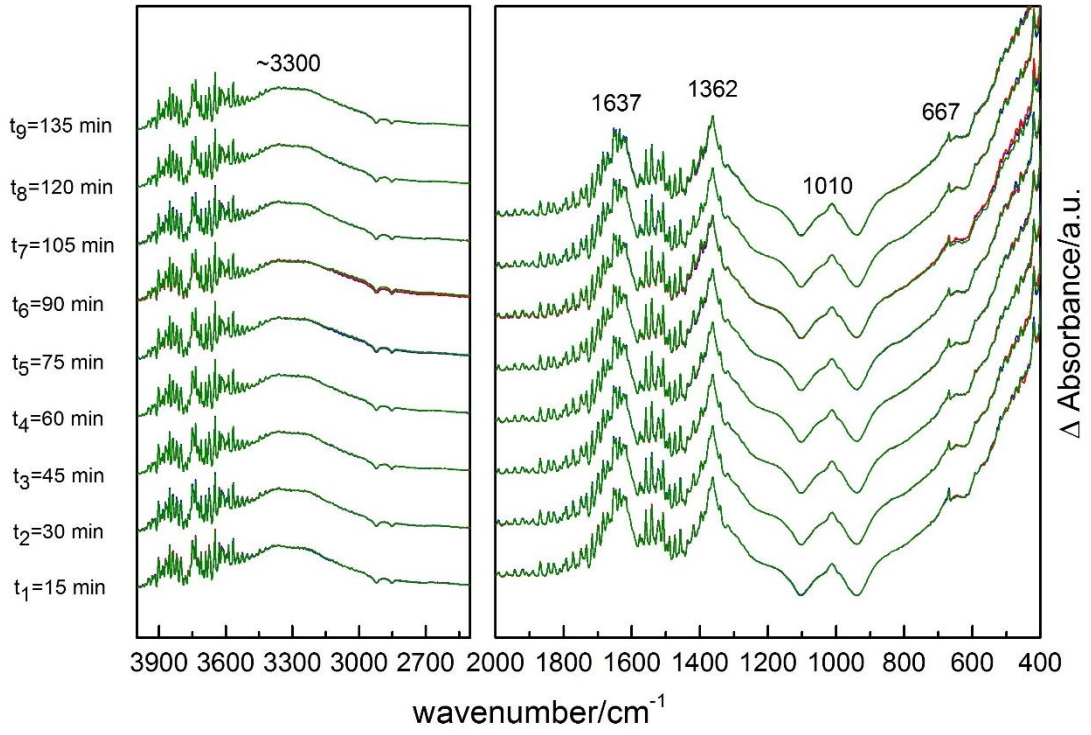

Figure 5-18. In situ FTIR absorbance difference spectra of CuO on BDD electrode in pH 8 Ar deoxygenated $KHCO_3$ with no applied potentials. The spectra were grouped in every 15 minutes, which is same time in each potential step: t_1=15 min, t_2=30 min, t_3=45 min, t_4=60 min, t_5=75 min, t_6=90 min, t_7=105 min, t_8=120 min, t_9=135 min. Blue, red and green line represent the first, middle and final scans.

Table 5-2. The obtained wave number of the characteristic adsorption peaks.

Peak position from Figure 5-18 (cm^{-1})	Expected bond	Peak position cm^{-1} Reference[22, 23, 24, 25]
3300	O-H	3250~3350
1637	C=O3	1633,1650,1620,1630
1362	C···O	1367,1368,1370
1010	C-O1+C-O2	1006,1001,1008,1010
667	O1=C=O2	662,655

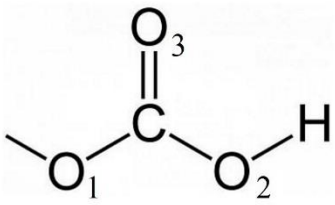

Figure 5-19. Skeletal formula of bicarbonate with number of oxygen atom labelled for Table 5-2.

Figure 5-18 illustrates the in situ FTIR spectra in pH 8 $KHCO_3$ solution under Ar deoxygenated with no potential applied during the measurement. Spectra were split to two wavenumber ranges 400-2000 cm^{-1} and 2500-4000 cm^{-1}. The background scan was measured with a clean BDD electrode. Table 5-2 summarizes the position of adsorption peaks and assignment of their corresponding modes, the label of the oxygen atoms are showed in Figure 5-19.

In the control measurement, the electrolyte contains K^+ and HCO_3^- ions. The broad wave around 3300 cm^{-1} can be assigned to OH stretching mode. The adsorption peak at 1637 cm^{-1} can be assigned to C=O3 stretching mode of bicarbonate. The 1362 cm^{-1} IR peak was attributed to the C···O stretching mode. The peak appearing at 1010 cm^{-1}

can be assigned as the coupling of the C-O1 and C-O2 stretching mode, and the 667 cm^{-1} peak corresponded to the O1=C=O2 bending mode. The IR spectra present characteristic HCO_3^- peaks from the buffer solution. These results are consistent with results obtained from others [20, 22-25]. The intensity and position of the IR bands in the control measurement stay stable over time.

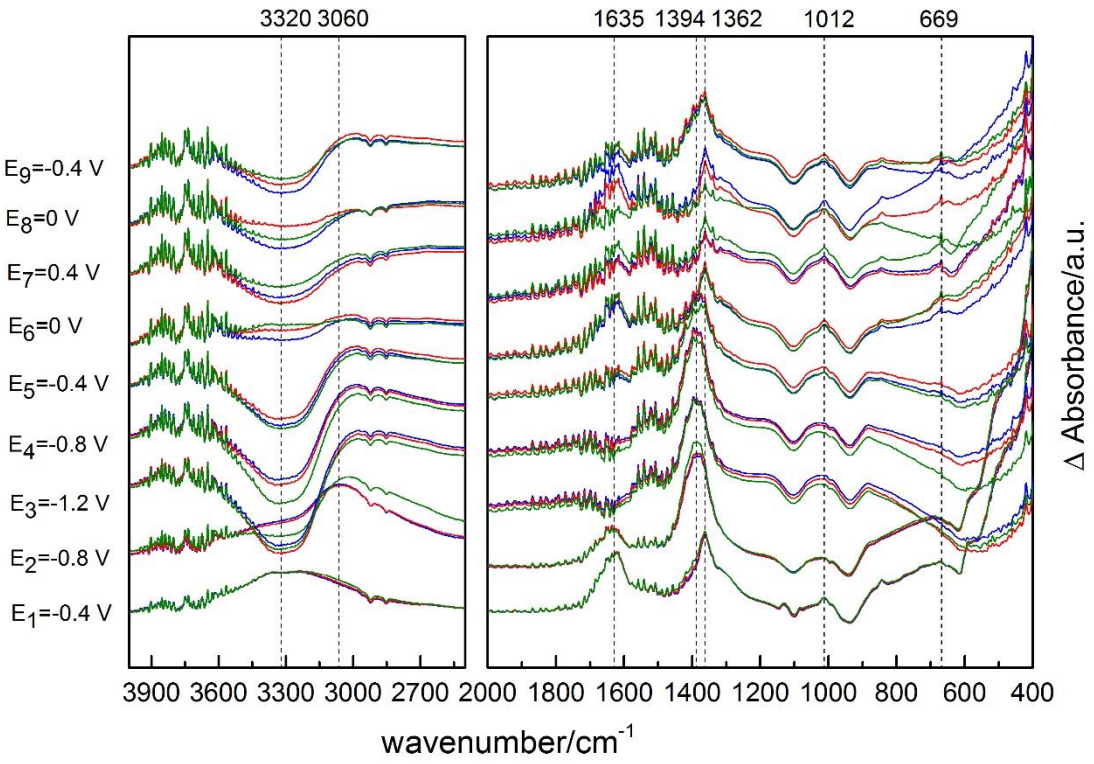

Figure 5-20. In situ FTIR absorbance difference spectra of CuO on BDD electrode in pH 8 Ar deoxygenated $KHCO_3$ with applied potentials. Potential steps applied: E_1=-0.4 V, E_2=-0.8 V, E_3=-1.2 V, E_4=-0.8 V, E_5=-0.4 V, E_6=0 V, E_7=0.4 V, E_8=0 V, E_9=-0.4 V. Each potential step held for 15 minutes, FTIR spectrum collected every 5 minutes, which is 3 scans in each potential stage. Blue, red and green line represent the first, middle and final scans.

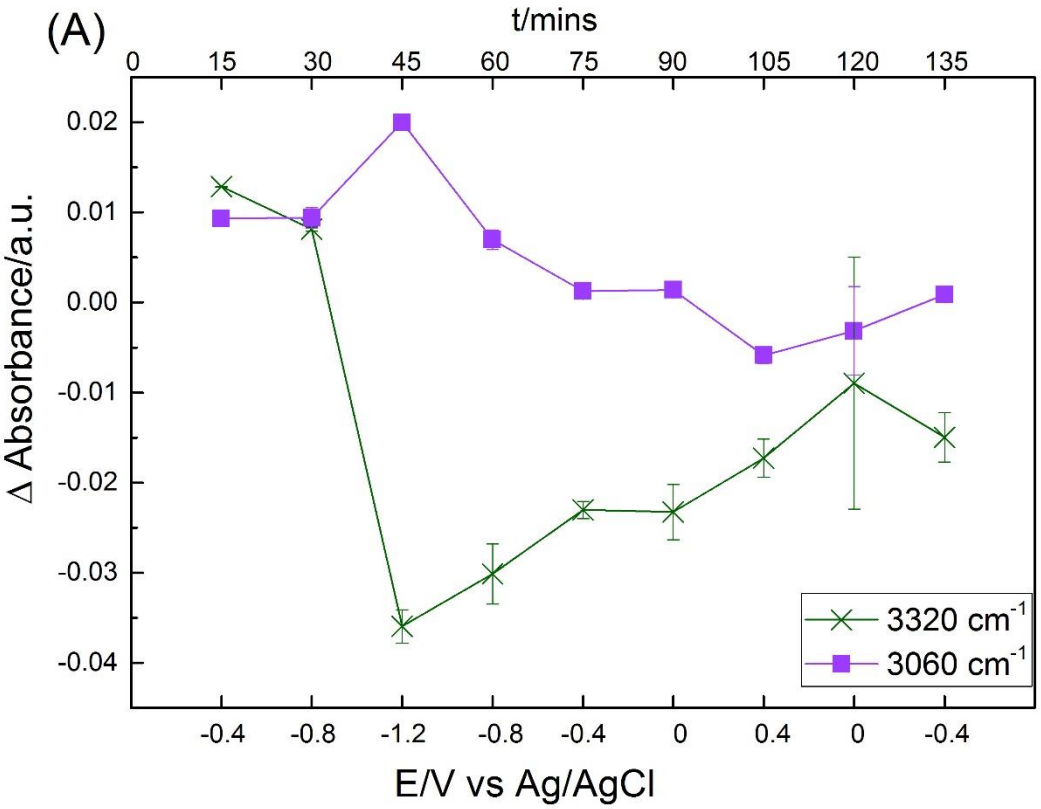
(A)
t/mins
0
15
30
45
60
75
90
105
120
135
0.02
0.01
0.00
-0.01
-0.02
-0.03
-0.04
Δ Absorbance/a.u.
3320 cm-1
3060 cm-1
-0.4
-0.8
-1.2
-0.8
-0.4
0
0.4
0
-0.4
E/V vs Ag/AgCl

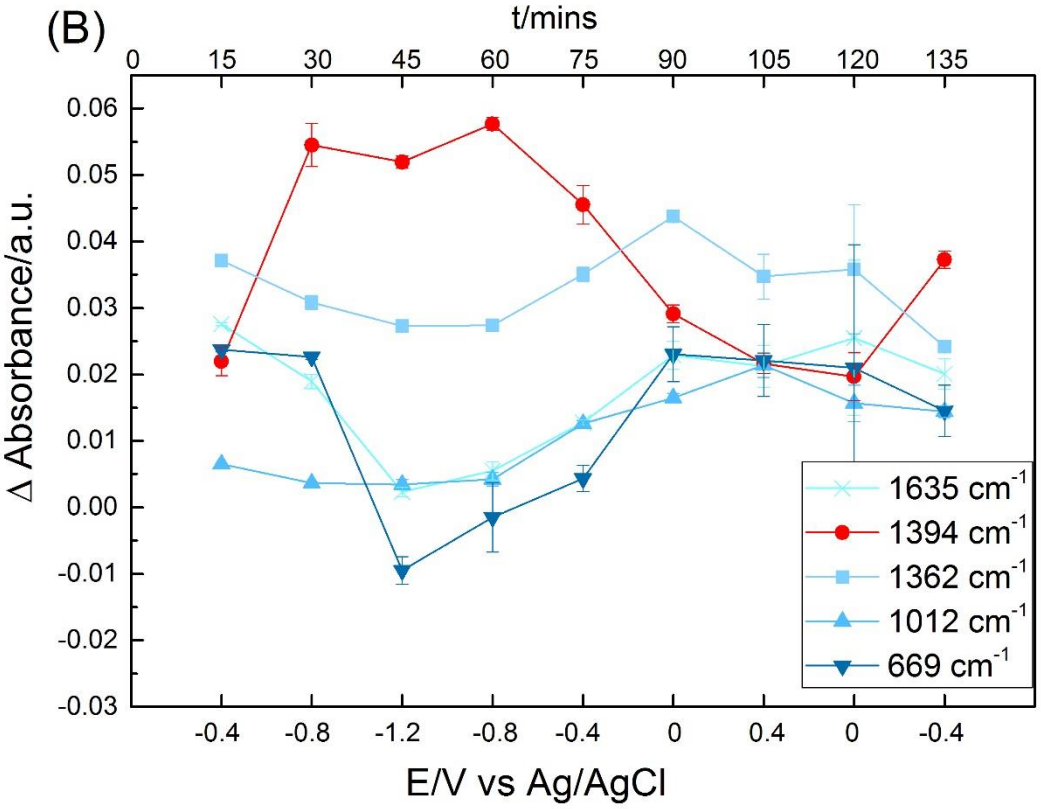
(B)
t/mins
0
15
30
45
60
75
90
105
120
135
0.06
0.05
0.04
0.03
0.02
0.01
0.00
-0.01
-0.02
-0.03
Δ Absorbance/a.u.
1635 cm-1
1394 cm-1
1362 cm-1
1012 cm-1
669 cm-1
-0.4
-0.8
-1.2
-0.8
-0.4
0
0.4
0
-0.4
E/V vs Ag/AgCl

Figure 5-21. The intensity of the IR peaks as a function of time and potential plot from In situ FTIR absorbance difference spectra of CuO on BDD electrode in pH 8 Ar deoxygenated $KHCO_3$ solution. (A) water bands, (B) HCO_3^- and CO_3^{2-} bands.

Figure 5-20 presents the FTIR absorbance difference spectra in pH 8 $KHCO_3$ solution under Ar deoxygenated with applied potential. The IR band at 3320 cm^{-1} corresponds to surface adsorbed water. From E_2=-0.8 V to E_3=-1.2 V, the IR band at 3320 cm^{-1} decreased with negative potential, while a new water band assigned as surface bonded water at 3060 cm^{-1} increased. As described from Figure 5-21 (A), this negative correlation between two water peaks is caused by the onset of HER.

Absorbance peaks at 1635, 1362, 1012 and 669 cm^{-1} are contributed by HCO_3^- from electrolyte. The 1394 cm^{-1} IR band has been assigned as CO_3^{2-} band. This CO_3^{2-} band increased and the HCO_3^- bands decreased at negative applied potential of -0.4→-1.2→-0.8 V. After E_4=-0.8 V, the CO_3^{2-} and HCO_3^- have opposite trends, where the absorbance intensity of CO_3^{2-} decreases and that of HCO_3^- increases. This has been discussed previously as adsorption selectivity for different species on the electrode at particular potential.

5.9 FTIR for pH 8 $KHCO_3$ solution in CO_2 saturated conditions

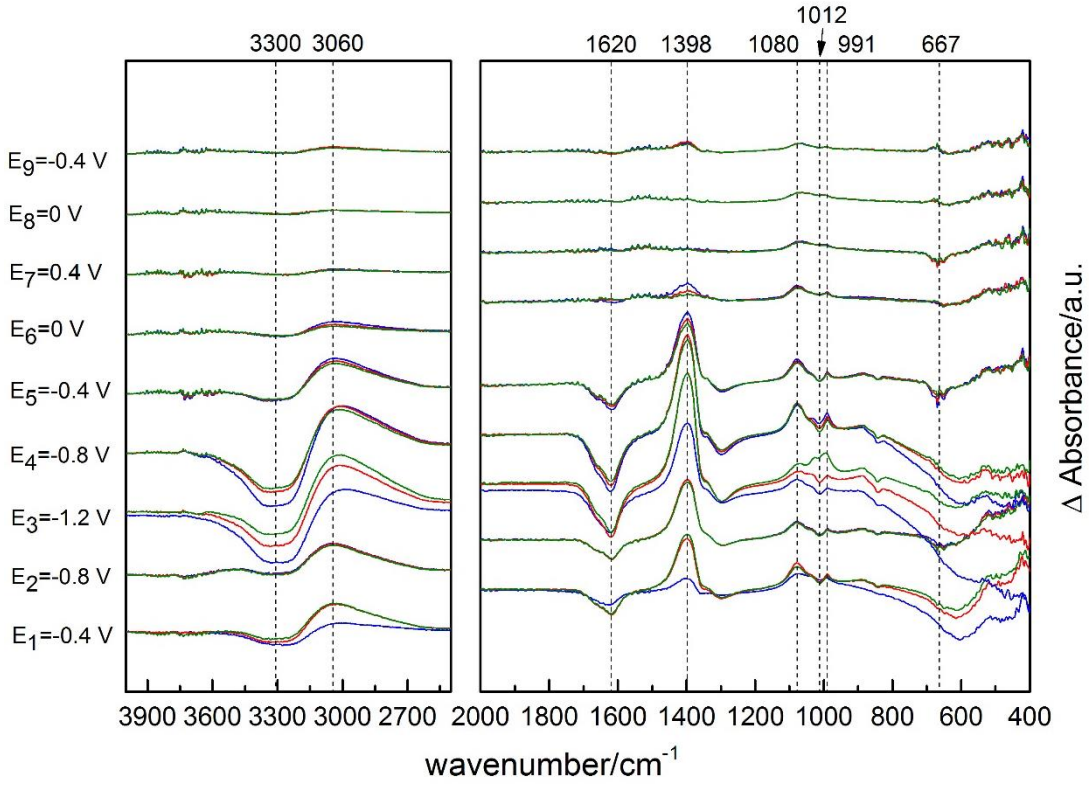

Figure 5-22. In situ FTIR absorbance difference spectra of CuO on BDD electrode in pH 8 CO_2 saturated $KHCO_3$ solution with applied potentials. Potential steps applied: E_1=-0.4 V, E_2=-0.8 V, E_3=-1.2 V, E_4=-0.8 V, E_5=-0.4 V, E_6=0 V, E_7=0.4 V, E_8=0 V, E_9=-0.4 V. Each potential step held for 15 minutes, FTIR spectrum collected every 5 minutes, which is 3 scans in each potential stage. Blue, red and green line represent the first, middle and final scans.

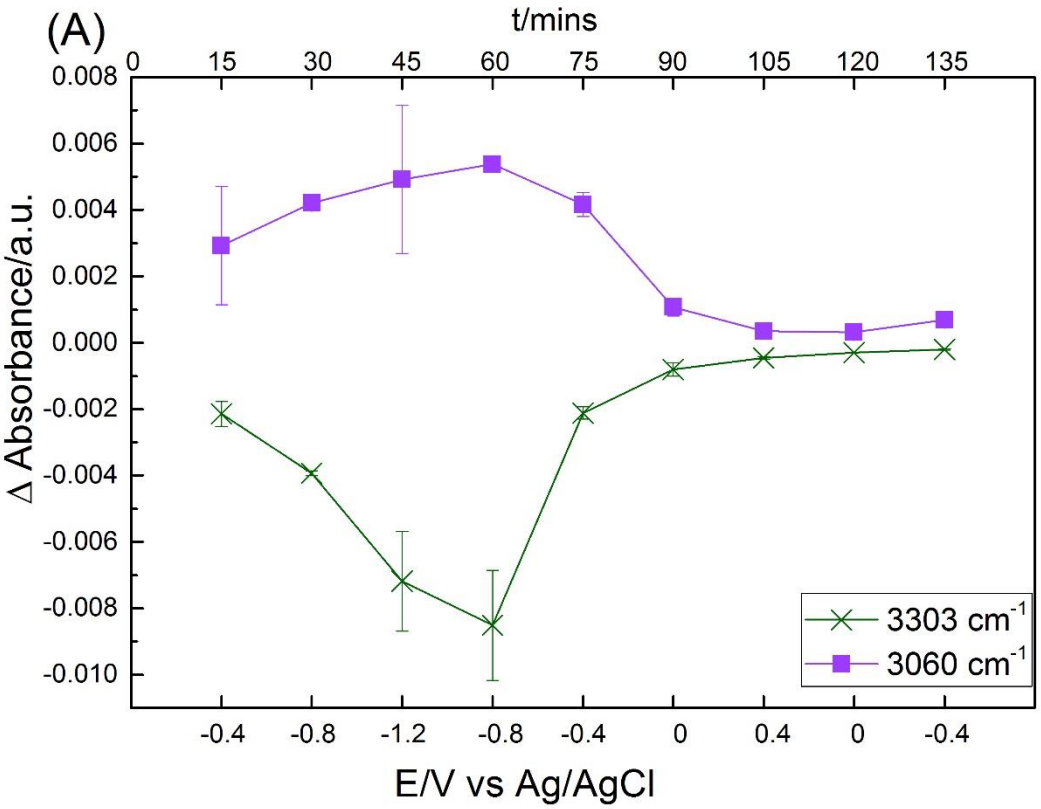
(A)
t/mins
0
15
30
45
60
75
90
105
120
135
0.008
0.006
0.004
0.002
0.000
-0.002
-0.004
-0.006
-0.008
-0.010
Δ Absorbance/a.u.
-0.4
-0.8
-1.2
-0.8
-0.4
0
0.4
0
-0.4
E/V vs Ag/AgCl
3303 cm-1
3060 cm-1

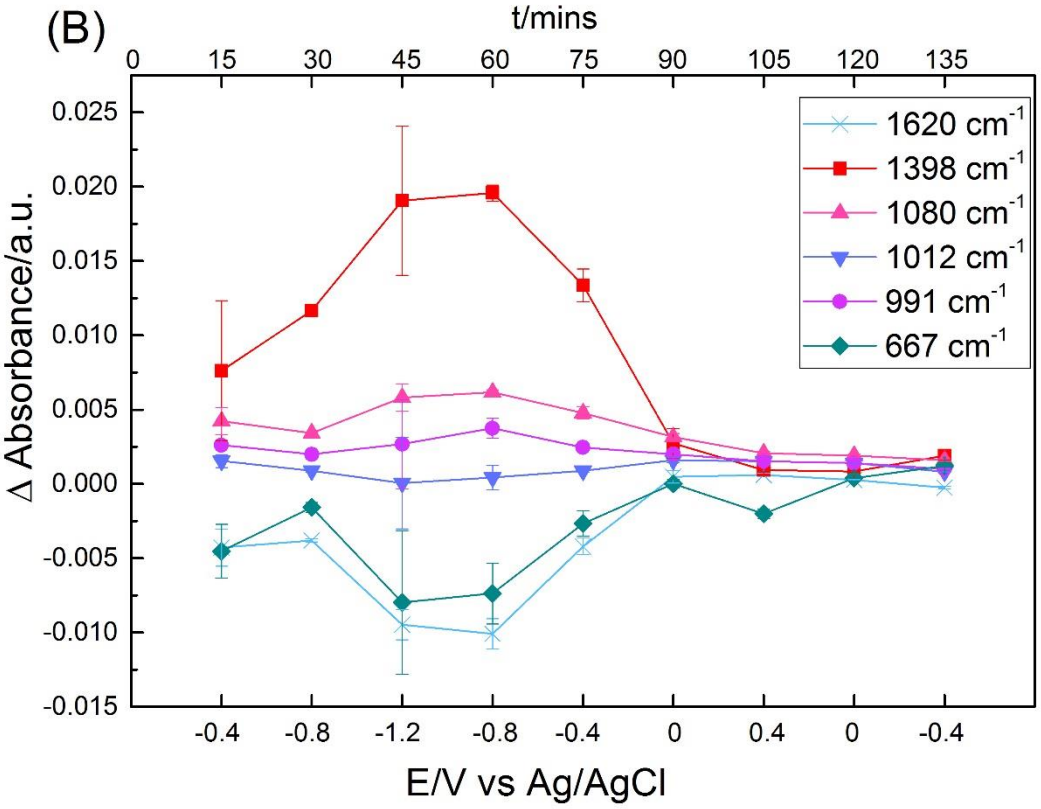
(B)
t/mins
0
15
30
45
60
75
90
105
120
135
0.025
0.020
0.015
0.010
0.005
0.000
-0.005
-0.010
-0.015
Δ Absorbance/a.u.
-0.4
-0.8
-1.2
-0.8
-0.4
0
0.4
0
-0.4
E/V vs Ag/AgCl
1620 cm-1
1398 cm-1
1080 cm-1
1012 cm-1
991 cm-1
667 cm-1

Figure 5-23. The intensity of the IR peaks as a function of time and potential plot from In situ FTIR absorbance difference spectra of CuO on BDD electrode in pH 8 $KHCO_3$ solution saturated with CO_2. (A) water bands, (B) HCO_3^- and CO_3^{2-} bands.

Figure 5-22 shows the FTIR absorbance difference spectra of CuO on BDD electrode in pH 8 $KHCO_3$ solution with applied potentials in CO_2 saturated conditions. Spectra were split to 400-2000 cm^{-1} and 2500-4000 cm^{-1} wavenumber ranges. The water and carbonate/bicarbonate bands in CO_2 saturated condition are summarized in Figure 5-23.

The two water bands have similar changing trend compared with in Ar deoxygenated conditions at applied potential (Figure 5-21 (A) and Figure 5-23 (A)). IR bands at 1620, 1012, 667 cm^{-1} have been assigned as HCO_3^- related adsorption peaks. New IR peaks appeared in the lower wavenumber region at 991 and 1080 cm^{-1}. The changing trend of the two peaks is consistent with 1398 cm^{-1} in Figure 5-23 (B). The 991 and 1080 cm^{-1} IR peaks might relate to CO_3^{2-} species [25] from dissolved CO_2 in the solution.

5.10 CO_2 reduction products on copper oxide catalyst

In order to understand the CO_2 reduction mechanism, the reduction products need to be analysed. The liquid phase reduction products were analysed by nuclear magnetic resonance (NMR) spectroscopy. The constant potential electrocatalysis measurements were carried out at -1.2 V for 8 hours in the standard three-electrode CO_2 saturated electrochemical cell. The after reaction electrolyte was qualitative analysed using Bruker advance III 600 MHz ^1H NMR spectroscopy.

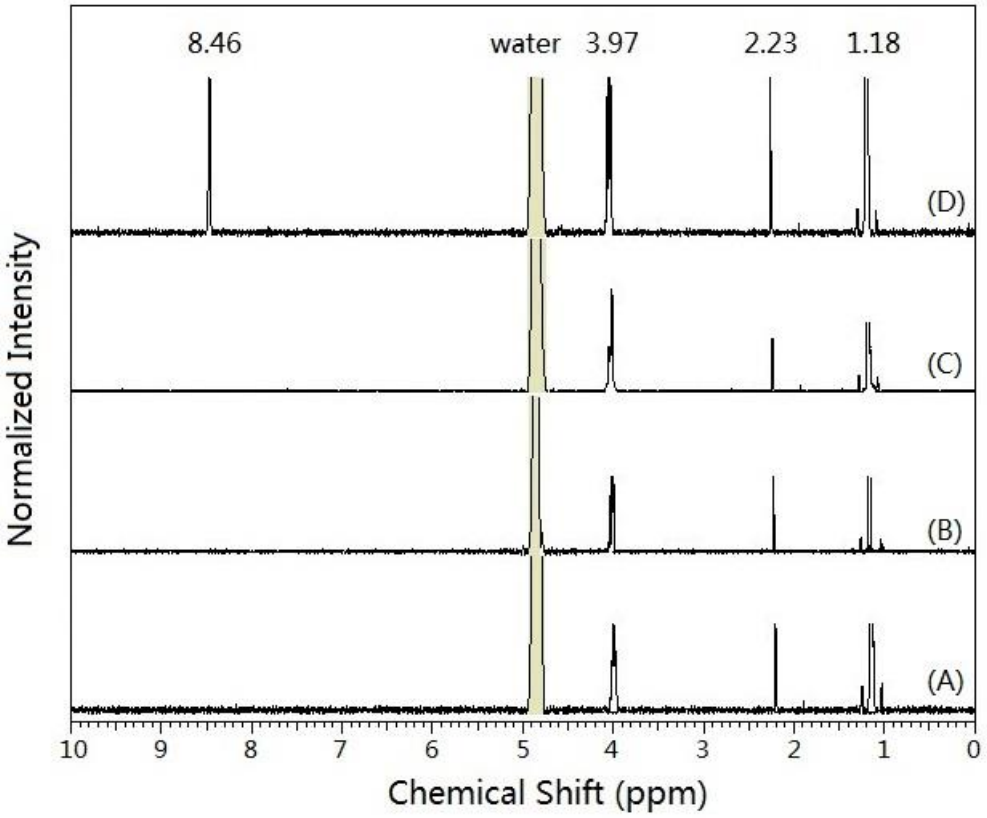

Figure 5-24. ^{1}H NMR spectra for the electrolyte in 0.2 M pH 7 PBS in: (A) Ar deoxygenated solution without application of potential; (B) Ar deoxygenated solution at -1.2 V for 8 hours; (C) CO_2 saturated solution without application of potential; (D) CO_2 saturated solution at -1.2 V for 8 hours.

Figure 5-24 shows the ^{1}H NMR spectra of three control experiments (A, B, C) and one in pH 7 CO_2 saturated solution (D) with holding potential at -1.2 V for 8 hours. The yellow shaded peak at 4.9 ppm is the peak for water. The contaminants in control experiments are assigned to iso-propanol by Spectral Database for Organic Compounds [26]. The peaks at 3.97, 2.23, 1.18 ppm are attributed by CH-, OH-, CH_3-functional groups from iso-propanol, respectively. The residual iso-propanol comes from the solvent for catalyst suspension. The peak position at 8.46 ppm is only seen in the CO_2 saturated with applied potentials study, identified as formic acid [26, 27]. The peak for formic acid also can be observed in pH 8 and 9 CO_2 saturated solutions (Figure A-23). The liquid phase product of CO_2 reduction is formic acid in our study.

5.11 Discussions

It can be observed from the FTIR spectra that different species are adsorbed on the electrode surface at different pH value of the solutions and in Ar deoxygenated or CO_2 saturated conditions. The adsorption also shows selectivity of the electrode for different species at particular potentials. The FTIR spectra are consistent with the CV results and the two ex situ measurements in general.

To be more specific, the results of the experiments taken in Ar deoxygenated solution are discussed as below. In the first negative sweep at E_1=-0.4 V, CuO remains unchanged from results for all measurements. FTIR spectra show more anions adsorbed onto the electrode surface, generating bands for electrolyte species (phosphate species from PBS, bicarbonate species from $KHCO_3$ solution) and water because of applied potential.

At E_2=-0.8 V, Cu(II) starts to reduce, the current magnitude decreases and a reduction peak is observed in the cyclic voltammogram. Consistent with this assignment, in XPS and Raman spectra, both Cu(II) and Cu(I) peaks exist at this potential. But CuO band in FTIR spectra does not change until the applied potential at -1.2 V. This relates to the passivating layer on the catalyst which causes the cathodic peak to be observed at more negative potential on the first scan. The IR band related to Cu-O stretch mode is clearly observed at the first scan, and disappeared in the following two scans at E_3=-1.2 V in Ar deoxygenated solutions in pH 4, 7 and 9 (no CuO related peaks can be observed in pH 8 Ar deoxygenated solution). Since no Cu_2O related bands can be observed, this implies that at -1.2 V, Cu(II) is reduced to Cu(0) directly on the first negative sweep. XPS spectra show the same result, the sample surface is dominated by Cu(I)/Cu(0) after application of potential at -1.2 V. In bulk material, not all of CuO is reduced, peaks for CuO and Cu_2O are obtained together in the Raman spectrum.

After one cyclic sweep, Cu(II) should be regenerated as indicated by the cyclic voltammogram that oxidation peak can be observed at positive potential, to maintain its activity for following reduction. The peak III in cyclic voltammogram should represent the oxidation from Cu(0) to Cu(II) in pH 7 Ar deoxygenated solution (Equation 3-3b). Not all of the reduced Cu species are oxidised, the results of different

measurements are consistent with each other in general. Cu(II) peaks re-emerge in FTIR, XPS and Raman spectrum after one complete cycle. The FTIR spectra show the CuO formed at the end of the first cycle may not have the same structure as that at E_1=-0.4 V. As can be seen the cyclic voltammogram figure in Ar deoxygenated solutions, the magnitude of peaks I and II increase initially with continued cycling then reach a steady value. This indicates a consistent thickness redox-active surface layer is formed. So on the electrode surface and in the bulk, Cu(II) peaks all dominate in XPS and Raman spectra at the end of multicycles.

After introduction of CO_2 in the solution, the FTIR spectra show different trends. The results of all of the experiments undertaken in CO_2 saturated solution can be discussed as below. In the first negative sweep at E_1=-0.4 V, CuO remains unchanged in cyclic voltammogram, XPS, Raman, and FTIR spectra. There is an increase in carbonate related species absorbance intensity observed in FTIR spectra at E_1=-0.4 V. From -0.8 V, the current magnitude increases in the cyclic voltammogram figure, this takes place at less negative potential than in Ar deoxygenated conditions. But the current magnitude is highly depended on pH value compared to Ar deoxygenated conditions. In XPS spectra, the proportion of Cu(II) peaks is larger than in Ar deoxygenated conditions at -0.8 V in four pH values (pH 4, 7, 8, and 9). This implies some competitive processes take place prior to CuO reduction and HER, and so Cu(II) reduction is inhibited.

With the introduction of CO_2, not all of Cu(II) is reduced to Cu(I)/Cu(0) at E_3=-1.2 V in XPS and Raman spectra, since the CuO peaks can be observed. From Figure 5-6 FTIR spectra in pH 7 CO_2 saturated PBS, the Cu_2O band can be observed at -1.2 V, which means not all of Cu(I) is reduced to Cu(0). This is consistent with the ex situ measurements. After cyclic sweeps, both Cu(I)/Cu(0) and Cu(II) related peaks can be observed in XPS and Raman spectra. The Cu(I)/Cu(0) is not re-oxidised to Cu(II) completely. The electrode surface adsorbs HCO_3^-/CO_3^{2-} and/or other reaction intermediates during the experiments with the presence of CO_2 in the system. It can be assumed that CuO catalyst has different chemical behaviour and electron transfer process with the applied potential when CO_2 is present in solution.

5.12 Summary

Combining the results from electrochemical measurement with in situ and ex situ spectroscopic studies, the electrochemical behaviour of CuO catalyst in Ar deoxygenated solutions is clear on the whole, such as reduction reaction equations, proportion of different components and adsorbed species with applied potentials. Based on this information, the different behaviour of CuO catalyst comes from the introduction of CO_2. The CO_2 involved reactions therefore can be investigated compared with the results in Ar deoxygenated solutions. The liquid phase product in CO_2 saturated solutions is formic acid.

References

[1] Gandhi S, Subramani RH, Ramakrishnan T, Sivabalan A, Dhanalakshmi V, Nair MG, Anbarasan R. Ultrasound assisted one pot synthesis of nano-sized CuO and its nanocomposite with poly (vinyl alcohol). Journal of Materials Science. 2010 Mar 1;45(6):1688-94.

[2] Yu Q, Huang H, Chen R, Wang P, Yang H, Gao M, Peng X, Ye Z. Synthesis of CuO nanowalnuts and nanoribbons from aqueous solution and their catalytic and electrochemical properties. Nanoscale. 2012;4(8):2613-20.

[3] Tejedor-Tejedor MI, Anderson MA. The protonation of phosphate on the surface of goethite as studied by CIR-FTIR and electrophoretic mobility. Langmuir. 1990 Mar;6(3):602-11.

[4] Elzinga EJ, Sparks DL. Phosphate adsorption onto hematite: an in situ ATR-FTIR investigation of the effects of pH and loading level on the mode of phosphate surface complexation. Journal of Colloid and Interface Science. 2007 Apr 1;308(1):53-70.

[5] He Z, Honeycutt CW, Xing B, McDowell RW, Pellechia PJ, Zhang T. Solid-state Fourier transform infrared and ^{31}P nuclear magnetic resonance spectral features of phosphate compounds. Soil Science. 2007 Jul 1;172(7):501-15.

[6] Brandán SA, Díaz SB, González JL, Disalvo EA, Altabef AB. Experimental and theoretical study of the hydration of phosphate groups in esters of biological interest. Spectrochimica Acta Part A: Molecular and Biomolecular Spectroscopy. 2007 Apr 30;66(4):884-97.

[7] Han JK, Song HY, Saito F, Lee BT. Synthesis of high purity nano-sized

hydroxyapatite powder by microwave-hydrothermal method. Materials Chemistry and Physics. 2006 Oct 10;99(2):235-9.

[8] Water structure and science. 26 May 2016. [Accessed 2 June 2016]; Available from: http://www1.lsbu.ac.uk/water/water_vibrational_spectrum.html.

[9] Lappi SE, Smith B, Franzen S. Infrared spectra of $H_2{}^{16}O$, $H_2{}^{18}O$ and D_2O in the liquid phase by single-pass attenuated total internal reflection spectroscopy. Spectrochimica Acta Part A: Molecular and Biomolecular Spectroscopy. 2004 Sep 30;60(11):2611-9.

[10] Bonner OD, Curry JD. Infrared spectra of liquid H_2O and D_2O. Infrared Physics. 1970 Jun 30;10(2):91-4.

[11] Martin HB, Argoitia A, Landau U, Anderson AB, Angus JC. Hydrogen and oxygen evolution on boron-doped diamond electrodes. Journal of the Electrochemical Society. 1996 Jun 1;143(6):L133-6.

[12] Infrared spectroscopy. 21 July 2015. [Accessed 2 June 2016]; Available from: http://chemwiki.ucdavis.edu/Textbook_Maps/Organic_Chemistry_Textbook_Maps/Map%3A_Organic_Chemistry_With_a_Biological_Emphasis_(Soderberg)/Chapter_04%3A_Structure_Determination_I/4.2%3A__Infrared_spectroscopy.

[13] Infrared: Interpretation. 7 June 2015. [Accessed 2 June 2016]; Available from: http://chemwiki.ucdavis.edu/Core/Physical_Chemistry/Spectroscopy/Vibrational_Spectroscopy/Infrared_Spectroscopy/Infrared%3A_Interpretation.

[14] Lefez B, Souchet R, Kartouni K, Lenglet M. Infrared reflection study of CuO in thin oxide films. Thin Solid Films. 1995 Nov 1;268(1):45-8.

[15] Zhang YX, Huang M, Li F, Wen ZQ. Controlled synthesis of hierarchical CuO nanostructures for electrochemical capacitor electrodes. International Journal of Electrochemical Science. 2013 Jun 1;8:8645-61.

[16] Gupta K, Bersani M, Darr JA. Highly efficient electro-reduction of CO_2 to formic acid by nano-copper. Submitted to Green Chemistry (2016).

[17] Lear T, Marshall R, Lopez-Sanchez JA, Jackson SD, Klapötke TM, Bäumer M, Rupprechter G, Freund HJ, Lennon D. The application of infrared spectroscopy to probe the surface morphology of alumina-supported palladium catalysts. The Journal of Chemical Physics. 2005 Nov 1;123(17):174706.

[18] Nagase K, Zheng Y, Kodama Y, Kakuta J. Dynamic study of the oxidation state of copper in the course of carbon monoxide oxidation over powdered CuO and Cu_2O. Journal of Catalysis. 1999 Oct 1;187(1):123-30.

[19] Miller FA, Wilkins CH. Infrared spectra and characteristic frequencies of inorganic ions. Analytical Chemistry. 1952 Aug;24(8):1253-94.

[20] Kagi H, Nagai T, Loveday JS, Wada C, Parise JB. Pressure-induced phase transformation of kalicinite ($KHCO_3$) at 2.8 GPa and local structural changes around hydrogen atoms. American Mineralogist. 2003 Oct 1;88(10):1446-51.

[21] Abouelhassan S, Salman F, Elmansy M, Sheha E. Characterization of $KHCO_3$ single crystal. Surface Review and Letters. 2004;11(1):1-4.

[22] Baldassarre M, Barth A. The carbonate/bicarbonate system as a pH indicator for infrared spectroscopy. Analyst. 2014;139(9):2167-76.

[23] Eckold G, Grimm H, Stein-Arsic M. Proton disorder and phase transition in $KHCO_3$. Physica B: Condensed Matter. 1992 Jun 2;180:336-8.

[24] Hage W, Hallbrucker A, Mayer E. Carbonic acid: synthesis by protonation of bicarbonate and FTIR spectroscopic characterization via a new cryogenic technique. Journal of the American Chemical Society. 1993 Sep;115(18):8427-31.

[25] Richner G, Puxty G. Assessing the chemical speciation during CO_2 absorption by aqueous amines using in situ FTIR. Industrial & Engineering Chemistry Research. 2012 Oct 26;51(44):14317-24.

[26] Spectral database for organic compound. 18 March 2016. [Accessed 29 July 2016]; Available from: http://sdbs.db.aist.go.jp/sdbs/cgi-bin/direct_frame_top.cgi.

[27] Roldan A, Hollingsworth N, Roffey A, Islam HU, Goodall JB, Catlow CR, Darr JA, Bras W, Sankar G, Holt KB, Hogarth G. Bio-inspired CO_2 conversion by iron sulfide catalysts under sustainable conditions. Chemical Communications. 2015;51 (35):7501-4.

Chapter 6

Conclusions and Future Work

6.1 Conclusions

The aim of this thesis was to investigate the electrochemical behaviour of copper oxide catalyst material under condition of carbon dioxide reduction. Two types of buffer solutions with five pH values, from pH 4 to pH 11 were investigated. Several electrochemical and spectroscopic methods were introduced in the study, such as cyclic voltammetry, electrocatalysis, XPS, Raman, and FTIR. The following section summarizes the major findings of the study.

6.1.1 Summary of the study

Chapter 3 investigated the electrochemistry of CuO modified electrode with cycled potentials. The electrochemical behaviour of the catalyst is dependent on the pH value and the presence and absence of CO_2 in the system. In Ar deoxygenated solutions, the electrode surface is covered with water related species and electrolyte related species. With the application of negative potential, Cu(II) is reduced to Cu(I) or Cu(0), and water is split due to HER. In CO_2 saturated solutions, the electrode surface adsorbs different CO_2 dissolved species in different pH conditions, which influences the electrochemical behaviour of the catalyst material. The current magnitude is suppressed in pH 4 and pH 7, but enhanced in pH 8, 9 and 11 CO_2 saturated solutions compared with in Ar deoxygenated solutions in same pH values. The pH 4 PBS conditions shows most suppression compared with other conditions, hence acidic solution is not suitable for CO_2 reduction on CuO material.

Chapter 4 investigated the ex situ XPS and Raman spectroscopies of CuO modified electrode after electrocatalysis measurements. The XPS spectra show less Cu(II) is reduced in CO_2 saturated solution than in Ar deoxygenated solution at same pH values, which means Cu(II) reduction reaction occurs less effectively in CO_2 saturated solution. The charge passed on the electrode may not all participate in Cu(II) reduction, since the current onset is observed at less negative potential in CO_2 saturated solutions. So some of the charge passed may be attributed to CO_2 related reactions in pH 8, 9 and 11 solutions. In neutral and alkaline solutions, the proportion of Cu(II) decreases with the increasing pH value after cycled potential. So the lower pH value shows better stability of the catalyst after a complete cyclic sweep. The pH 11 PBS conditions shows worst stability among three PBS conditions, therefore is not suitable for CO_2

reduction on CuO material. The results of Raman spectra are consistent with XPS results in general. Besides, the spectra show the corresponding reaction equations are influenced by different pH solutions. CuO is reduced to Cu_2O, then oxidised back to CuO in pH 4 and 7 solutions, while oxidised to $Cu(OH)_2$ after one cyclic potential in pH 8 and 9 solutions.

Chapter 5 investigated the in situ FTIR spectroscopy of adsorbed species on electrode surface with applied potentials. It can be observed that Cu(II) is reduced to Cu(I) and Cu(0) at negative potential with HER, and different CO_2 related species are adsorbed on the electrode surface. In pH 4 solutions, CO_2 dissolved as molecular CO_2 and is adsorbed on electrode surface. It has been observed that the current magnitude is suppressed in CO_2 saturated solution compared to Ar deoxygenated solution. Since CO_2 related bands can be observed in FTIR spectra, molecular CO_2 is adsorbed on electrode surface. The adsorbed CO_2 blocks the electrode surface and does not promote the CO_2 reduction. Roldan suggested the non-active behaviour is caused by the linear shape of the adsorbed CO_2 [1] through Cu-O bond on electrode surface between CuO and CO_2 (Figure 6-1 (A)). In pH 7 solution, CO_2 dissolves to HCO_3^- with smaller proportion of molecular CO_2. Although still suppressed compared with in Ar deoxygenated solution, the presence of HCO_3^- in pH 7 CO_2 saturated solution enhances current magnitude compared with in pH 4 CO_2 saturated solution. This indicates that the increasing current magnitude relates to less molecular CO_2 and more HCO_3^- adsorption. In pH 8 and 9 solutions, the CO_2 dissolves to HCO_3^- and CO_3^{2-}. The current magnitudes are enhanced in CO_2 saturated solutions. This indicates that the presence of HCO_3^- and CO_3^{2-} promote the electrode surface reaction. The activation for further reaction of adsorbed HCO_3^- and CO_3^{2-} species is attributed to the non-linear bonding in the molecule. The ability to be activated on the surface through two Cu-O bonds to the electrode surface (Figure 6-1 (B), (C)) [1]. Therefore, pH 7, 8, 9 should be the suitable pH conditions for CO_2 reduction on CuO catalyst.

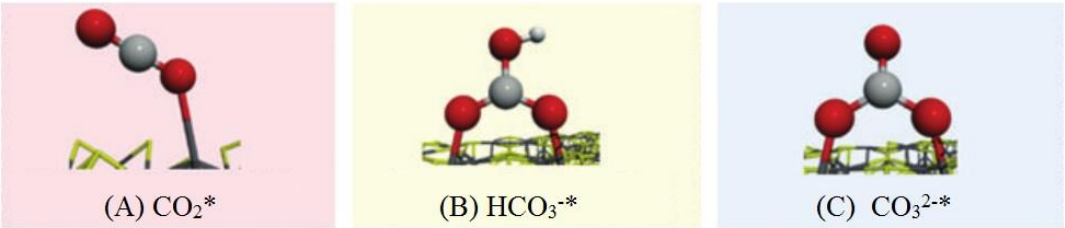

Figure 6-1. Adsorbed CO_2 related species and their proposed structures on electrode surface [1].

The results from different measurements are consistent with each other in general. From the results, the electrochemical behaviour of CuO catalyst is clear in this study, including reduction reaction equations, proportion of different components and adsorption species with applied potentials. The liquid phase product of CO_2 reduction using CuO catalyst in our experiments is formic acid. Based on these information and previous research, one proposed mechanism of CO_2 reduction will be discussed in the following section.

6.1.2 Proposed CO_2 reduction mechanism on copper oxide catalyst

It has been discussed in section 1.7.1 that the first step of CO_2 reduction is one electron added to adsorbed CO_2 to form CO_2^- anion radical. And the reaction intermediate should be carboxyl and CO through C-intermediated pathway. Combining with our research results and literature, a schematic of the reaction pathway and proposed adsorbed structure of related species are shown in Figure 6-2. CO_2 firstly dissolves in solution, then adsorbs on electrode surface as HCO_3^- and/or CO_3^{2-}. The adsorbed species receives one electron to form adsorbed CO_2^-* while losing OH and/or O. The CO_2^-* is protonated on the oxygen to form adsorbed carboxyl. The intermediate COOH bonds with H atom from solution or HER to form formic acid.

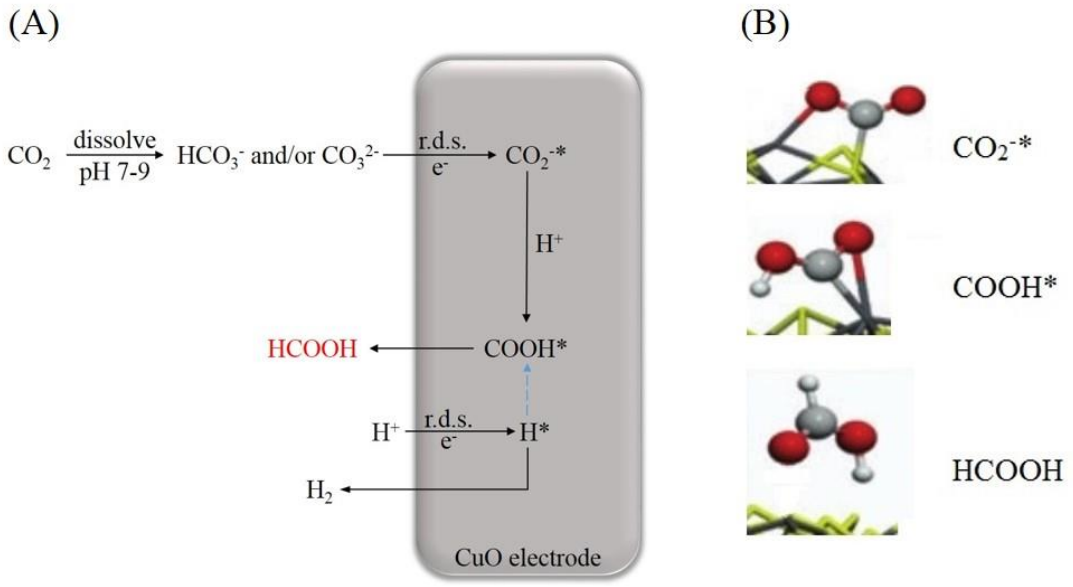

Figure 6-2. (A) Schematic reaction pathways on CuO modified electrode surface, (B) proposed adsorbed structure [1].

Electrochemical studies carried out in this project have shown the reduction potential of CuO nanoparticle materials is influenced by pH value and the presence and absence of CO_2 in the system. The results of ex situ XPS and Raman spectroscopic studies show that reduction of the Cu(II) is inhibited in the presence of CO_2, and the stability of catalyst is influenced by pH value of the solution. Using In situ IR spectroscopy to analyse the binding species on the surface of CuO at applied potentials. CO_2 is predicted to bind on the surface with non-linear structure. The main product is formic acid at the reduction potentials applied in the experiments. The aim and objectives of the project is generally fulfilled in the study. The future work to further understand the catalytic performance is proposed in the end of the thesis.

6.2 Future work

This study explores the relationship between pH values, adsorbed CO_2 related species and CuO catalyst behaviour in CO_2 electrochemical reduction to formic acid. Ex situ analysis of the after reaction electrodes show mixed oxidation states (Cu(II), Cu(I), and Cu(0)) on electrode surface. It is not clear in our study which oxidation state of the catalyst is the active species in the CO_2 reduction, and whether different oxidation states influence the reduction mechanism and products selectivity. Hence, copper

oxide materials of different oxidation state, such as Cu_2O, Cu_4O_3, and mixed phases materials can be used to clarify the reaction pathways.

The reduction rates and efficiencies are not analysed in our study. In order to improve the reduction efficiency and find the optimum reaction conditions, gas phase products and quantitative liquid phase products can be measured by gas chromatography and NMR spectroscopy. The proposed reduction pathway involve hydrogenation, and will have interaction with the HER. Hence, it will also help to fully understand the reaction pathways involving hydrogenation on electrode.

In summary, in order to improve the reliability of the research results, more experiments on copper oxides for CO_2 reduction need to be carried out to improve the understanding depth. The active sites of CO_2 reduction and products distribution need to be analysed and clarified.

References

[1] Roldan A, Hollingsworth N, Roffey A, Islam HU, Goodall JB, Catlow CR, Darr JA, Bras W, Sankar G, Holt KB, Hogarth G. Bio-inspired CO_2 conversion by iron sulfide catalysts under sustainable conditions. Chemical Communications. 2015;51 (35):7501-4.

Appendix

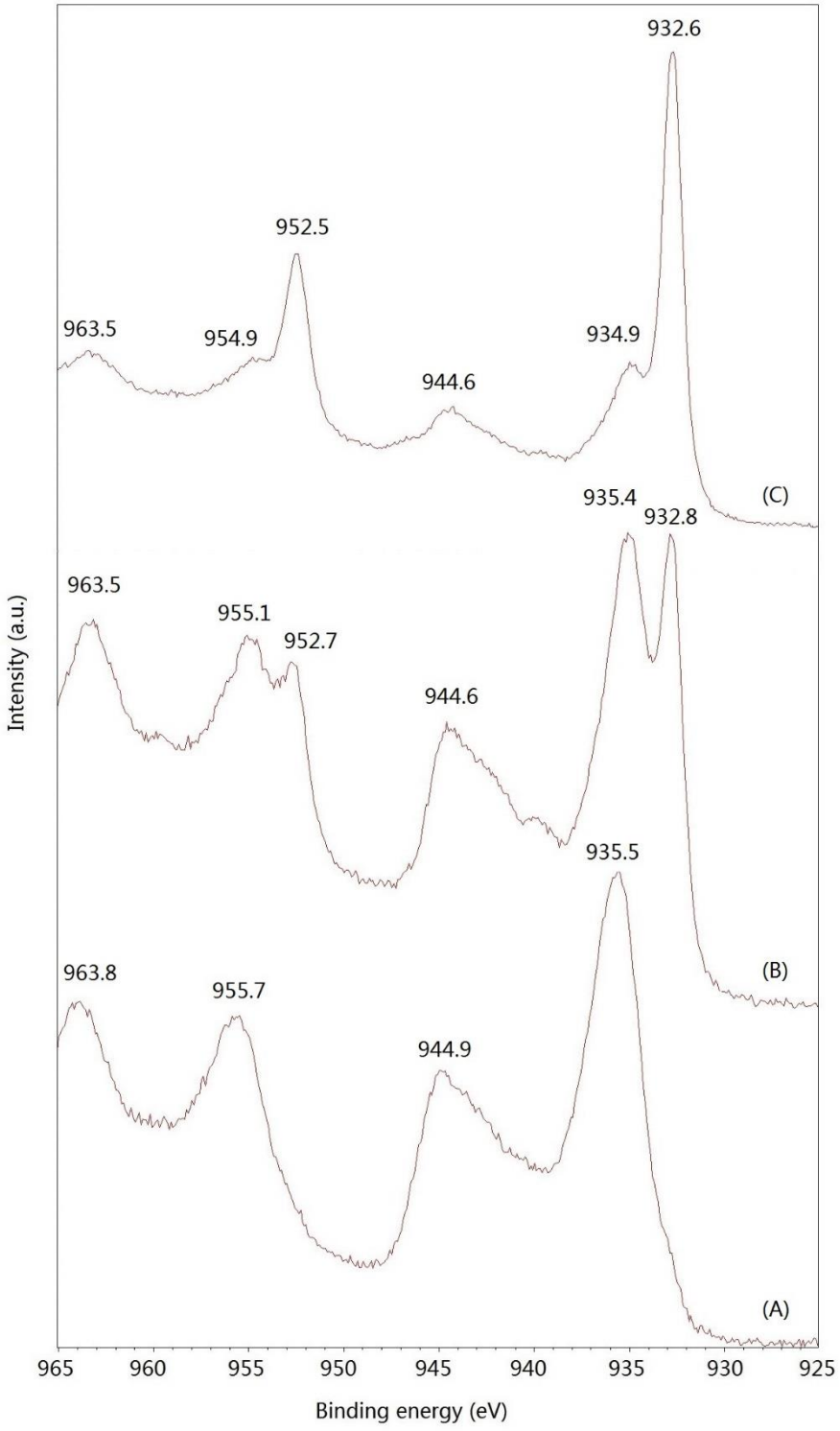

Figure A-1. High resolution Cu 2p XPS spectra for the electrode after applying potential in pH 4 Ar deoxygenated PBS at (A) -0.4 V; (B) -0.8 V; (C) -1.2 V.

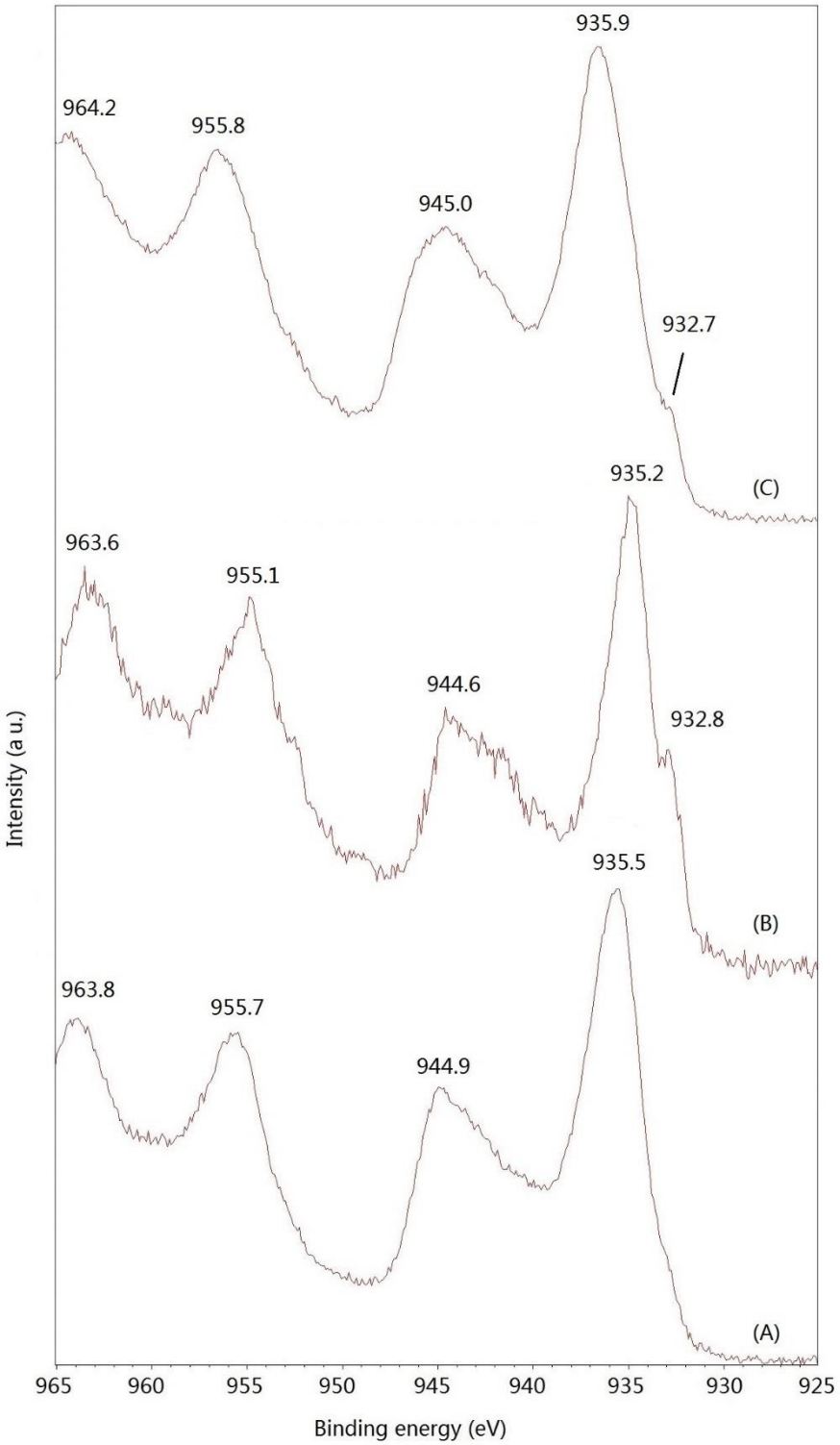

Figure A-2. High resolution Cu 2p XPS spectra for the electrode in pH 4 Ar deoxygenated PBS after: (A) holding 15 minutes at -0.4 V; (B) 1 cycle; (C) 10 cycles. For (B) and (C) the potential was scanned from 0→-1.2→0.4→0 V vs. Ag/AgCl. υ=100 mV·s^{-1}.

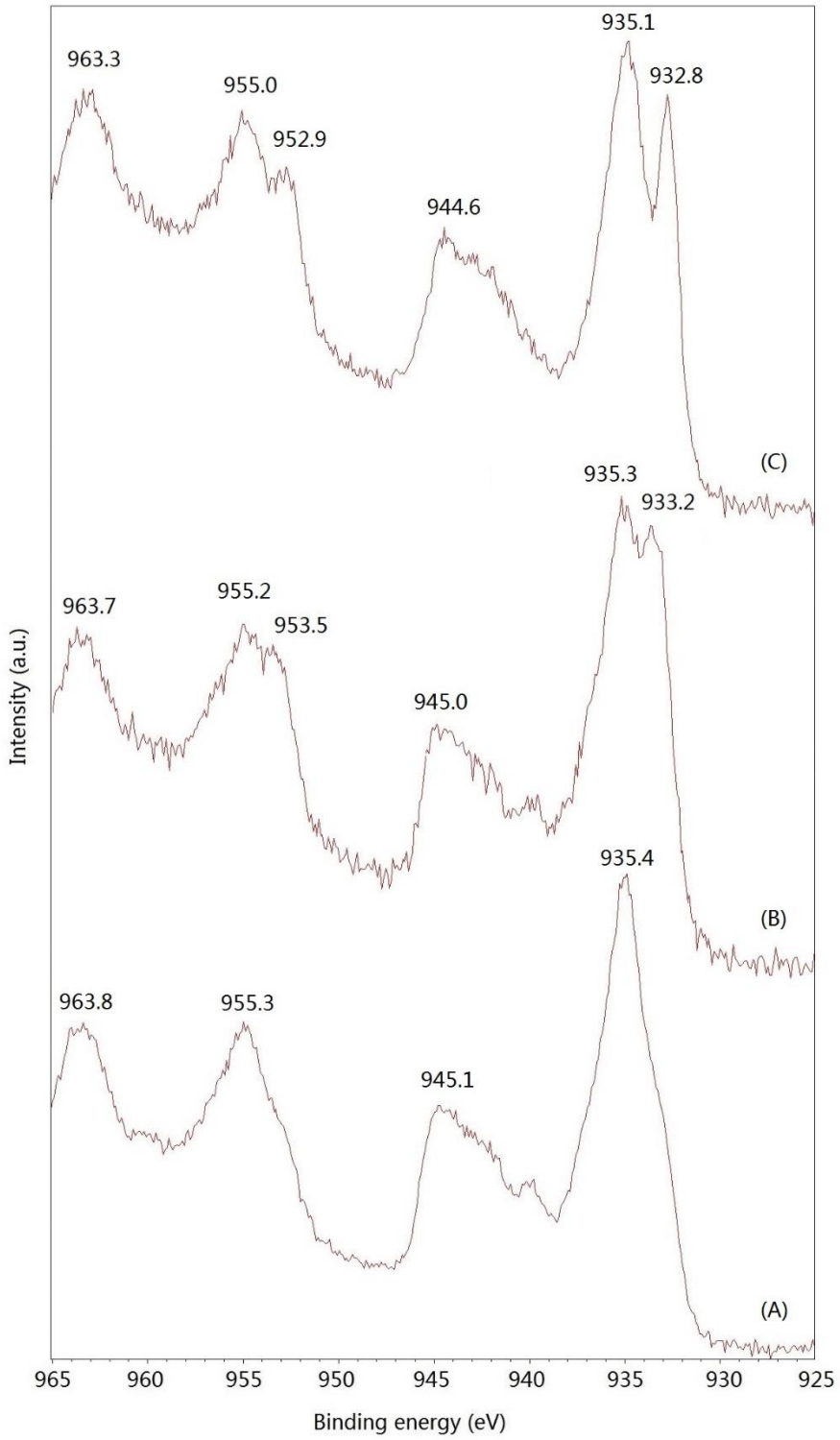

Figure A-3. High resolution Cu 2p XPS spectra for the electrode after applying potential in pH 4 CO_2 saturated PBS at (A) -0.4 V; (B) -0.8 V; (C) -1.2 V.

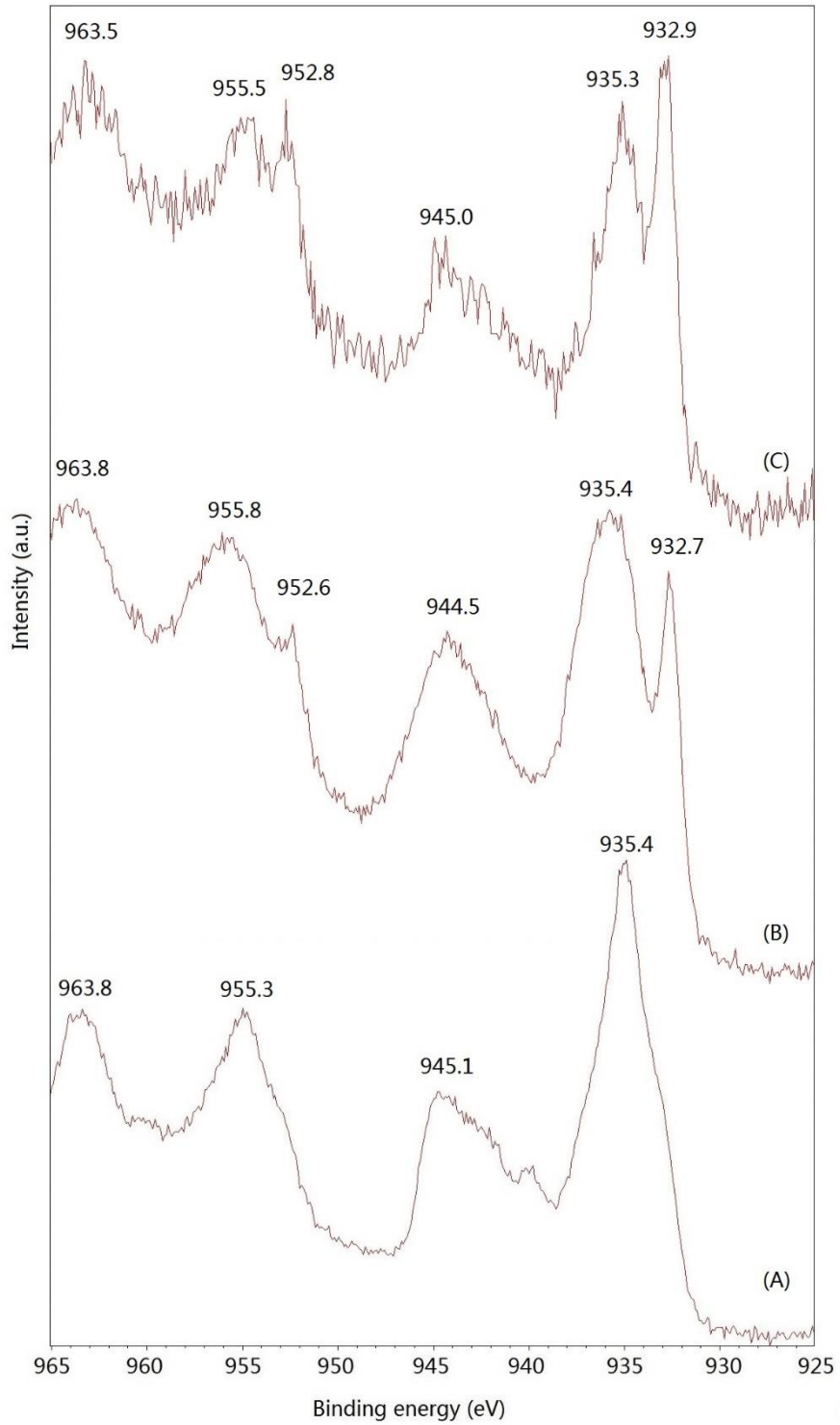

Figure A-4. High resolution Cu 2p XPS spectra for the electrode in pH 4 CO_2 saturated PBS after: (A) holding 15 minutes at -0.4 V; (B) 1 cycle; (C) 10 cycles. For (B) and (C) the potential was scanned from 0→-1.2→0.4→0 V vs. Ag/AgCl. υ=100 mV·s^{-1}.

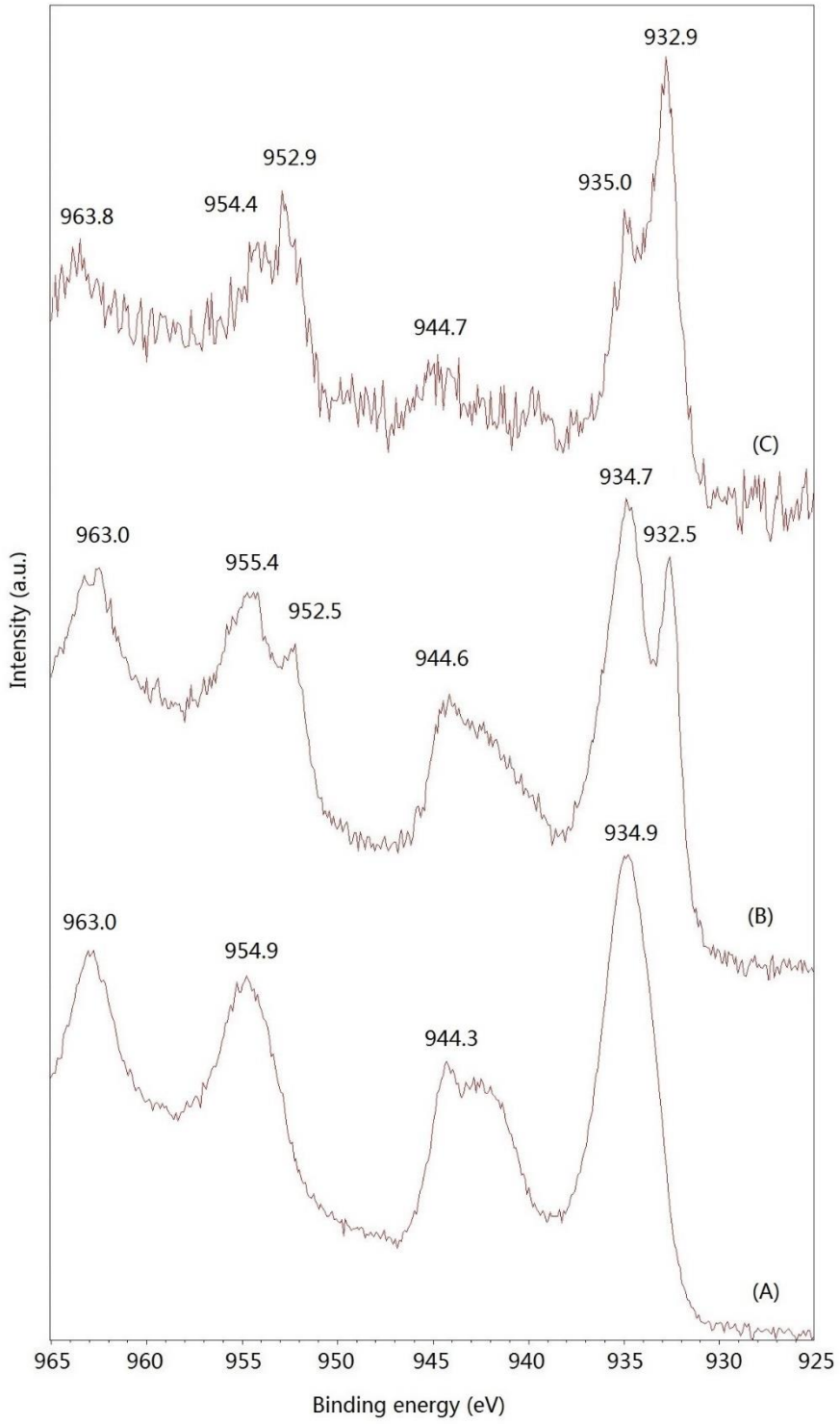

Figure A-5. High resolution Cu 2p XPS spectra for the electrode after applying potential in pH 9 Ar deoxygenated PBS at (A) -0.4 V; (B) -0.8 V; (C) -1.2 V.

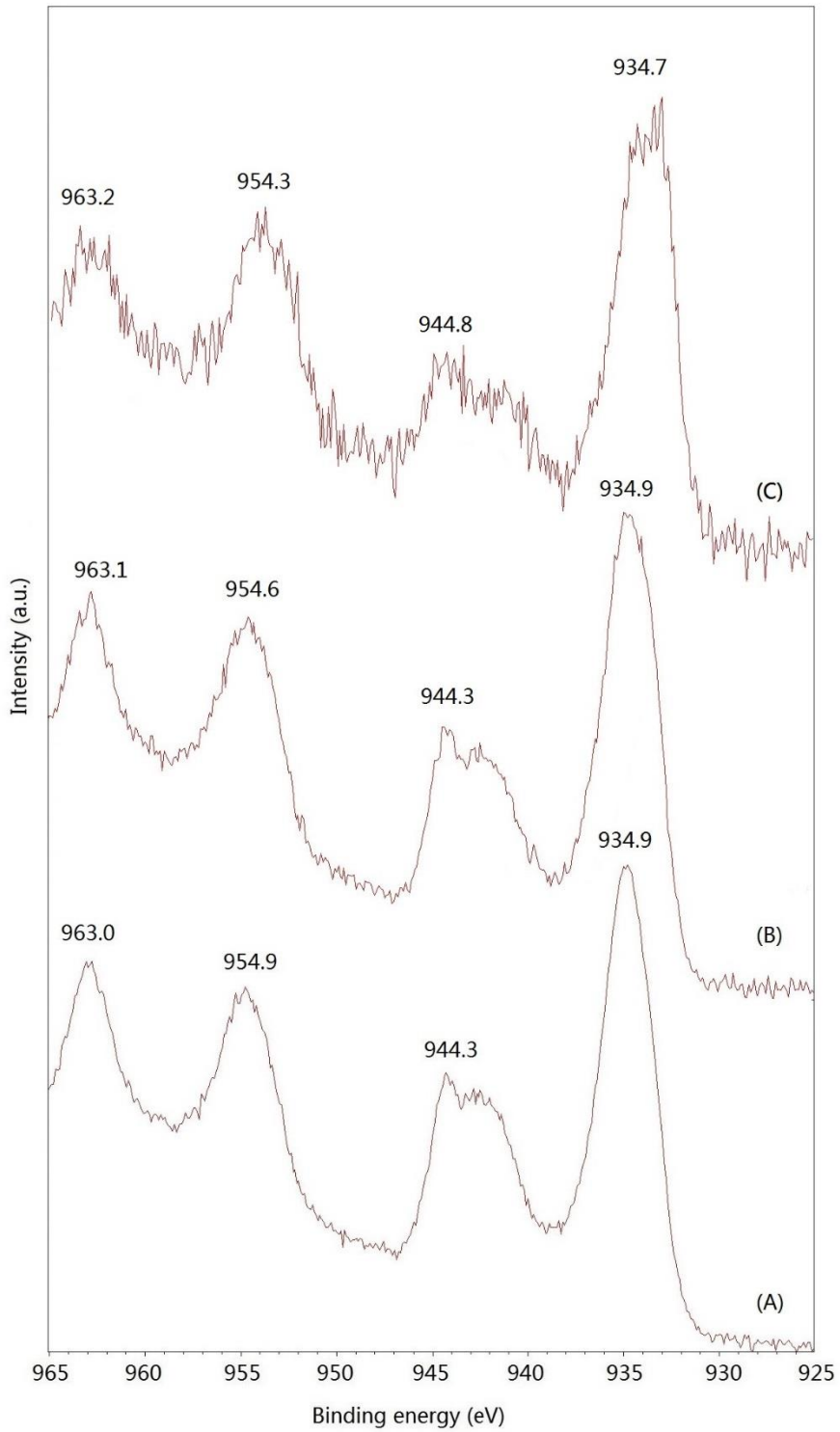

Figure A-6. High resolution Cu 2p XPS spectra for the electrode in pH 9 Ar deoxygenated PBS after: (A) holding 15 minutes at -0.4 V; (B) 1 cycle; (C) 10 cycles. For (B) and (C) the potential was scanned from 0→-1.2→0.4→0 V vs. Ag/AgCl. υ=100 mV·s^{-1}.

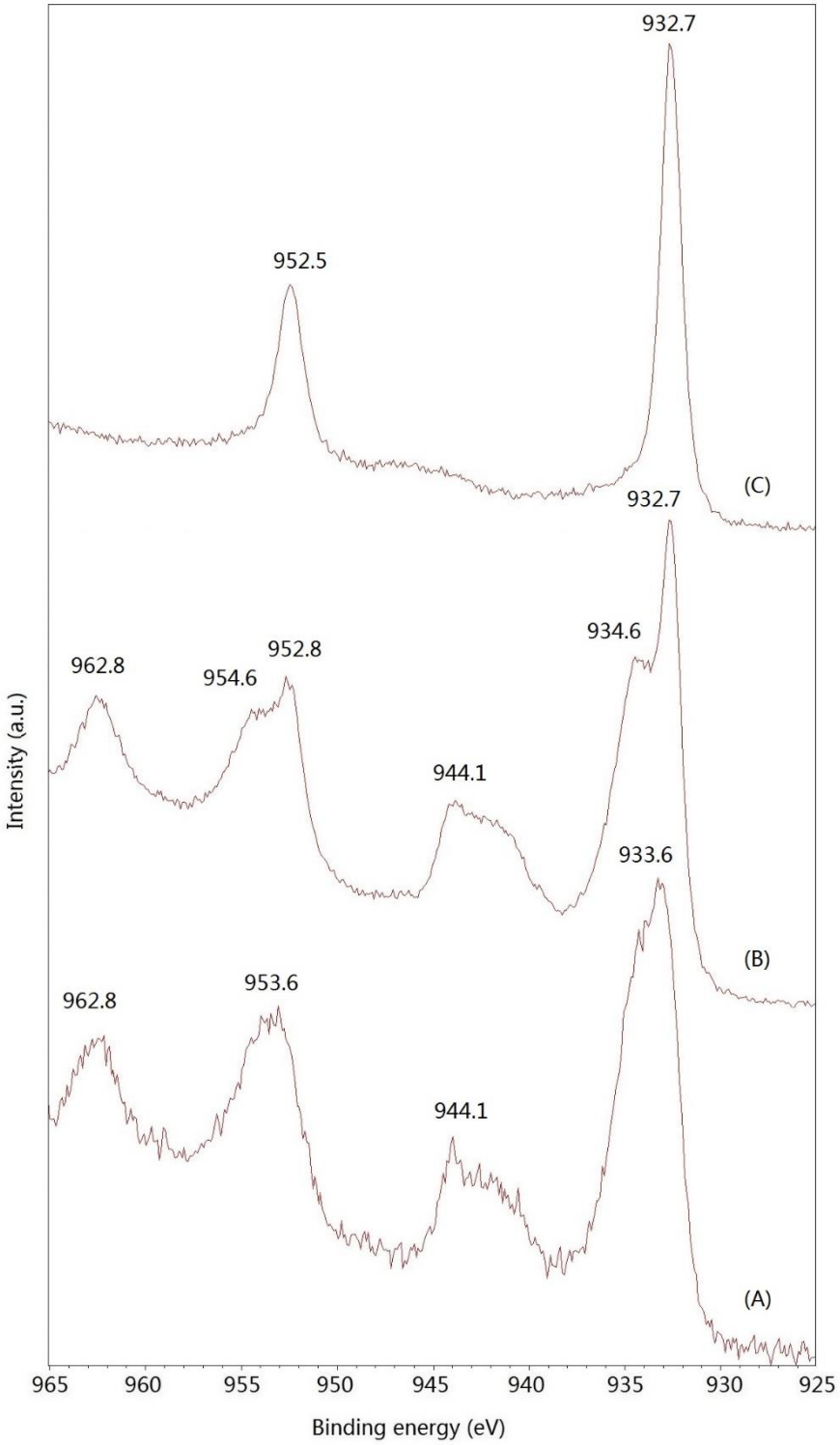

Figure A-7. High resolution Cu 2p XPS spectra for the electrode after applying potential in pH 9 CO_2 saturated PBS at (A) -0.4 V; (B) -0.8 V; (C) -1.2 V.

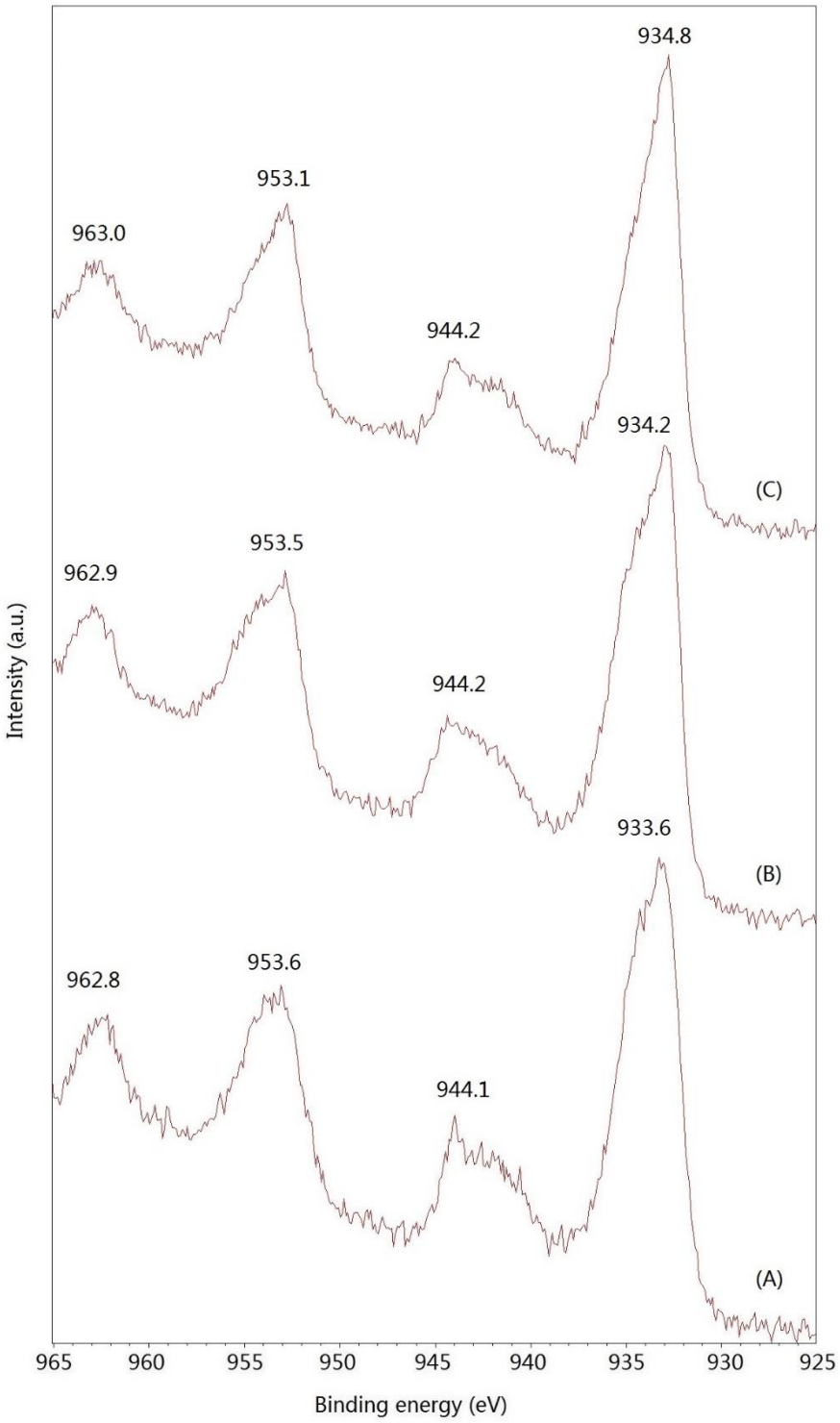

Figure A-8. High resolution Cu 2p XPS spectra for the electrode in pH 9 CO_2 saturated PBS after: (A) holding 15 minutes at -0.4 V; (B) 1 cycle; (C) 10 cycles. For (B) and (C) the potential was scanned from 0→-1.2→0.4→0 V vs. Ag/AgCl. υ=100 $mV \cdot s^{-1}$.

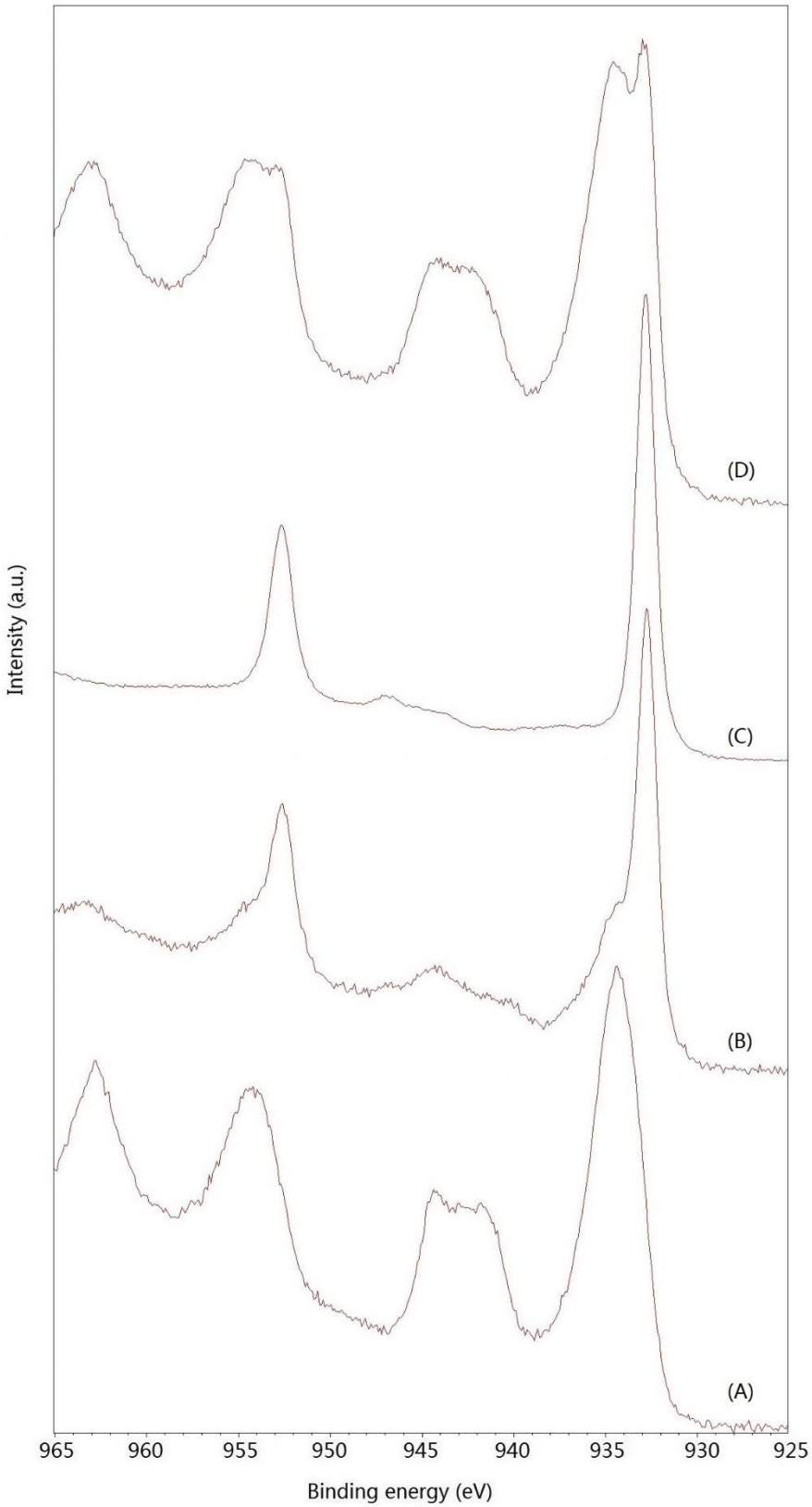

Figure A-9. High resolution Cu 2p XPS spectra for the electrode after applying potential in pH 8 Ar deoxygenated $KHCO_3$ solution after holding 15 minutes at (A) -0.4 V; (B) -0.8 V; (C) -1.2 V. (D) 1 cycle with potential scanned from 0→-1.2→0.4→0 V vs. Ag/AgCl. υ=100 $mV \cdot s^{-1}$.

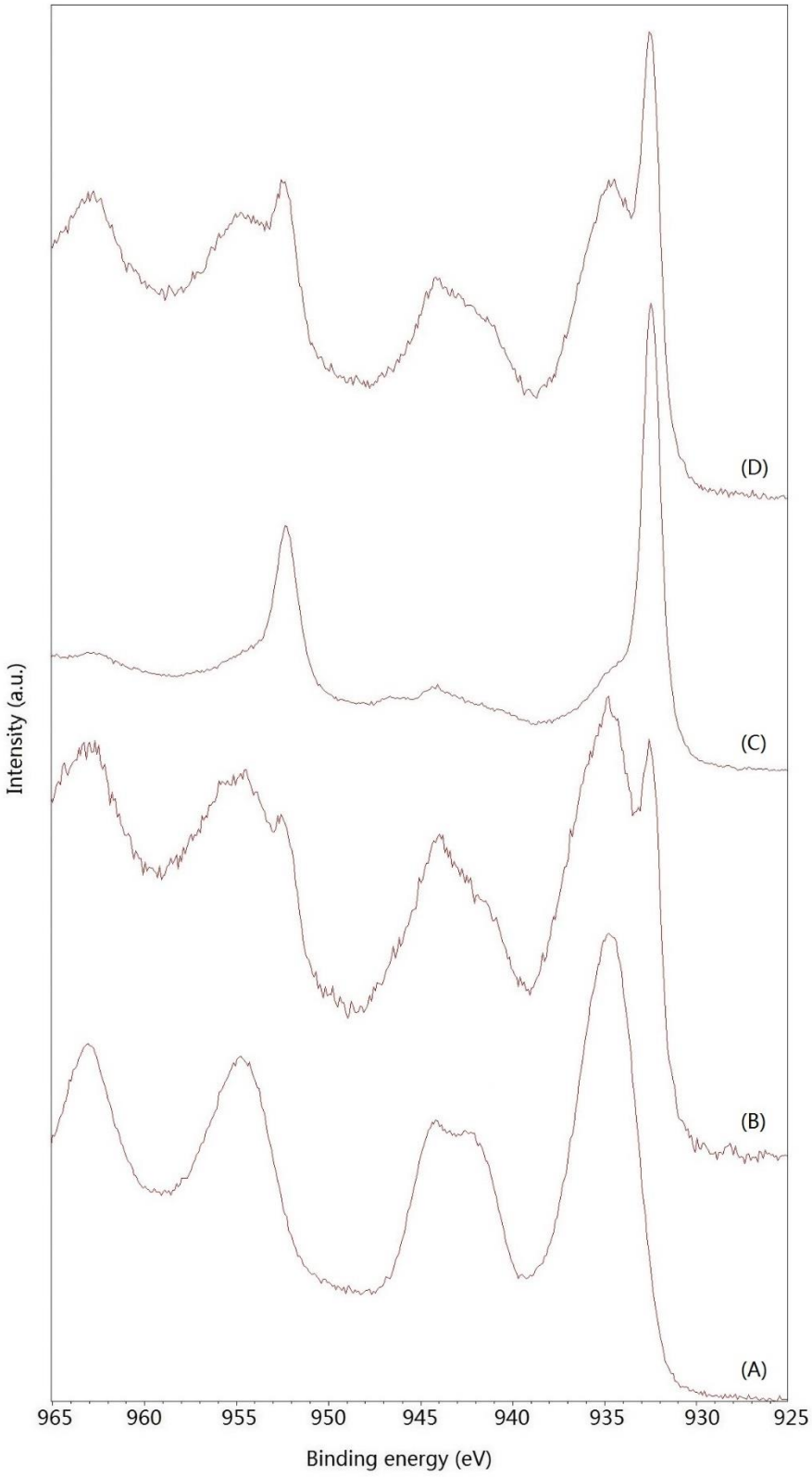

Figure A-10. High resolution Cu 2p XPS spectra for the electrode after applying potential in pH 8 CO_2 saturated $KHCO_3$ solution after holding 15 minutes at (A) -0.4 V; (B) -0.8 V; (C) -1.2 V. (D) 1 cycle with potential scanned from 0→-1.2→0.4→0 V vs. Ag/AgCl. υ=100 $mV \cdot s^{-1}$.

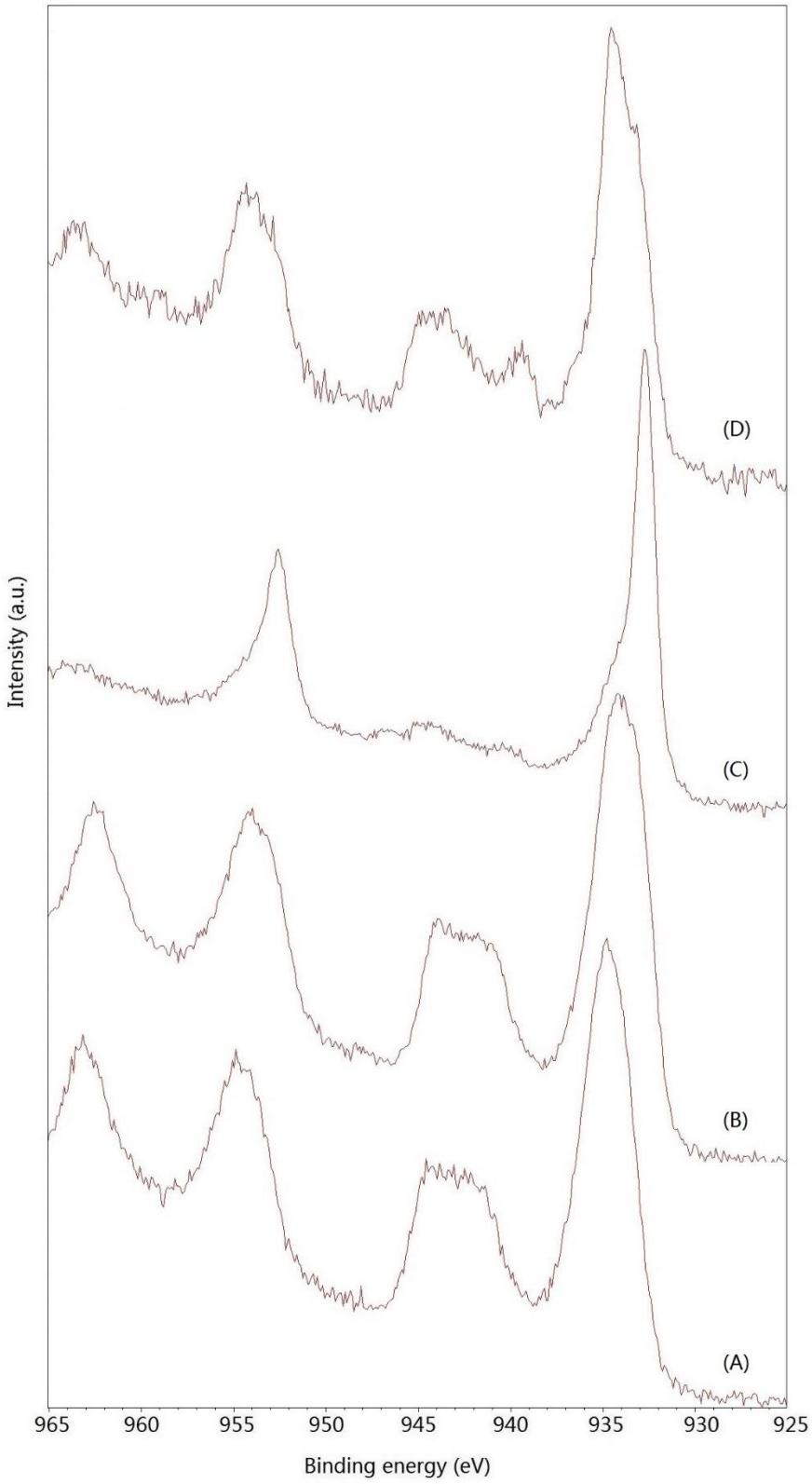

Figure A-11. High resolution Cu 2p XPS spectra for the electrode after applying potential in pH 11 Ar deoxygenated K_2CO_3 solution after holding 15 minutes at (A) -0.4 V; (B) -0.8 V; (C) -1.2 V. (D) 1 cycle with potential scanned from 0→-1.2→0.4→0 V vs. Ag/AgCl. υ=100 mV·s^{-1}.

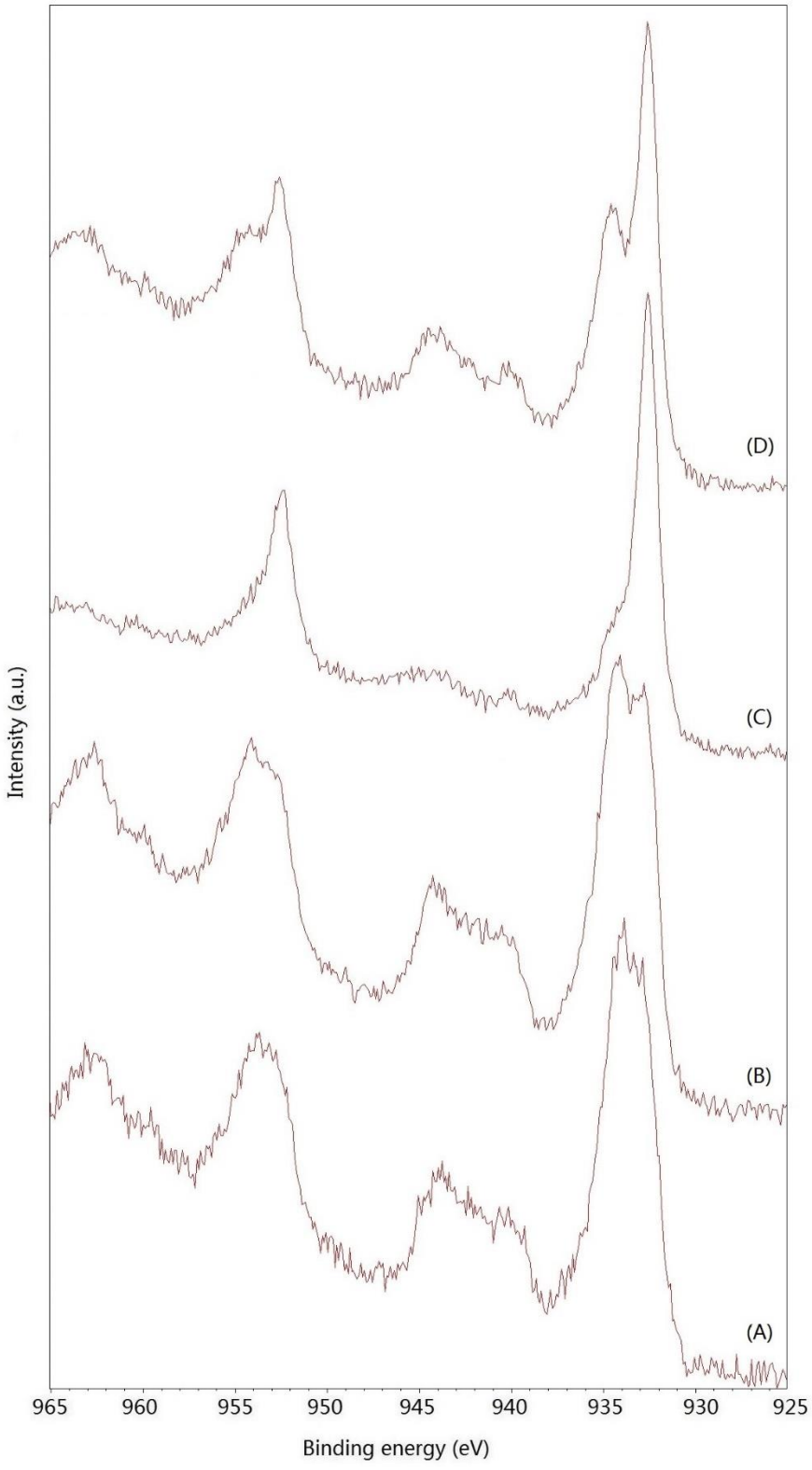

Figure A-12. High resolution Cu 2p XPS spectra for the electrode after applying potential in pH 11 CO_2 saturated K_2CO_3 solution after holding 15 minutes at (A) -0.4 V; (B) -0.8 V; (C) -1.2 V. (D) 1 cycle with potential scanned from 0→-1.2→0.4→0 V vs. Ag/AgCl. υ=100 $mV \cdot s^{-1}$.

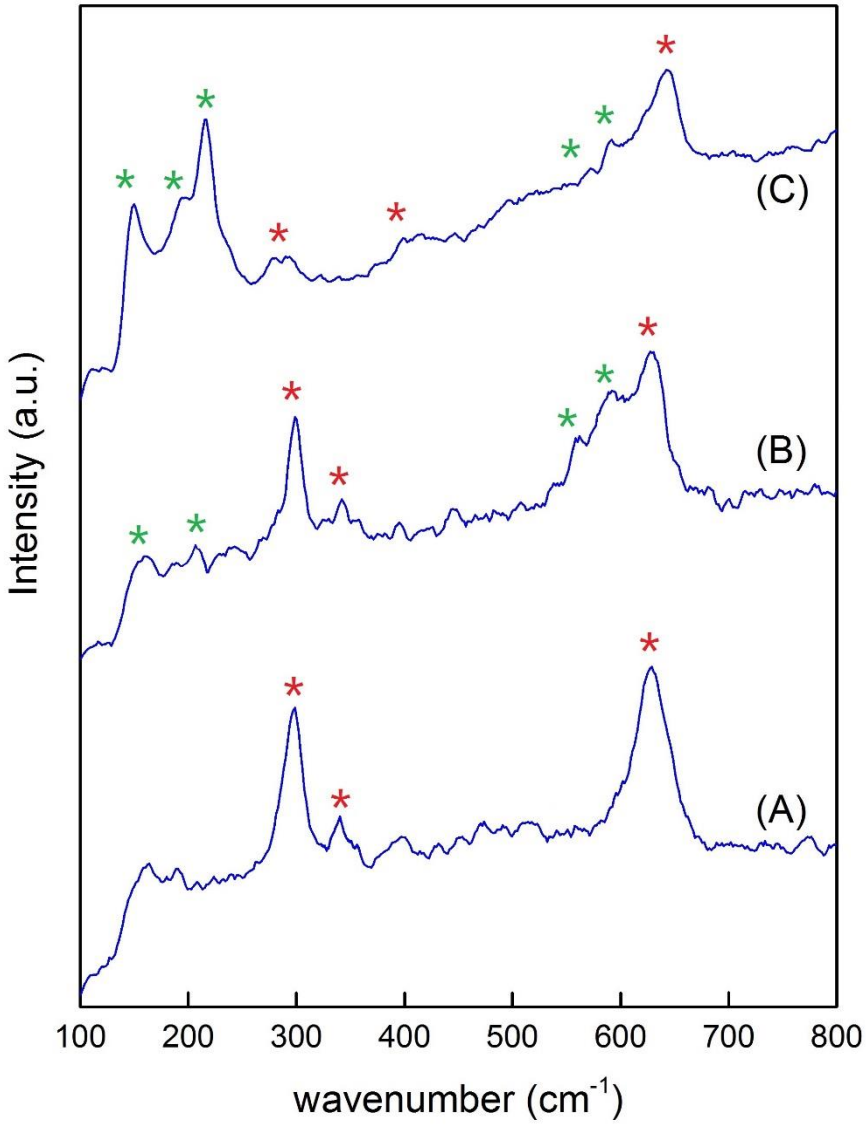

Figure A-13. Raman spectra for the electrode after applying potential in pH 4 Ar deoxygenated PBS at (A) -0.4 V; (B) -0.8 V; (C) -1.2 V. Red star: CuO mode, green star: Cu_2O mode.

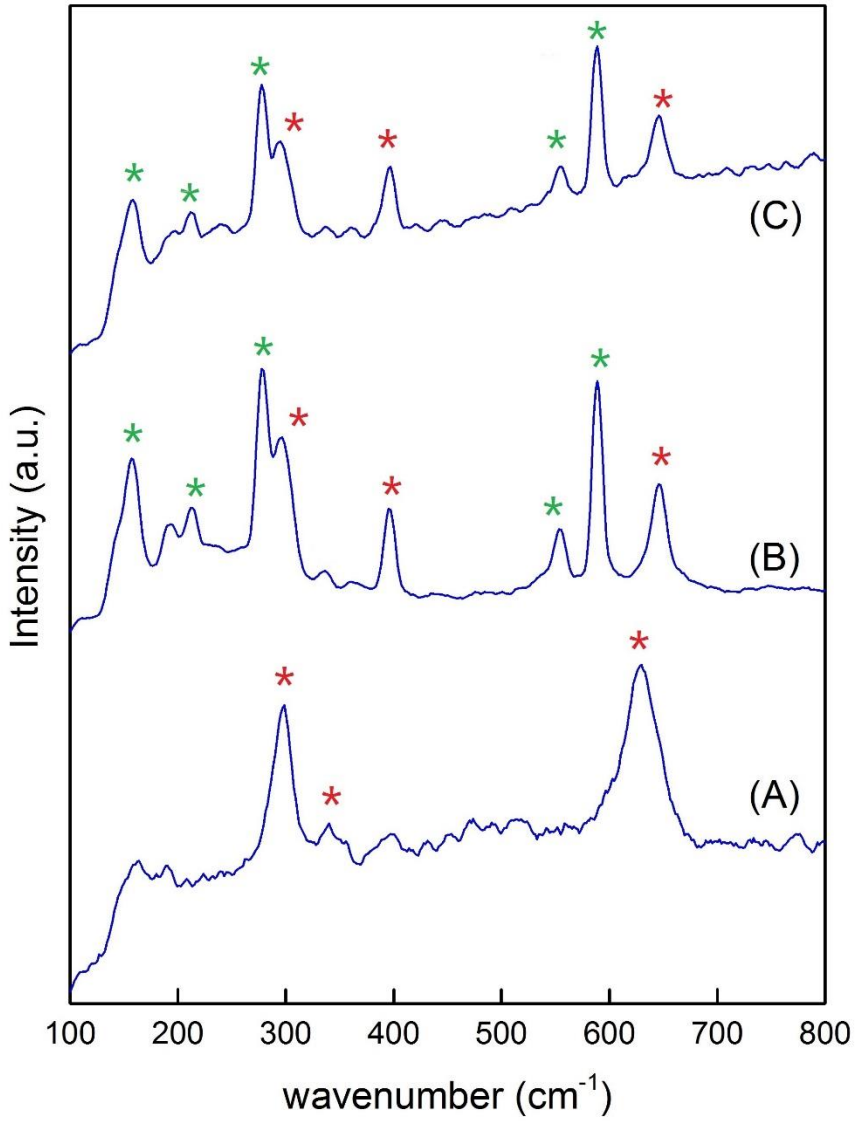

Figure A-14. Raman spectra for the electrode in pH 4 Ar deoxygenated PBS after: (A) holding 15 minutes at -0.4 V; (B) 1 cycle; (C) 10 cycles. For (B) and (C) the potential was scanned from 0→-1.2→0.4→0 V vs. Ag/AgCl. υ=100 mV·s^{-1}. Red star: CuO mode, green star: Cu_2O mode.

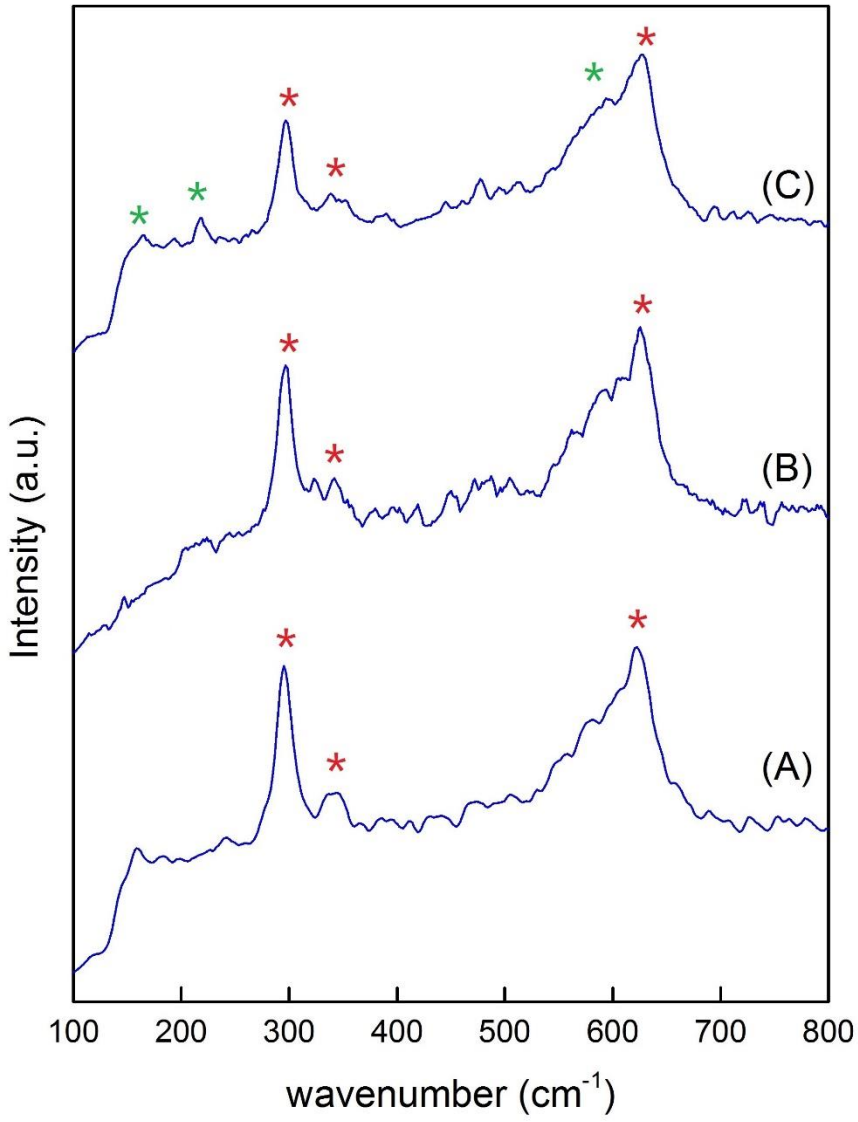

Figure A-15. Raman spectra for the electrode after applying potential in pH 4 CO_2 saturated PBS at (A) -0.4 V; (B) -0.8 V; (C) -1.2 V. Red star: CuO mode, green star: Cu_2O mode.

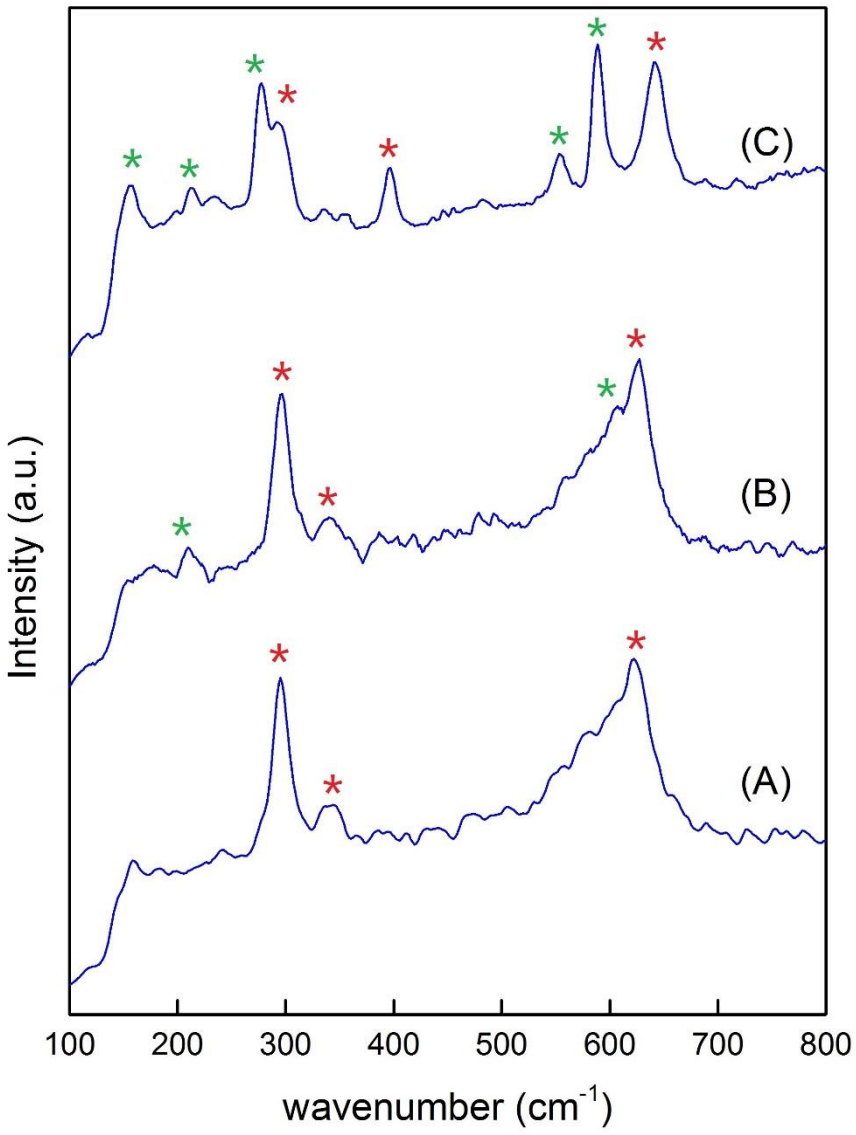

Figure A-16. Raman spectra for the electrode in pH 4 CO_2 saturated PBS after: (A) holding 15 minutes at -0.4 V; (B) 1 cycle; (C) 10 cycles. For (B) and (C) the potential was scanned from 0→-1.2→0.4→0 V vs. Ag/AgCl. υ=100 mV·s^{-1}. Red star: CuO mode, green star: Cu_2O mode.

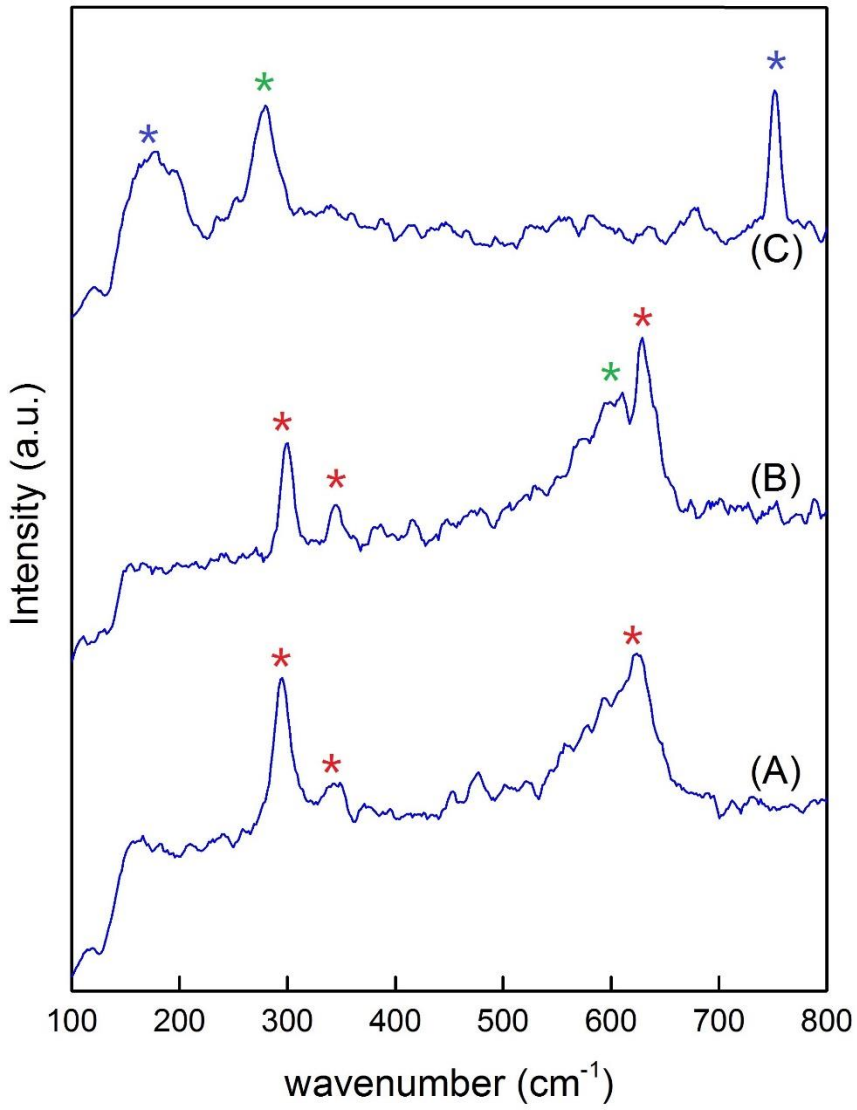

Figure A-17. Raman spectra for the electrode after applying potential in pH 9 Ar deoxygenated PBS at (A) -0.4 V; (B) -0.8 V; (C) -1.2 V. Red star: CuO mode, green star: Cu_2O mode, blue star: $Cu(OH)_2$ mode.

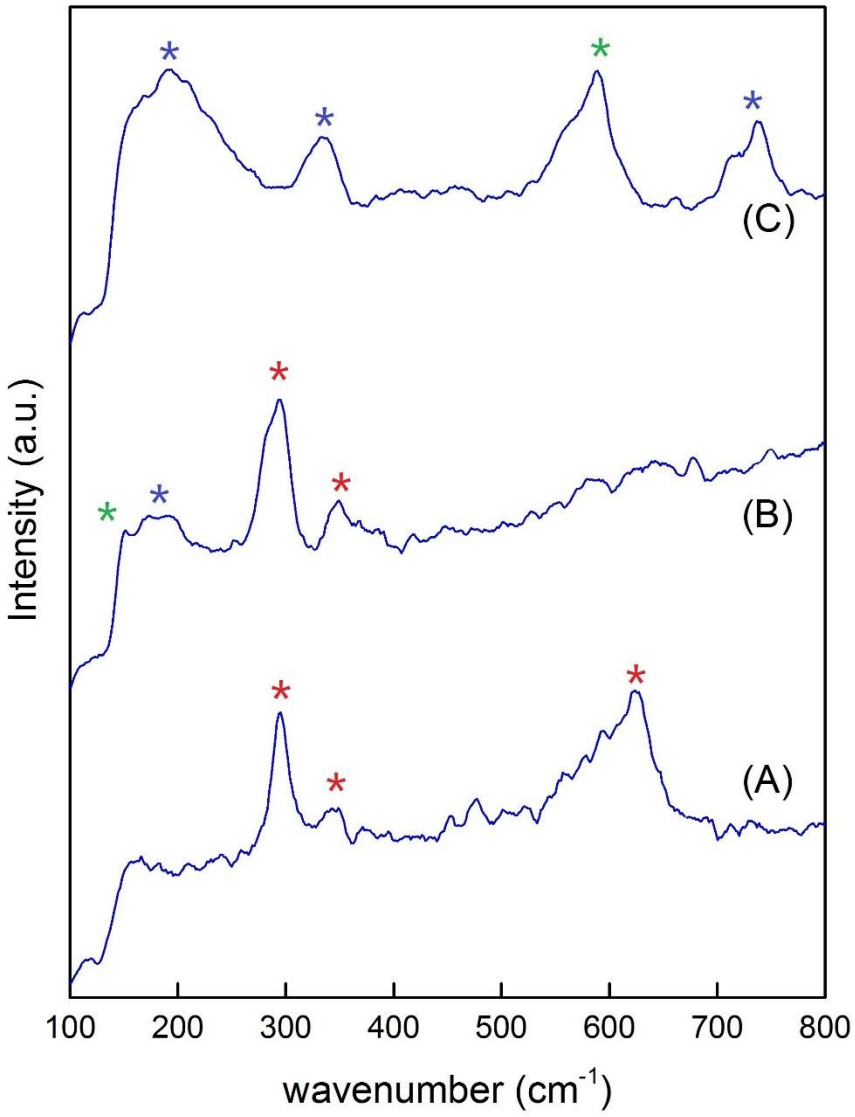

Figure A-18. Raman spectra for the electrode in pH 9 Ar deoxygenated after: (A) holding 15 minutes at -0.4 V; (B) 1 cycle; (C) 10 cycles. For (B) and (C) the potential was scanned from 0→-1.2→0.4→0 V vs. Ag/AgCl. υ=100 mV·s^{-1}. Red star: CuO mode, green star: Cu_2O mode, blue star: $Cu(OH)_2$ mode.

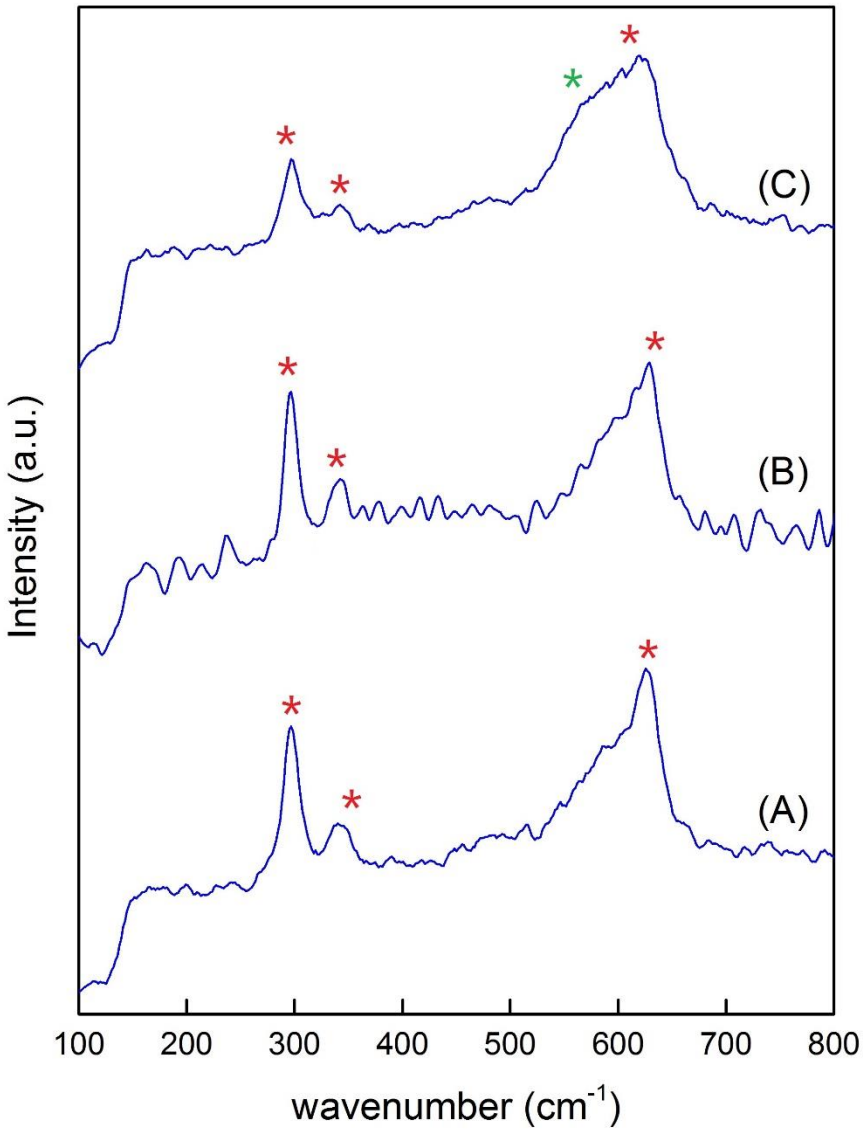

Figure A-19. Raman spectra for the electrode after applying potential in pH 9 CO_2 saturated PBS at (A) -0.4 V; (B) -0.8 V; (C) -1.2 V. Red star: CuO mode, green star: Cu_2O mode.

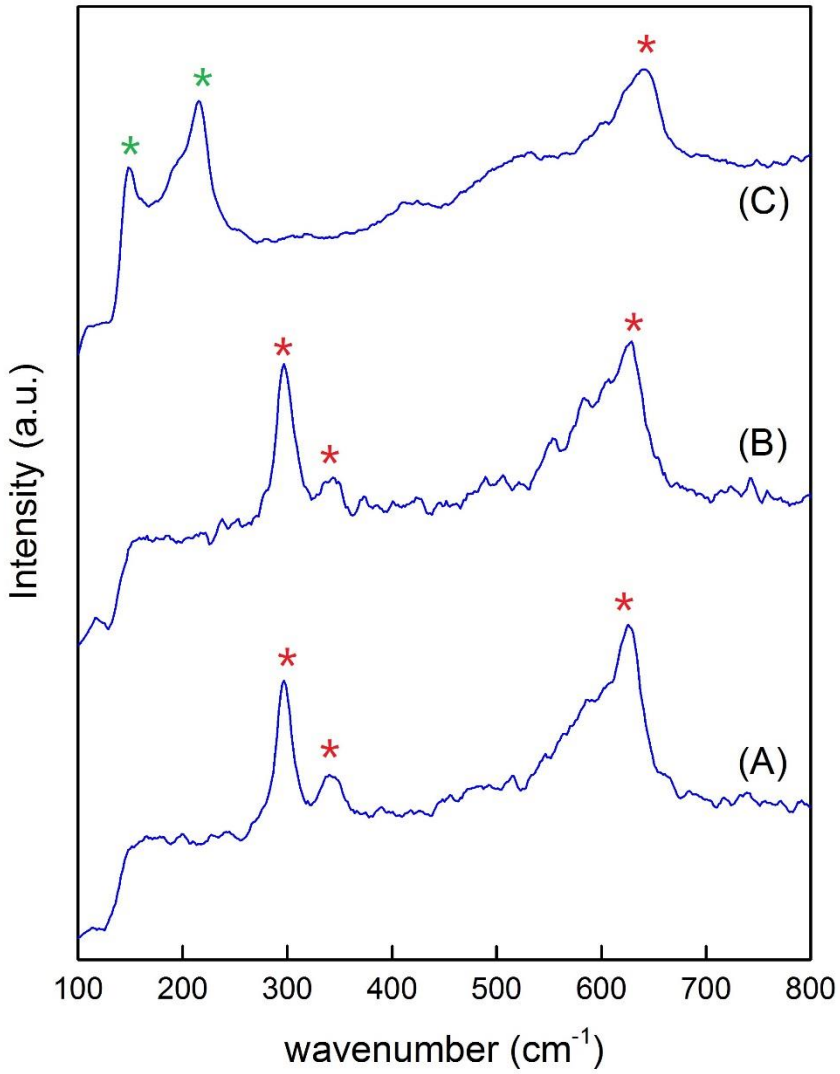

Figure A-20. Raman spectra for the electrode in pH 9 CO_2 saturated PBS after: (A) holding 15 minutes at -0.4 V; (B) 1 cycle; (C) 10 cycles. For (B) and (C) the potential was scanned from 0→-1.2→0.4→0 V vs. Ag/AgCl. υ=100 $mV \cdot s^{-1}$. Red star: CuO mode, green star: Cu_2O mode.

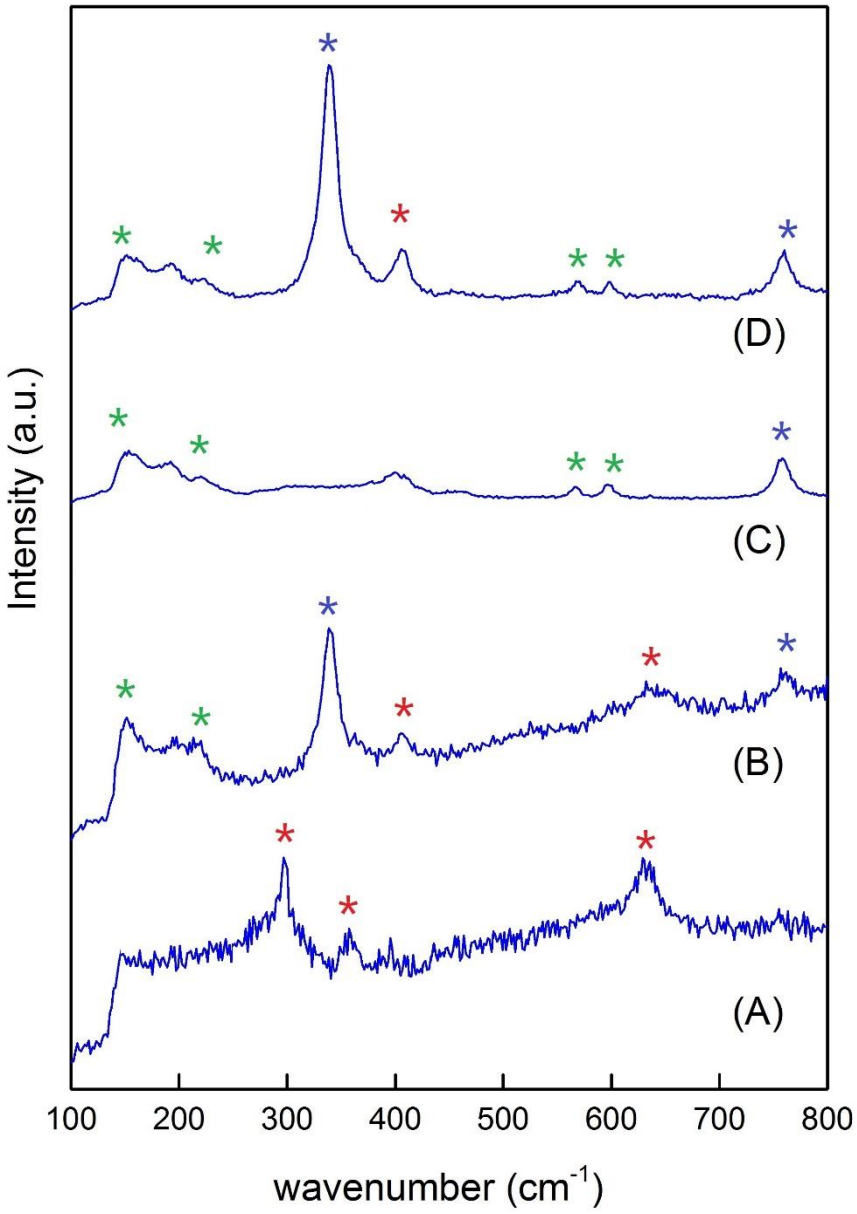

Figure A-21. Raman spectra for the electrode in pH 8 Ar deoxygenated $KHCO_3$ solution after holding 15 minutes at (A) -0.4 V; (B) -0.8 V; (C) -1.2 V. (D) 1 cycle with potential scanned from 0→-1.2→0.4→0 V vs. Ag/AgCl. υ=100 mV·s^{-1}. Red star: CuO mode, green star: Cu_2O mode, blue star: $Cu(OH)_2$ mode.

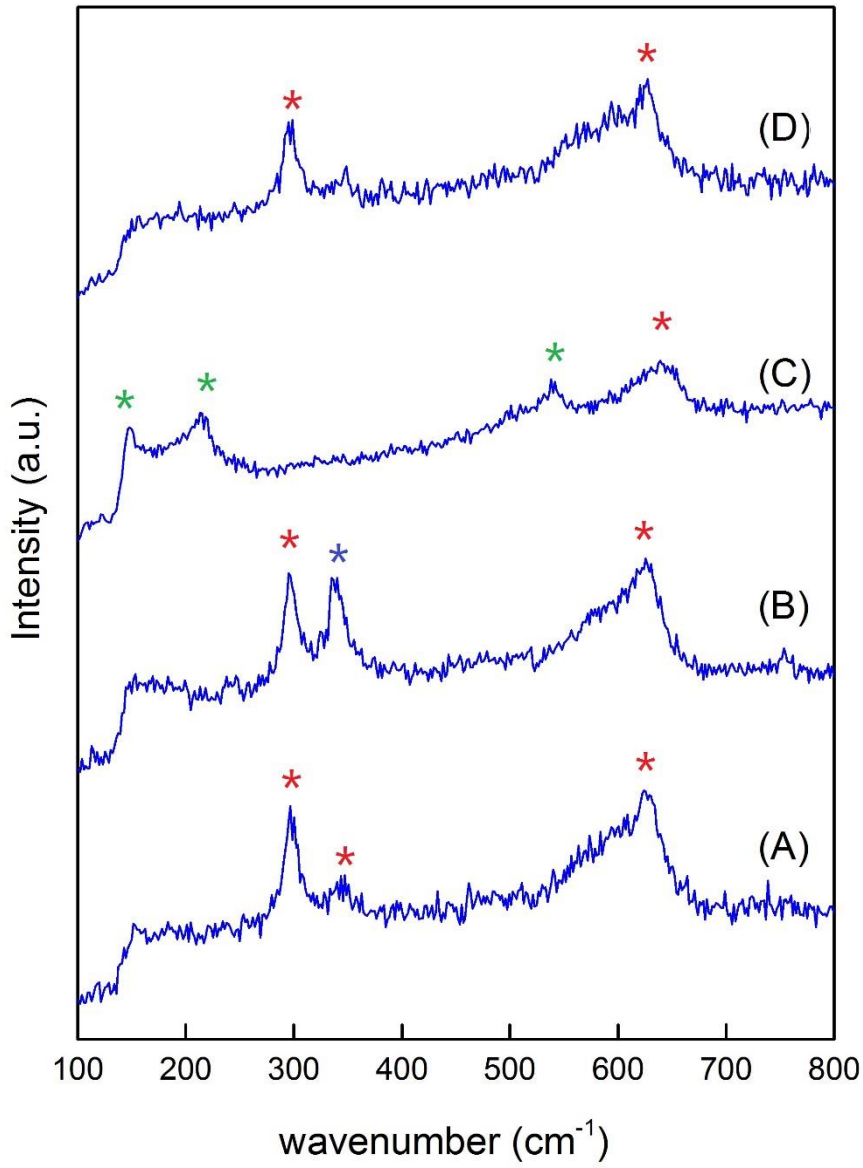

Figure A-22. Raman spectra for the electrode in pH 8 CO_2 saturated $KHCO_3$ solution after holding 15 minutes at (A) -0.4 V; (B) -0.8 V; (C) -1.2 V. (D) 1 cycle with potential scanned from 0→-1.2→0.4→0 V vs. Ag/AgCl. υ=100 $mV \cdot s^{-1}$. Red star: CuO mode, green star: Cu_2O mode, blue star: $Cu(OH)_2$ mode.

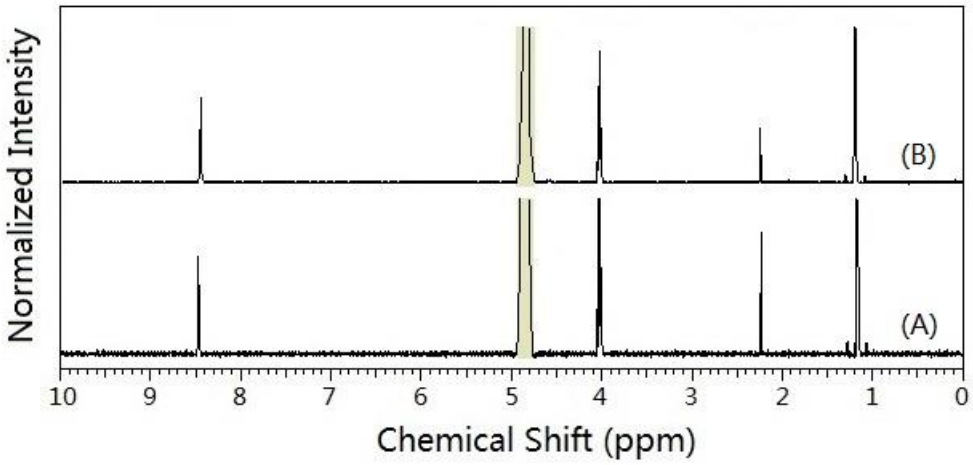

Figure A-23. ^{1}H NMR spectra for the electrolyte for CO_2 saturated solution at -1.2 V for 8 hours in (A) 0.2 M pH 9 PBS, (B) 0.5 M pH 8 $KHCO_3$ solution.